REMTECH inc.

Huntsville, Alabama

TABLE OF CONTENTS

VOLUME I

TABLE OF CONTENTS CONTINUED

FOREWORD

This document is the final report describing the results of a study conducted by REMTECH, Inc. under Contract NAS8-33373 for the Systems Dynamics Laboratory of the National Aeronautic and Space Administration (NASA) Marshall Space Flight Center (MSFC). This fulfills the reporting requirements of the last three statements of work under this contract. NASA technical coordination for the study was provided by Mr. Lee Foster, ED33, of the Thermal Environments Branch of the Systems Dynamics Laboratory.

ABSTRACT

This report discusses the evaluation of aerothermal flight measurements made on the orbital flight test Space Shuttle External Tanks (ETs). Six ETs were instrumented to measure various quantities during flight; including heat transfer, pressure, and structural temperature. The flight data was reduced and analyzed against math models established from an extensive wind tunnel data base and empirical heat-transfer relationships. This analysis has supported the validity of the current aeroheating methodology and existing data base; and, has also identified some problem areas which require methodology modifications.

Section 1

INTRODUCTION

The Space Shuttle Program dedicated the first four flights as Orbital Flight Tests (OFTs). These flights used vehicle elements outfitted with Development Flight Instrumentation (DFI) in order to verify the Space Shuttle system (see Fig. 1.1 for the Shuttle launch configuration) for operational use. The External Tanks (ETs) used on STS-5 and STS-7, although these were considered operational flights, were also instrumented with DFI. Of interest for this report is the aerothermal DFI, consisting of total and radiation calorimeters, pressure sensors, and thermocouples.

The basic purpose of this post-flight data evaluation is to verify the ET ascent aeroheating methodology which has been established from an extensive wind tunnel data base and theoretical considerations. The evaluation will examine the validity of the wind tunnel simulations of the vehicle geometry and flight conditions, and indicate the viability of the procedure used in scaling the model data to flight conditions. An additional objective of the flight data evaluation is to isolate and improve those portions of the methodology shown to be inadequate by the flight data.

References 1 and 2 give details of flight evaluation conducted after the STS-1 aerothermal data became available. The OFT flights were flown in progressively more severe missions insofar as aeroheating environments are concerned. STS-1 through STS-4

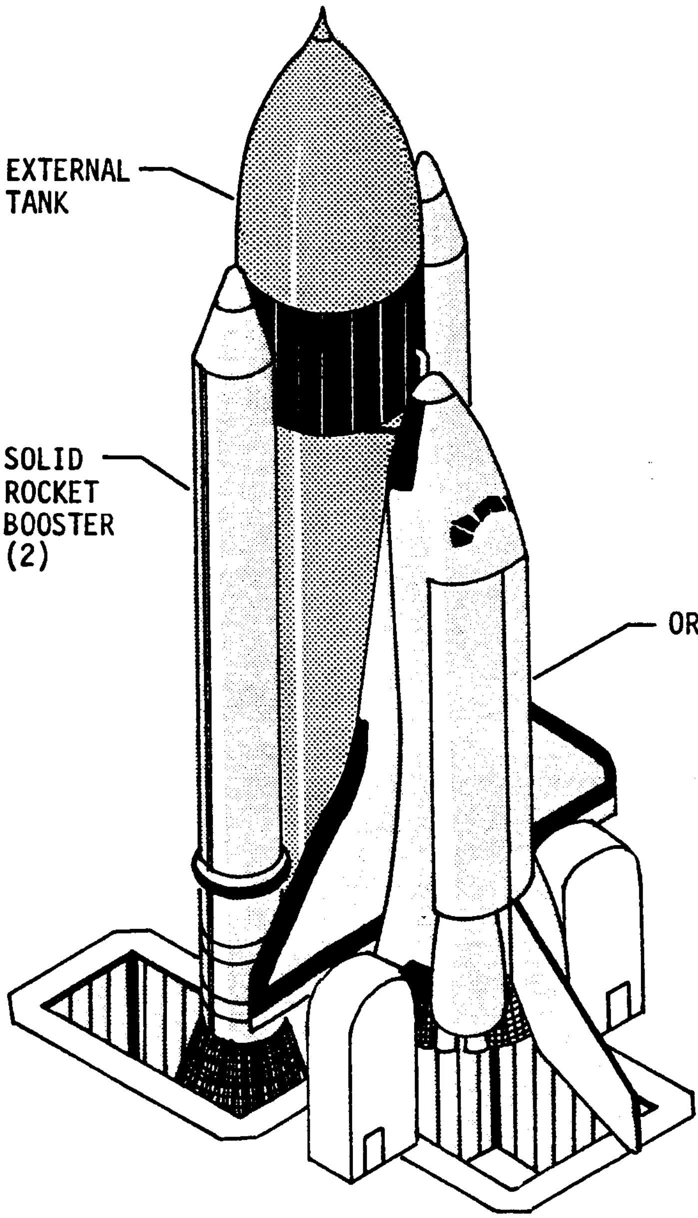

Fig. 1.1 Space Shuttle Launch Configuration

flights were specifically designed for the collection of various kinds of flight data, whereas flights STS-5 and STS-7 were used both for measuring flight data and for flight operational purposes. The flight evaluation in this document has resulted in determining scalability of ground test data to flight conditions. The results of the flight evaluation have already been used in updating the design aeroheating data base so that work can proceed in removing undue conservatism in the prediction methodology. This has enabled optimization of the thermal protection system (TPS) for the ET external surface, thus increasing the amount of Shuttle payload and reducing cost.

Evaluation of the flight aerothermal data required the following: (1) definition of the flight trajectories; (2) the Development Flight Instrumentation wind tunnel data base; (3) flowfield and heat-transfer math models for subsonic, supersonic, and hypersonic flight conditions; and (4) flight data reduction procedure. The intent of this report is to present the evaluation of the OFT ET flight data using the methodology developed at MSFC and REMTECH over the last few years.

Section 2 in this report describes the Development Flight Instrumentation package used to measure heat-transfer rate, pressure, and structural temperature on the OFT flight vehicles.

Section 3 details the various flight trajectories; all the aerothermal flight measurements; the complete data reduction procedure, including the appropriate corrections; and, finally, the analysis of the flight data in conjunction with the flight predictions.

Section 4 discusses the updates necessary for the overall prediction methodology, including updates necessary for the existing DFI data base from the OFT-derived statistical data base.

Section 5 discusses the overall conclusions and provides useful recommendations.

Volumes II and III of this document contain 5 Appendices. Appendix A contains plots for the aerothermal comparisons, where the figures are numbered as A.xx. In a similar fashion, Appendix B contains flight-derived h_i/h_u vs. M_∞ plots, where the figures are numbered as B.xx. The write-up in Volume I of this document refers to these figures time and again.

Section 2

DEVELOPMENT FLIGHT INSTRUMENTATION

The instrumented ETs were outfitted with various types of gages. Due to the extremely cold surfaces of the aluminum structure, which contains liquid Oxygen (LO_2) and liquid Hydrogen (LH_2), a design was required to house and insulate the pressure transducers, microphones, and calorimeters from the cryogenic temperatures. Instrument modules, which isolated the sensors but which protruded above the surrounding TPS surface, were designed to minimize local flow disturbances. These designs, referred to as instrumentation islands, were flat-topped circular modules, ranging in diameter from 8-14 inches and having shallow ablator material (SLA-561) ramps of approximately 12 degrees. The SLA-561 ramps were blended in with the surrounding foam insulation (CPR-488) such that flow disturbances created by the island itself would have negligible effects on the measurements. Details of the ET instrumentation island used on the LO_2 and LH_2 tank sidewalls are given in Fig. 2.1. The islands used in the stringered intertank region were somewhat different and are sketched in Fig. 2.2. More details about the island and instrument specifications are given in Ref. 3. Each island could house two or three kinds of instruments. The ET protuberances were instrumented by gages which were worked into the the structural member in such a manner that the effects of the gage on the local flow were negligible.

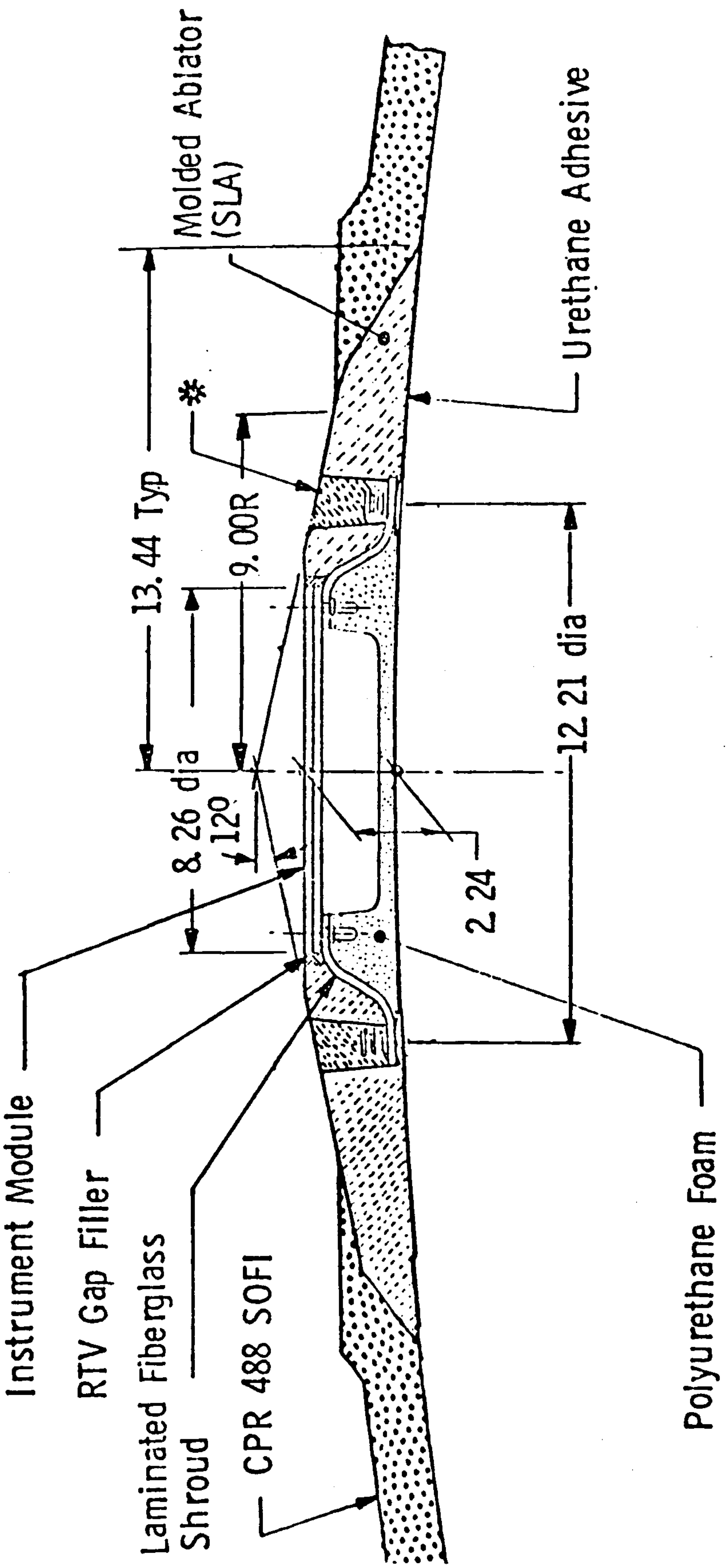

Fig. 2.1 Details of ET Instrumentation Island on LO_2 & LH_2 Tank Side Wall

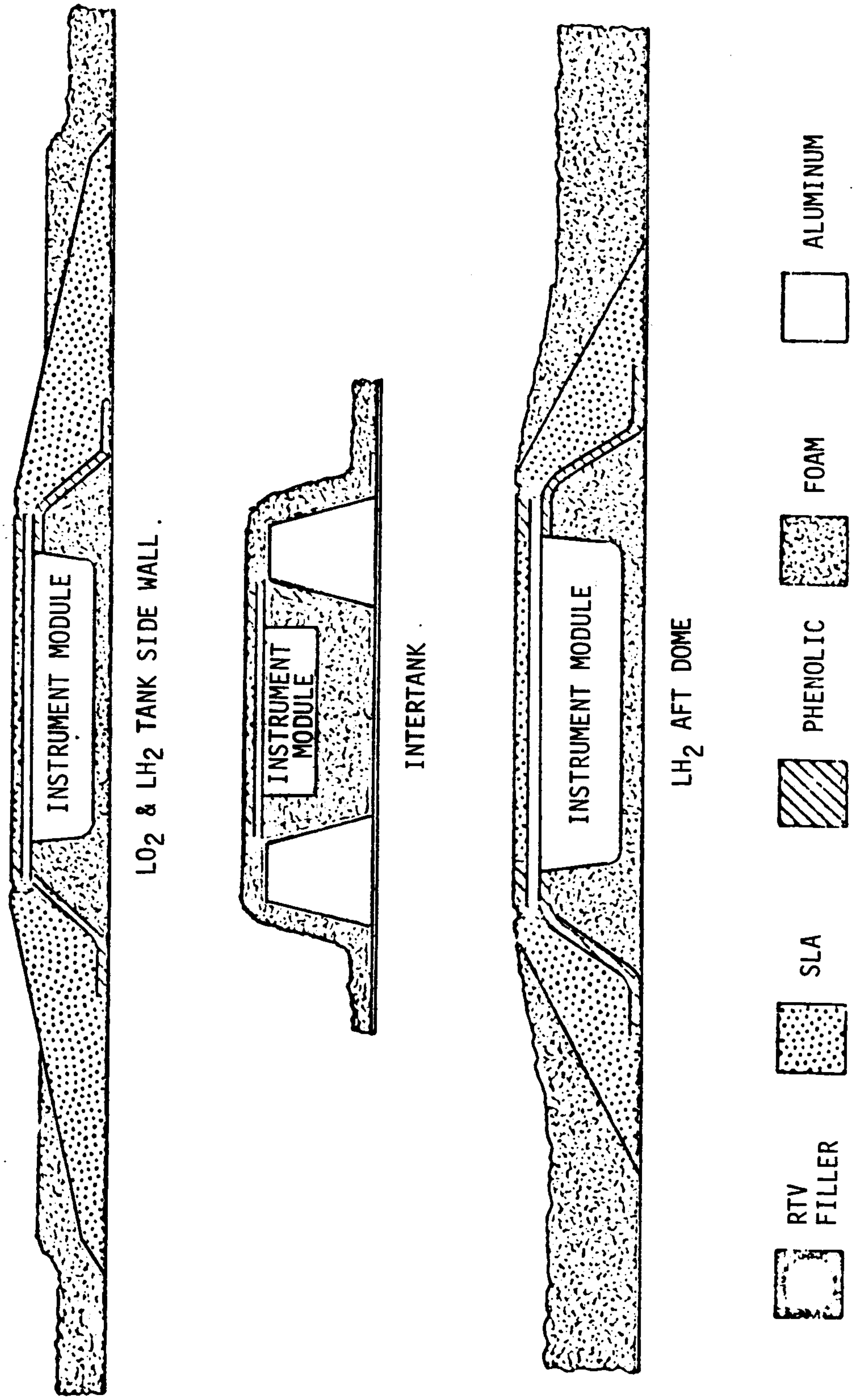

Fig. 2.2 ET Instrument Island Cross Sections

Of interest to the work in this report are the heat-transfer, pressure, and structural temperature measurements. The various measurements were obtained on six flight tanks during the OFT test program. There was a total of 41 heat-transfer, 28 pressure, and 61 structural temperature sensors that were installed during the various test flights. The details of the above gages are provided in Figs. 2.3 and 2.4 and Tables 2.1 - 2.3. The tables provide the measurement identification numbers (MSID), corresponding Rockwell International (RI) body points, and the location and description of the gages. The figures, on the other hand, give the relative location of the gages on the ET surface and its protuberances.

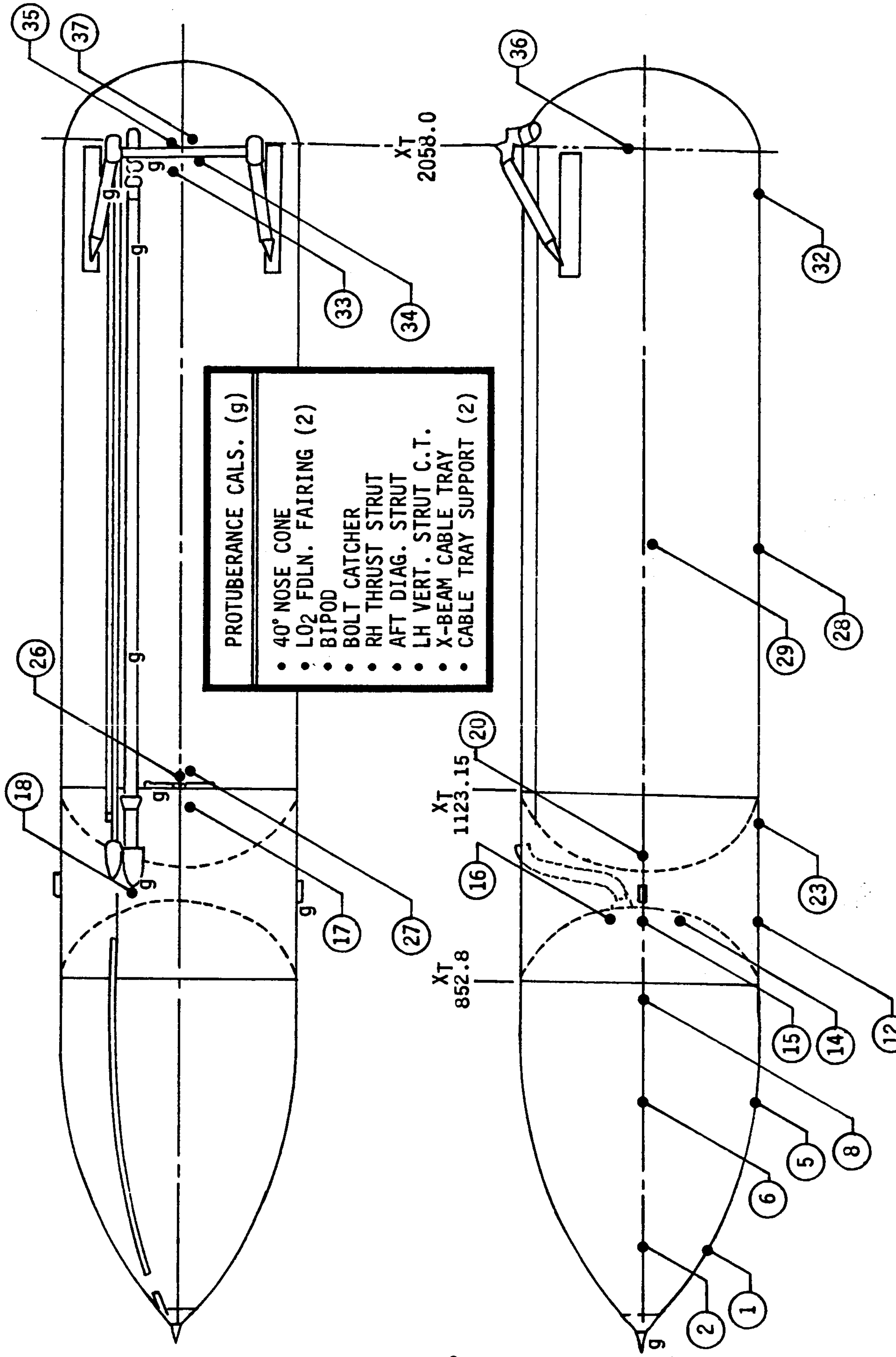

Fig. 2.3 Location of Acreage and Protuberance Islands and Gages

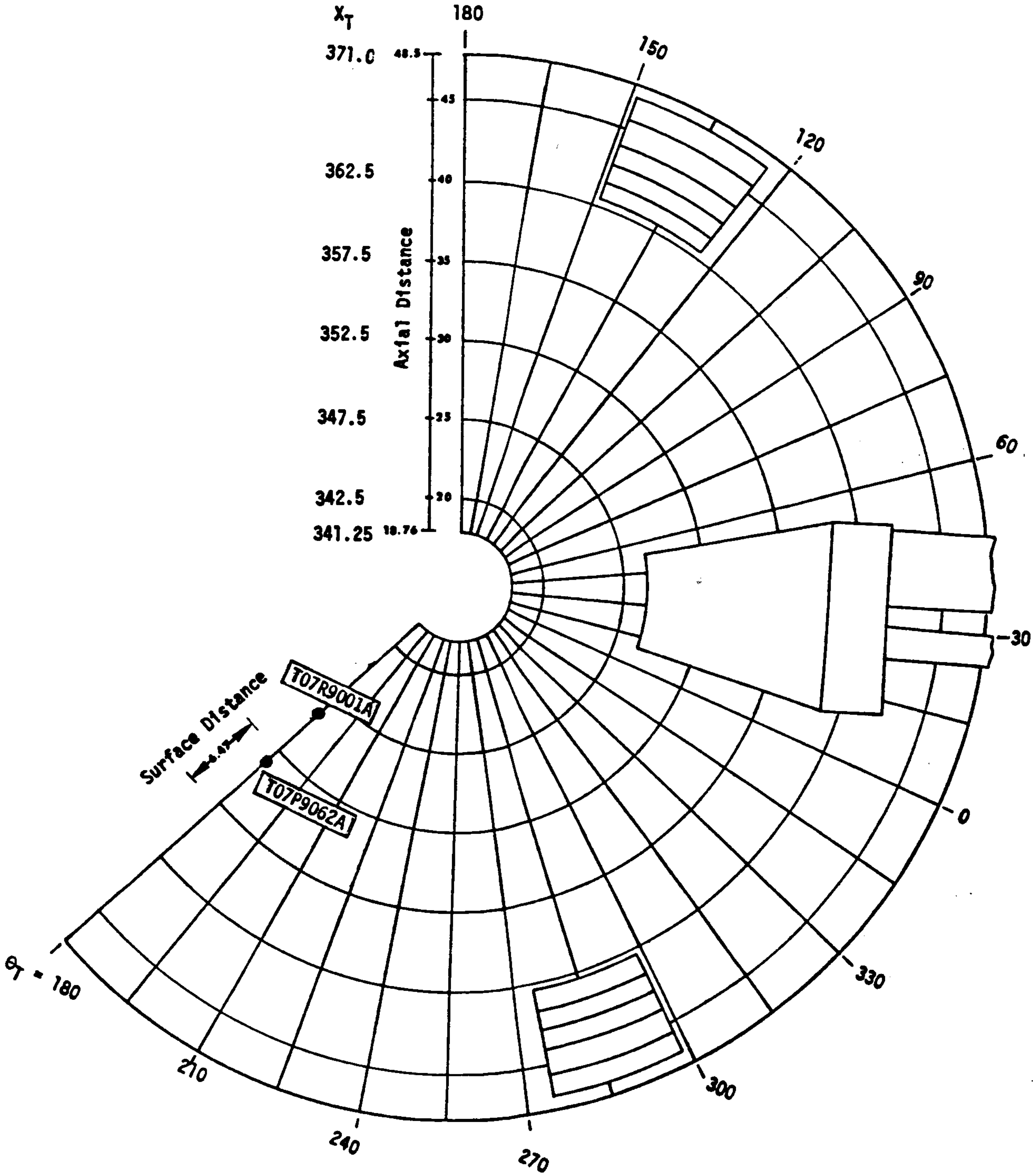

Fig. 2.4a Location of Gages T07R9001A and T07P9062A on the ET Nose 40° Cone (Actual Cone Angle = 39.38°)

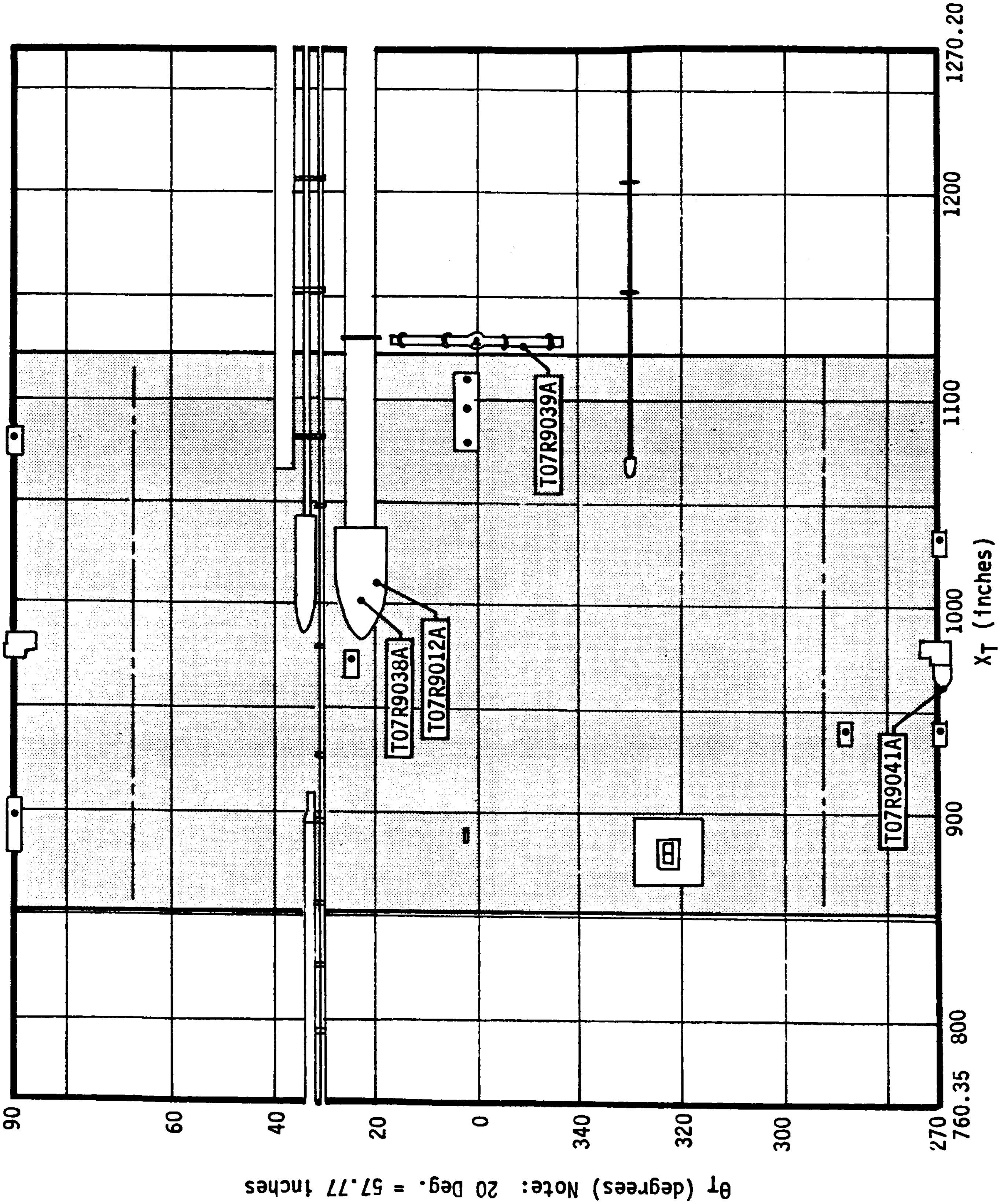

Fig. 2.4b Protuberance Gage Locations on Intertank Section

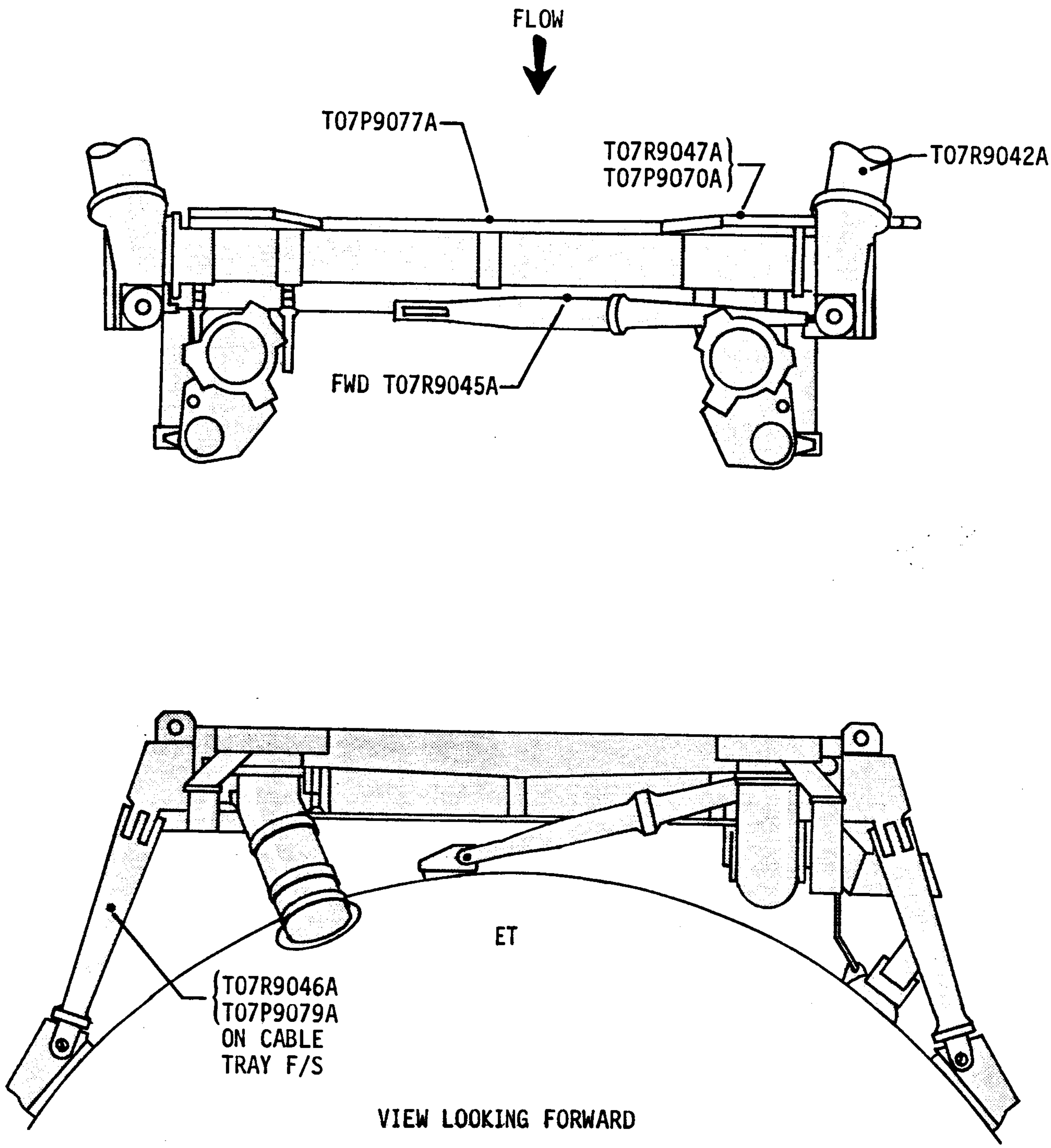

Fig. 2.4d Aft Strut Protuberance DFI Locations

TABLE 2.1
STS ET DFI GAGE LOCATIONS
(AEROHEATING MEASUREMENTS)

MEASUREMENT I.D.	RI BODY POINT	XT (in.)	THETA (deg.)	MEASUREMENT RANGE	GAGE TYPE	LOCATION
T07R9001A	90100	344.6	180.0	0 - 15	Ind. Gage	40° Cone
T07R9004A	91102	467.4	264.0	0 - 10	Island 2	LO2 Tank
T07R9005A	91101	467.4	174.0	0 - 10	Island 1	LO2 Tank
T07R9007A	91106	672.5	270.0	0 - 5	Island 6	LO2 Tank
T07R9008A	91105	672.5	180.0	0 - 5	Island 5	LO2 Tank
T07R9010A	91108	825.5	270.0	0 - 5	Island 8	LO2 Tank
T07R9011A	92118	976.0	25.0	0 - 10	Island 18	Intertank
T07R9012A	95112	1008.0	21.0	0 - 10	Ind. Gage	LO2 Fdln. Fairing (side)
T07R9013A	392117	1110.4	2.5	0 - 10	Island 17(3)	Intertank
T07R9014A	92116	941.4	288.6	0 - 10	Island 16	Intertank
T07R9015A	92115	941.4	270.0	0 - 15	Island 15	Intertank
T07R9016A	92114	941.4	251.4	0 - 10	Island 14	Intertank
T07R9017A	92112	941.4	180.0	0 - 5	Island 12	Intertank
T07R9018A	292117	1098.5	2.5	0 - 10	Island 17(2)	Intertank
T07R9019A	192117	1084.4	2.5	0 - 10	Island 17(1)	Intertank
T07R9020A	93127	1147.4	358.0	0 - 15	Island 27	LH2 Barrel
T07R9021A	92120	1034.2	270.0	0 - 5	Island 20	Intertank
T07R9022A	92123	1082.0	180.0	0 - 5	Island 23	Intertank
T07R9023A	92126	1130.3	0.0	0 - 15	Island 26	LH2 Barrel
T07R9025A	93129	1489.0	264.4	0 - 5	Island 29	LH2 Barrel
T07R9026A	93128	1489.0	172.5	0 - 5	Island 28	LH2 Barrel
T07R9027A	93133	2017.0	5.6	0 - 10	Island 33	LH2 Barrel
T07R9028A	93135	2057.0	5.6	0 - 5	Island 35	LH2 Barrel
T07R9029A	93132	2002.5	168.7	0 - 5	Island 32	LH2 Barrel
T07R9030A	93134	2038.97	356.3	0 - 10	Island 34	LH2 Barrel
T07R9031A	93136	2057.0	276.0	0 - 15	Island 36	LH2 Barrel
T07R9032A	93137	2057.0	340.6	0 - 15	Island 37	LH2 Barrel
T07R9038A	95138	996.0	23.0	0 - 10	Ind. Gage	LO2 Fdln Fairing (top)
T07R9039A	95139	1129.9	356.0	0 - 45	Ind. Gage	ET/ORB Fwd LH Strut
T07R9040A	95140	1332.7	37.0	0 - 15	INd. Gage	Cable Tray Support
T07R9041A	95141	959.2	270.0	0 - 25	Ind. Gage	Bolt Catcher
T07R9042A	95142	2002.0	29.0	0 - 5	Ind. Gage	RH Thrust Strut
T07R9043A	95143	1914.1	37.0	0 - 15	Ind. Gage	Cable Tray Support
T07R9045A	95145	2058.0	10.0	0 - 10	Ind. Gage	Aft Diag. Strut
T07R9046A	95146	2100.0	45.0	0 - 5	Ind. Gage	LH Vert Strut Cable Tray
T07R9047A	95147	2035.0	26.0	0 - 10	Ind. Gage	Fwd. LO2 Fdln/X-Beam Cable Tray

Table 2.2
STS ET DFI GAGE LOCATIONS
(PRESSURE MEASUREMENT)

MEASUREMENT I.D.	XT (in.)	THETA (deg.)	MEASUREMENT RANGE	GAGE DESCRIPTION	LOCATION
T07P9061A	328.8	180.0	0 - 15	Press Sense Port	Nose Cap Press - Z Port
T07P9062A	353.5	180.0	0 - 10	Press Sense Port	Nose Cap Press
T07P9064A	467.4	264.0	0 - 10	Island 2	LO2 TK Press 2
T07P9065A	467.4	174.0	0 - 10	Island 1	LO2 TK Press 3
T07P9066A	672.5	270.0	0 - 10	Island 6	LO2 TK Press 4
T07P9067A	672.5	180.0	0 - 10	Island 5	LO2 TK Press 5
T07P9069A	973.8	25.0	0 - 10	Island 18	Intertank Press 1
T07P9070A	948.0	270.0	0 - 10	Island 15	Intertank Press 2
T07P9071A	1106.4	2.5	0 - 10	Island 17 (3)	Intertank Press 3
T07P9072A	1079.0	180.0	0 - 5	Island 23	Intertank Press 4
T07P9074A	1489.0	172.5	0 - 5	Island 28	LH2 Tk Barrel Press 2
T07P9075A	2002.0	168.8	0 - 5	Island 32	LH2 TK Barrel Press 3
T07P9076A	2039.0	356.3	0 - 5	Island 34	LH2 TK Barrel Press 4
T07P9077A	------	-----	0 - 10	Ind. Gage	Aft Attach Crossbeam Cable Tray Press
T07P9078A	------	-----	0 - 10	Assoc. Gage (9047)	Fwd LO2 Fdin/X-Beam Cable Tray Press
T07P9079A	------	-----	0 - 10	Assoc. Gage (9046)	ET/ORB LH Vert Strut Cable Tray Press
T07P9550A	327.7	0.0	0 - 15	Press Sense Port	Nose Cap Total Press
T07P9551A	328.8	z-axis	-2 - +2	Press Sense Port	Nose Cap Diff-Press-Pitch
T07P9552A	378.8	y-axis	-2 - +2	Press Sense Port	Nose Cap Diff-Press-Yaw
T07P9560A	903.2	90.0	0 - 15	Island 11	Intertank Compt Ext Press 1
T07P9561A	1075.9	90.0	0 - 15	Island 21	Intertank Compt Ext Press 2

Table 2.3a

DFI SUMMARY
Thermocouples on the ET Protuberances

Measurement I. D.	RI Body Point	XT (In.)	THETAT (deg.)	Measurement Range	Kind of Gage	Location
T09T9553A		350.0		-100 +100	T/C	Nose Cap AADS package
T09T9602A				-300 +100	T/C	LO2 Fwd Cover Plate
T09T9633A				0 +350	T/C	Mid ET/ORB Fwd Attach LH (Look fwd)
T09T9634A		1332.7	37.0	0 +350	T/C	Cable Tray
T09T9635A				0 +350	T/C	ET/ORB Fwd Attach RH (Look fwd)
T09T9636A				-100 +200	T/C	+Y ET/SRB Fwd. Attach-Fwd Sur
T09T9637A				0 +350	T/C	+Y ET/ORB RH Thrust Strut Bottom MTD Fwd Sur
T09T9638A				0 +350	T/C	+Y ET/ORB Thrust Strut Top Mt. Fw Sur
T09T9639A				0 +350	T/C	Mid Rt Half Vert Strut Fwd
T09T9640A				0 +350	T/C	Mid Rt Half Vert Strut Aft
T09T9641A				0 +350	T/C	Mid Crossbeam Fwd Sur
T09T9642A				0 +350	T/C	Mid Crossbeam Aft Sur
T09T9643A				-315 +200	T/C	ET/R SRB Aft Attach (+Y) +Z side
T09T9644A				-315 +200	T/C	ET/R SRB Aft Attach (+Y) -Z side
T09T9645A				0 +350	T/C	Mid Diag. Strut (-x side)
T09T9647A		451.0	32	0 +350	T/C	Cable Tray
T09T9648A		739.0	32	0 +350	T/C	Cable Tray
T09T9649A		1232.0	38	0 +350	T/C	Cable Tray
T55T9001A				0 +165	T/C	RSS Panel
T55T9011A		1800.0	32	0 +350	T/C	Cable Tray (LSC)
T55T9012A		850.0	32	0 +350	T/C	Cable Tray (LSC)
T09T9670A				-300 +350	T/C	LO2 UMB Plate Fwd
T09T9671A				-300 +350	T/C	LO2 UMB Plate Aft

Table 2.3b

DFI BODY POINT SUMMARY
Skin Thermocouples

Measurement I. D.	RI Body Point	XT (in.)	THETAT (deg.)	Measurement Range	Kind of Gage	Location
T09T9601A	90301	344.6	180.0	-300 +500	T/C	LO2 Tank
T09T9603A	91303	379.0	0.0	-300 +500	T/C	LO2 Tank
T09T9604A	91304	379.0	90.0	-300 +500	T/C	LO2 Tank
T09T9605A	91305	379.0	180.0	-300 +500	T/C	LO2 Tank
T09T9606A	91306	421.0	90.0	-300 +500	T/C	LO2 Tank
T09T9607A	91307	451.0	0.0	-300 +500	T/C	LO2 Tank
T09T9608A	91308	451.0	90.0	-300 +500	T/C	LO2 Tank
T09T9609A	91309	451.0	180.0	-300 +500	T/C	LO2 Tank
T09T9610A	91310	480.0	90.0	-300 +500	T/C	LO2 Tank
T09T9662A	91362	524.0	90.0	-300 +500	T/C	LO2 Tank
T09T9663A	91363	596.0	0.0	-300 +500	T/C	LO2 Tank
T09T9664A	91364	596.0	180.0	-300 +500	T/C	LO2 Tank
T09T9665A	91365	839.0	90.0	-300 +500	T/C	LO2 Tank
T09T9611A	92311	889.0	90.0	-200 +200	T/C	Intertank
T09T9612A	92312	924.0	90.0	-200 +200	T/C	Intertank
T09T9666A	92366	977.0	58.0	-200 +200	T/C	Intertank
T09T9667A	92367	1072.0	1.0	-200 +200	T/C	Intertank
T09T9668A	92368	1104.0	1.0	-200 +200	T/C	Intertank
T09T9669A	92369	1104.0	28.0	-200 +200	T/C	Intertank
T09T9615A	93315	1137.0	0.0	-430 +100	T/C	LH2 Tank
T09T9616A	93316	1137.0	30.0	-430 +100	T/C	LH2 Tank
T09T9617A	93317	1137.0	60.0	-430 +100	T/C	LH2 Tank
T09T9618A	93318	1137.0	90.0	-430 +100	T/C	LH2 Tank
T09T9619A	93319	1168.0	0.0	-430 +100	T/C	LH2 Tank
T09T9620A	93320	1168.0	60.0	-430 +100	T/C	LH2 Tank
T09T9621A	93321	1168.0	90.0	-430 +100	T/C	LH2 Tank
T09T9622A	93322	1232.0	0.0	-430 +100	T/C	LH2 Tank
T09T9623A	93323	1232.0	60.0	-430 +100	T/C	LH2 Tank
T09T9624A	93324	1489.0	60.0	-430 +100	T/C	LH2 Tank
T09T9625A	93325	1618.0	60.0	-430 +100	T/C	LH2 Tank
T09T9626A	93326	1745.0	0.0	-430 +100	T/C	LH2 Tank
T09T9627A	93327	1745.0	60.0	-430 +100	T/C	LH2 Tank
T09T9628A	93328	1874.0	60.0	-430 +100	T/C	LH2 Tank
T09T9629A	93329	1900.0	60.0	-430 +100	T/C	LH2 Tank
T09T9630A	93330	2046.0	0.0	-430 +100	T/C	LH2 Tank
T09T9631A	93331	2046.0	60.0	-430 +100	T/C	LH2 Tank

Section 3

FLIGHT DATA EVALUATION

As described in Section 1, the purpose of the flight evaluation was to build confidence into the existing wind tunnel data base and math models which are utilized in predicting local aerothermal quantities. An additional and very important aspect of the flight evaluation was to check scalability of ground test data to flight, to isolate those portions of the data base and math model proven inadequate, and to update the methodology as a whole. This section contains a description of the OFT trajectories, aerothermal measurements with associated inherent errors, flight data reduction and flight data analysis.

3.1 TRAJECTORIES

The six flights for which ET DFI measurements were obtained were STS-1, 2, 3, 4, 5 and 7. On STS-6, only SRB DFI aeroheating measurements were taken. Generally speaking, the launch vehicle was subjected to an increase in heating on successive flights. This observation is based on heating indicators run for the stagnation point of a one-foot radius sphere for the above trajectories.

All the above trajectories were obtained from ESDB (Engineering Support Data Base) (Ref. 4) of NASA Marshall Space Flight Center in the form of list-directed files. The final trajectory data were usually available in the ESDB within a few days after the flights. MIPS (Marshall Interactive Periphery System) (Ref. 5) was utilized to make plots of altitude vs. velocity, and time-histories of freestream Mach number, dynamic pressure, freestream static temperature, pressure, and density as presented in Figs. 3.1, 3.5, 3.6, 3.7, 3.8 and 3.9, respectively.

The altitude-velocity plots, which are given between lift-off and trajectory times close to MECO (Main-Engine-Cut-off) in Figs. 3.1a and 3.1b, show that flights 5, 6 and 7 are fairly close to each other, whereas flights 1, 2, 3 and 4 were somewhat different from each other in the first stage and significantly different from each other in the second stage. This observation is made clearer in Figs. 3.2 and 3.3. Figure 3.2 gives altitude-velocity variation in the first stage along with the peak heating rates and heat loads between t = 0 to t = 125 secs. based on a one-foot radius sphere. Also given in the figure is a plot of the design trajectory (RI 1980 thermal design trajectory is a mission 3A dispersed Right Quartering Head Wind, engine out @ 260 sec. Abort-Once-Around case). Clearly, the design trajectory is hotter than all the OFT trajectories. Figure 3.3 gives the differences between altitude-velocity profiles for the second stage flight. Again, the design trajectory is hotter than the OFT trajectories both in the second stage and total flight from lift-off to MECO, as seen from the table in Fig. 3.3. The heating indicators for all the above trajectories along with the design trajectory are given for a 70-150 sec. range in Fig. 3.4, which shows calculated cold-wall (T_W=0^{O}F) heating rates as a function of time for a

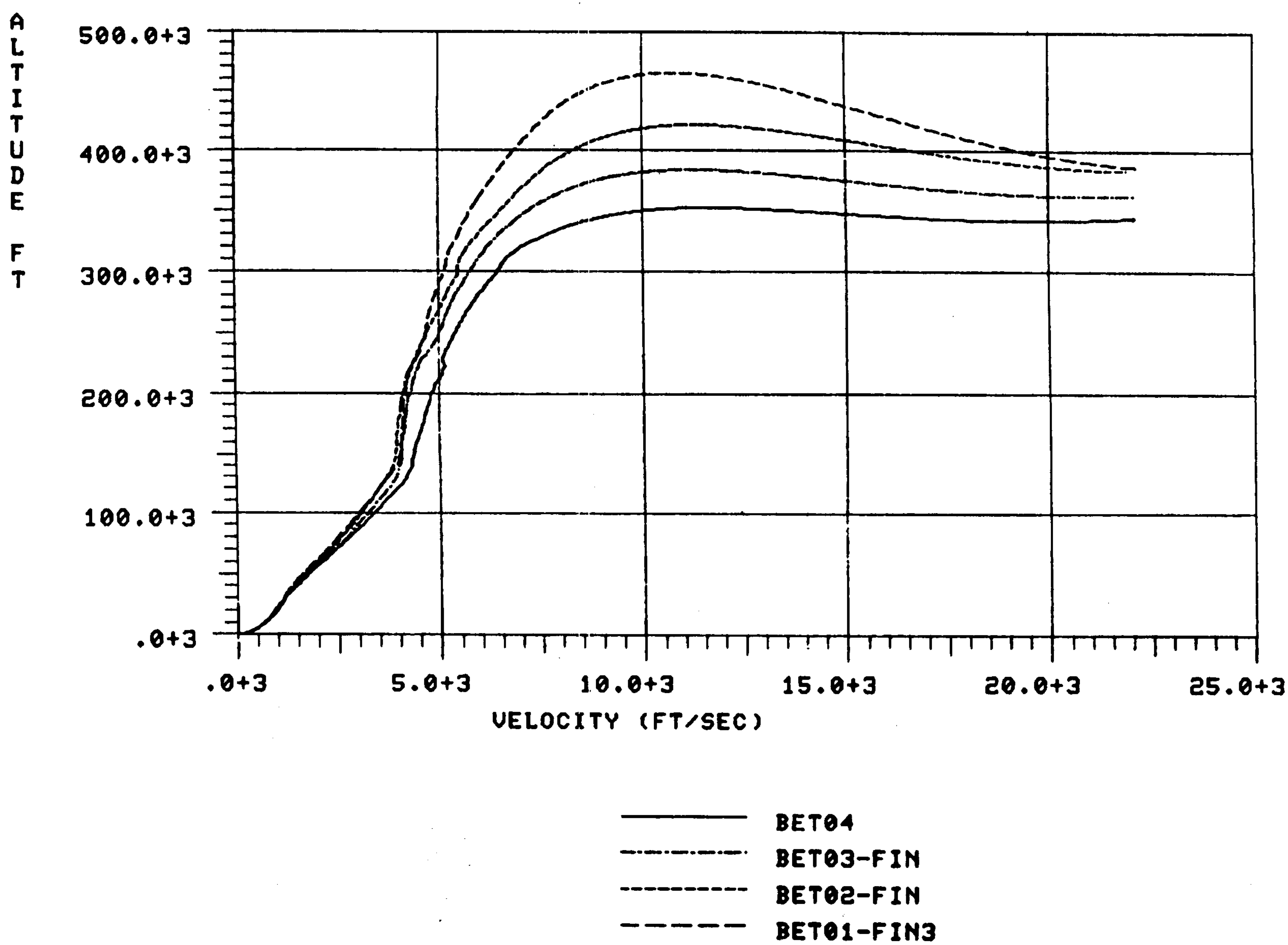

Fig. 3.1a Altitude-Velocity Variation for STS 1-4 Trajectories

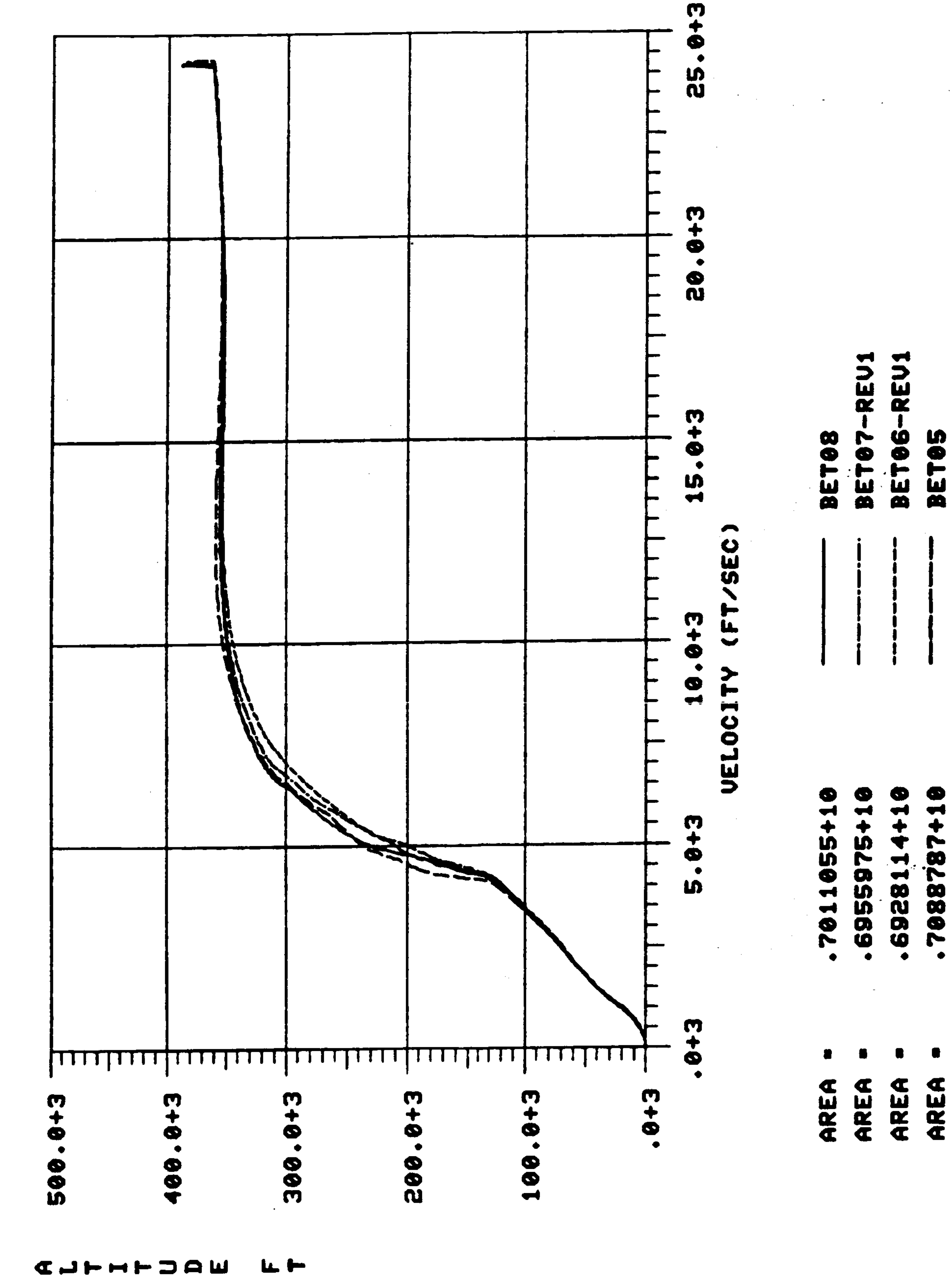

Fig. 3.1b Altitude-Velocity Variation for STS 5-8 Trajectories

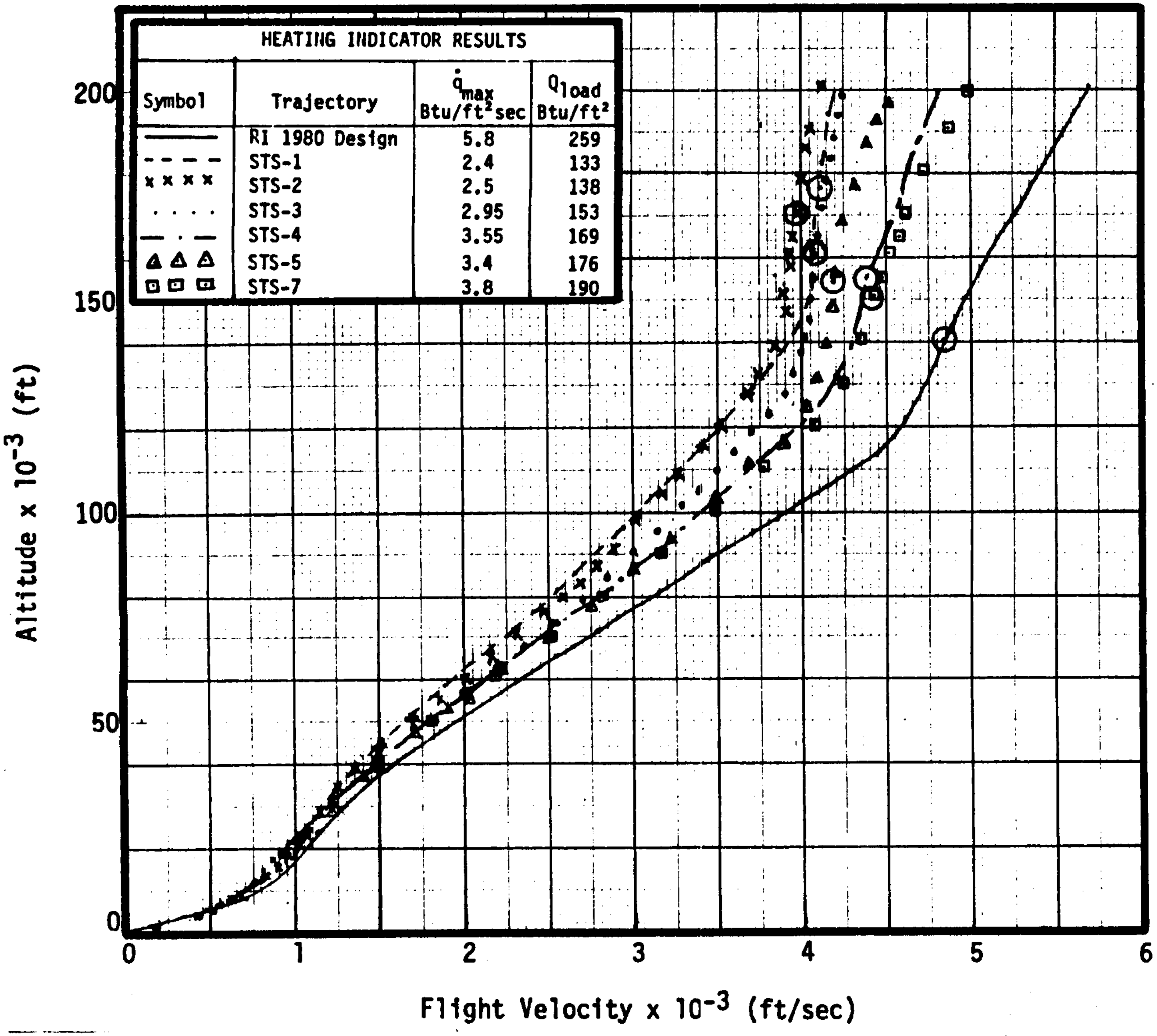

Symbol	Trajectory	$\dot{q}_{max}$ Btu/ft²sec	Q_{load} Btu/ft²
———	RI 1980 Design	5.8	259
- - - -	STS-1	2.4	133
x x x x	STS-2	2.5	138
. . . .	STS-3	2.95	153
— · —	STS-4	3.55	169
△ △ △	STS-5	3.4	176
⊡ ⊡ ⊡	STS-7	3.8	190

NOTES:

- Q_{load} is the integral of the heating rates from 0 Secs. to 125 Secs.
- ⊙ denotes SRB staging
- The RI 1980 thermal design trajectory is a Mission 3A disp.

  RQHW engine out @ 260 sec.

Fig 3.2 Comparison Of Trajectories (First Stage)

ORIGINAL PAGE IS
OF POOR QUALITY

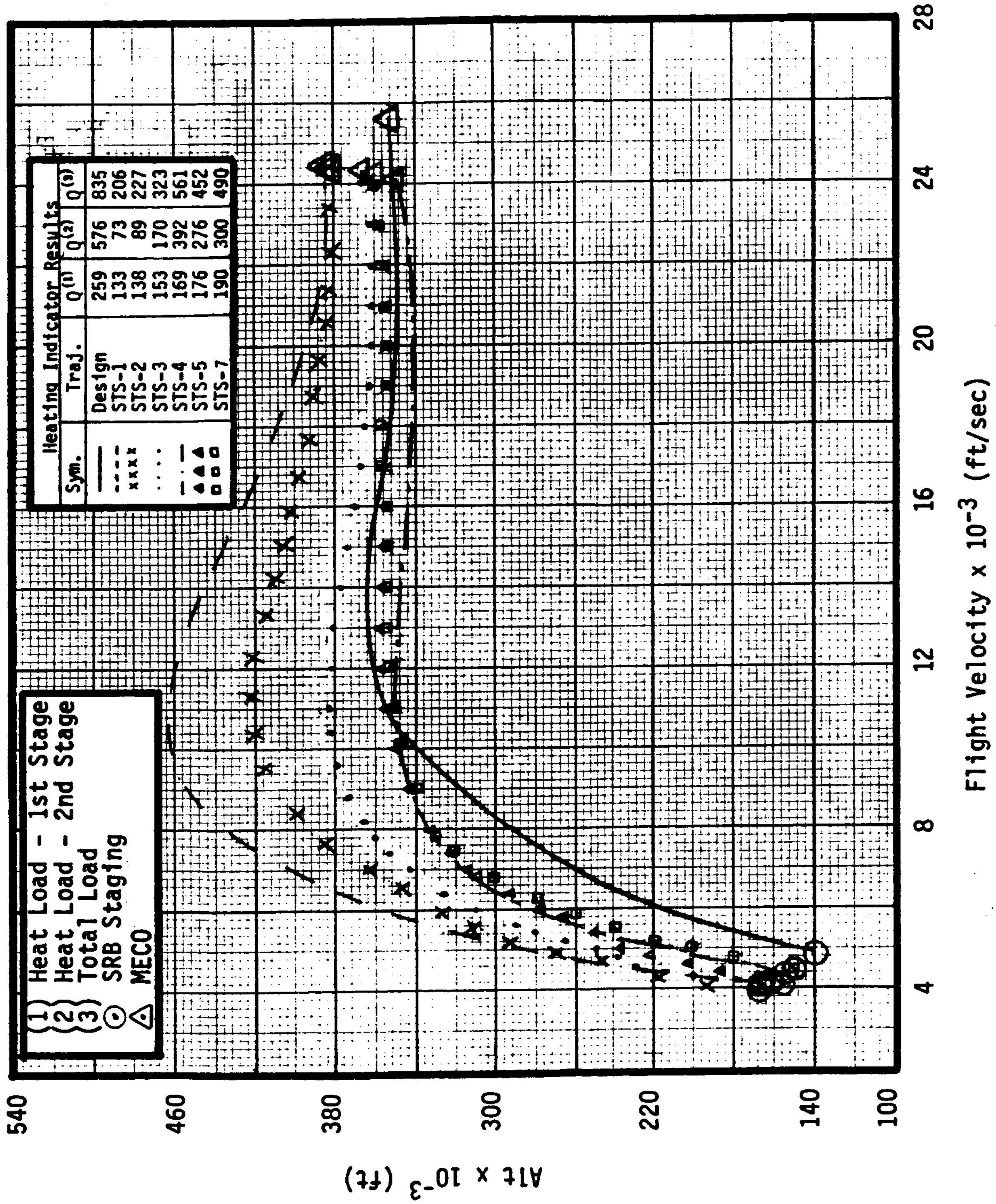

Fig. 3.3 Comparison Of Trajectories (Second Stage)

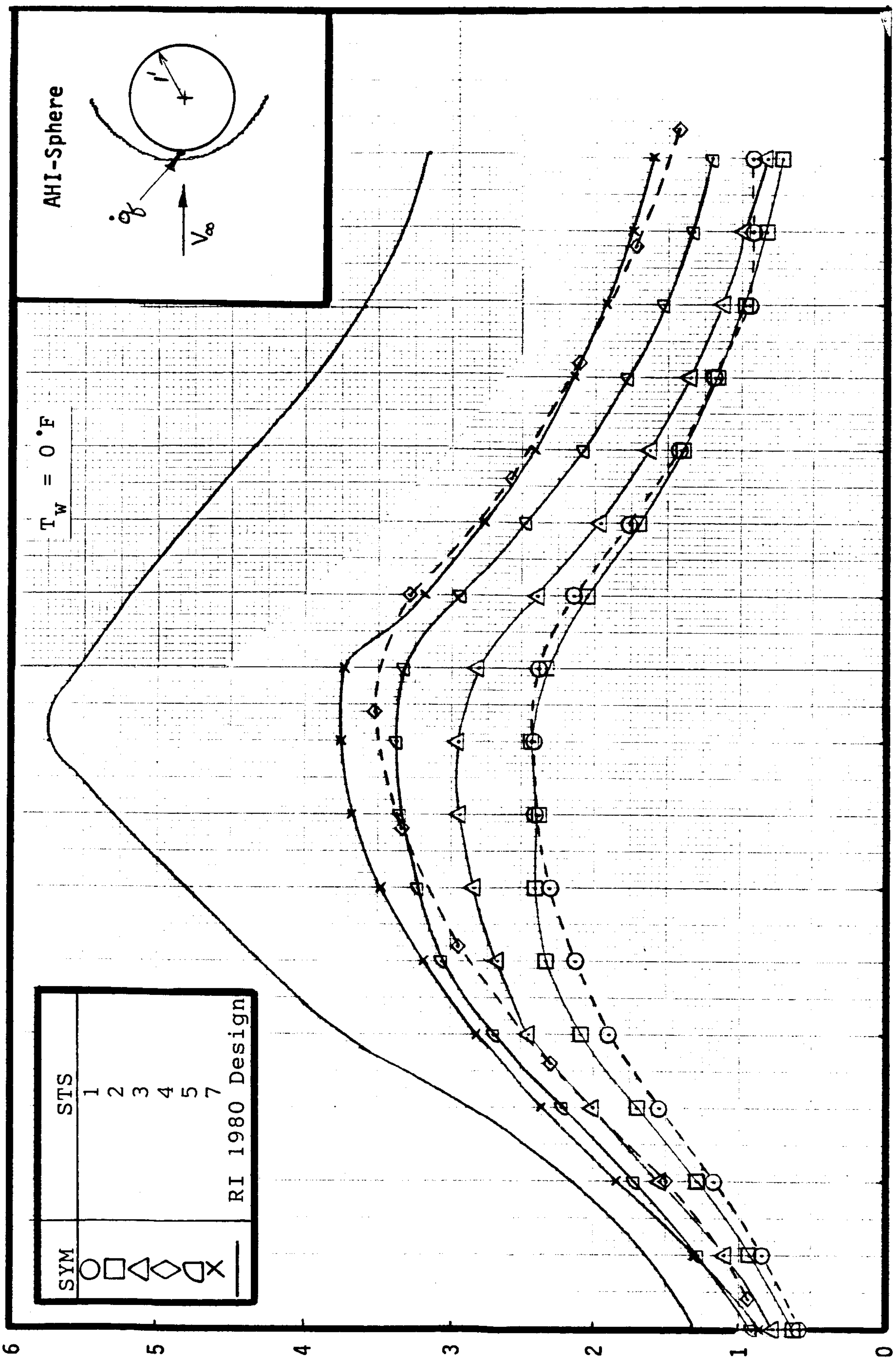

Fig. 3.4 Comparison Of AHI Results For STS Trajectories

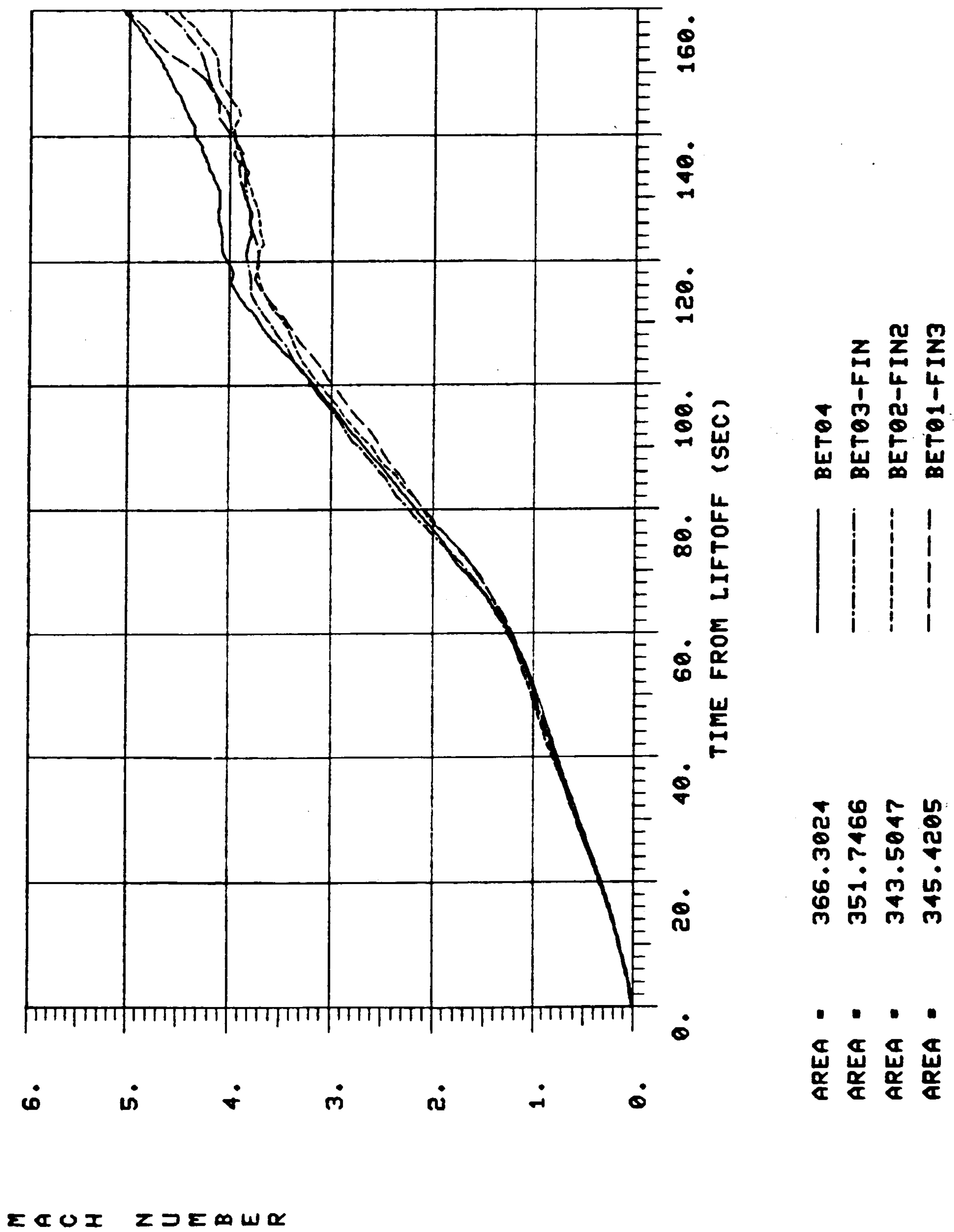

Fig. 3.5a Freestream Mach Number Time-Histories for STS 1-4 Trajectories

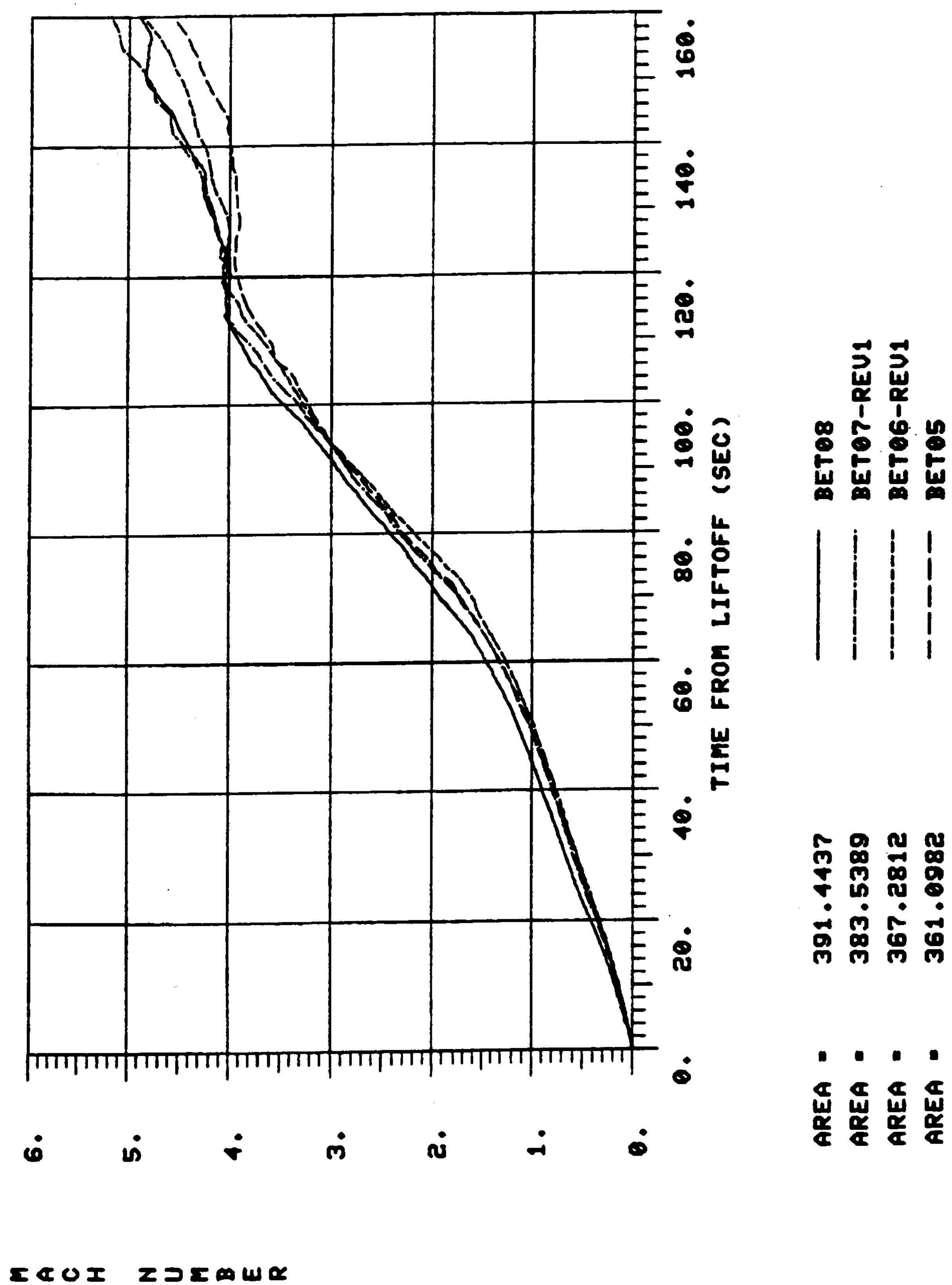

Fig. 3.5b Freestream Mach Number Time-Histories for STS 5-8 Trajectories

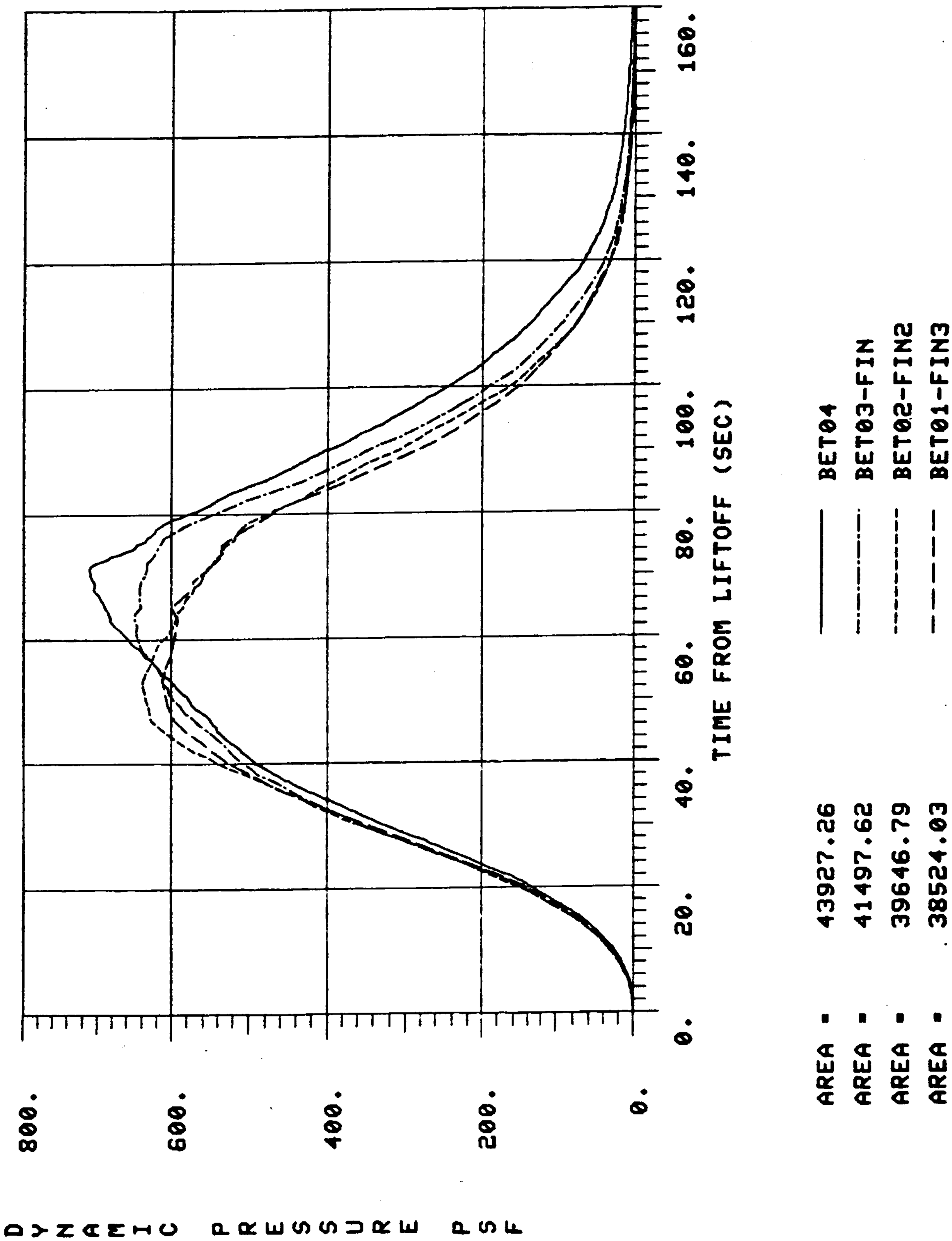

Fig. 3.6a Dynamic Pressure Time-Histories for STS 1-4 Trajectories

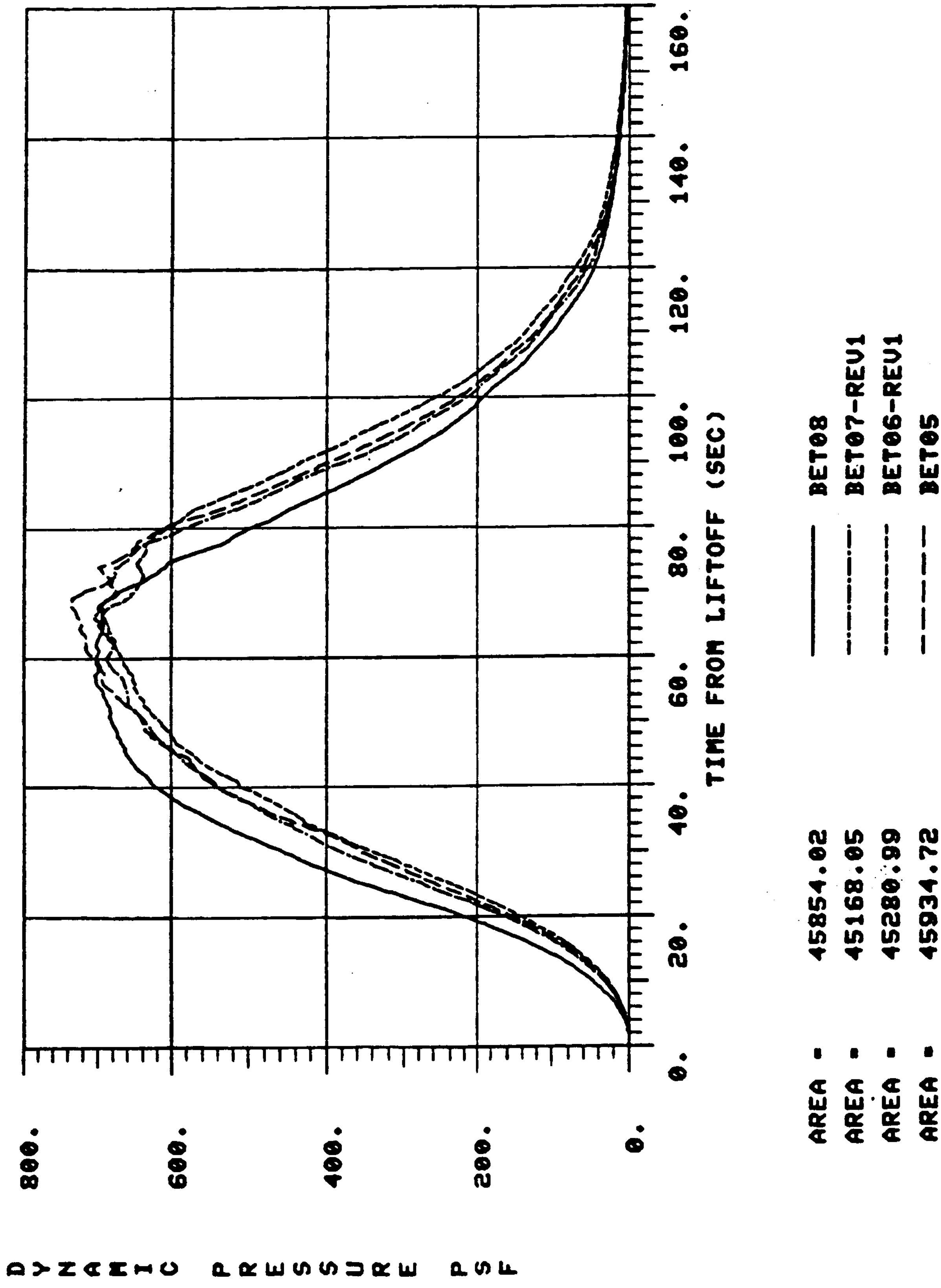

Fig. 3.6b Dynamic Pressure Time-Histories for STS 5-8 Trajectories

REMTECH INC.

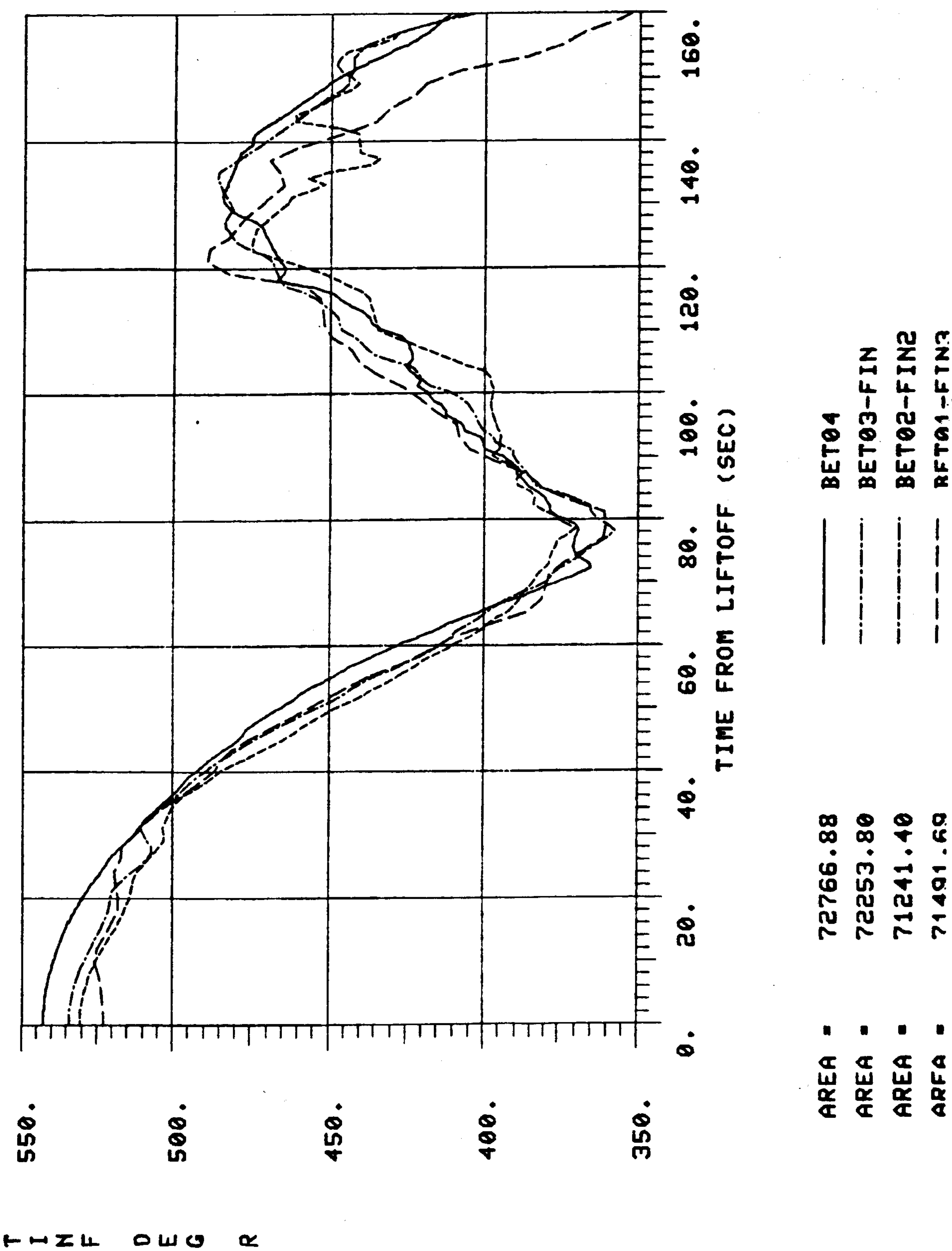

Fig. 3.7a Ambient Static Temperature Time-Histories for STS 1-4 Trajectories

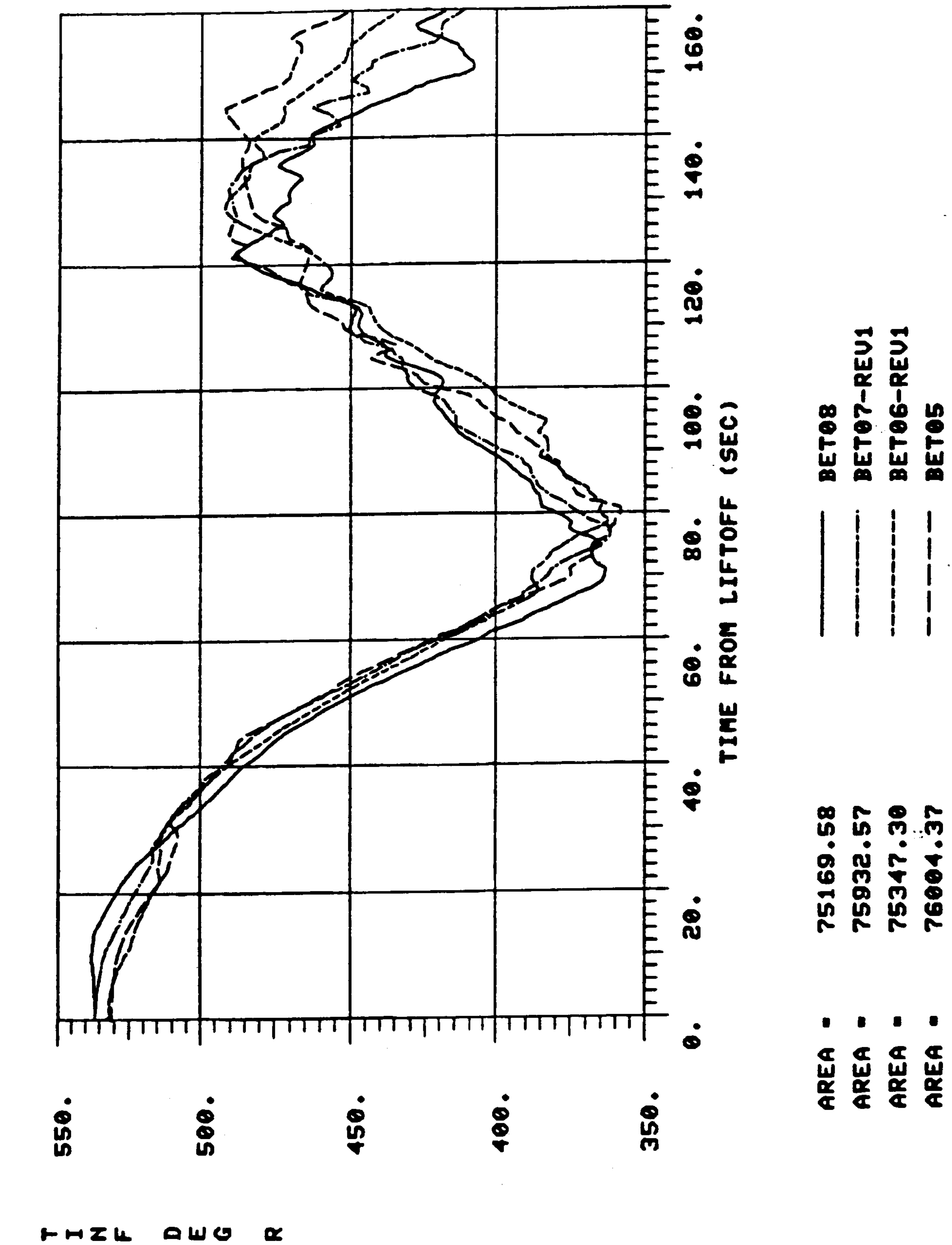

Fig. 3.7b Ambient Static Temperature Time-Histories for STS 5-8 Trajectories

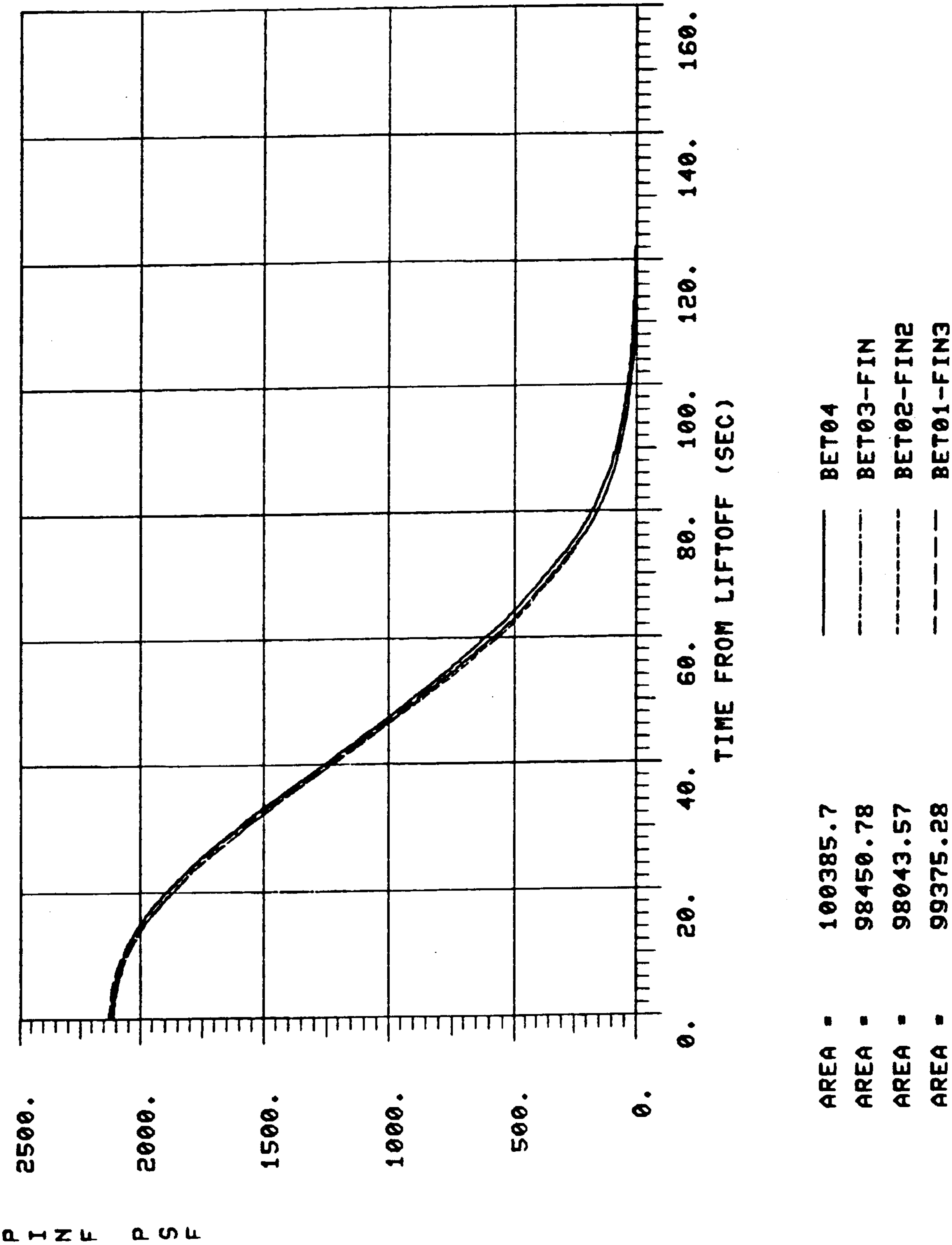

Fig. 3.8a Ambient Pressure Time-Histories for STS 1-4 Trajectories

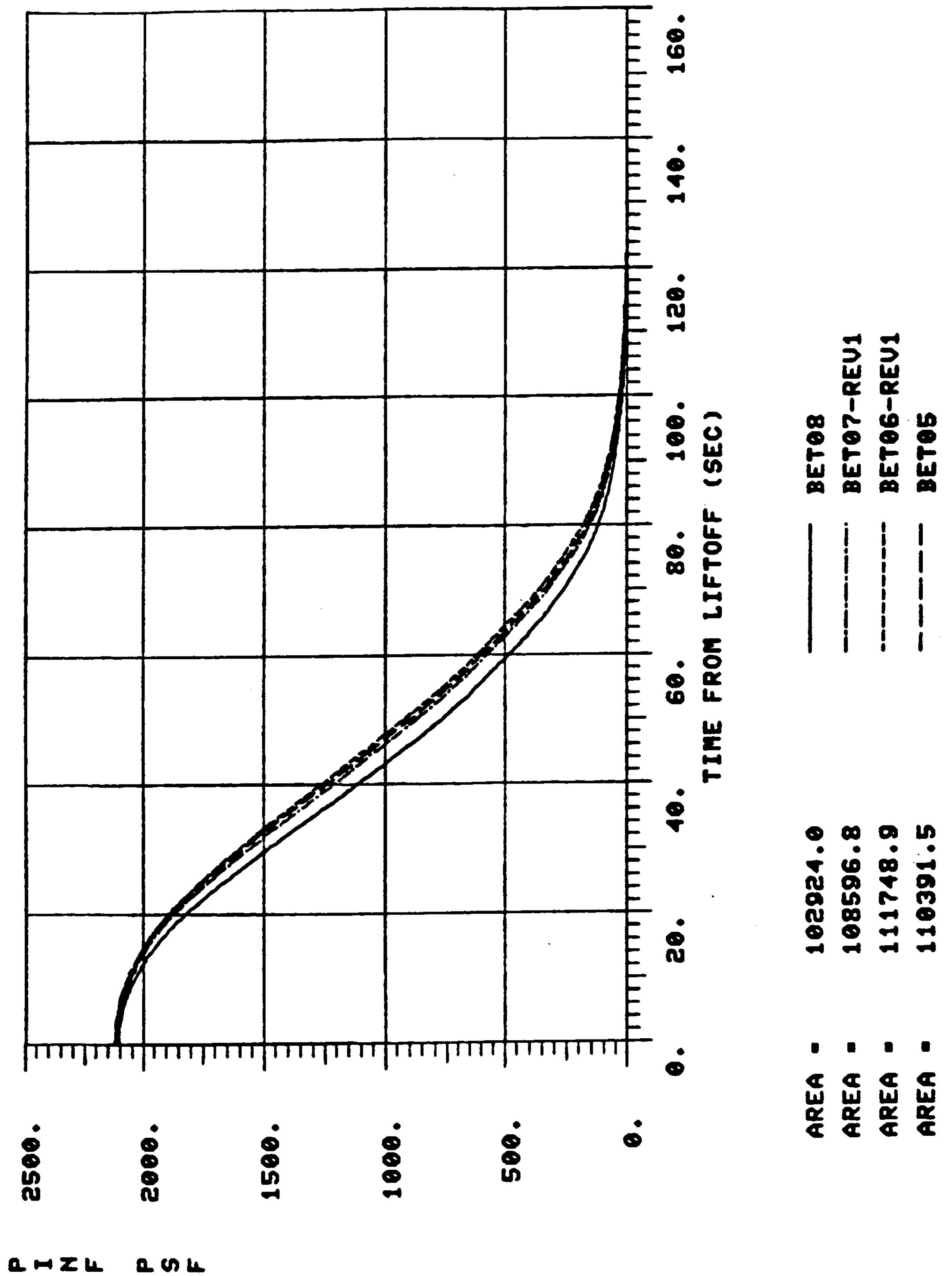

Fig. 3.8b Ambient Pressure Time-Histories for STS 5-8 Trajectories

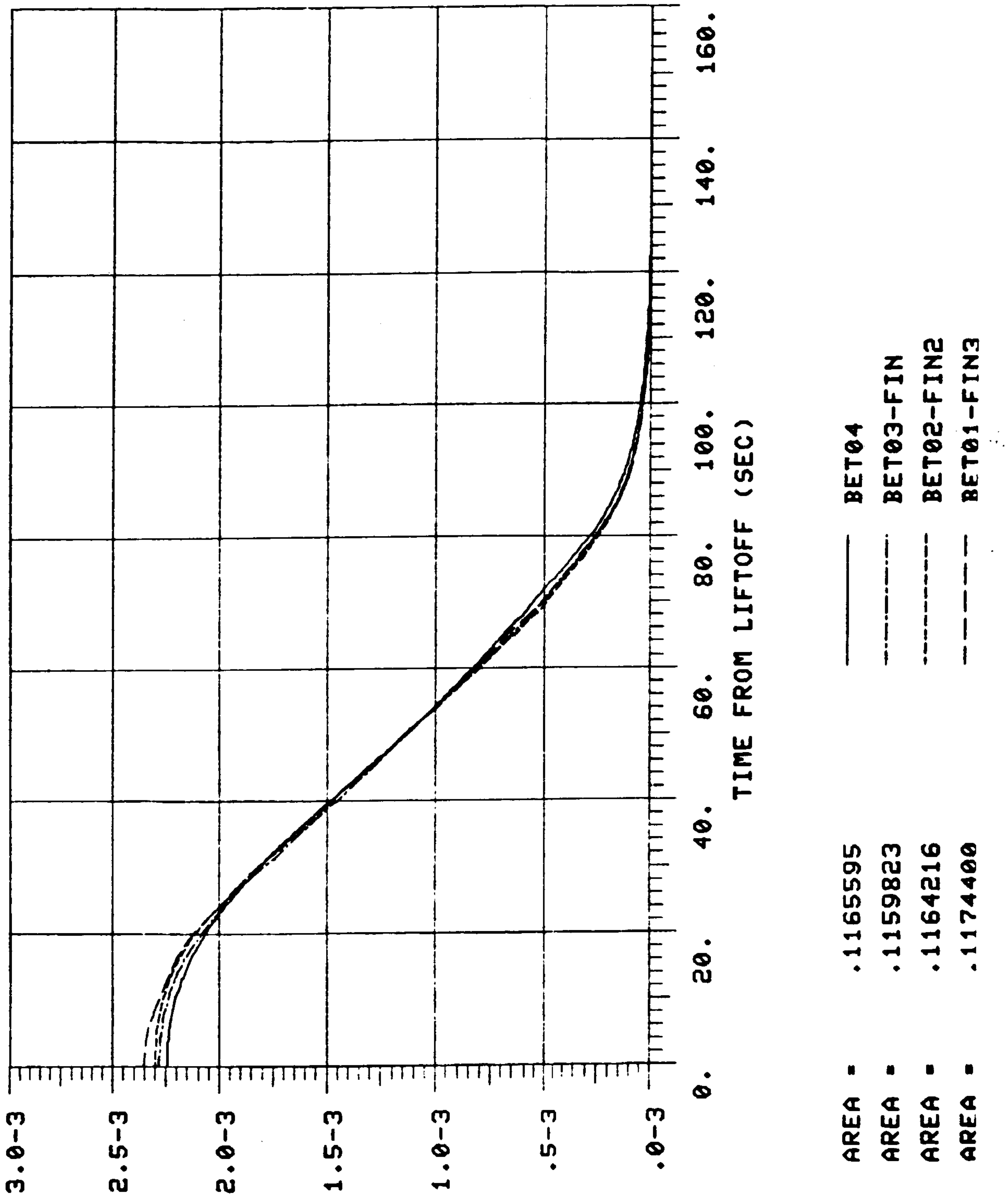

Fig. 3.9a Ambient Density Time-Histories for STS 1-4 Trajectories

one-foot radius sphere. It is clearly observed that the design trajectory peak value is highest of all followed by STS-7, STS-4, STS-5, STS-3, STS-2, and STS-1, respectively.

Figures 3.10 and 3.11 give angle of attack (α) and sideslip angle (β) histories with respect to trajectory time from t = 50 sec. to t = 160 sec. Figure 3.12 gives the freestream Mach number time history. Figures 3.13a and 3.13b, on the other hand, give the variation of α and β with freestream Mach number. Figures 3.14 and 3.15 give α, and β variations respectively with trajectory time for both the first and second stage flights. It is seen that the magnitudes of α, β combinations are generally within the design envelope of $-5 \leq \alpha \leq +5$ and $-11 \leq \beta \leq +11$ degrees in the peak heating range occurring somewhere between 90 and 110 sec. It is further observed that the α values are only positive and β values are quite close to zero for the six OFT flights during the peak heating period. The β range in the design envelope contains high values of +11 degrees because of possible SRB thrust mismatch during SRB tailoff; however, such high values were not observed in the flights as evident from Fig. 3.11 or Fig. 3.14b. The details of the characteristics for all the flight trajectories have been reported in Refs. 6 - 11.

3.2 AEROTHERMAL MEASUREMENTS AND INHERENT ERRORS

The heat-transfer and pressure measurements were taken on most of the DFI island and gage locations described in Section 2. The flight data were recorded by on-board recorders and put into STSDB

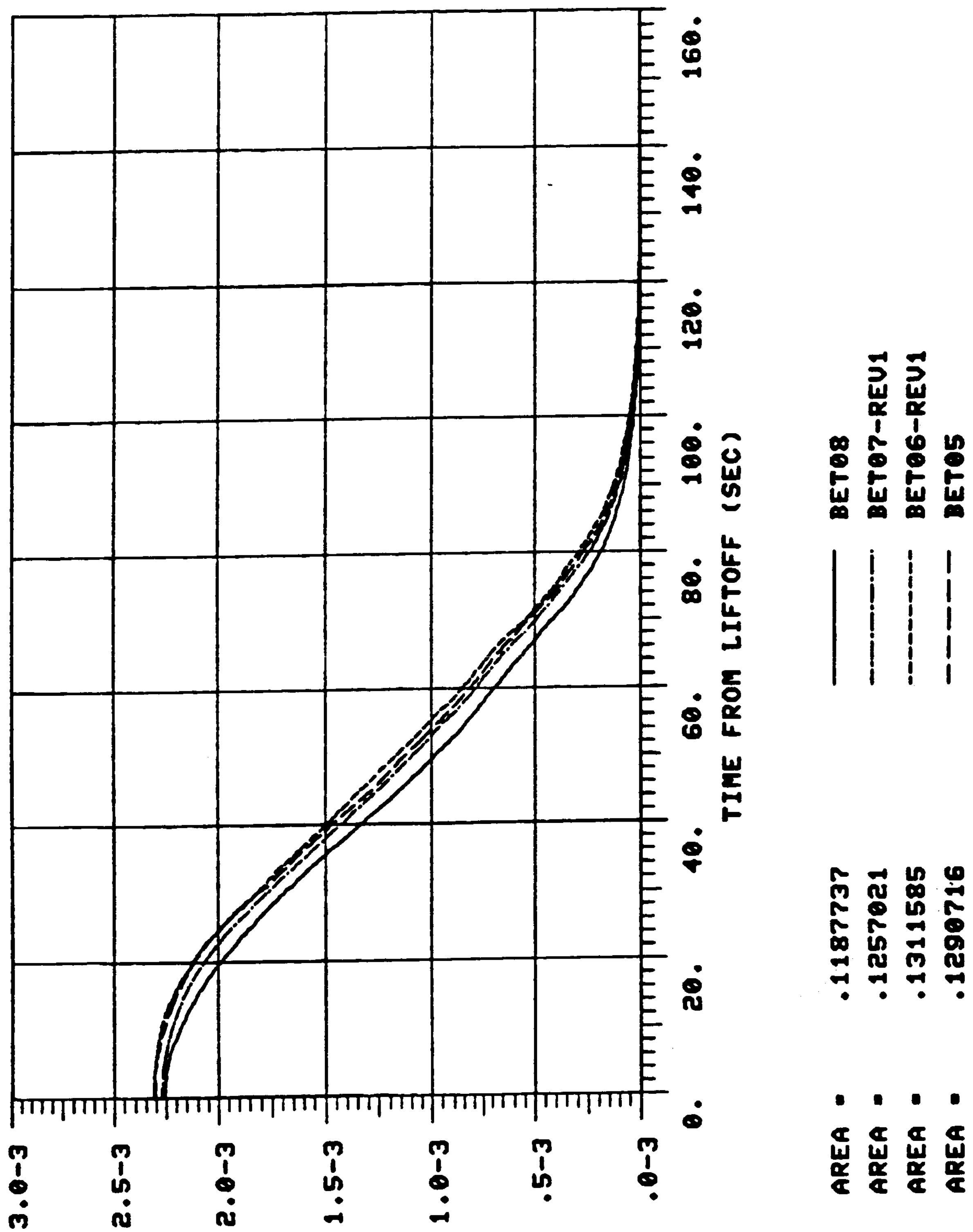

Fig. 3.9b Ambient Density Time-Histories for STS 5-8 Trajectories

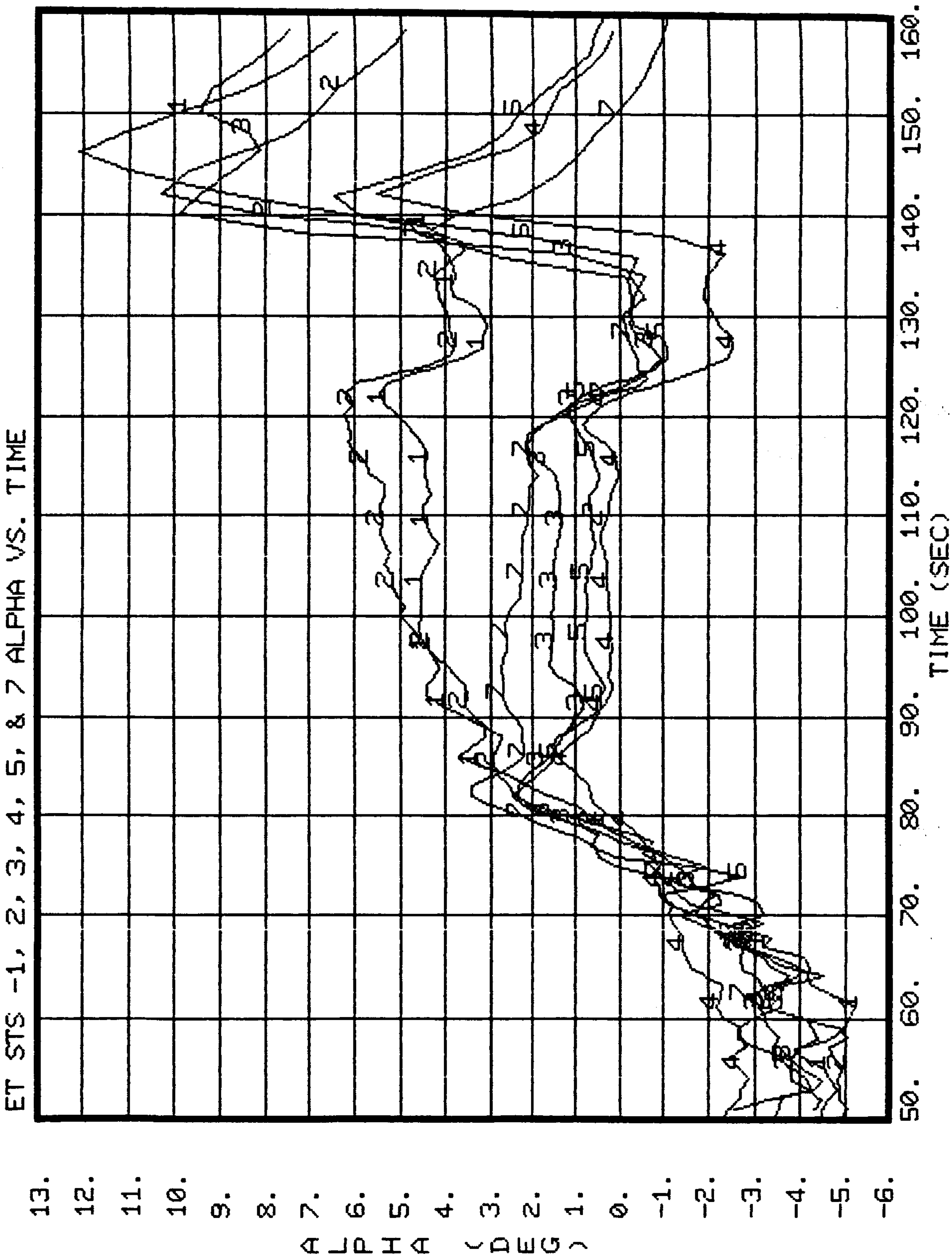

Fig. 3.10 Alpha Time-History for STS 1-7 Trajectories

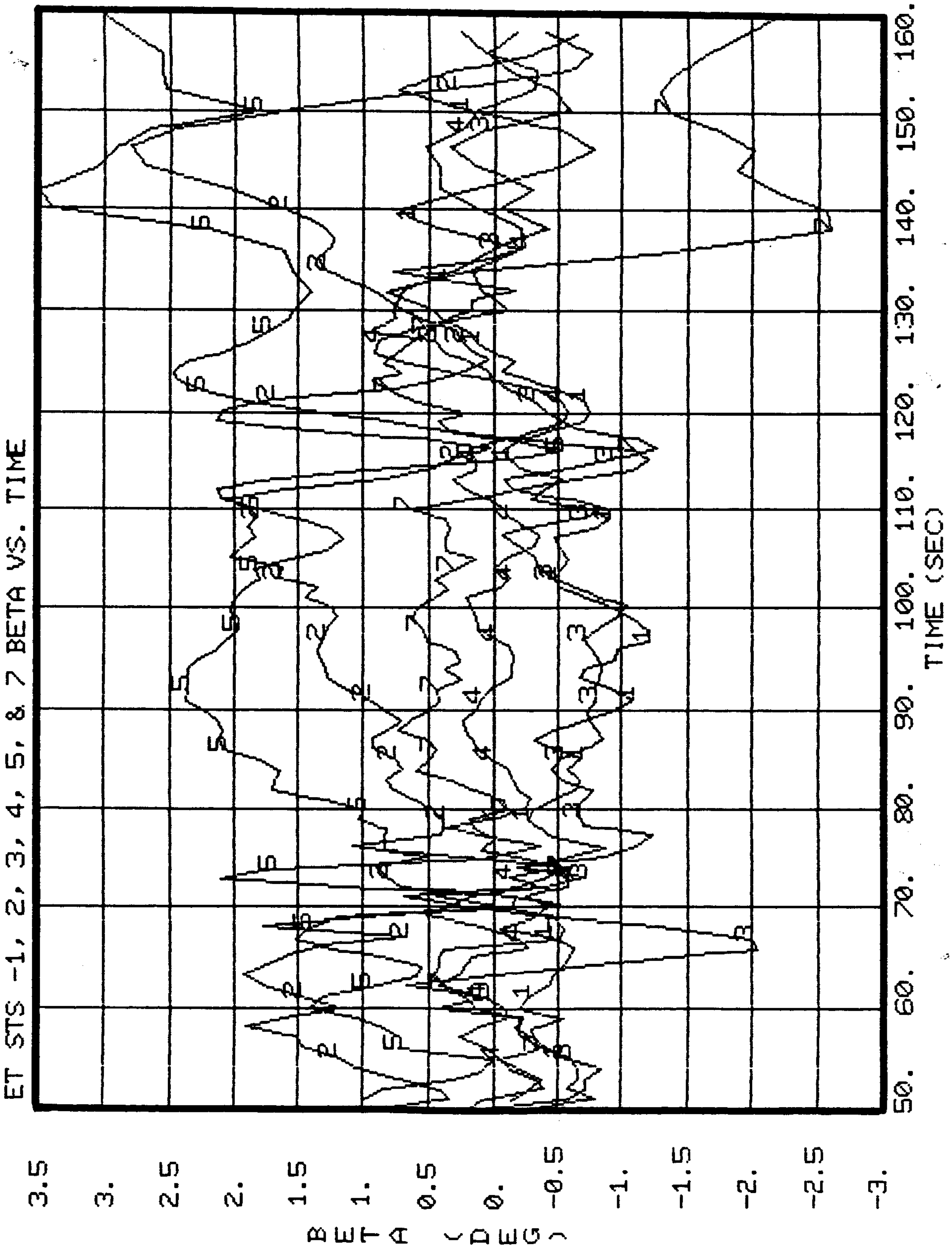

Fig. 3.11 Beta Time-History for STS 1-7 Trajectories

REMTECH INC.

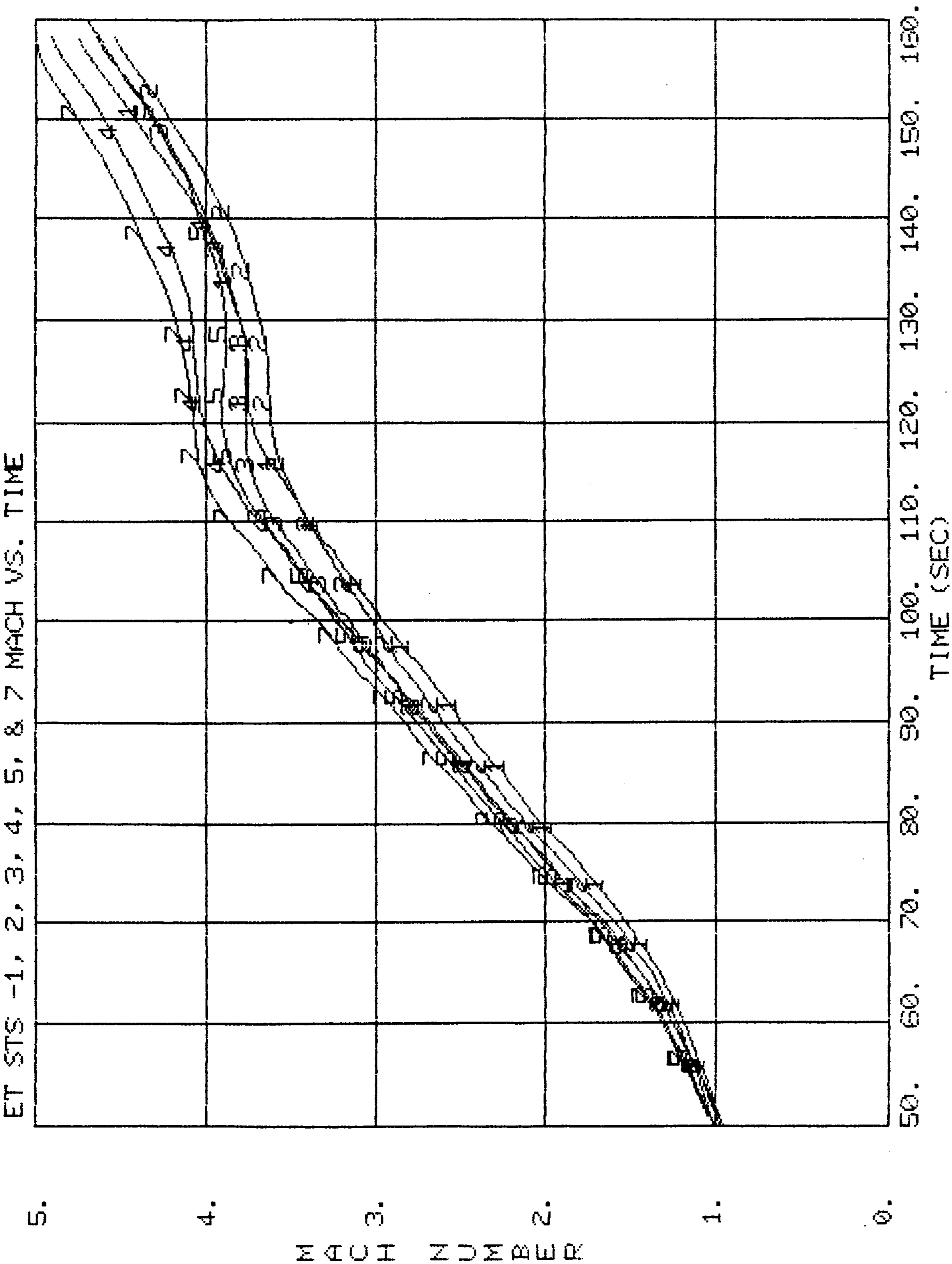

Fig. 3.12 Freestream Mach Number Time-History for STS 1-7 Trajectories

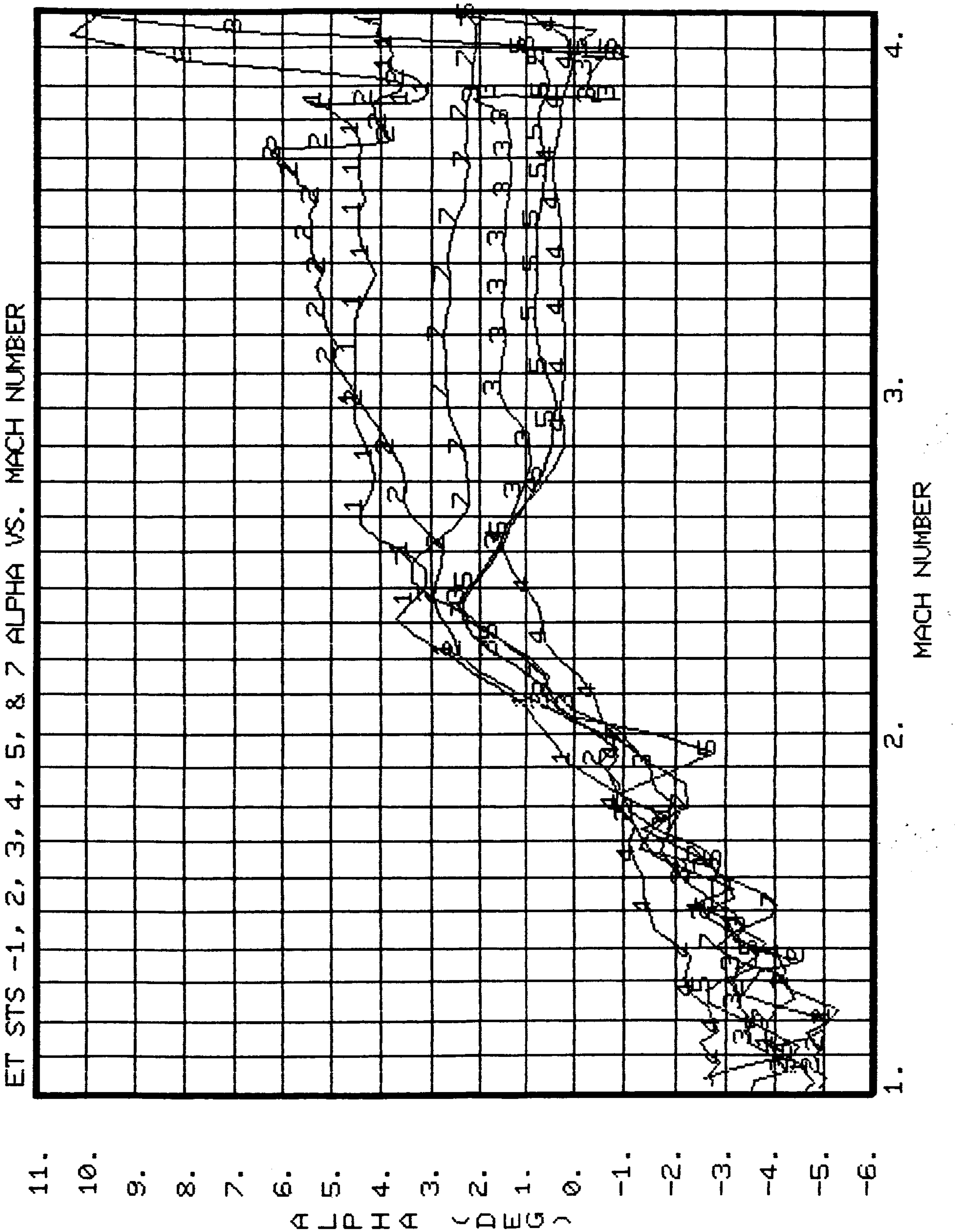

Fig. 3.13a Alpha-Mach Number Variation in STS 1-7 Trajectories

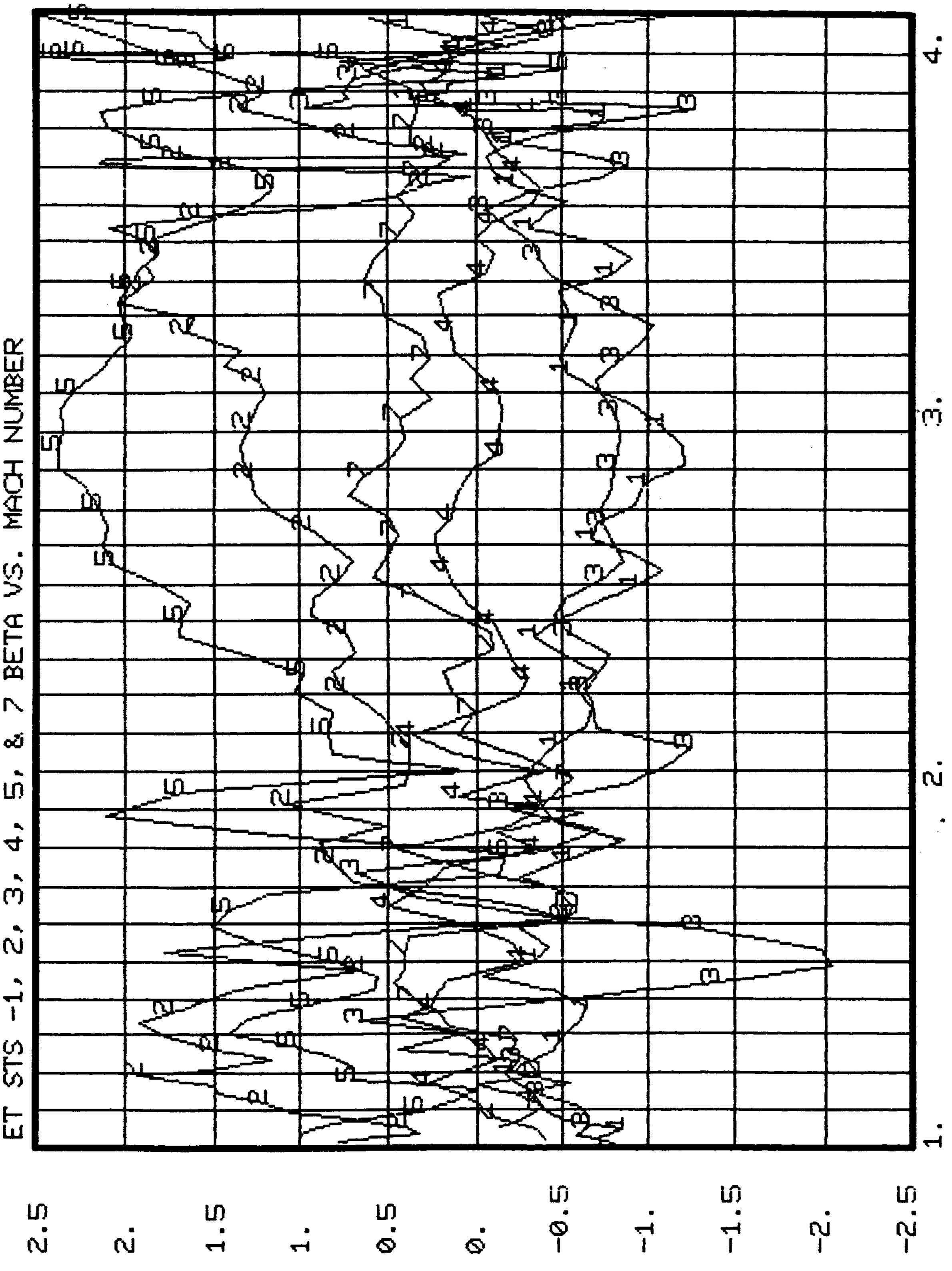

Fig. 3.13b Beta-Mach Number Variation in STS 1-7 Trajectories

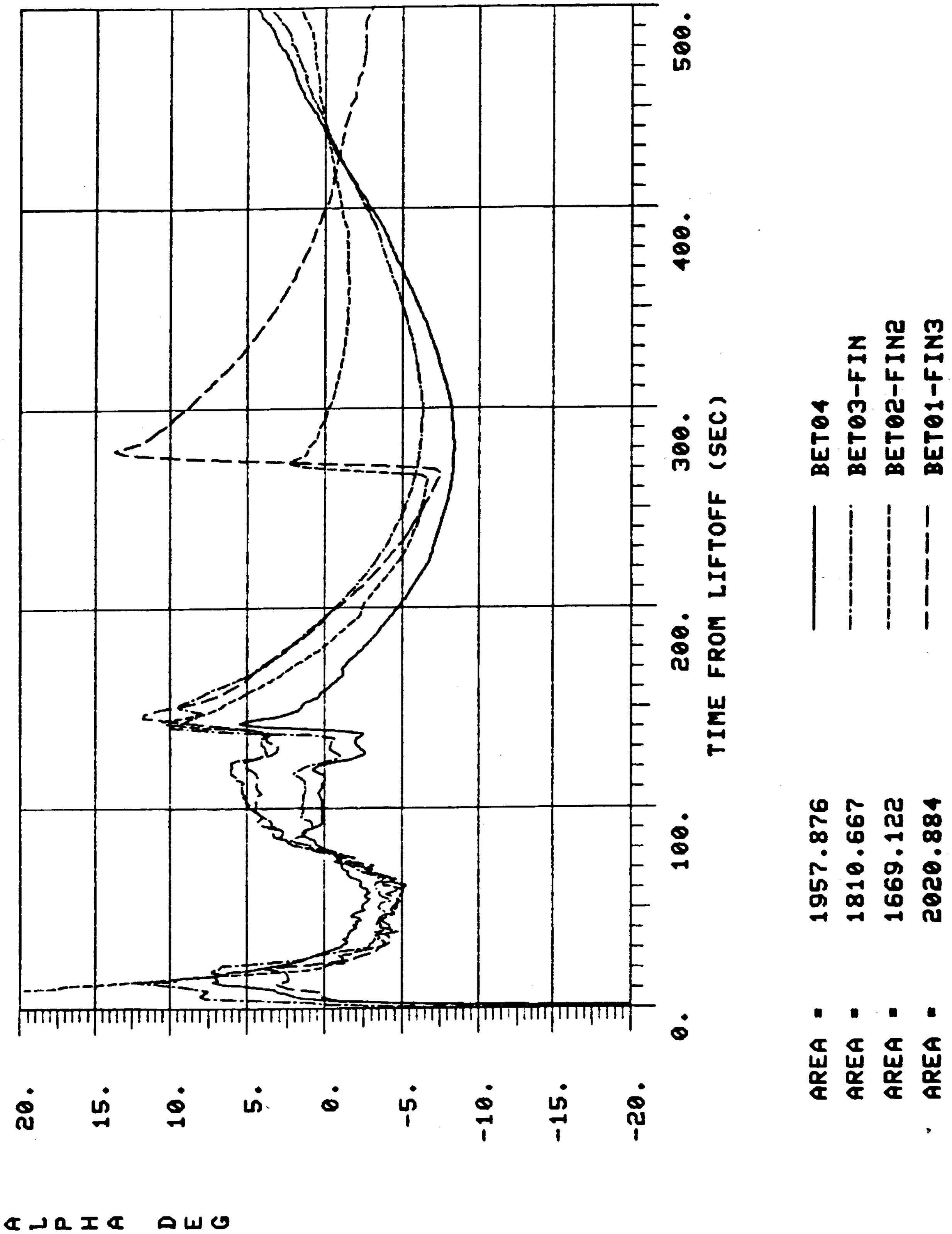

Fig. 3.14a Alpha Time-Histories between Lift-Off and MECO for STS 1-4 Trajectories

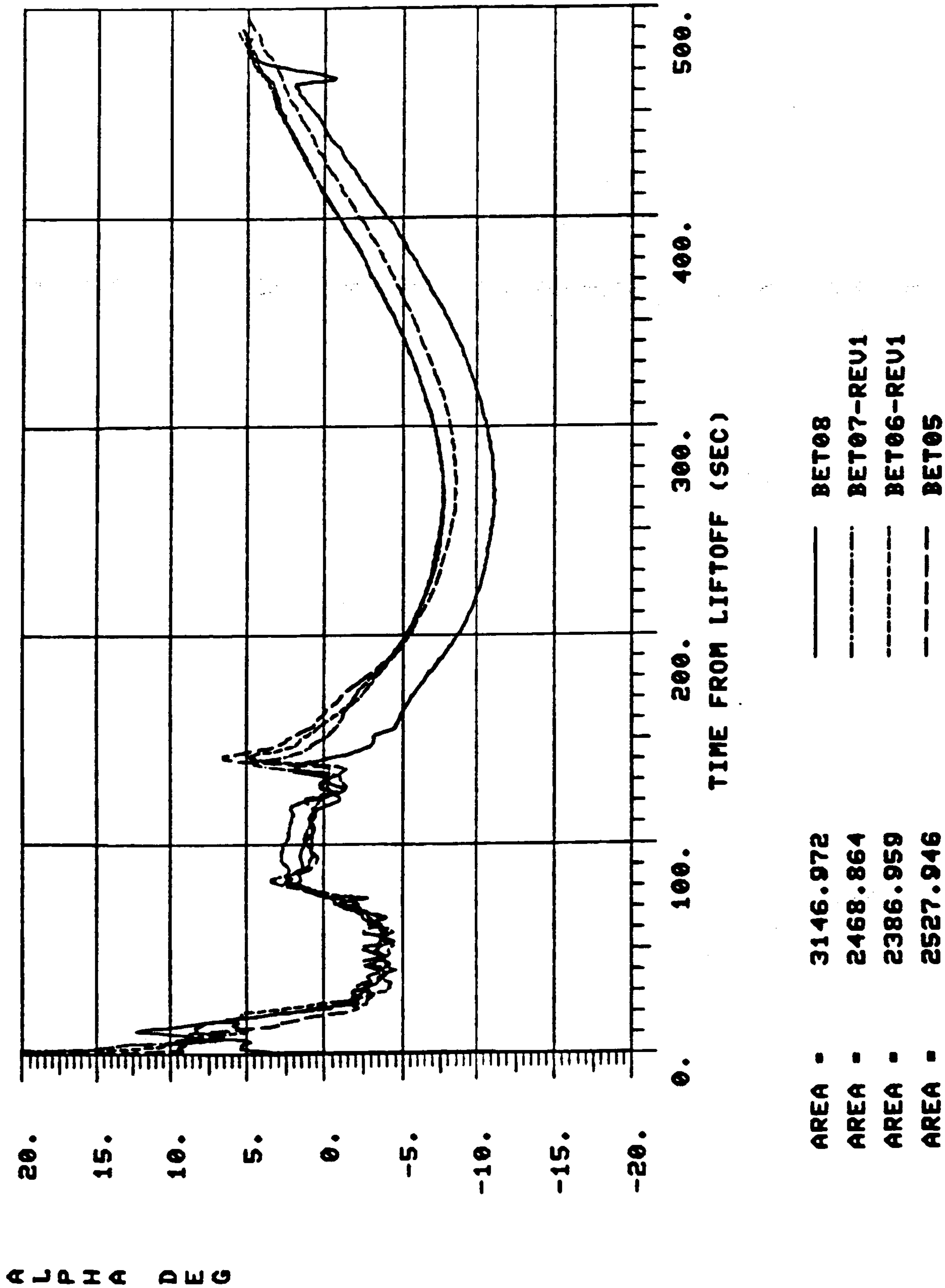

Fig. 3.14b Alpha Time-Histories between Lift-Off and MECO for STS 5-8 Trajectories

REMTECH INC.

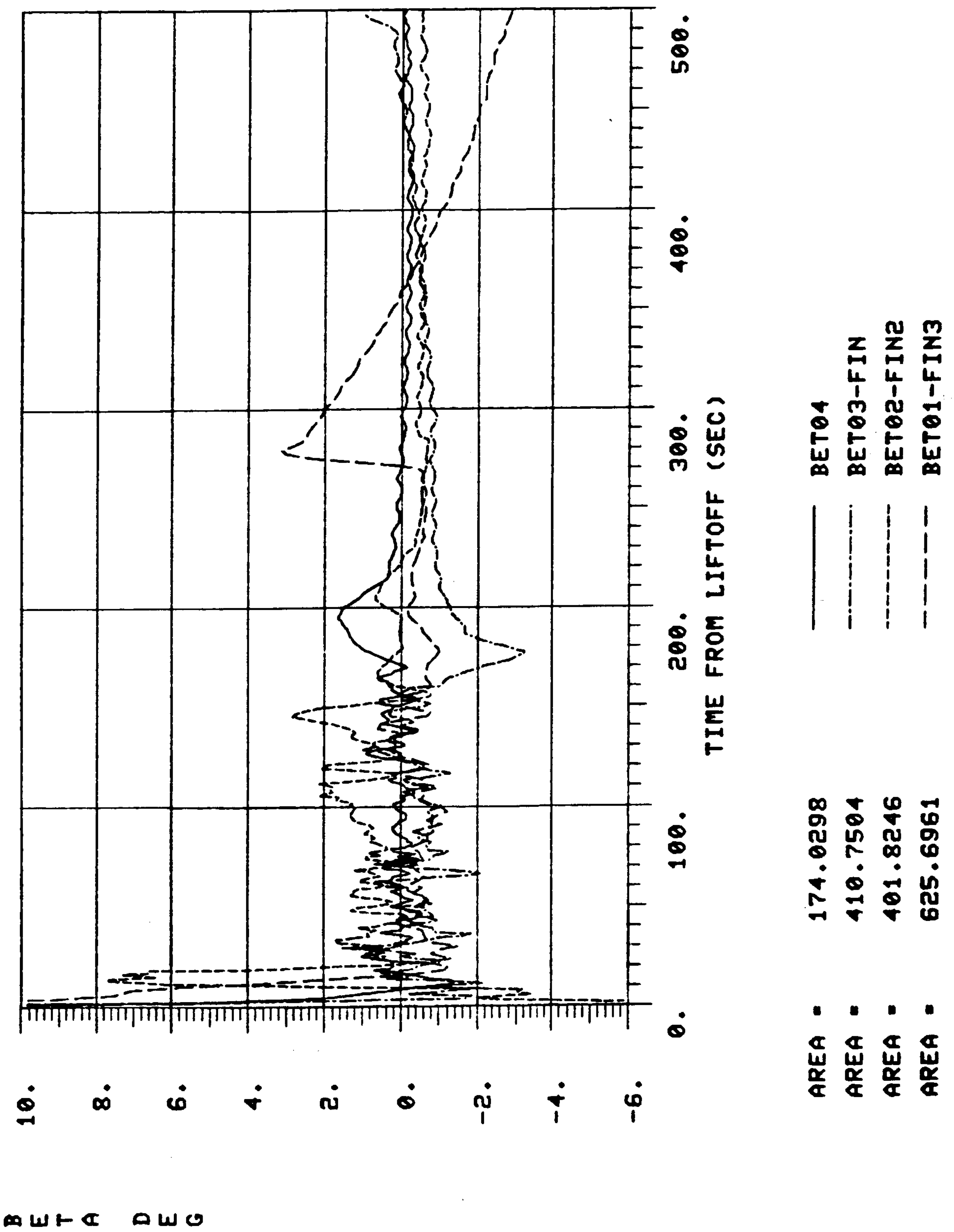

Fig. 3.15a Beta Time-Histories between Lift-Off and MECO for STS 1-4 Trajectories

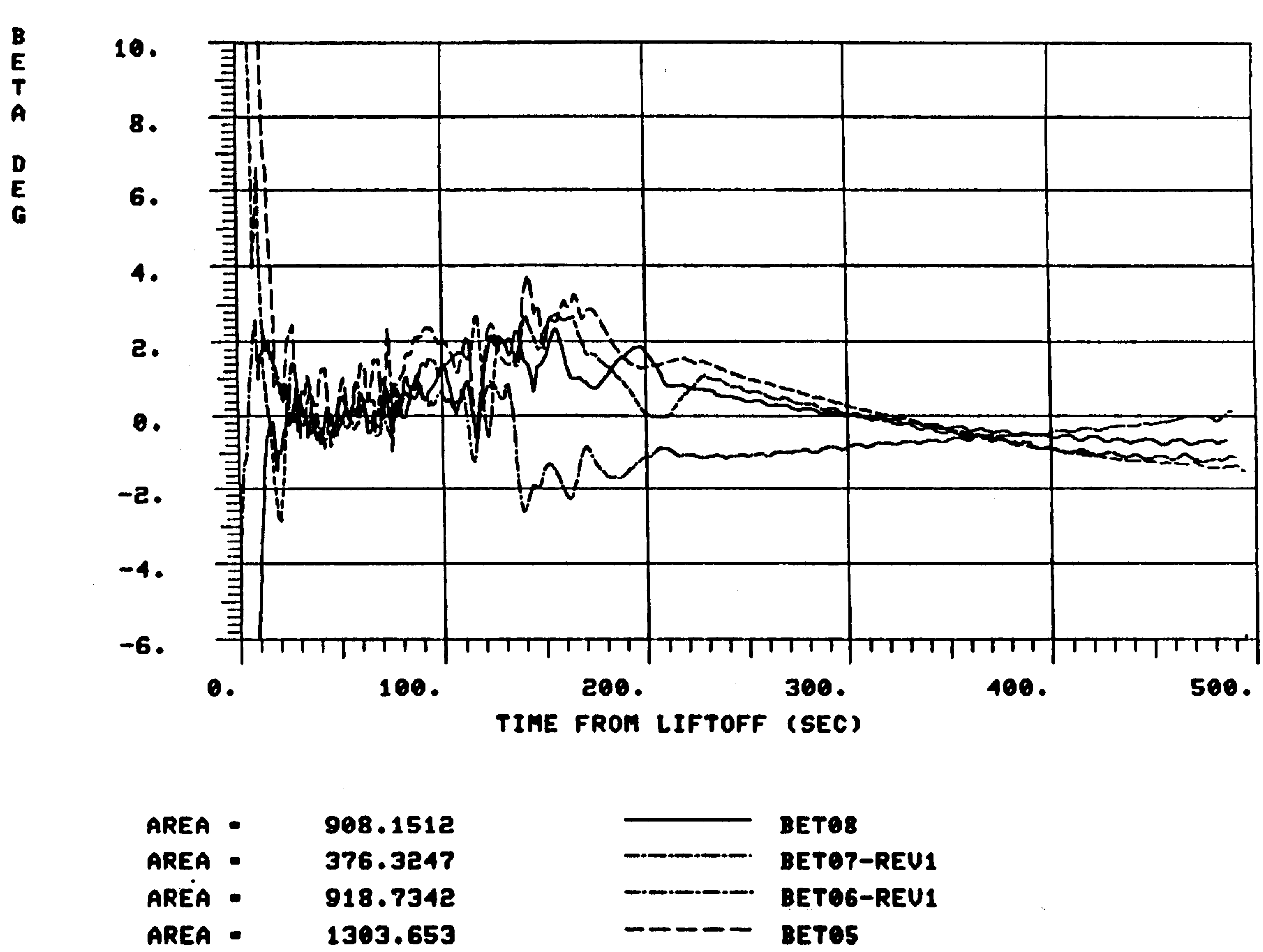

Fig. 3.15b Beta Time-Histories between Lift-Off and MECO for STS 5-8 Trajectories

(STS Data Base) for use by the scientific community. It should be noted that the recorded data usually are available in counts or milli-volts. The counts are converted to engineering units by the appropriate Shuttle contractor with the use of the calibration curves supplied by the gage manufacturer, and loaded into STSDB. The aerothermal measured data in engineering units were retrieved from ESDB and STSDB and documented in Refs. 6 - 11 for each of the instrumented flights. An in-house code was written by REMTECH personnel to read the tabulated data in STSDB and to create a file containing the heating rate information for all the gages at each time point. This file was then used in the MIPS to create a list-directed file, accessible by MIPS for easy manipulation of the data either for printing or for plotting purposes.

Thermal Instrumentation errors occur generally in four areas: (1) the inherent design of the instrument, (2) the onboard signal conditioning and acquisition, (3) the installation and external environmental conditions, and (4) the data processing. A comprehensive outline of the ET data acquisition system and an error analysis of the calorimeter, radiometer, and resistance thermometer are given in Ref. 3. The measurement errors have various sources. The first area depends on the manufacturer, whereas the second area depends on the procedure adopted to record flight data. The third area partially depends on the installation procedure and the external environmental conditions, which will be discussed later; and the last area depends on the ground-computer processing of the flight data by the data processing contractor.

The evaluation of the measured data examined some of the predominant errors caused by the external environmental conditions. One of these errors is due to "temperature mismatch" occurring at the measuring gage interface because of the passage of the flow over dissimilar surface materials with different surface temperatures. The other error is due to the contribution of "plume-induced" heating to the aeroheating measurements. The presence of protuberances, TPS erosion, ablation, and exochemical thermo effects will also alter the calorimeter and pressure data from that of the undisturbed or pure geometric interference flow conditions. Since most of the acreage gages are total calorimeters, they measure both convective and radiative heating. A few of the gages show "pegged" readings because of the measurement values beyond the gages' measuring range, whereas a few of the gages seem to have failed in flight due to unknown reasons.

Table 3.1 summarizes all the heat-transfer gages that were designed to be connected in the DFI flights to measure aeroheating. Some of these were not connected for reasons of safety to the orbiter, as has been described in Ref. 1 and elsewhere. The inherent and suspected errors in the rest of the measurements are also summarized in Table 3.1. Table 3.2 summarizes all the errors associated with the pressure measurements taken in the DFI flights. The heat-transfer measurements are summarized for all the ET

Table 3.1 - Summary of DFI Aeroheating Measurements *

MSID	Installation Gage Type	STS-1	STS-2	STS-3	STS-4	STS-5	STS-7
9001	Ind. Gage	TM	TM	TM	TM	TM	TM
9003	I 3	NC	NC	NC	NC	NC	NC
9004	I 2	NC	TM	TM	TM	TM	TM
9005	I 1	NC	TM	TM	TM	TM	TM
9006	I 4	NC	NC	NC	NC	NC	NC
9007	I 6	NC	TM	TM	TM	TM	TM
9008	I 5	NC	TM	TM	TM	TM	TM
9009	I 7	NC	NC	NC	NC	NC	NC
9010	I 8	NC	TM	TM	TM	TM	TM
9011	I 18						
9012	Ind. Gage						
9013	I 17(3)						
9014	I 16						
9015	I 15						
9016	I 14						
9017	I 12						
9018	I 17(2)						
9019	I 17(1)						
9020	I 27	NC	NC	NC			
9021	I 20						
9022	I 23						
9023	I 26	NC	NC	NC			
9024	I 30	NC	NC	NC	NC	NC	NC
9025	I 29	NC	Failed	Failed		Failed	
9026	I 28	NC	Failed				
9027	I 33	NC	Plume	Failed	Plume	Plume	Plume
9028	I 35	NC	Plume	Failed	Plume	QM	Plume
9029	I 32	NC	Plume	Failed	Plume	Plume	Plume
9030	I 34	NC	Plume	Failed	Failed	Plume	Plume
9031	I 36	NC	Failed	QM	Plume	Plume	Plume
9032	I 37	NC	Plume	Failed	QM	Plume	Plume
9033	I 31	NC	NC	NC	NC	NC	NC
9038	Ind. Gage						
9039	Ind. Gage	NC	NC	NC	NC		Failed
9040	Ind. Gage	NC	NC	NC	NC		Failed
9041	Ind. Gage						
9042	Ind. Gage						
9043	Ind. Gage	NC	NC	NC	NC		
9045	Ind. Gage						
9046	Ind. Gage		Failed			Failed	Failed
9047	Ind. Gage					Failed	

* I - Island
NC - Not Connected
TM - Thermal Mismatch
QM - Questionable Measurements
Ind. Gage - Individual Gages

Table 3.2 - Summary of DFI Pressure Measurements *

MSID	Installation Gage Type	STS-1	STS-2	STS-3	STS-4	STS-5	STS-7
9061	Ind. Gage						
9062	Ind. Gage						Failed
9064	I 2						
9065	I 1	NC					
9066	I 6	NC					
9067	I 5	NC					
9069	I 18						
9070	I 15						
9071	I 17(3)						Failed
9072	I 23						
9074	I 28	NC	Failed	Failed			
9075	I 32	NC					Failed
9076	I 34	NC	Failed	Failed	QM		
9077	Ind. Gage						
9078	Associated Gage(with 9047)						
9079	Associated Gage(with 9046)						
9550	Ind. Gage						
9551	Ind. Gage						
9560	I 11						
9561	I 21						

I - Island
NC - Not Connected
Ind. Gage - Individual Gage

calorimeters in Figs. 3.16 - 3.28. The plots were accomplished by using the list-directed files and MIPS. Each plot compares the heat-transfer measurements for the six OFT missions in one of the two time ranges, 0 to 160 sec. and 150 sec. to MECO. Also given in each of these plots is the integrated heating load value for each of the missions. The plots have been assembled in groups of 2, 3 or 4 per page based on certain common characteristics on a particular region of the ET. Since the aeroheating is close to zero beyond t = 160 sec. for most of the gages lying aft of the LO_2 tank, they were not plotted in this report. However, such comparisons in their entirety are available in Ref. 10. The only such gages included in this report are 9001, 9005, 9008, 9017, 9004, 9007 and 9010, all located on the LO_2 tank with the exception of 9017, which is located on the bottom centerline on the inter-tank slightly aft of the LO_2 tank. Similar plots have been made for the pressure measurements in the 0 - 160 sec. range in Figs. 29 - 33.

3.3 AEROTHERMAL DATA REDUCTION

The flight data reduction procedure has been amply described in Ref. 1 prepared for the STS-1 data evaluation final report. The basic methodology remains the same. For the sake of completeness, the data reduction procedure is repeated here in flow-chart form in Figs. 3.34 and 3.35.

3.3.1 GENERAL PROCEDURE

The STS-1 data reduction was reported in detail in Ref. 1,

ORIGINAL PAGE IS
OF POOR QUALITY

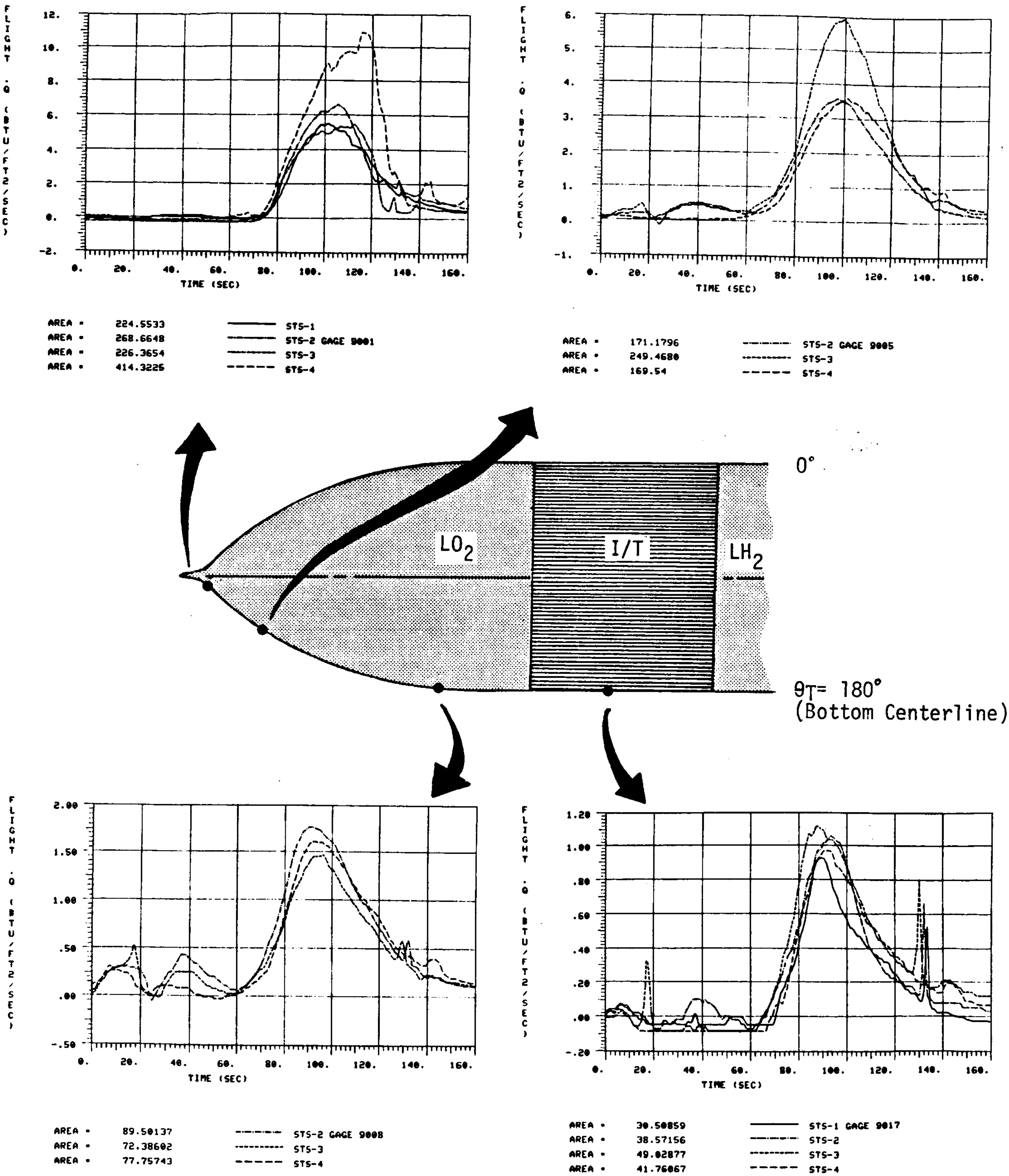

Fig. 3.16a LO_2 DFI Turbulent Heat-Transfer Rate Measurements On $\theta_T \approx 180^{\circ}$

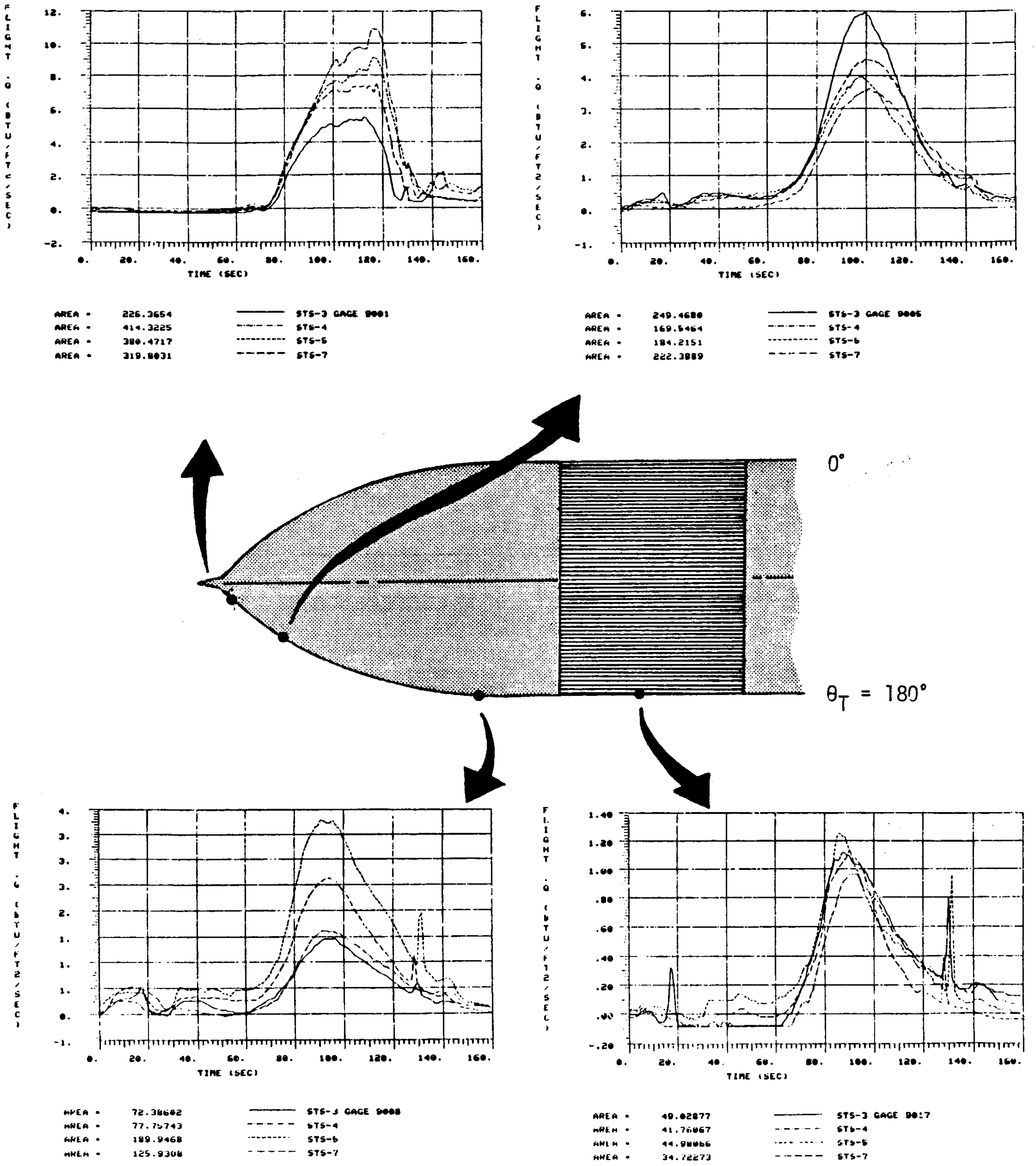

Fig. 3.16b DFI Turbulent Heat-Transfer Rate Measurements On $\theta_T \simeq 180^\circ$

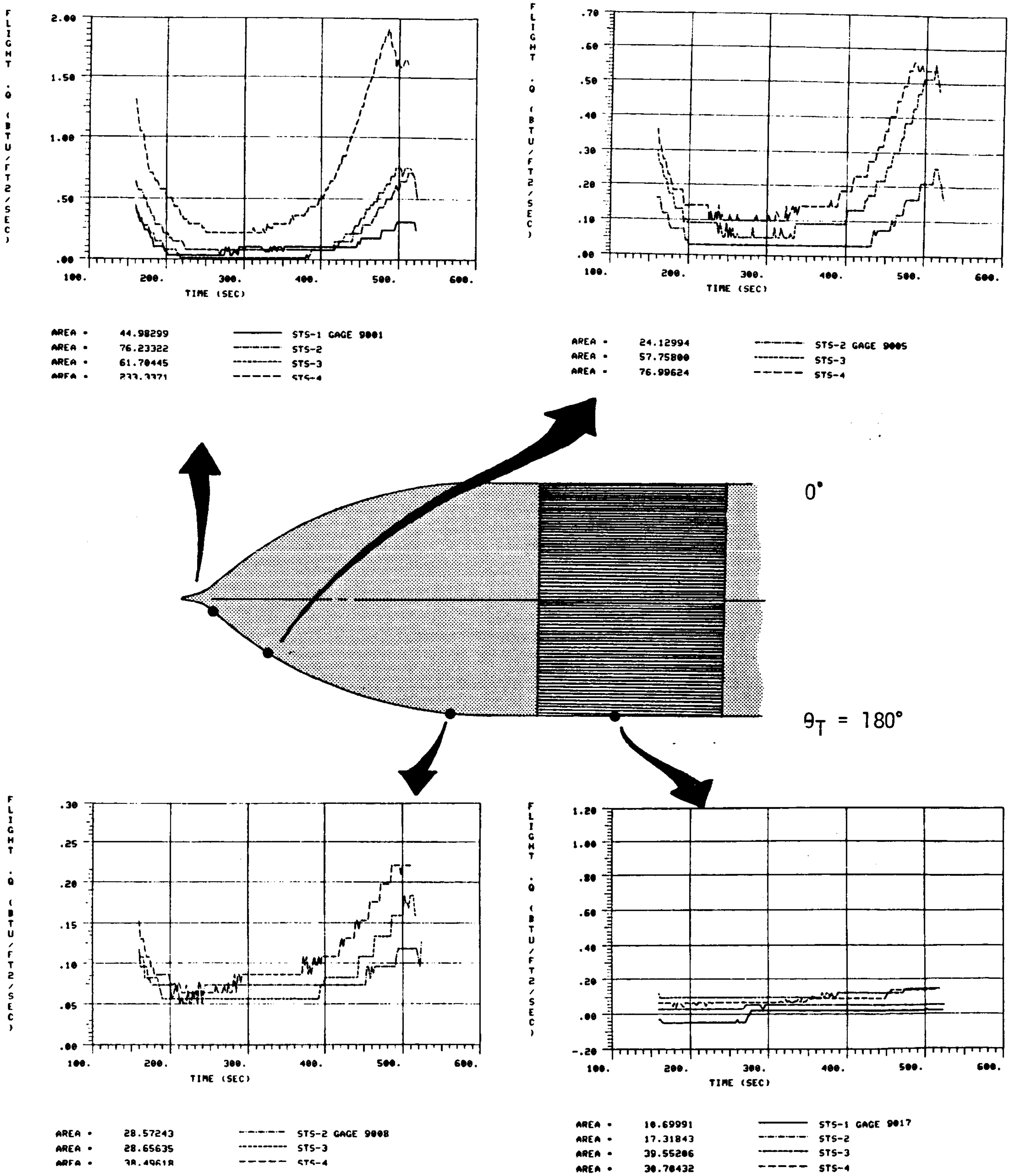

Fig. 3.17a LO_2 DFI Laminar/Rarefied Heat-Transfer Rate Measurements On $\theta_T \simeq 180^{\circ}$

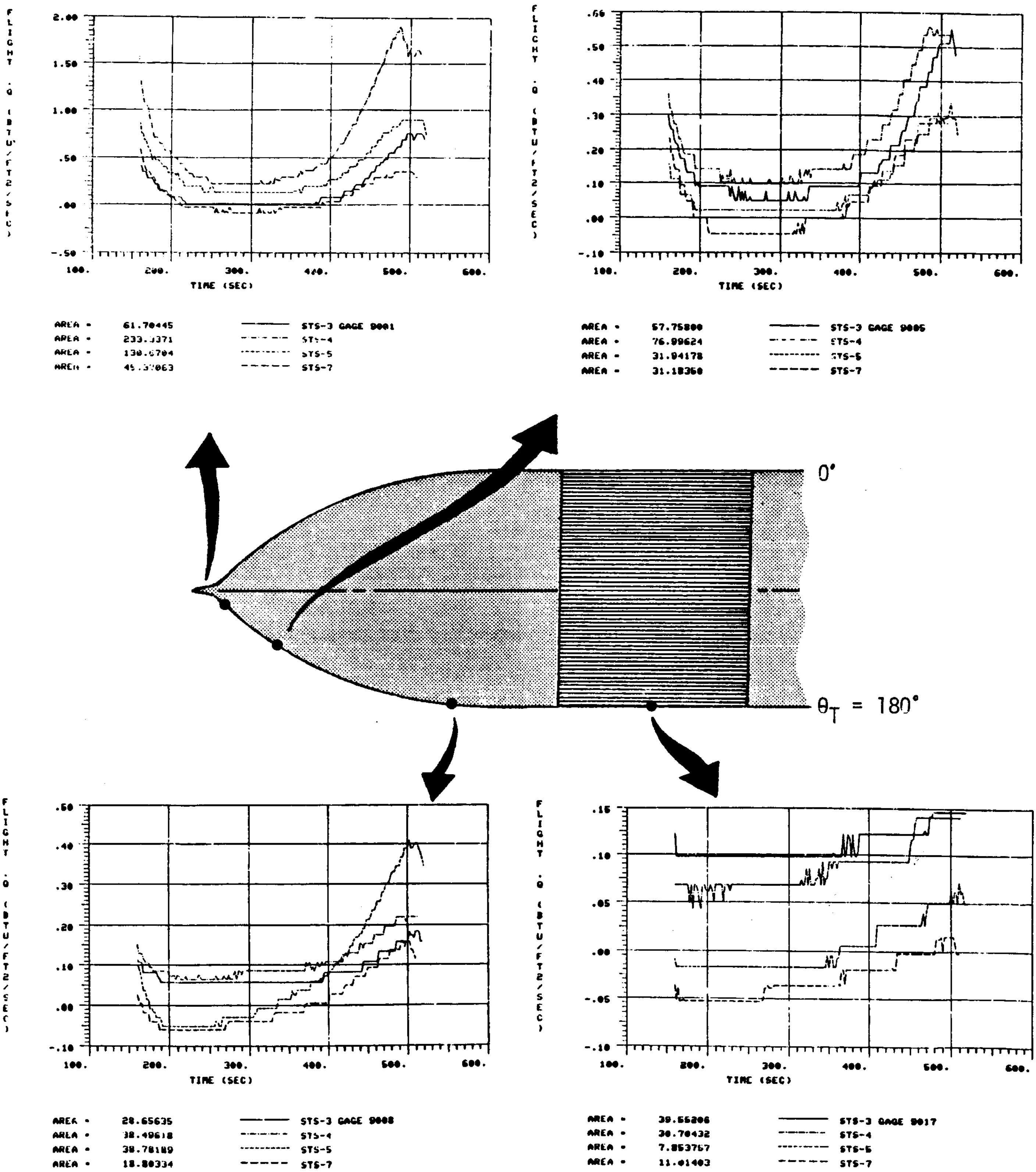

Fig. 3.17b LO_2 DFI Laminar/Rarefied Heat-Transfer Rate Measurements On $\theta_T \approx 180^{\circ}$

ORIGINAL PAGE IS
OF POOR QUALITY

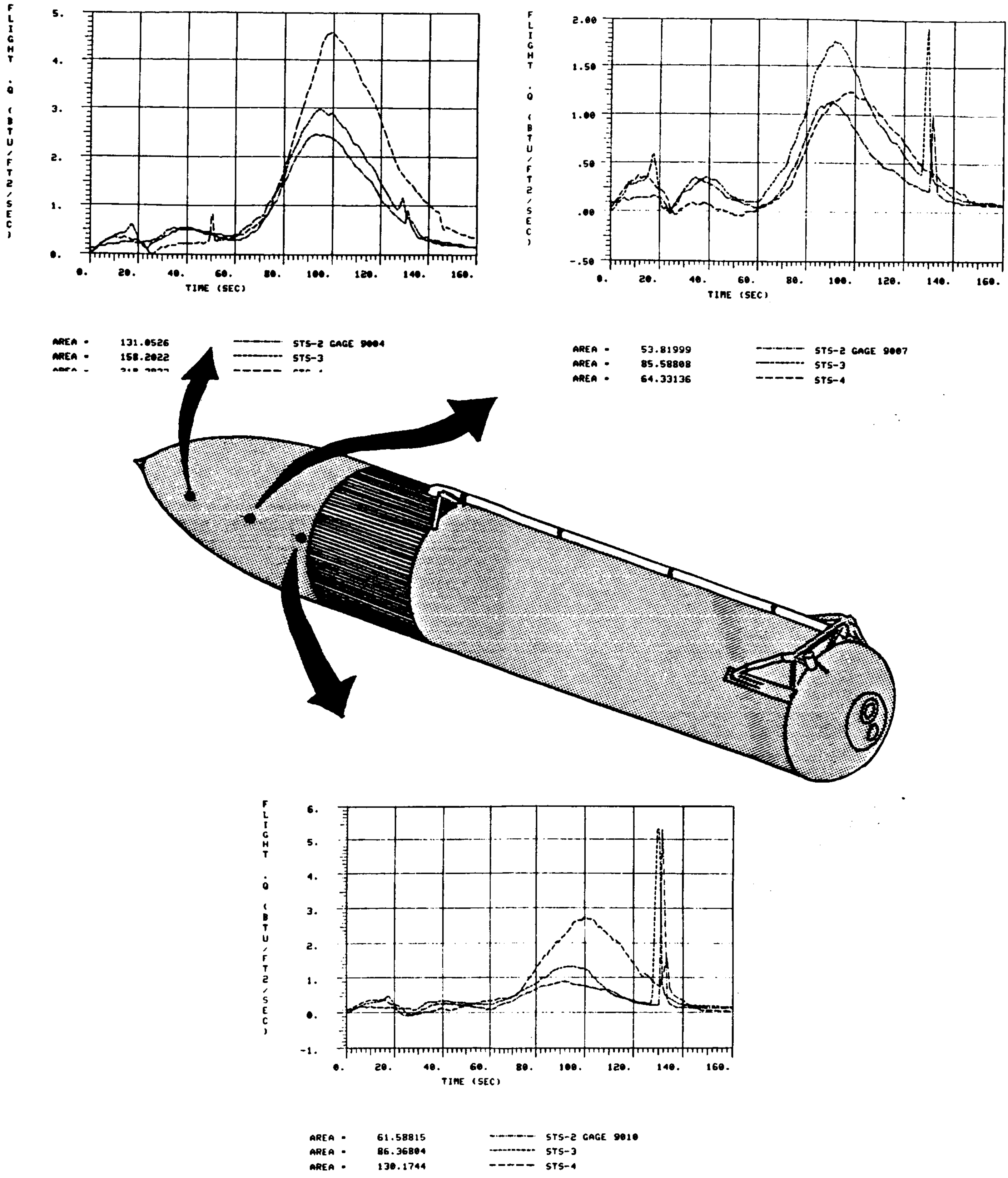

Fig. 3.18a LO_2 DFI Turbulent Heat-Transfer Rate Measurements On $\theta_T = 270^0$

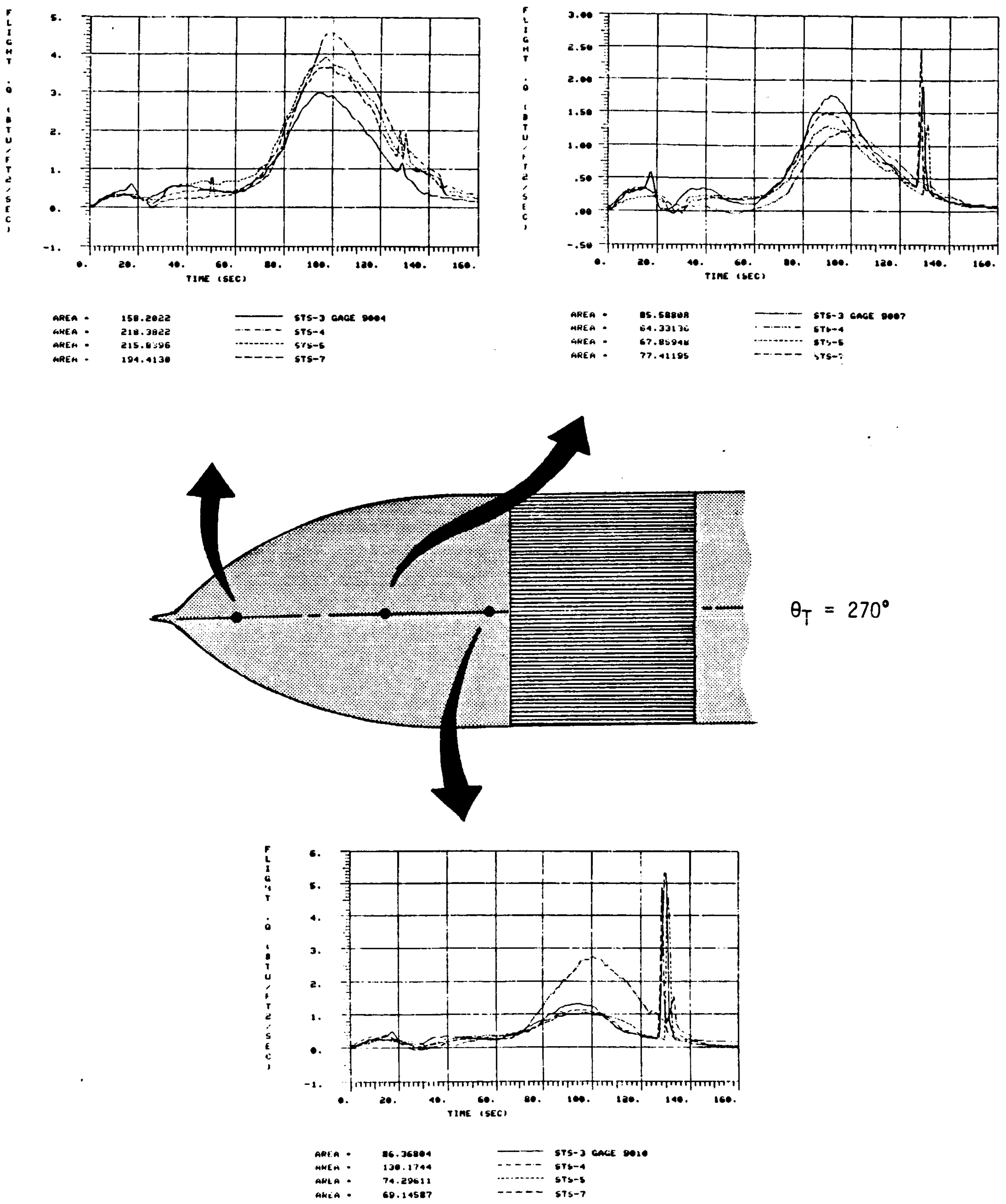

Fig. 3.18b LO_2 DFI Turbulent Heat-Transfer Rate Measurements On $\theta_T = 270^{\circ}$

ORIGINAL PAGE IS
OF POOR QUALITY

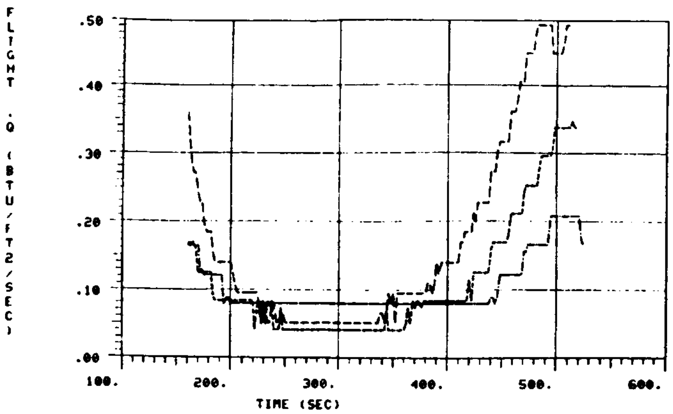

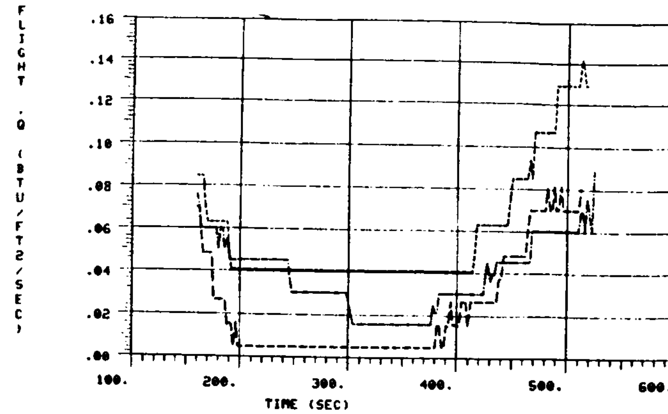

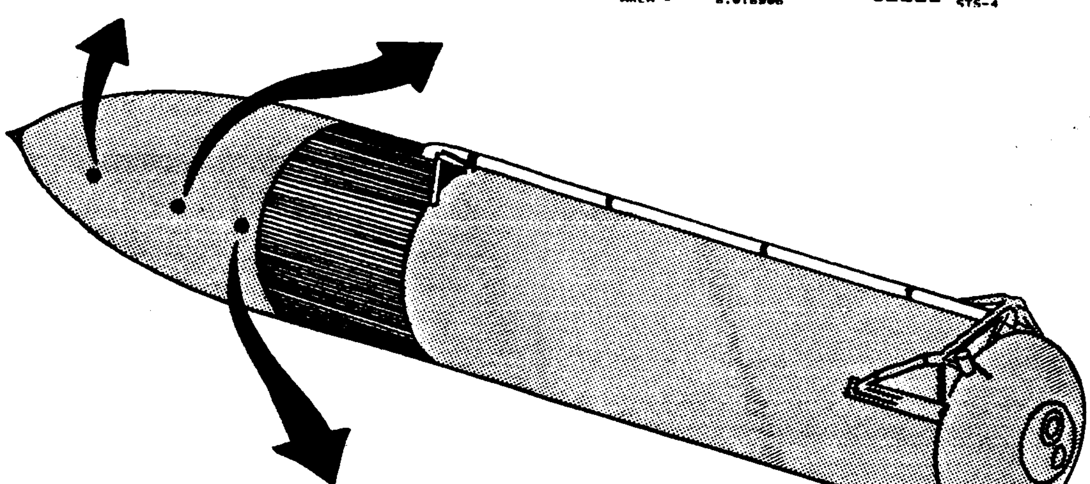

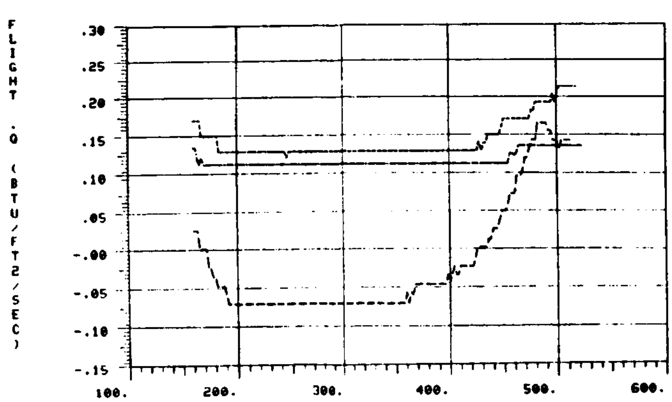

Fig. 3.19a LO_2 DFI Laminar/Rarefied Heat-Transfer Measurements On $\theta_T = 270^o$

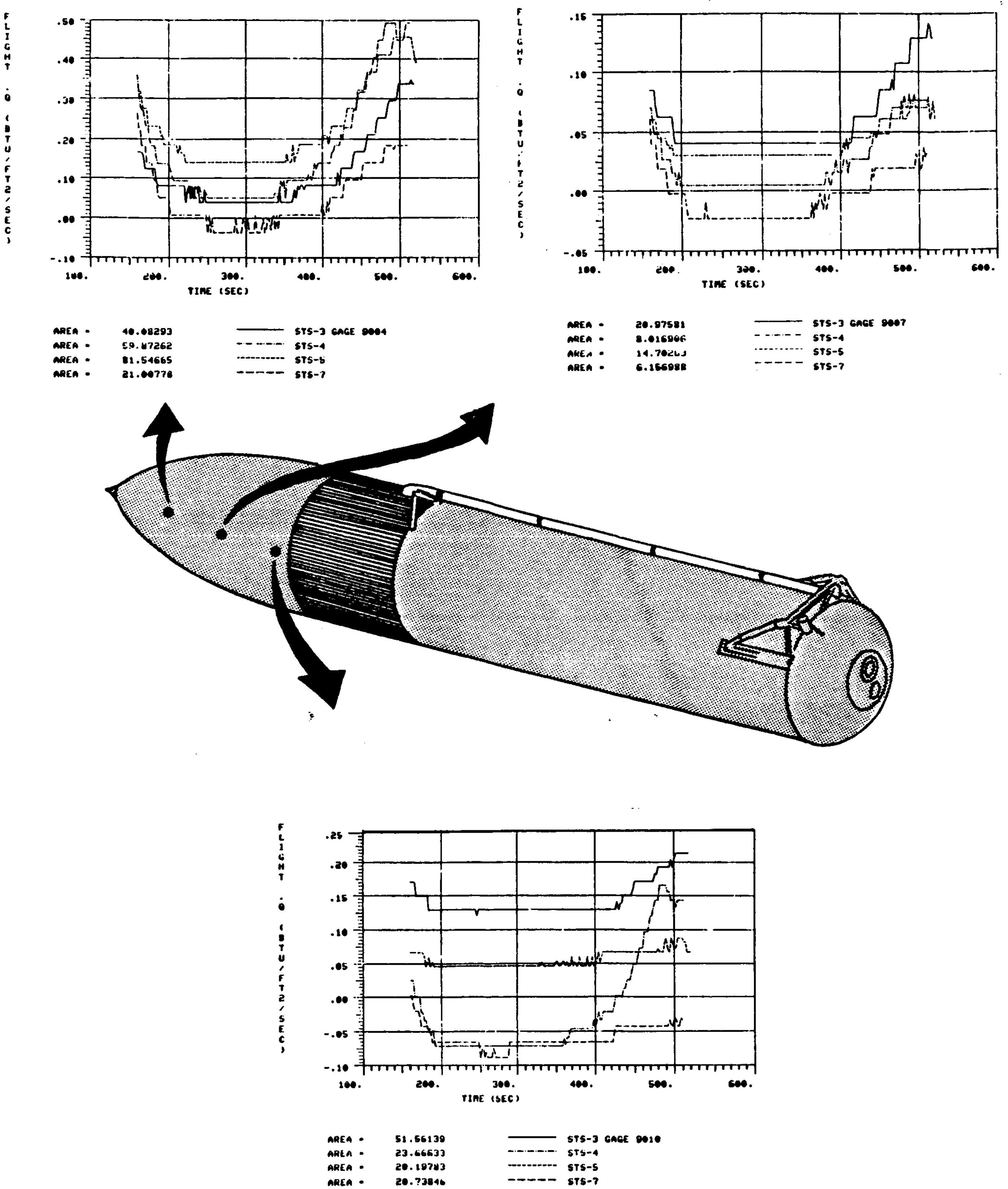

Fig. 3.19b LO$_2$ DFI Laminar/Rarefied Heat-Transfer Measurements On θ_T = 270^o

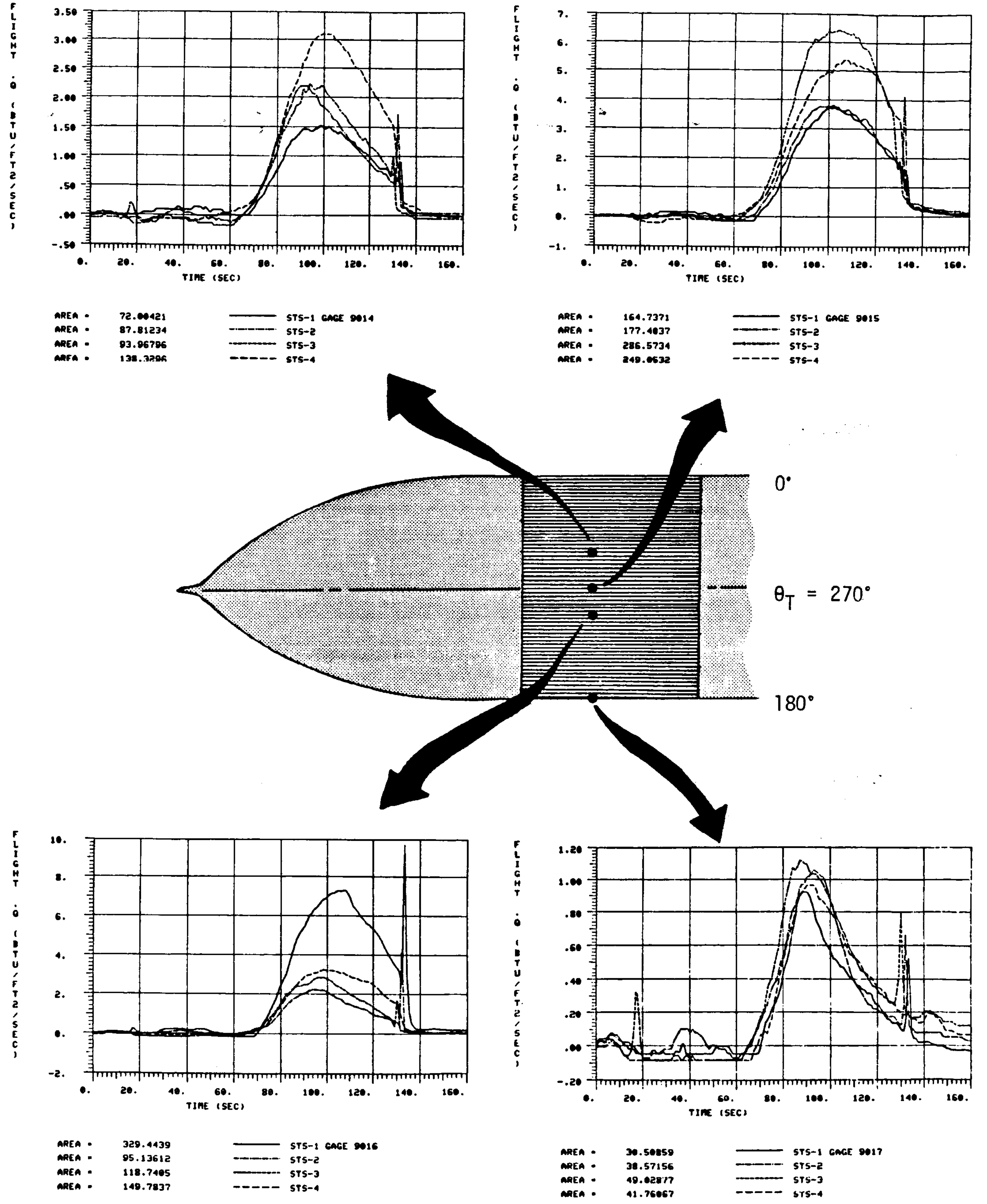

Fig. 3.20a Intertank DFI Turbulent Heat-Transfer Rate Measurements At $X_T \simeq 941.4"$

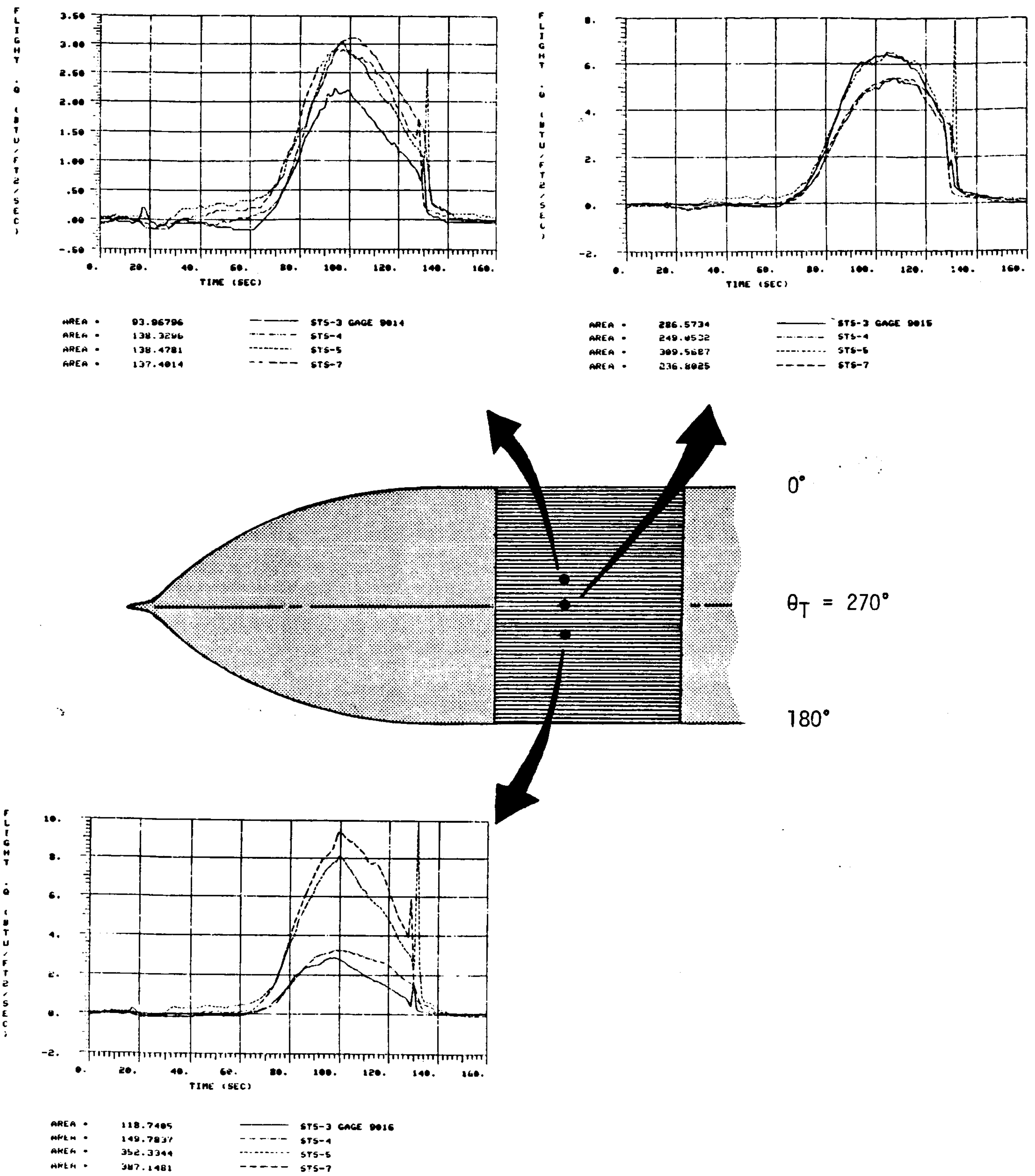

Fig. 3.20b Intertank DFI Turbulent Heat-Transfer Rate Measurements At $X_T \simeq 941.4"$

ORIGINAL PAGE IS
OF POOR QUALITY

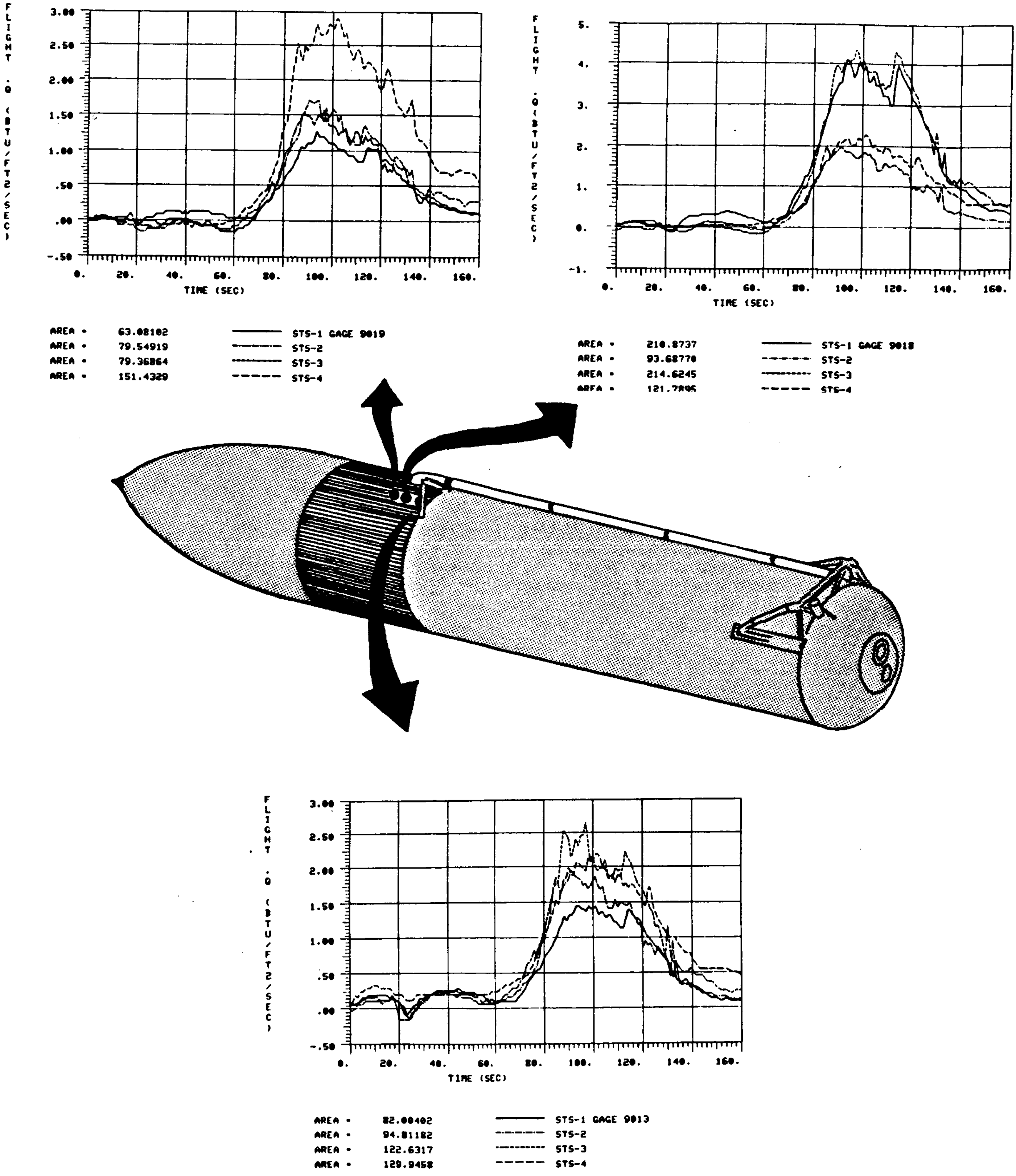

Fig. 3.21a Intertank DFI Heat-Transfer Rate Measurements On Island 17 ($\theta_T \approx 0°$)

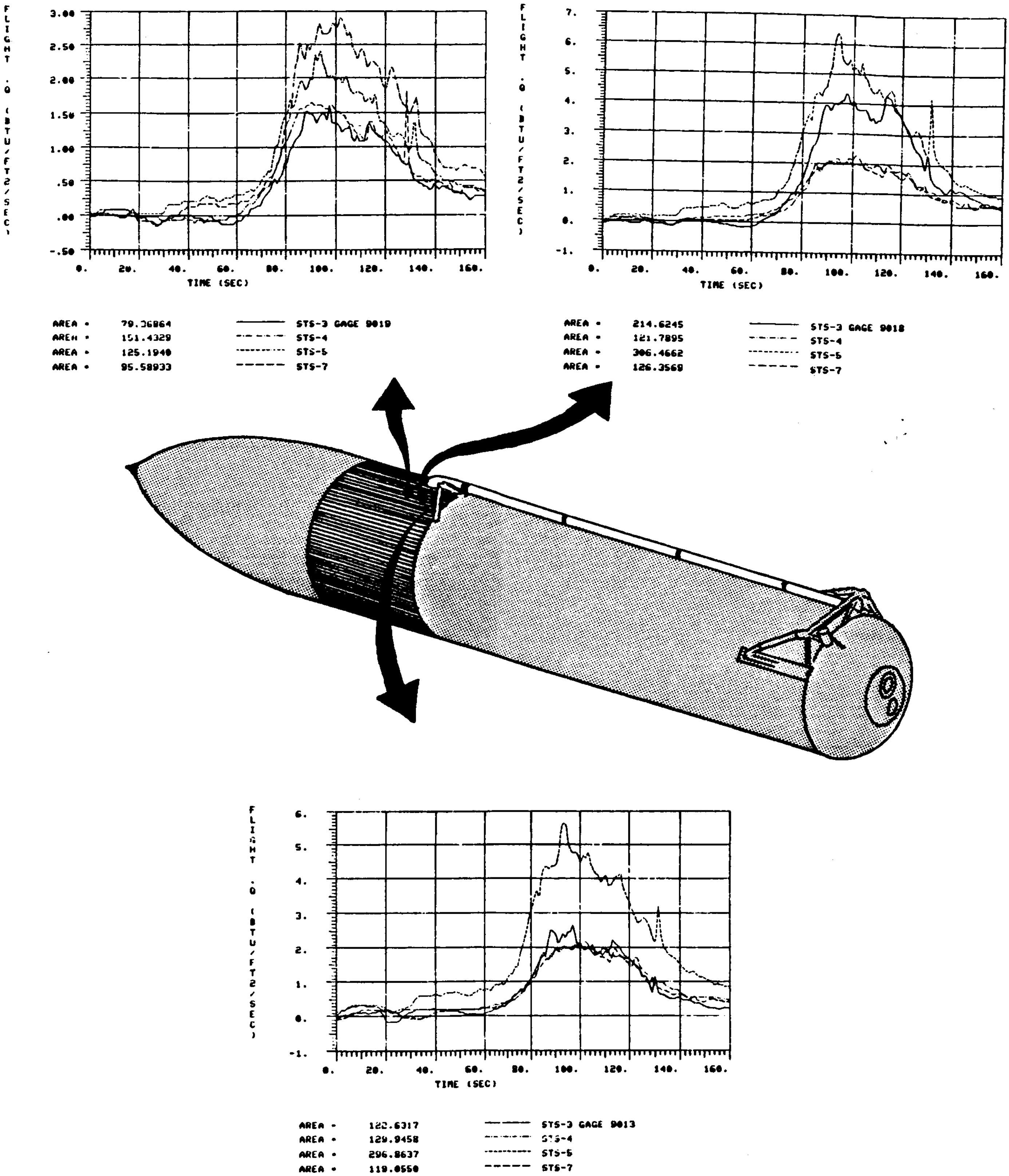

Fig. 3.21b Intertank DFI Heat-Transfer Rate Measurements On Island 17 ($\theta_T \approx 0°$)

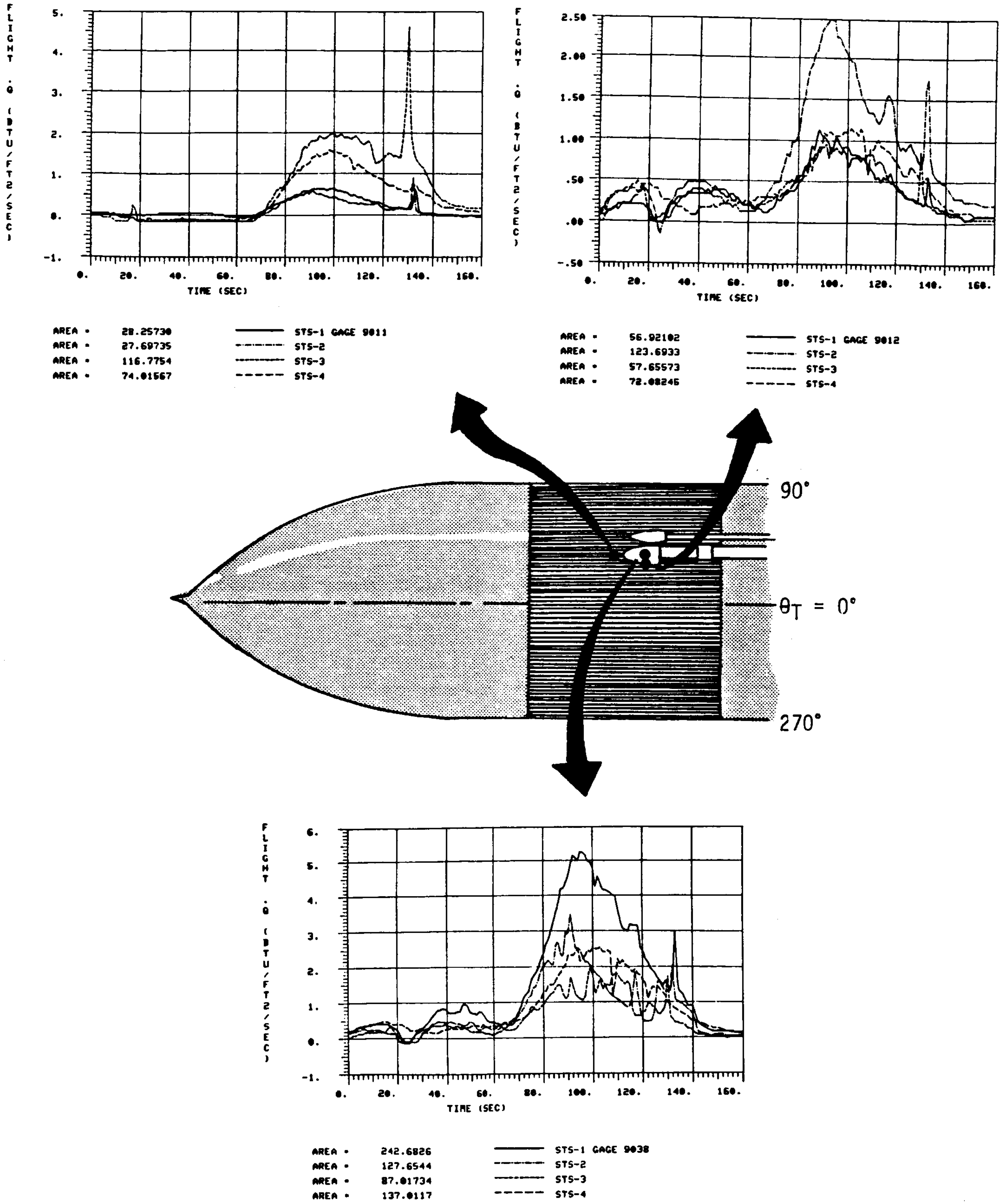

Fig. 3.22a Intertank DFI Heat-Transfer Rate Measurements On And Ahead Of The LO_2 Feed-line Forward Fairing

ORIGINAL PAGE IS
OF POOR QUALITY

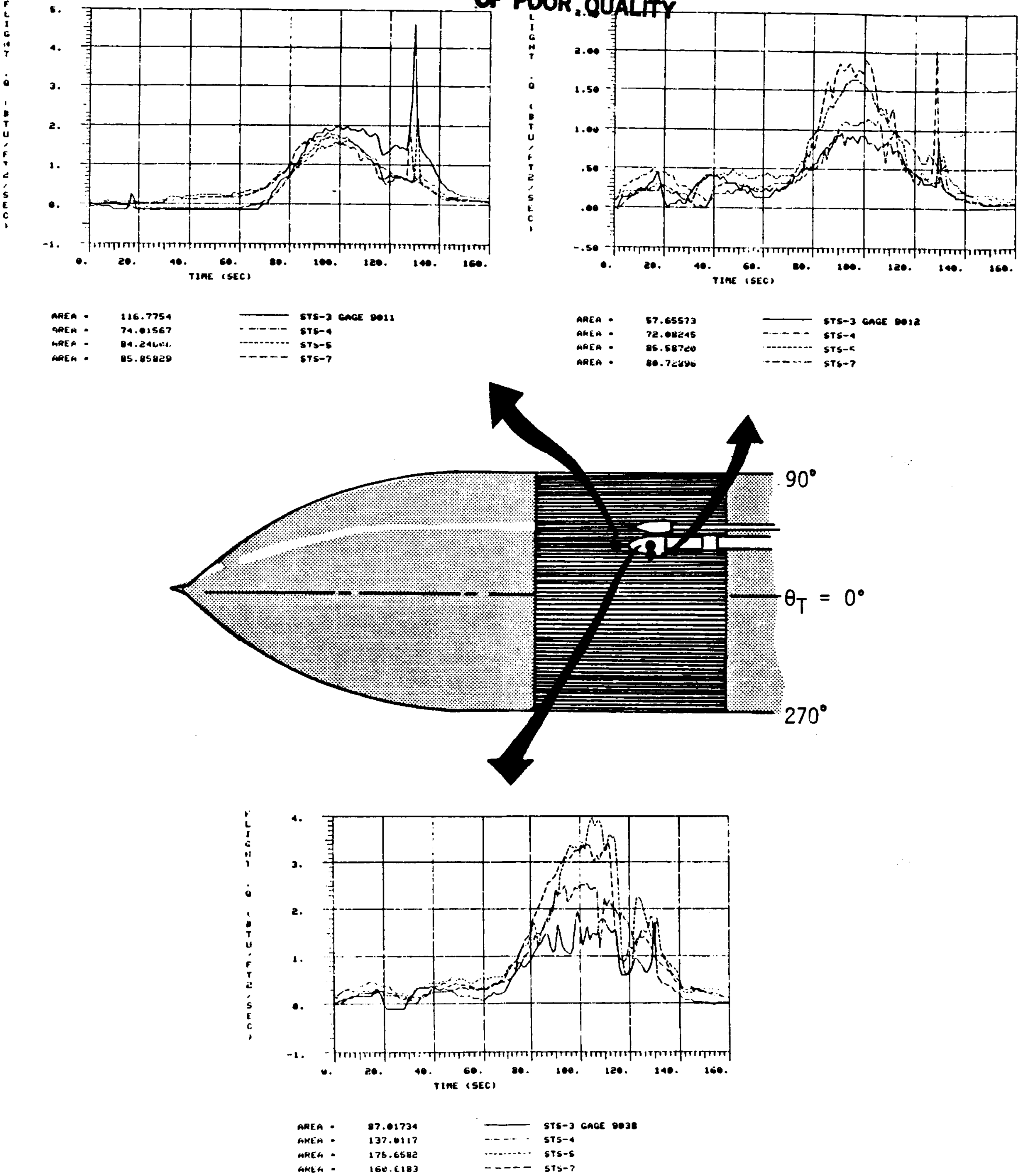

Fig. 3.22b Intertank DFI Heat-Transfer Rate Measurements On And Ahead Of The LO_2 Feedline Forward Fairing.

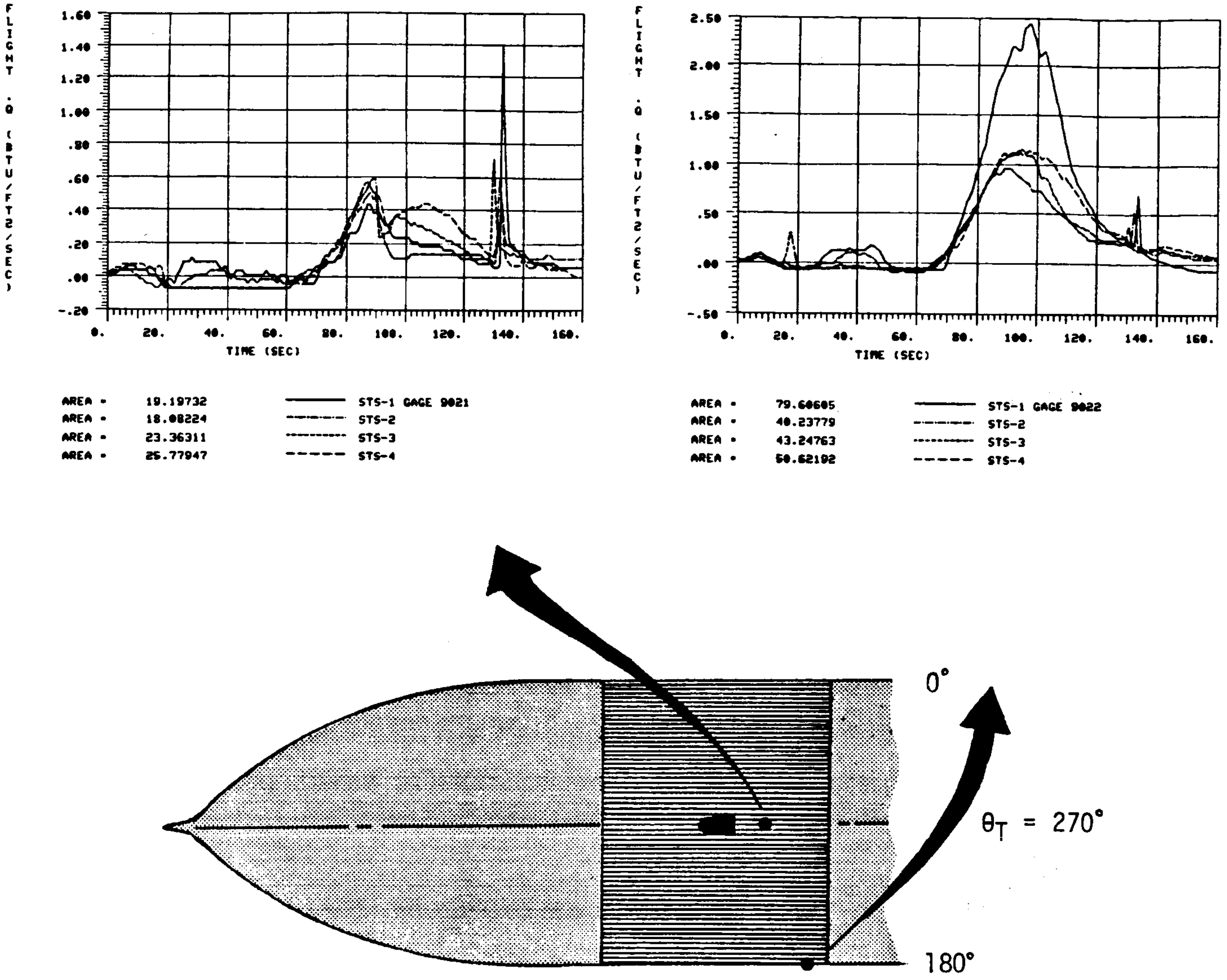

Fig. 3.23a Intertank DFI Heat-Transfer Rate Measurements Behind Bolt-Catcher And At The Bottom Centerline

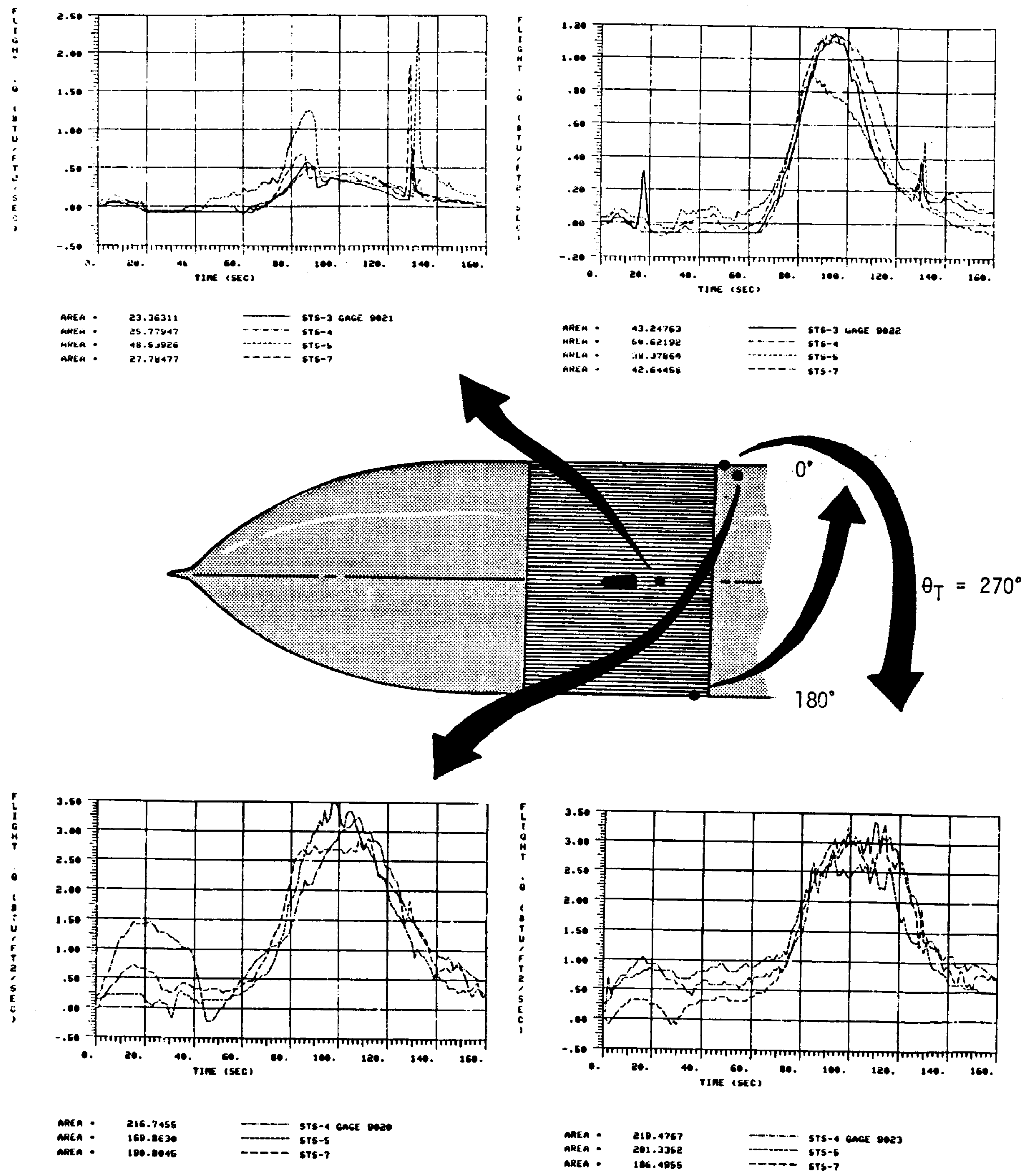

Fig. 3.23b Heat Transfer Rate Measurements Behind Bolt-Catcher And At The Bottom Centerline, And Measurements Behind The Bipod (A-Frame)

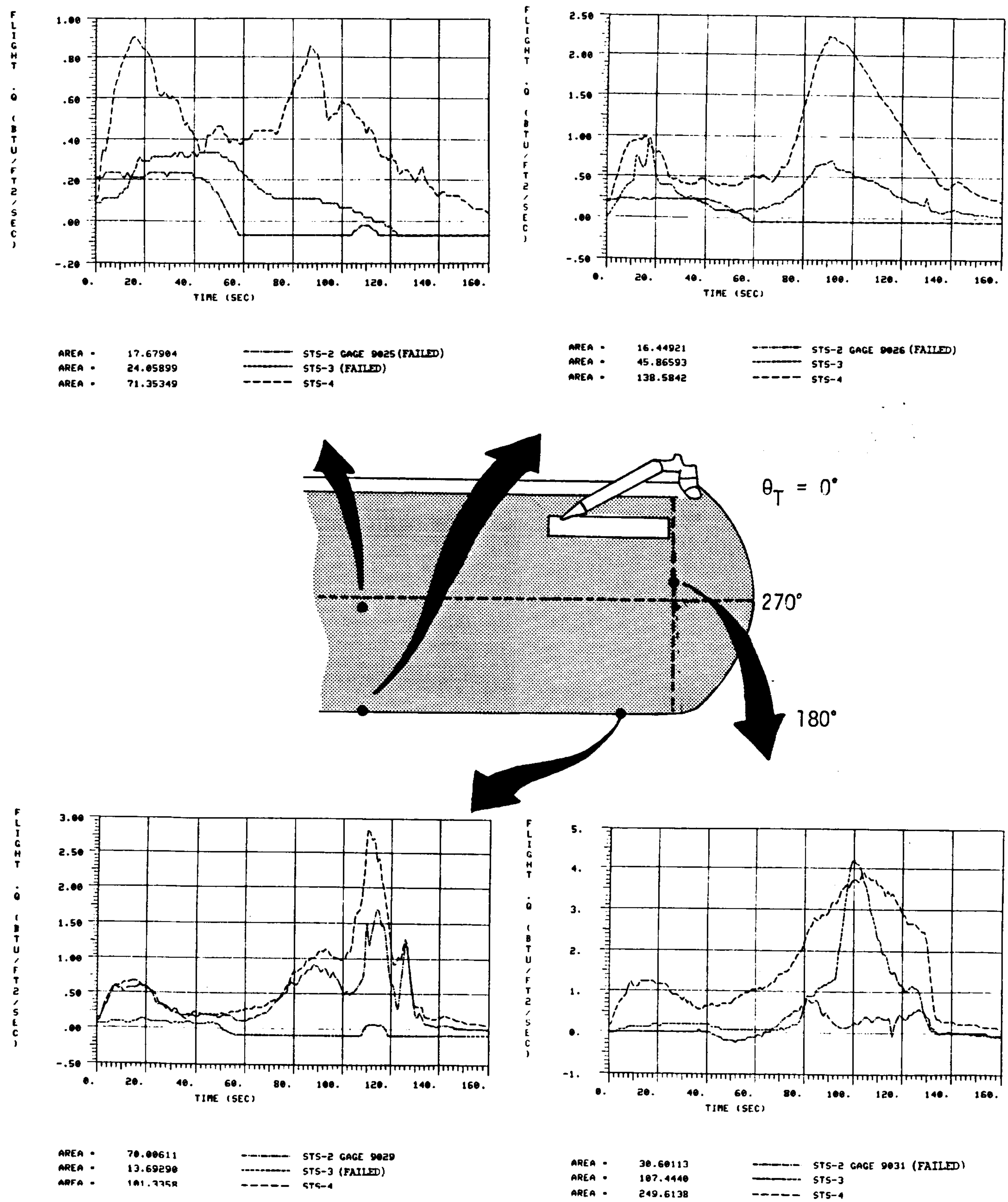

Fig. 3.24a LH_2 DFI Heat-Transfer Measurements On Mid-Body And Aft Body Locations

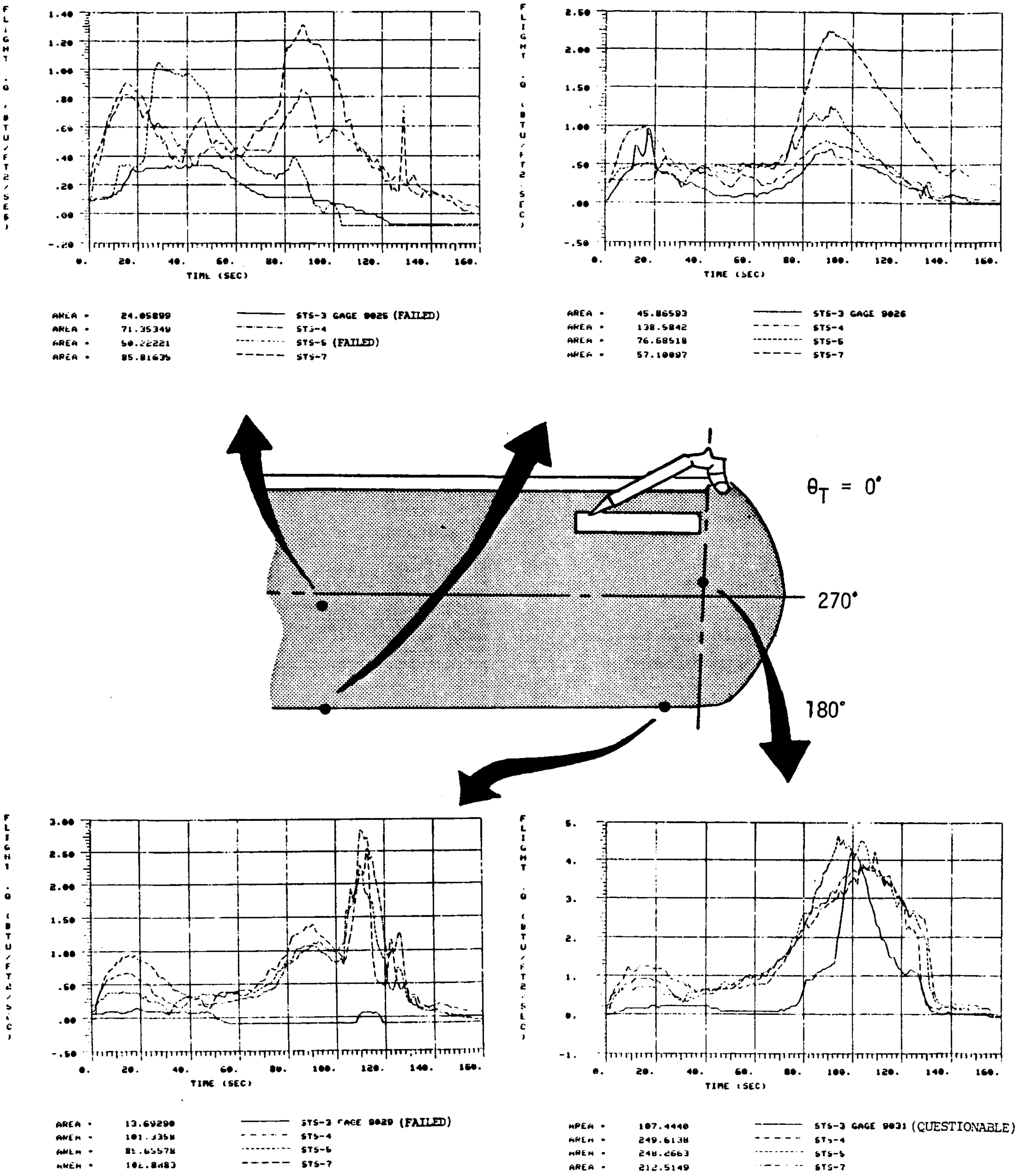

Fig. 3.24b LH$_2$ DFI Heat-Transfer Measurements On Mid-Body And Aft Body Locations

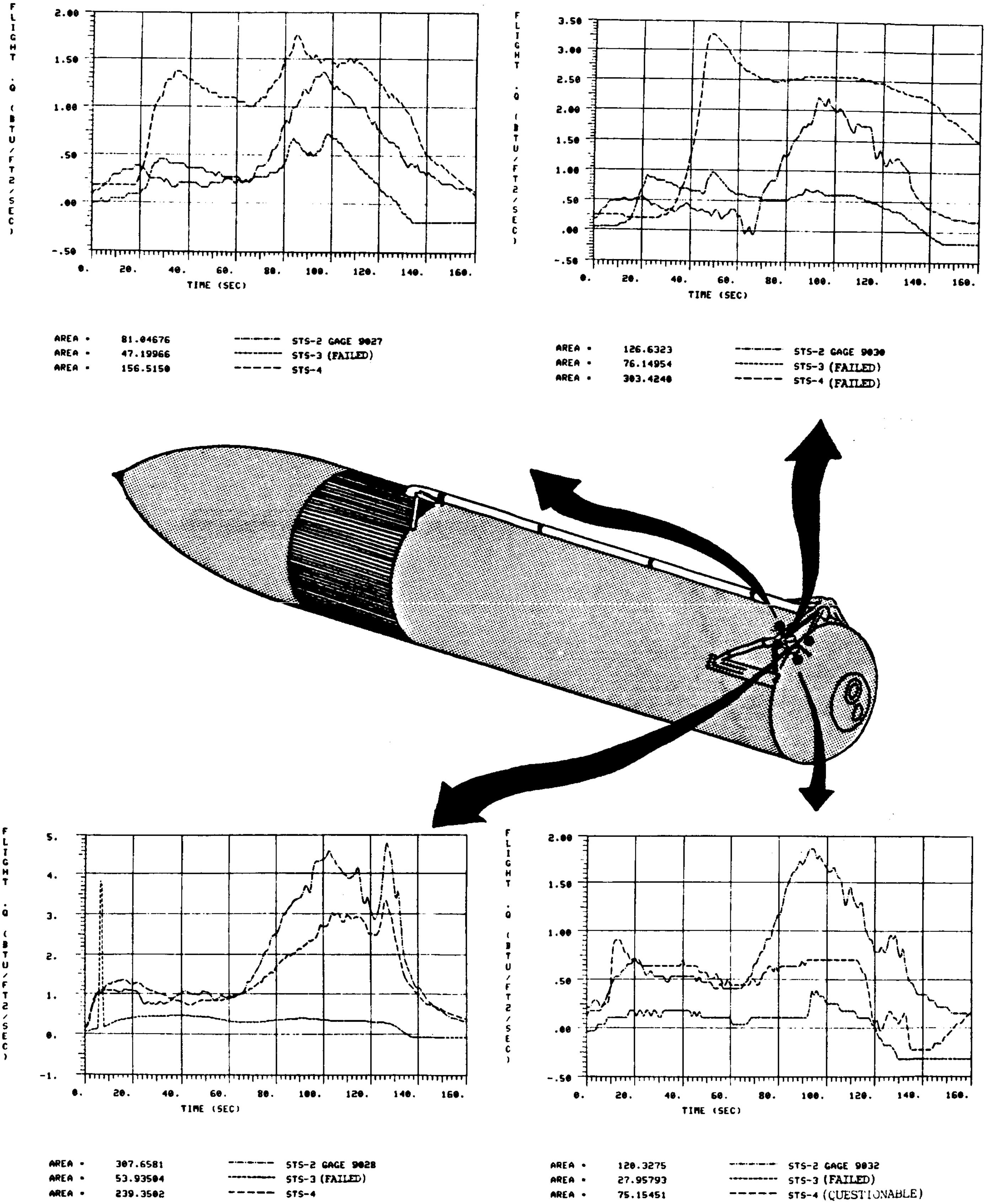

Fig. 3.25a LH$_2$ Acreage DFI Heat-Transfer Rate Measurements Around Aft Attach Structure

ORIGINAL PAGE IS OF POOR QUALITY

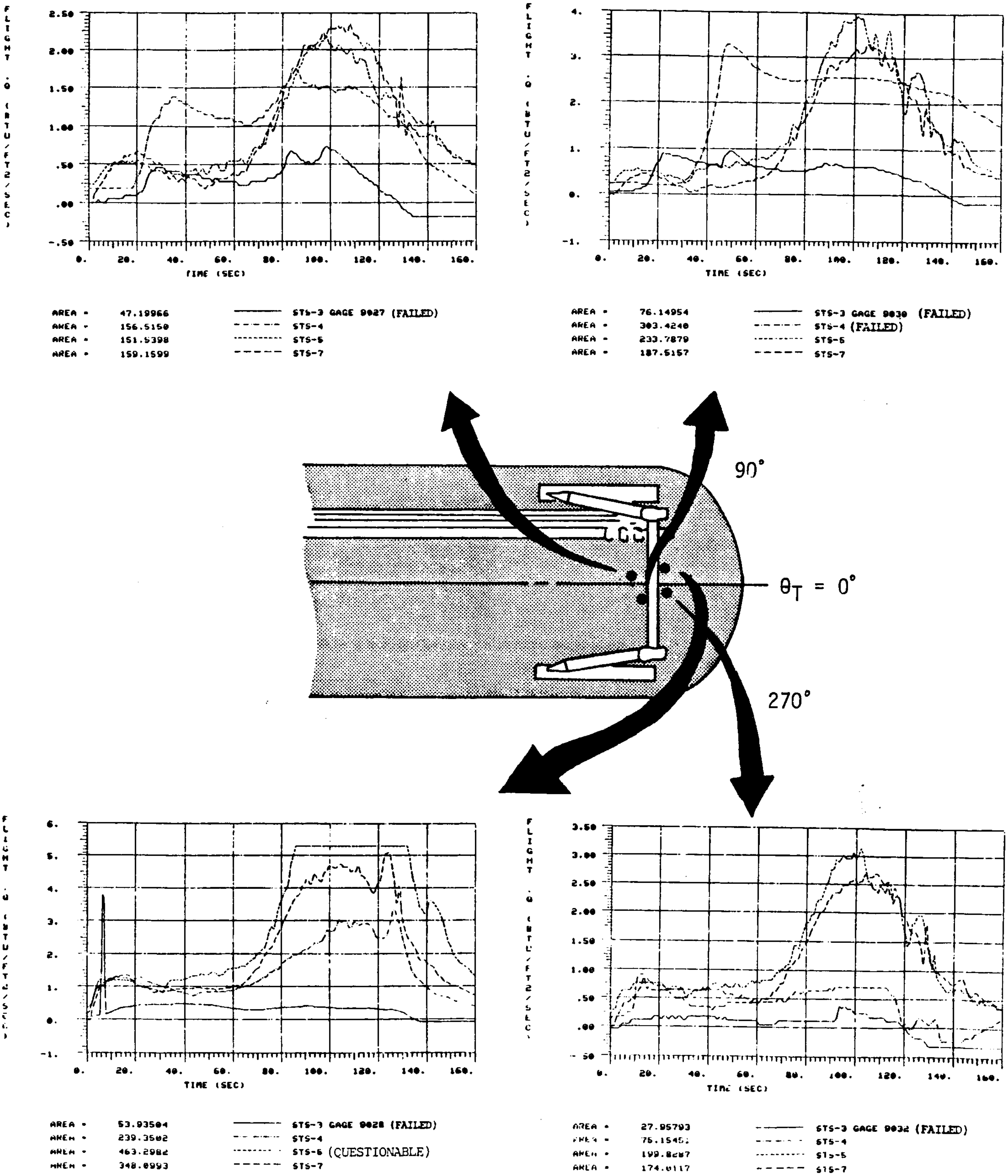

Fig. 3.25b LH_2 Acreage DFI Heat-Transfer Rate Measurements Around The AFT Attach Structure

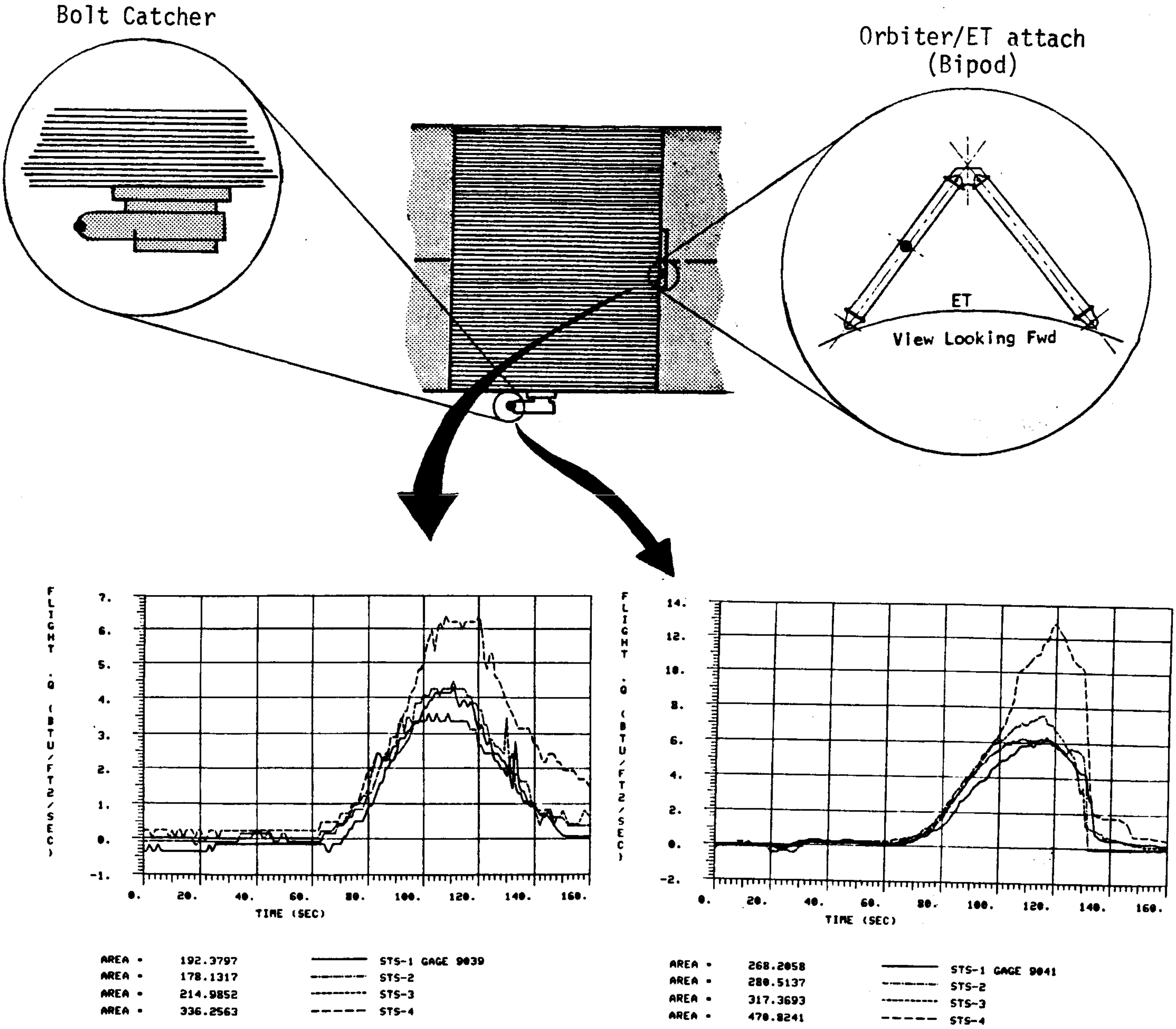

Fig. 3.26a Intertank Protuberance DFI Heat-Tranfer Rate Measurements On The Bolt-Catcher And Bi-Pod

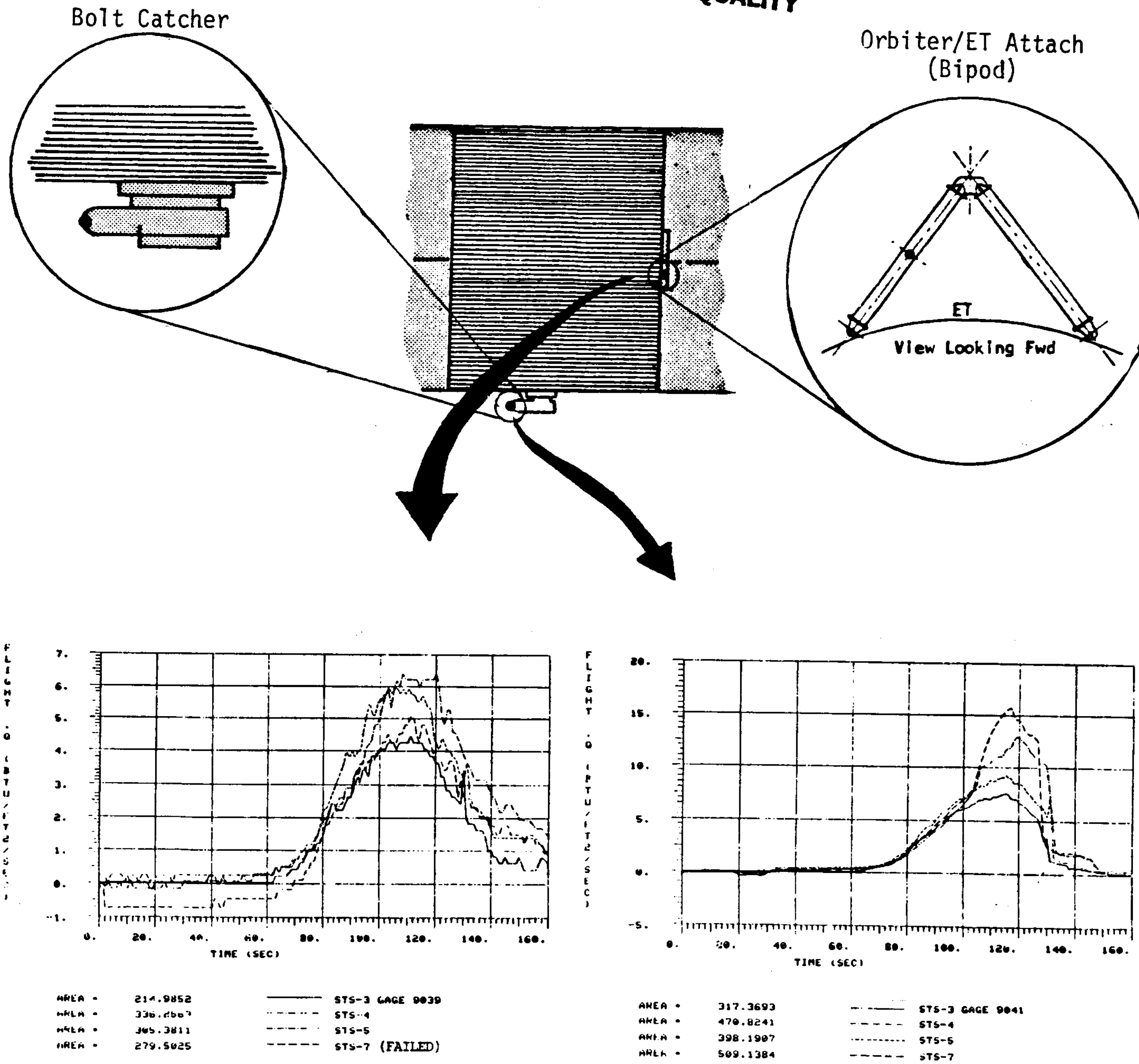

Fig. 3.26b Intertank Protuberance DFI Heat-Transfer Rate Measurements On The Bolt-Catcher And Bi-Pod

ORIGINAL PAGE IS
OF POOR QUALITY

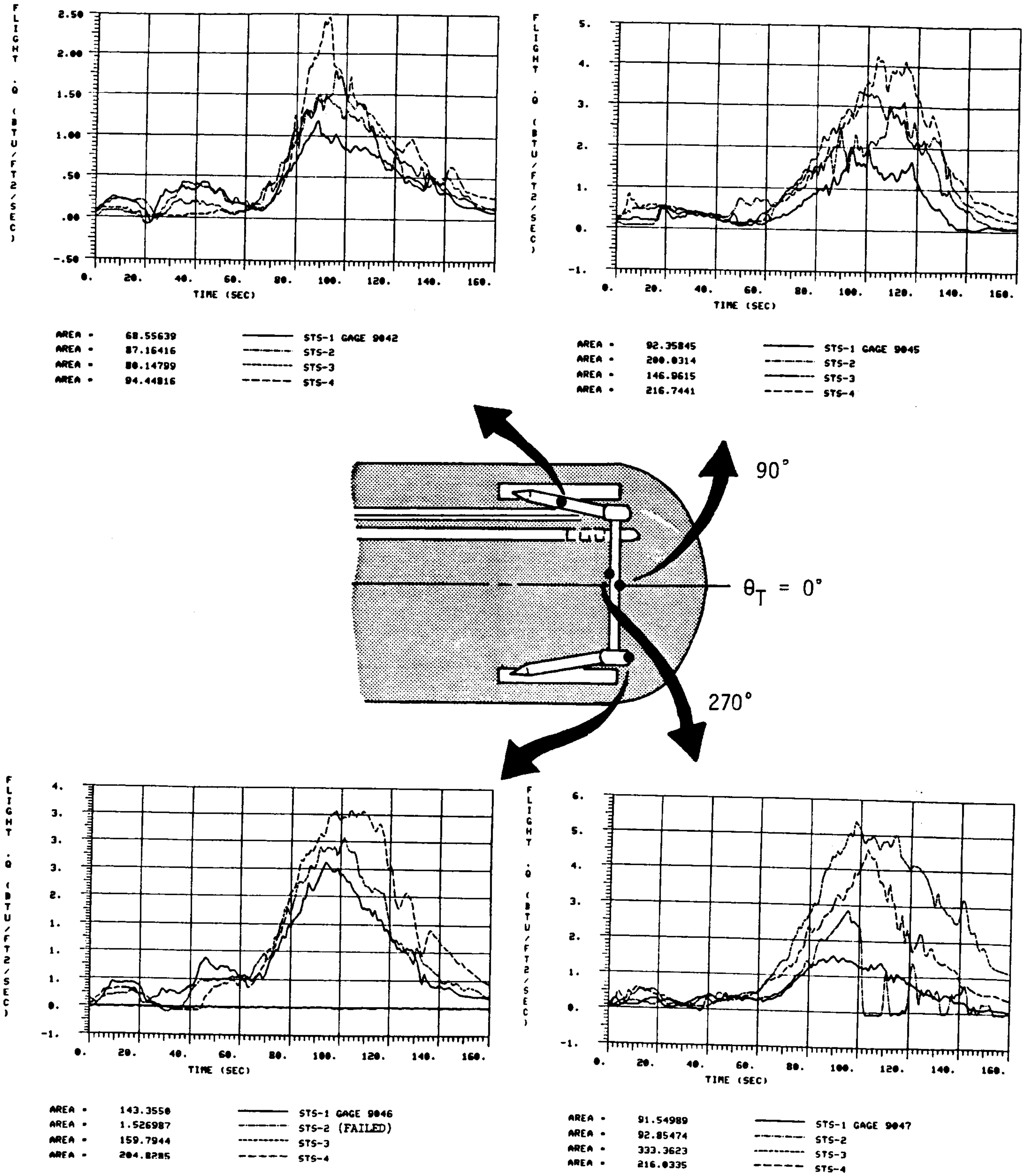

Fig. 3.27a LH_2 Protuberance DFI Heat-Transfer Rate Measurements On The Aft Attach Structure

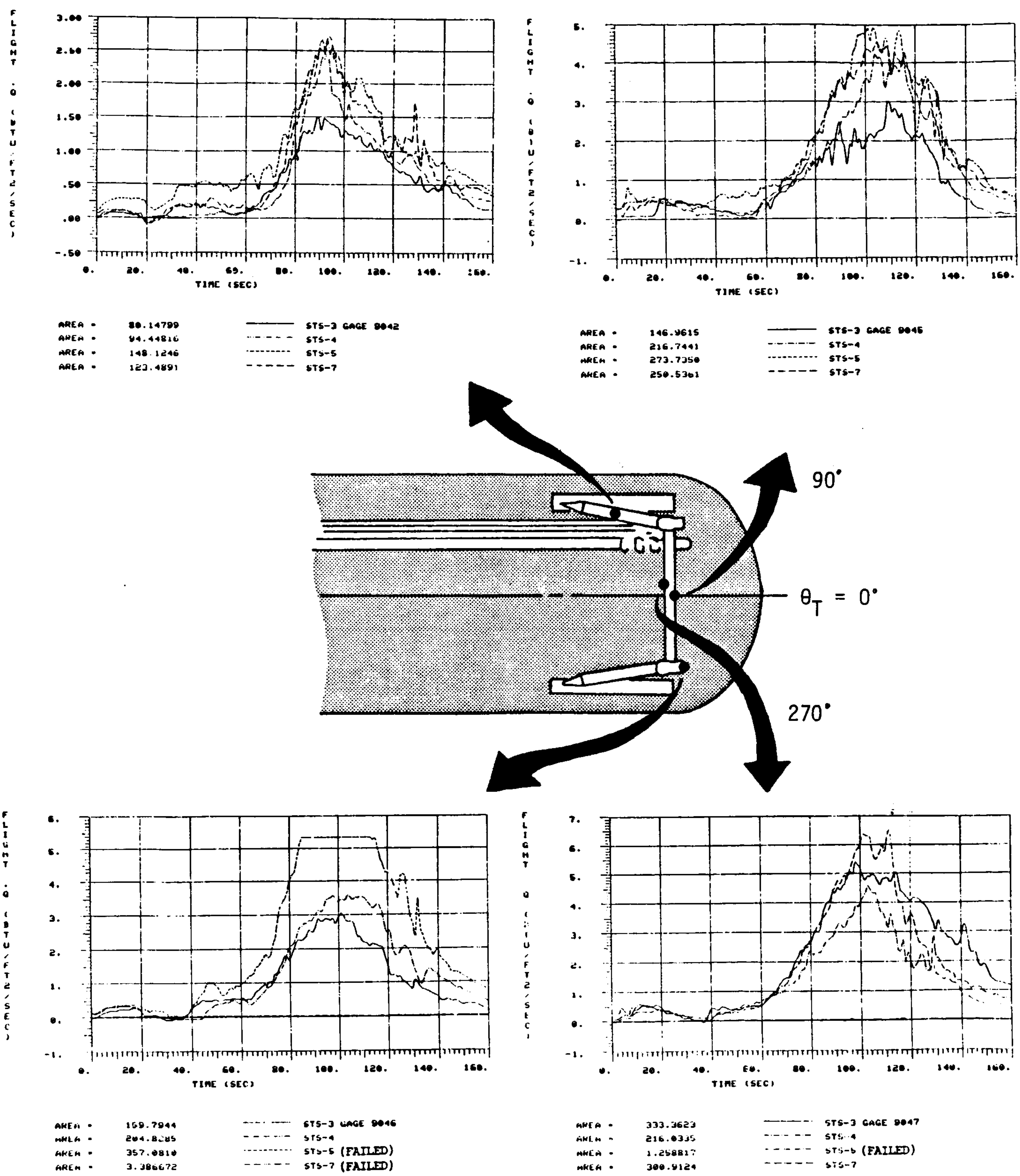

Fig. 3.27b LH$_2$ Protuberance DFI Heat-Transfer Rate Measurements On The Aft Attach Structure

ORIGINAL PAGE IS
OF POOR QUALITY

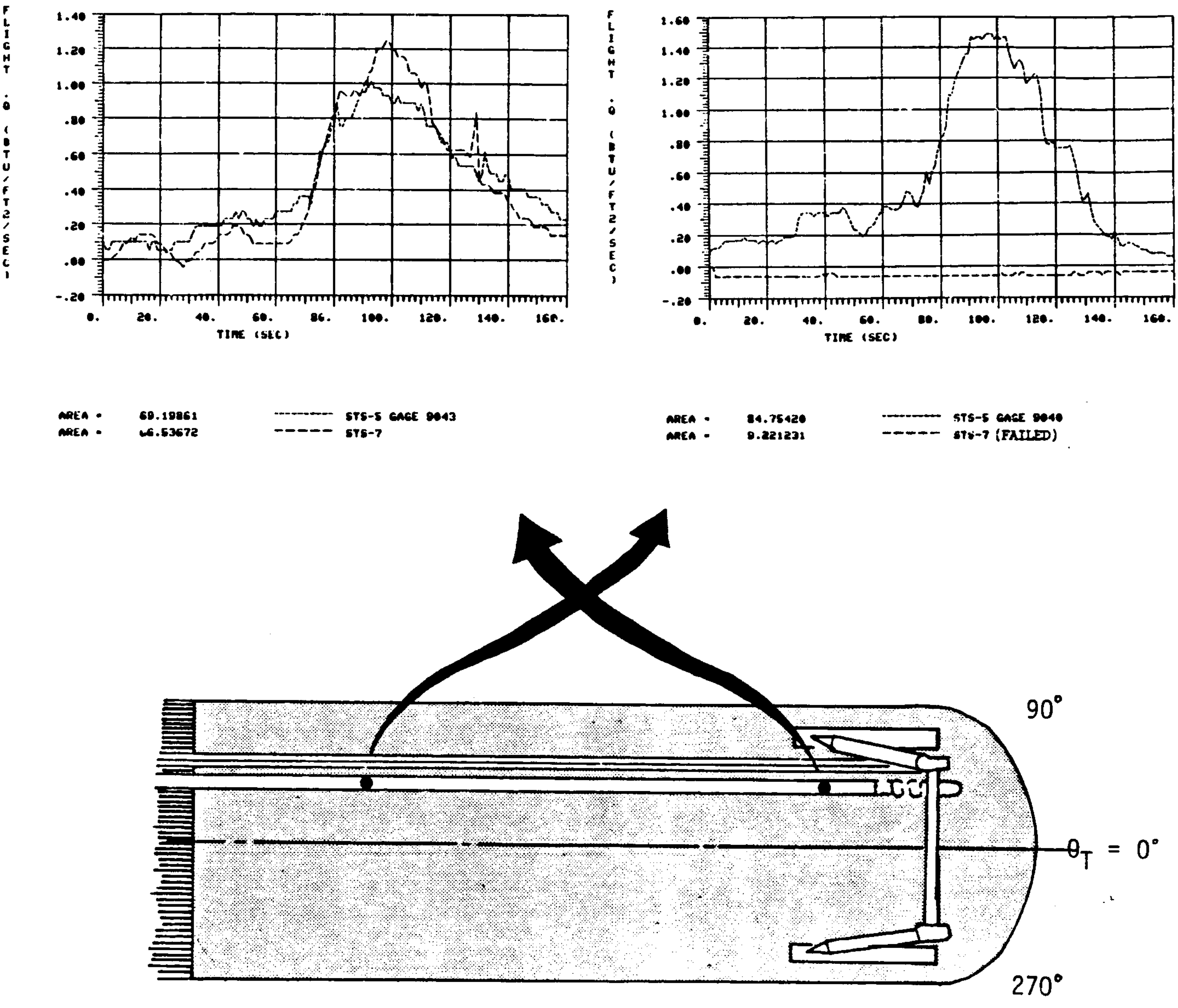

Fig. 3.28 LH_2 Protuberance DFI Heat-Transfer Rate Measurements On Cable Tray Supports

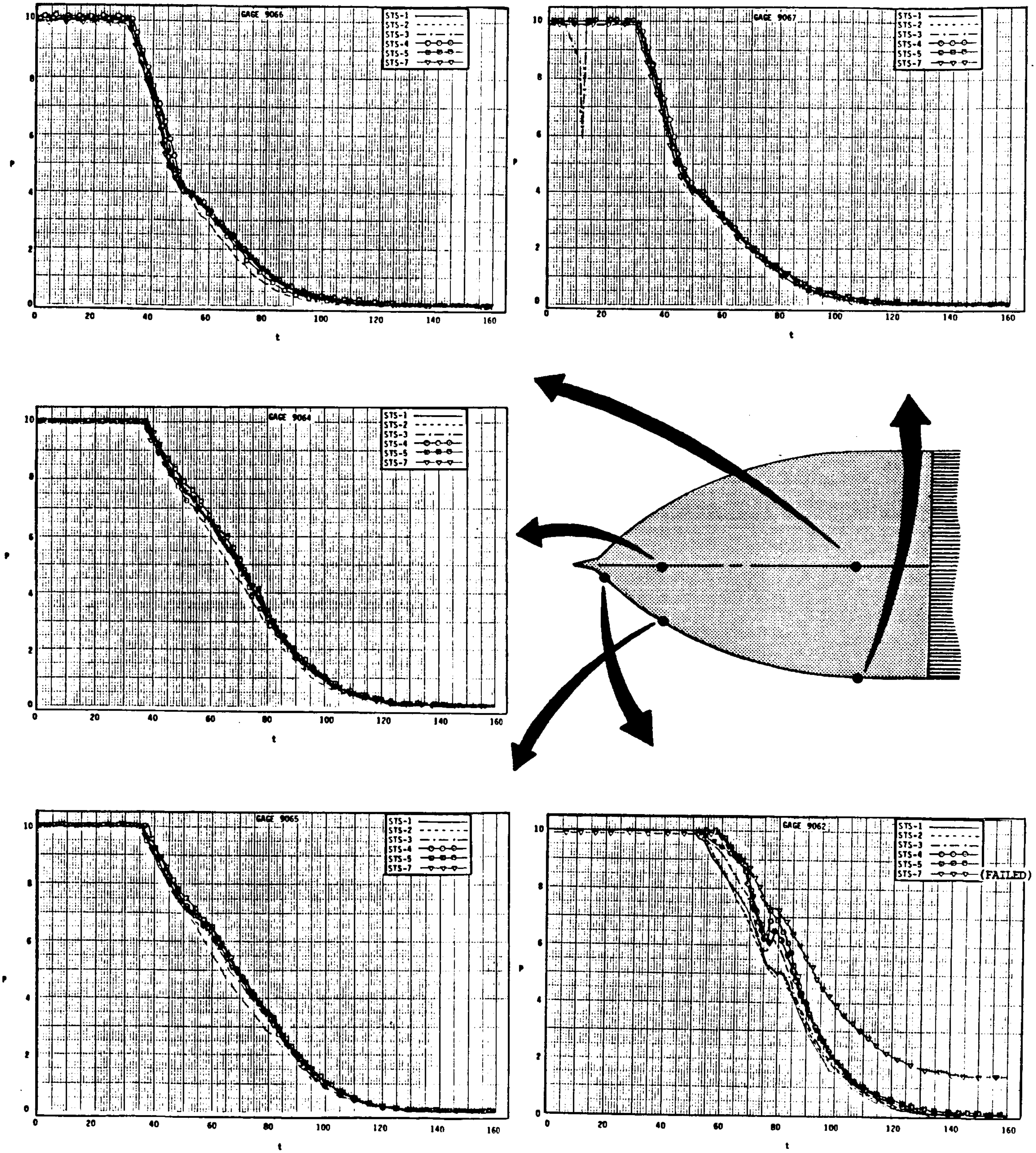

Fig. 3.29 LO_2 DFI Pressure Measurements

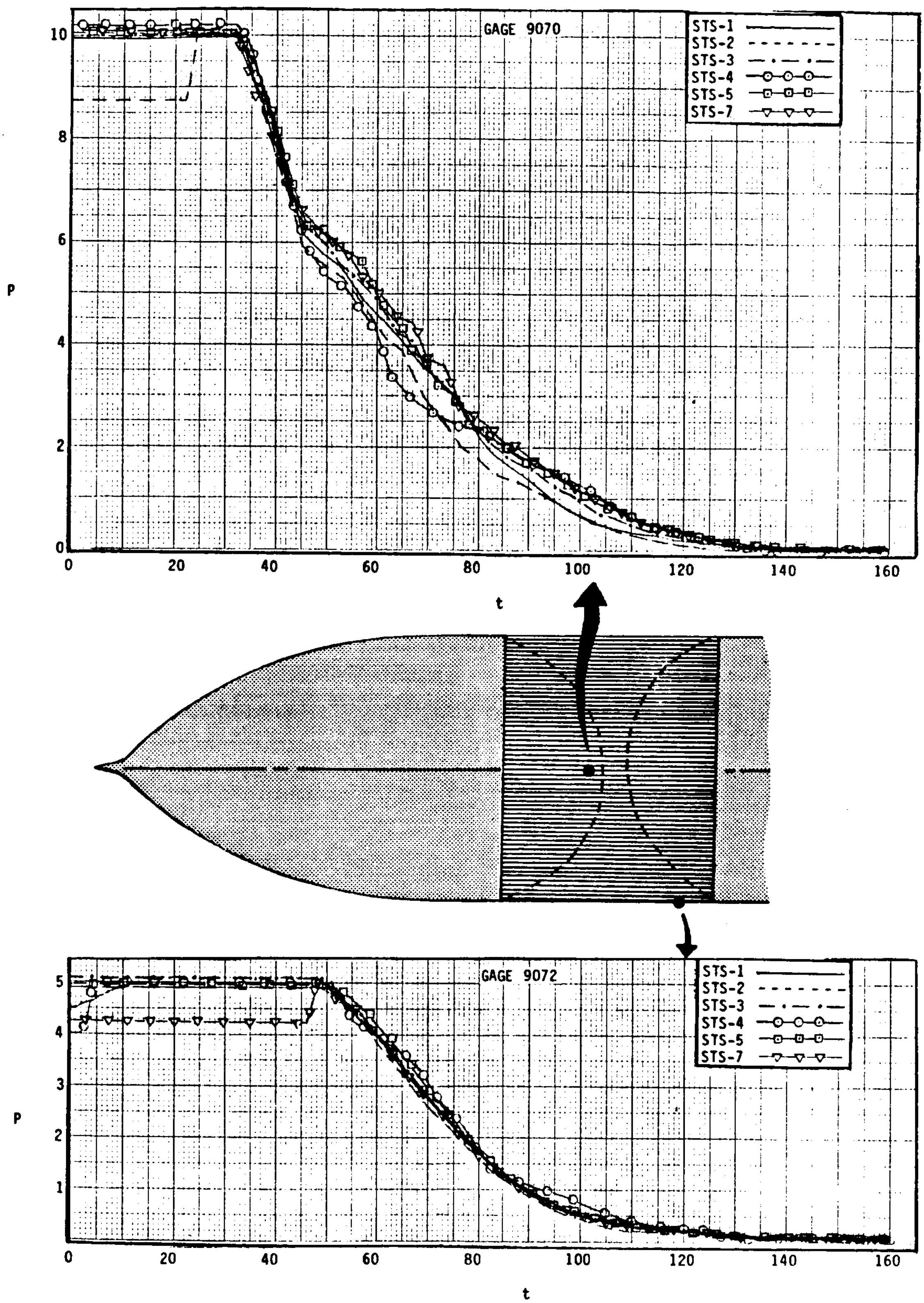

Fig. 3.30 Intertank DFI Pressure Measurements

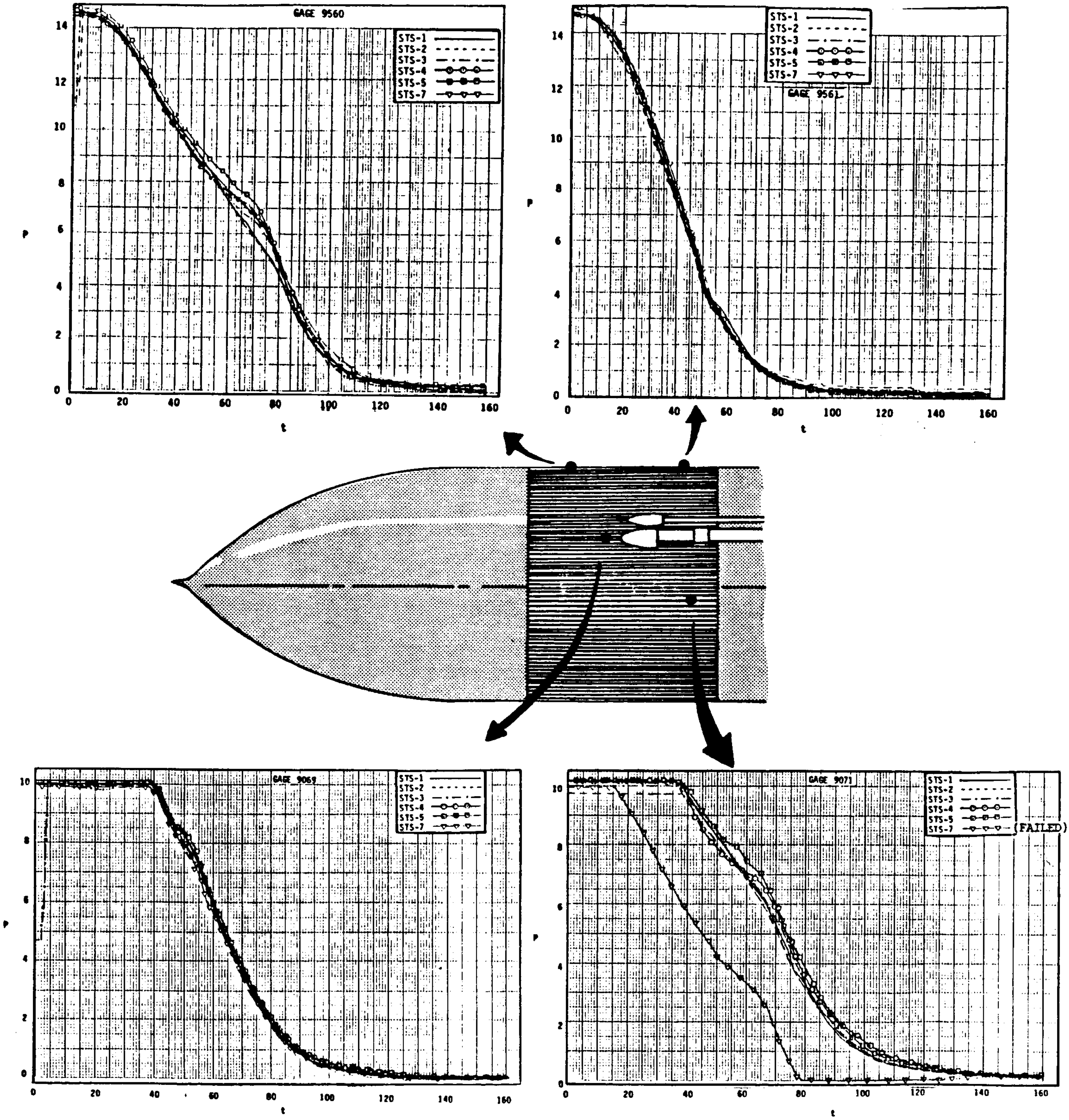

Fig. 3.31 Intertank DFI Pressure Measurements

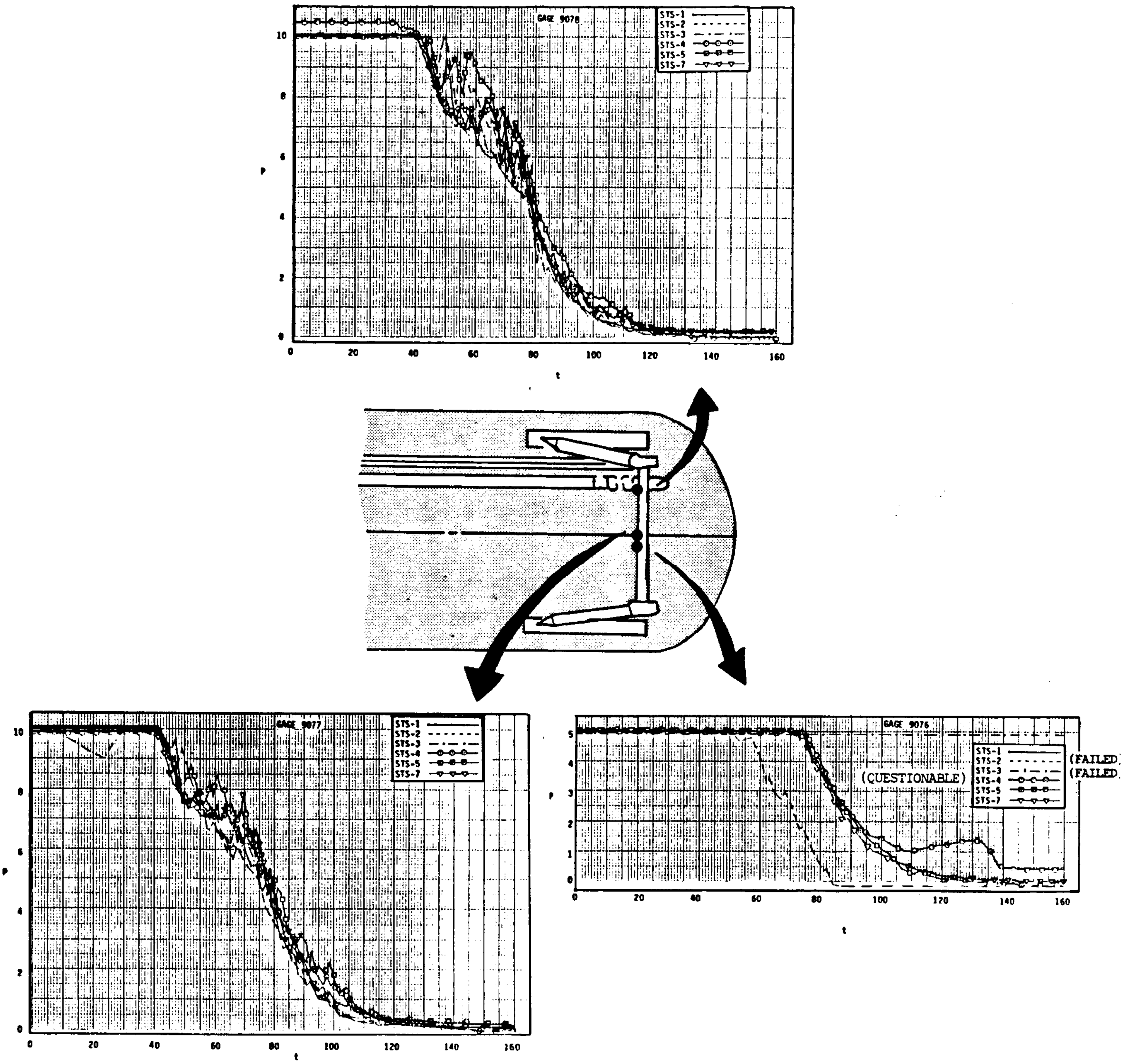

Fig. 3.32 LH_2 DFI Pressure Measurements

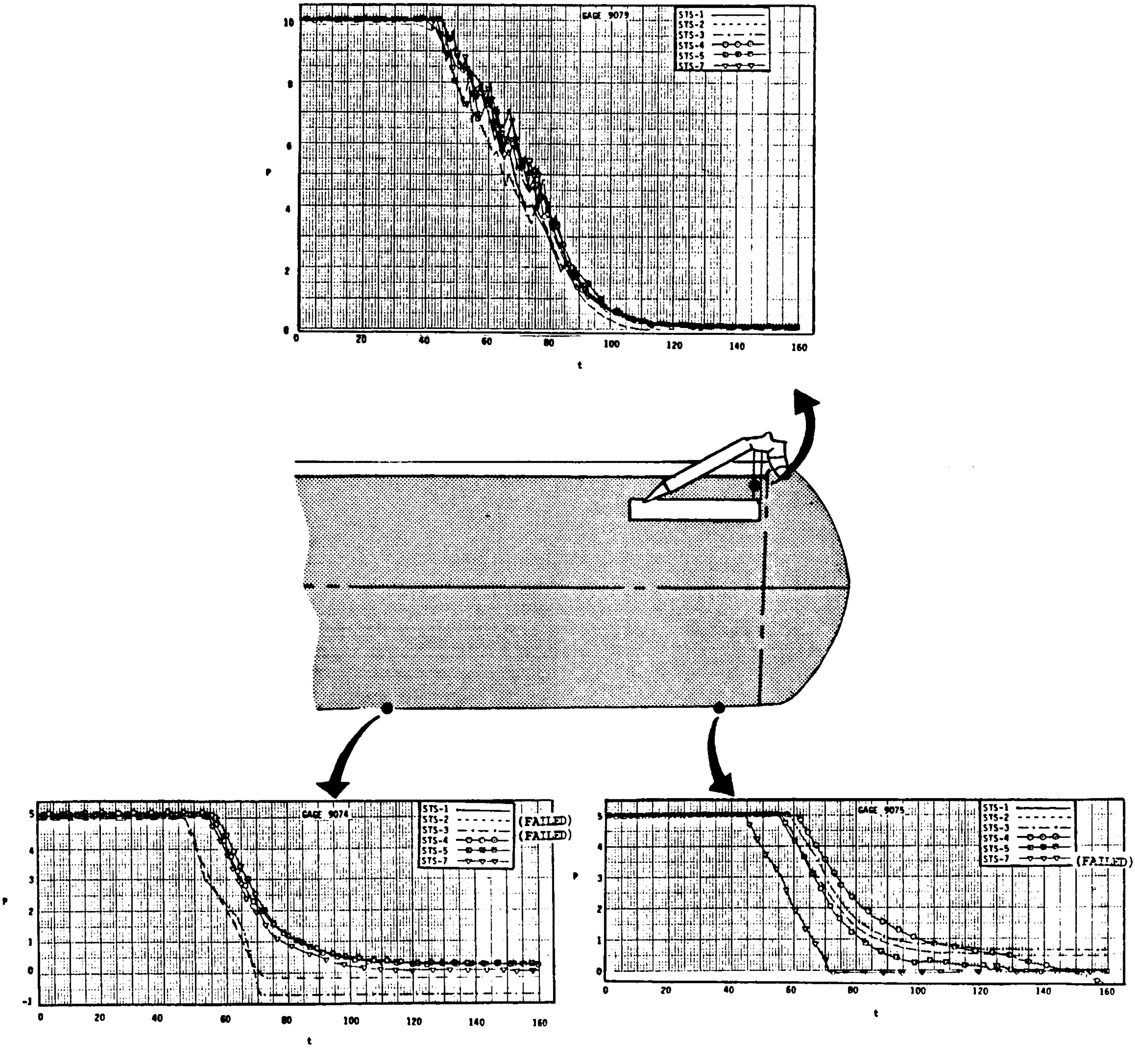

Fig. 3.33 LH_2 DFI Pressure Measurements

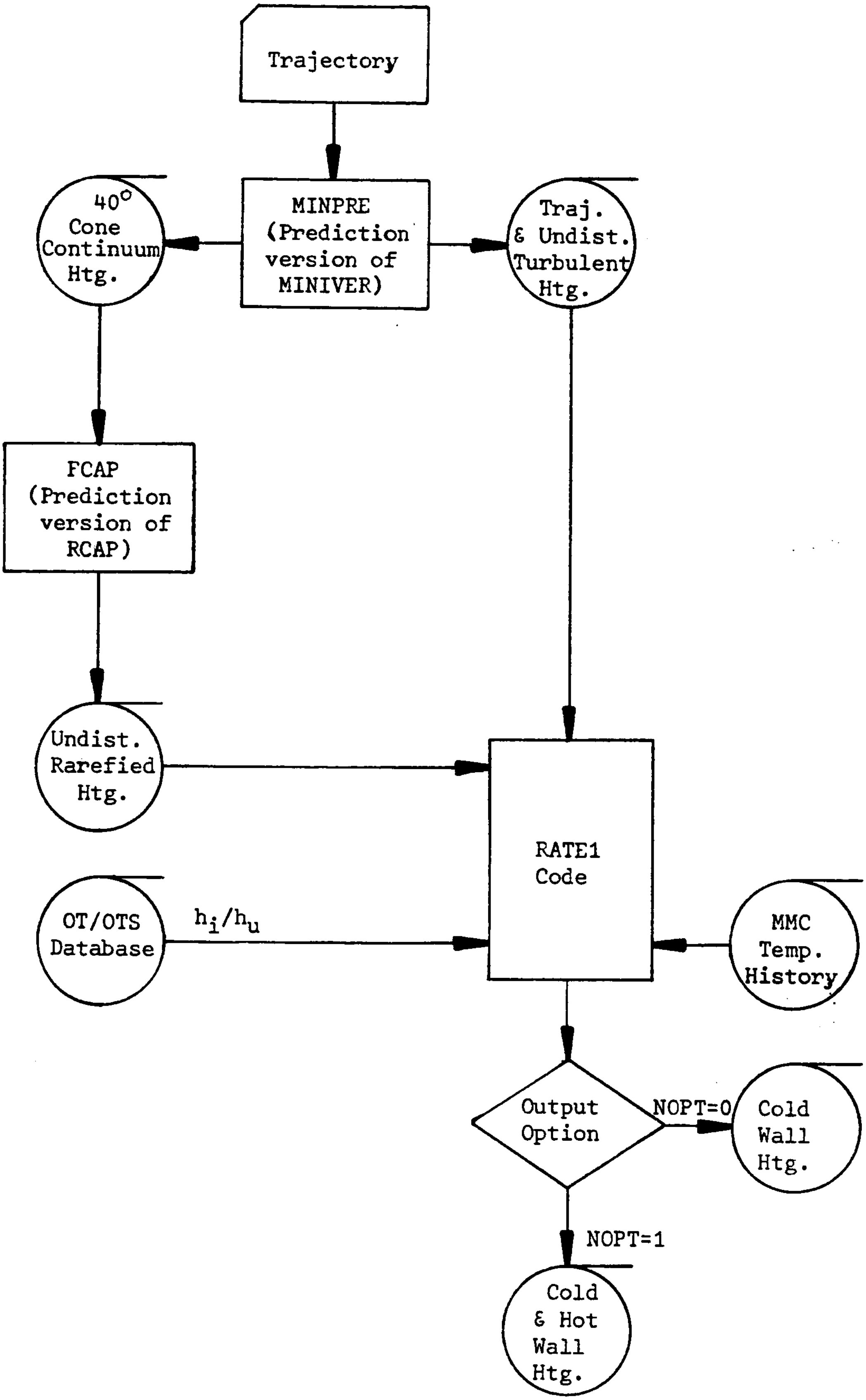

Fig. 3.34 Flow Chart Showing Flight Prediction Procedure

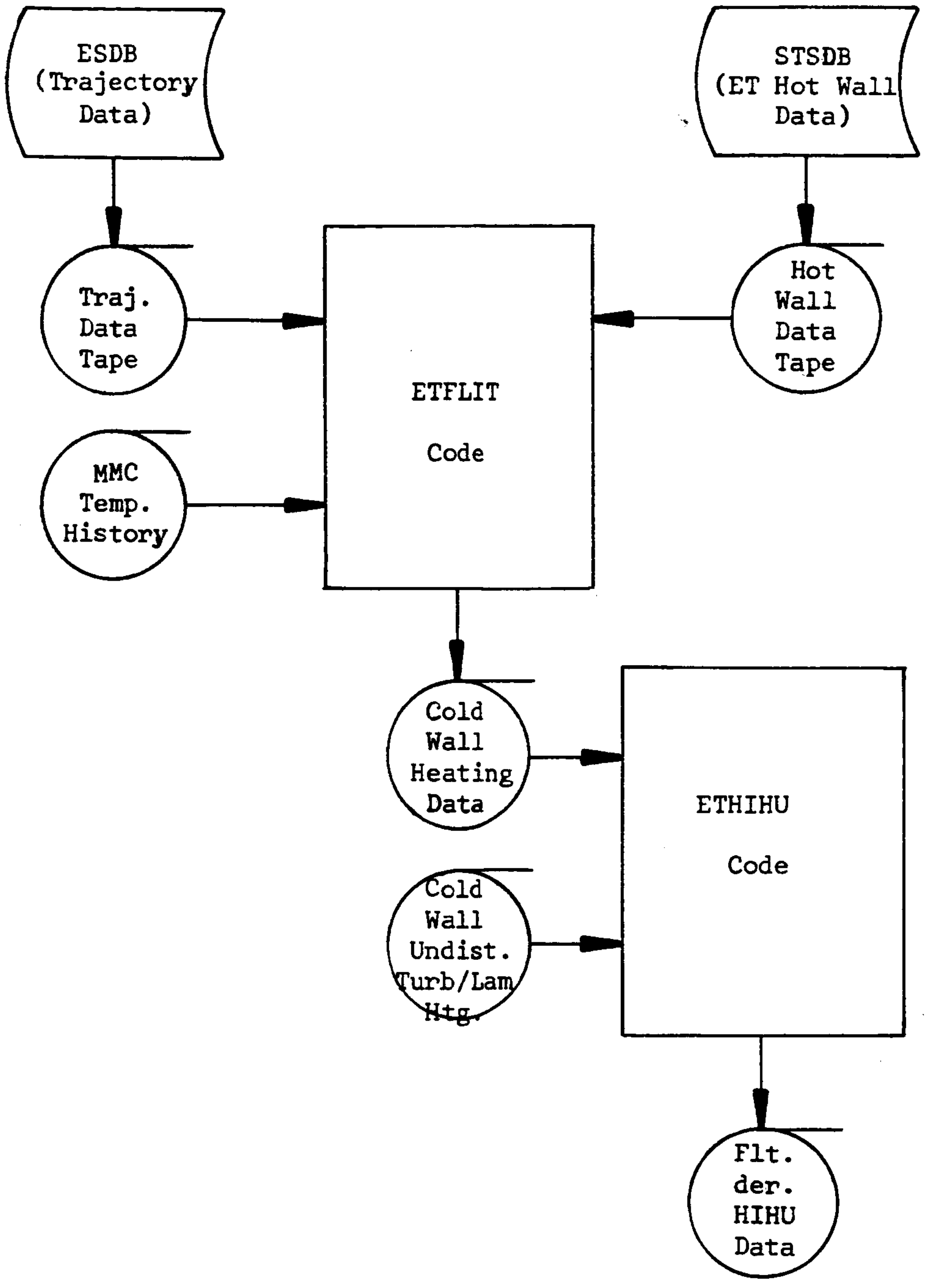

Fig. 3.35 Flow Chart Showing Flight Data Reduction Procedure

where examples of output from the MINPRE (Ref. 11), FCAP (Ref. 12) and RATE1 (Ref. 13) codes were given. The wind-tunnel-derived OTS/OT h_i/h_u data base was also documented in Ref. 1. A complete analysis of the measured heating rate data for STS-1 was documented in this report. The reduced data for all the OFT DFI flights are described below for each of the DFI gages. For each gage, $\dot{q}$ vs. trajectory time plots comparing flight with prediction, h_i/h_u vs. Mach number plots and, if available, pressure vs. trajectory time plots were assembled. Once this is accomplished for one flight, the same set of plots was assembled for the next flight and so on. These plots are documented in Appendix A (Volume II) of this report.

40 Degree Cone

Gage T07R9001A: As Fig. A.1a indicates, the post-flight prediction under-predicts the flight-measured hot-wall data. Reference 1 pointed out the fact that the h_i/h_u data base used in the STS-1 prediction was not fully turbulent and also, that a temperature mismatch existed in the flight measurements. The interference factor plots in Fig. A.1a point out the discrepancies between flight measurements and wind tunnel data base very clearly. Thus, thermal mismatch was applied to STS-1 flight reduction, and flight-derived h_i/h_u's were calculated. Based on these h_i/h_u's as a function of freestream Mach Number, the data base was changed for STS-1 in Ref. 19 and for all the successive flights. The hot-wall heating rate vs. trajectory time plots and the h_i/h_u vs. M_∞ plots are given in Figs. A.1a - A.1f. Pressure measurements made on Gage 9062 located slightly aft of Gage 9001 were also compared with prediction in these figures. The prediction pressures were derived from the interference factors and undisturbed pressure calculations, the details of which are given in Ref. 1.

LO_2 Tank

Gages 9004, 9005, 9007, 9008 and 9010, which are located on the LO_2 tank (Table 2.1), the undisturbed section of the flight ET vehicle, also experienced thermal mismatch. The details of the thermal mismatch analysis will be given in the next subsection. The heating rate comparison plots for the above gages are given in Figs. A.2 - A.6 in Appendix A. Each of these plots contains the measured flight data, thermal mismatch-corrected flight data and prediction. The corresponding h_i/h_u vs. M_∞ plots are also given in these figures. There were a total of 4 pressure gages, TO7P9064, TO7P9065, TO7P9066, and TO7P9067 (Table 2.2) connected in the LO_2 section of the tank. These gages correspond to Islands 2 (gage 9004), 1 (gage 9005), 6 (gage 9007) and 5 (gage 9008), respectively. The flight-measured pressures for the above gages were compared with predicted pressures in Figs. A.2 - A.5.

Intertank

Gages 9011, 9013, 9014, 9015, 9016, 9017, 9018, 9019, 9021, and 9022, located on the intertank section of the ET measure the major interference heating on the tank. The interference in the

OTS configuration is caused by the Orbiter nose shock impinging the boundary layer on the top of the vehicle and wrapping around it, and by the nose shocks from the two Solid Rocket Boosters on either side of the vehicle impinging on its two sides and wrapping around it. The heating rate comparison plots and the corresponding h_i/h_u vs. M_∞ plots are given in Figs. A.7 - A.16. In order to measure pressure time history in the intertank interference region, pressure gages 9069, 9070, 9071, and 9072 on four intertank islands (Table 2.2) were installed. In addition, Gages 9560 and 9561 were installed on the islands located on the $\theta_T = 90^o$ ray where no heat-transfer measurements were taken in any of the DFI flights.

LH_2 Tank Barrel

Gages 9020, 9023, 9025, 9026, 9027, 9028, 9029, 9030, 9031, and 9032, located on the LH_2 barrel section of the ET, measure the thermal environments behind the bipod, on the mid-barrel, and on the aft section near the ring-frame location of X_T = 2058 in. The last six gages located on the ET aft section contain contributions due to plume-induced heating effects and this has been taken into account in the data reduction and analysis, and will be discussed in detail in the next section. The $\dot{q}$ vs. time plots comparing the flight and predictions and the corresponding h_i/h_u vs. M_∞ comparison plots are given in Figs. A.17 - A.26. A total of three pressure measurements were taken on the LH_2 barrel. Pressure gages 9074, 9075 and 9076 were installed on the islands also containing the heat transfer gages. Comparison plots for pressure data are given in Figs. A.20, A.23, and A.24.

Protuberance Locations

A total of 10 individual gages were installed on various fairings, struts, supports, and cable trays. Gages 9012, 9038, 9039, 9040, 9041, 9042, 9043, 9045, 9046, and 9047 (Table 2.1) measured heat transfer data on some of these protuberances. All these gages were forward-facing gages which measured aeroheating values, whereas some of the other gages not described here measured wake and plume-dominated heating rates. The comparison plots are given in Figs. A.27 - A.36.

In order to calculate h_i/h_u for gages other than 9012, 9038, 9040, and 9043, h_i was calculated from the measured heating rates assuming stagnation conditions with recovery efficiency factor, R = 1 and h_u was the calculated flat plate value at the location of the protuberance. The above four gages were reduced with the same methodology as the other acreage gages. The h_i/h_u vs. M_∞ plots comparing flight and theory are also given in these figures. A total of three pressure measurements were taken on the protuberances. Gages 9077, 9078, and 9079 measured pressures on the aft attach structure of the vehicle.

3.3.2 CORRECTIONS IN DATA REDUCTION

The inherent errors that are thought to exist in the measurement of heat transfer rates at various sections of the ET were itemized in Table 3.1 in Subsection 3.2. Clearly, the errors occurring in the measurements are primarily due to thermal mismatch at the TPS/Gage interface and plume-induced heating contributions on the gages at the aft section of the ET. The corrections that are discussed below will result in providing corrected measured convective aeroheating rates for use in the evaluation.

3.3.2.1 THERMAL MISMATCH EFFECTS

The ET was instrumented with HyCal brand, Hy-therm Schmidt-Boelter type gages and HyCal Pill type gages to measure total heat transfer rates. The former type of gages were used on the ET nose cap and islands located on the acreage surface, whereas the latter type was used for struts or other protuberances.

The cold wall nature of the HyCal Hy-therm gage offers a distinct advantage of this type of gage over the slug calorimeter concept by reducing re-radiation from the sensor surface. However, a cold sensor placed in surrounding material with a higher temperature produces a large measurement error in a convective flux environment. When the flow passes over a temperature discontinuity (i.e. a cold sensor in a hot wall), the temperature gradient in the boundary layer must change drastically in order for the temperature profile to remain continuous. Since the thermal gradient of the gas at the wall is the driving potential of heat transfer, it too must change abruptly at the temperature jump. This boundary layer problem has historically been known as temperature mismatch.

The existence of the temperature mismatch effect in the ET heat-transfer measurements was observed in all flights starting with STS-2 flight measurements. The islands on the LO_2 tank section of the ET, which were instrumented starting with STS-2, showed very high discrepancies between flight-measured data and prediction (see Figs. A.3a - A.3e as examples). The underprediction in these island measurements was 100 percent or more in the peak heating region. Even though such large underpredictions are not noticeable on the interference flow regions such as the intertank or LH_2 barrel sections of the ET (see Figs. A.14a - A.14f as examples), temperature mismatch errors are also present in these measurements. In order to quantify the temperature mismatch effects and factor them out of the heat-transfer measurements, an extensive literature search was conducted. Most of the applicable work referenced the analysis made by Rubesin (Ref. 14), Westkaemper (Ref. 15) and Eckert (Ref. 16).

An applicable temperature mismatch correlation developed by Westkaemper for measuring gages was first utilized to calculate the ratio of an average heat-transfer coefficient over the gage to that for an isothermal wall. The correlation is reproduced below:

$$\frac{\bar{h}(W,L)}{h(W,o)} = F(L/W)\,\frac{(T_{W_1} - T_O)}{(T_{W_2} - T_O)} + H(L/W)\,\frac{(T_{W_2} - T_{W_1})}{(T_{W_2} - T_O)} \qquad (3.1)$$

where

$$F(L/W) = \frac{5}{4}\,\frac{[1-(L/W)^{0.8}]}{(1-L/W)}$$

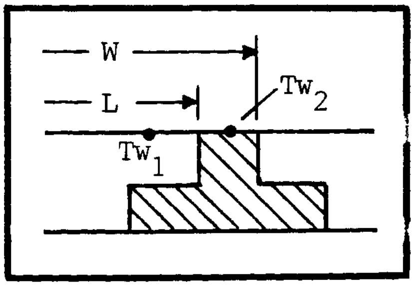

$$H(L/W) = \frac{5}{4}\,\frac{(L/W)^{0.8}}{(1-L/W)}\left[\left(\frac{W}{L}\right)^{0.9} -1\right]^{8/9}$$

For $L/W \geq 0.9$, $F(L/W) \simeq 1.0$ (accuracy within 1%)

Then, Eq. 3.1 reduces to

$$\frac{\bar{h}(W,L)}{h(W,o)} = 1 + \left[H(L/W)-1\right]\frac{(T_{W_2} - T_{W_1})}{(T_{W_2} - T_O)} \tag{3.2}$$

$$= 1 + H'(L/W)\,\frac{(T_{W_2} - T_{W_1})}{(T_{W_2} - T_O)} \tag{3.3}$$

where the function $H'(L/W)$ is plotted in Fig. 3.36 as a function of L/W.

In this expression (Eq. 3.2), T_O should be the recovery temperature, as suggested by Eckert (Ref. 15). The gage temperature, T_{W_1}, was obtained from the thermal analyzer program developed by Martin Marietta Corporation (MMC). The upstream surface temperature, T_{W_1}, was also obtained from MMC. In order to do this, it was at first assumed that

$$T_{W_1} = T_O$$

Then,

$$h(W,o) = h(W,L)/\,[1 + H'(L/W)]$$

The values of corrected heat-transfer coefficient as a function of trajectory time were supplied to MMC for their thermal

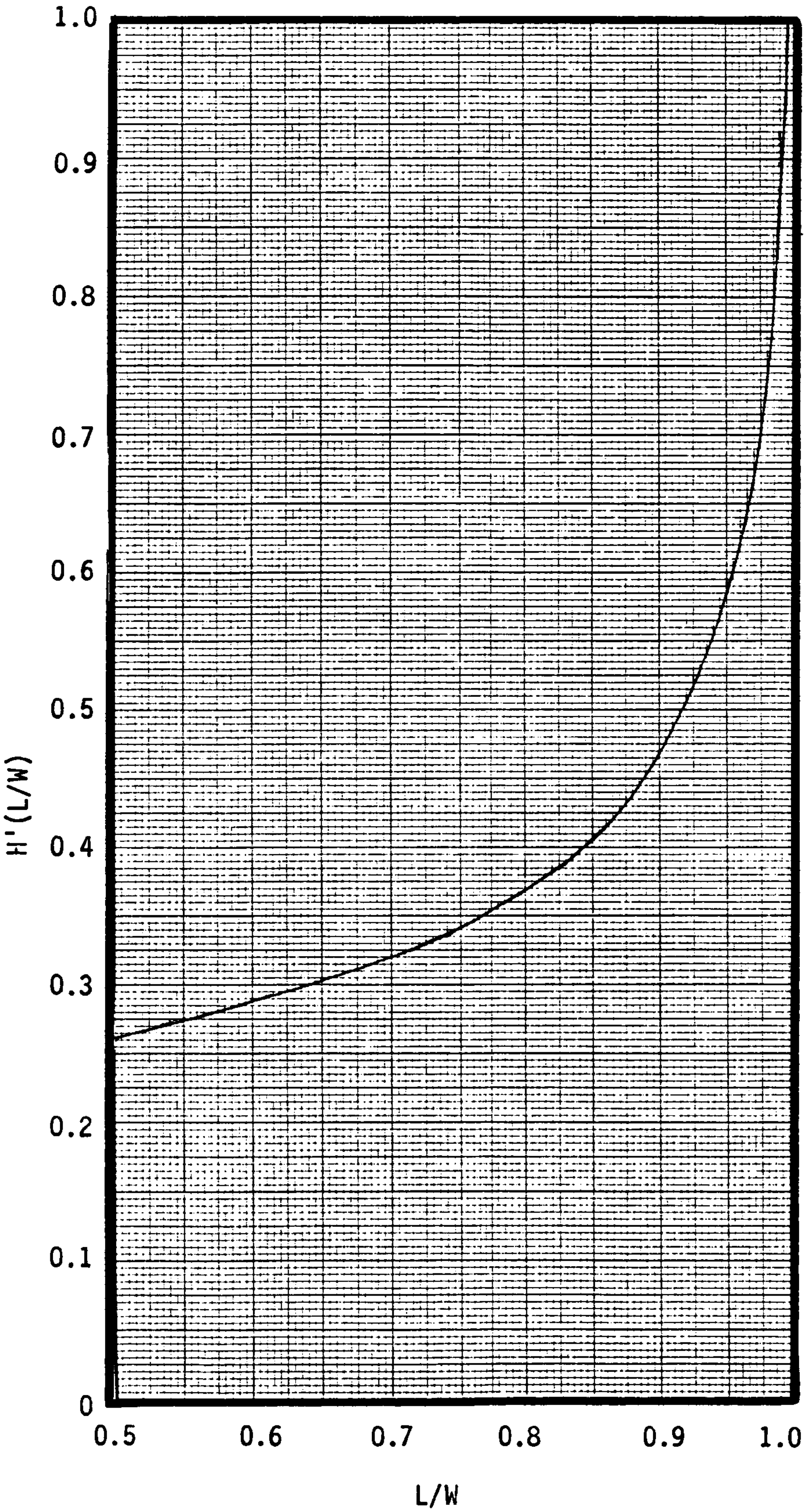

Fig. 3.36 Numerical Values of H'(L/W) (Westkaemper) in Equation

analysis of the SOFI (Spray-On-Foam-Insulation) material. It was found for Islands 1, 2, 5, and 6 in STS-2 flight that the SOFI wall temperatue tracked the adiabatic wall temperature up to approximately 100 sec. (Figs. 3.37a - 3.37d), beyond which adiabatic wall temperature deviates considerably from the calculated wall temperature. Thus, in the peak heating regime lying somewhere between 90 to 100 secs., the assumption that $T_{W_1} = T_O$ is a valid one, and no more iterations on thermal analysis are necessary to calculate the wall temperature.

A numerical approach using BLIMPK (Ref. 17) was then followed to examine the temperature distribution in the boundary layer as the flow passes from a hot surface to a cold gage and the corresponding heat-transfer characteristics. Another motivation to run BLIMPK was for comparison with the above-described empirical correlation. BLIMPK was run for $M_\infty = 3$ condition in STS-2 flight for all the islands and gage 9001 located on the LO_2 tank and 40 deg. cone, respectively. As examples, Figs. 3.38 - 3.40 were prepared to compare the flight measurement, BLIMPK calculations, and the Westkaemper correlation for gages located on the bottom center-line ($\theta_T = 180^O$). In order to examine the temperature gradient at the wall as the flow passes from the hot wall to the cold gage, Figs. 3.41 and 3.42 were prepared for Gages 9001 and 9005 (Island 1), respectively. For Gage 9001, the static temperature distribution in the boundary layer immediately upstream of the cold gage, i.e., at S = 0.9 ft. looks quite normal with the

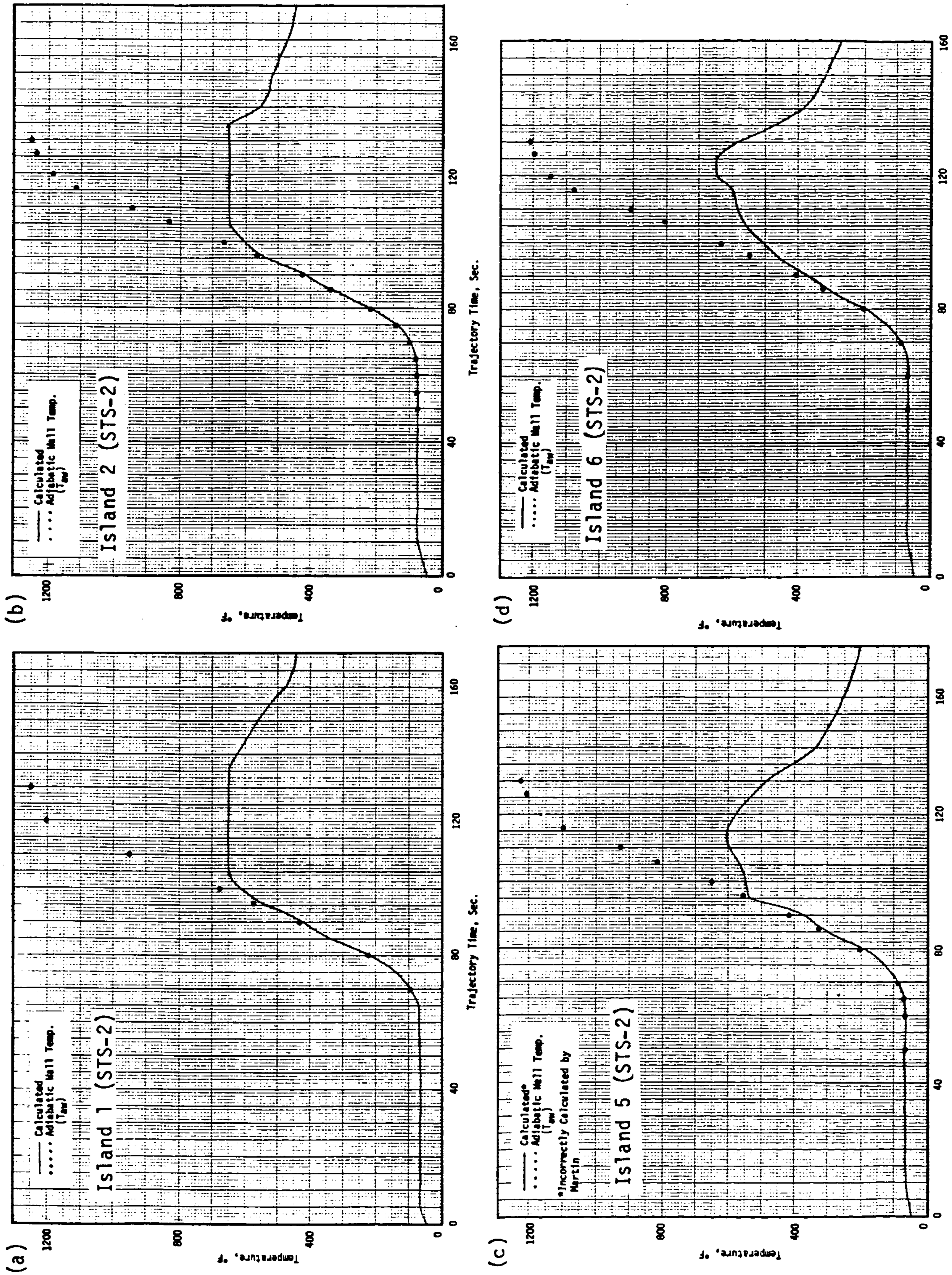

Fig. 3.37 Wall (SOFI) Temperature Calculations by Martin Marietta Corporation

ORIGINAL PAGE IS
OF POOR QUALITY

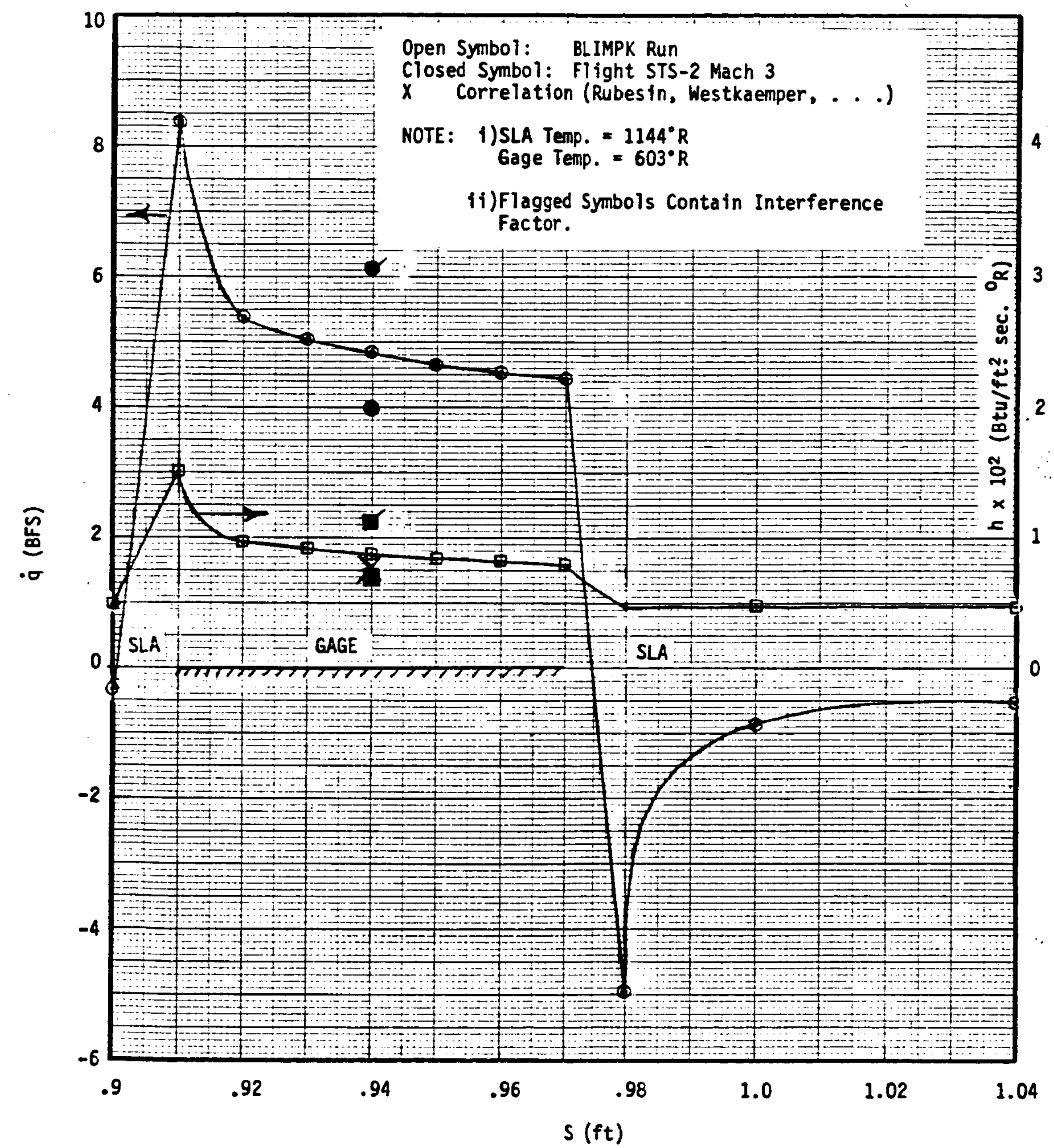

Fig. 3.38 BLIMPK Run for STS-2 ET Gage 9001 (Located on ET 40 deg. Nose Cone) Showing the Effects of Temperature Mismatch (θ_T=180°)

ORIGINAL PAGE IS
OF POOR QUALITY

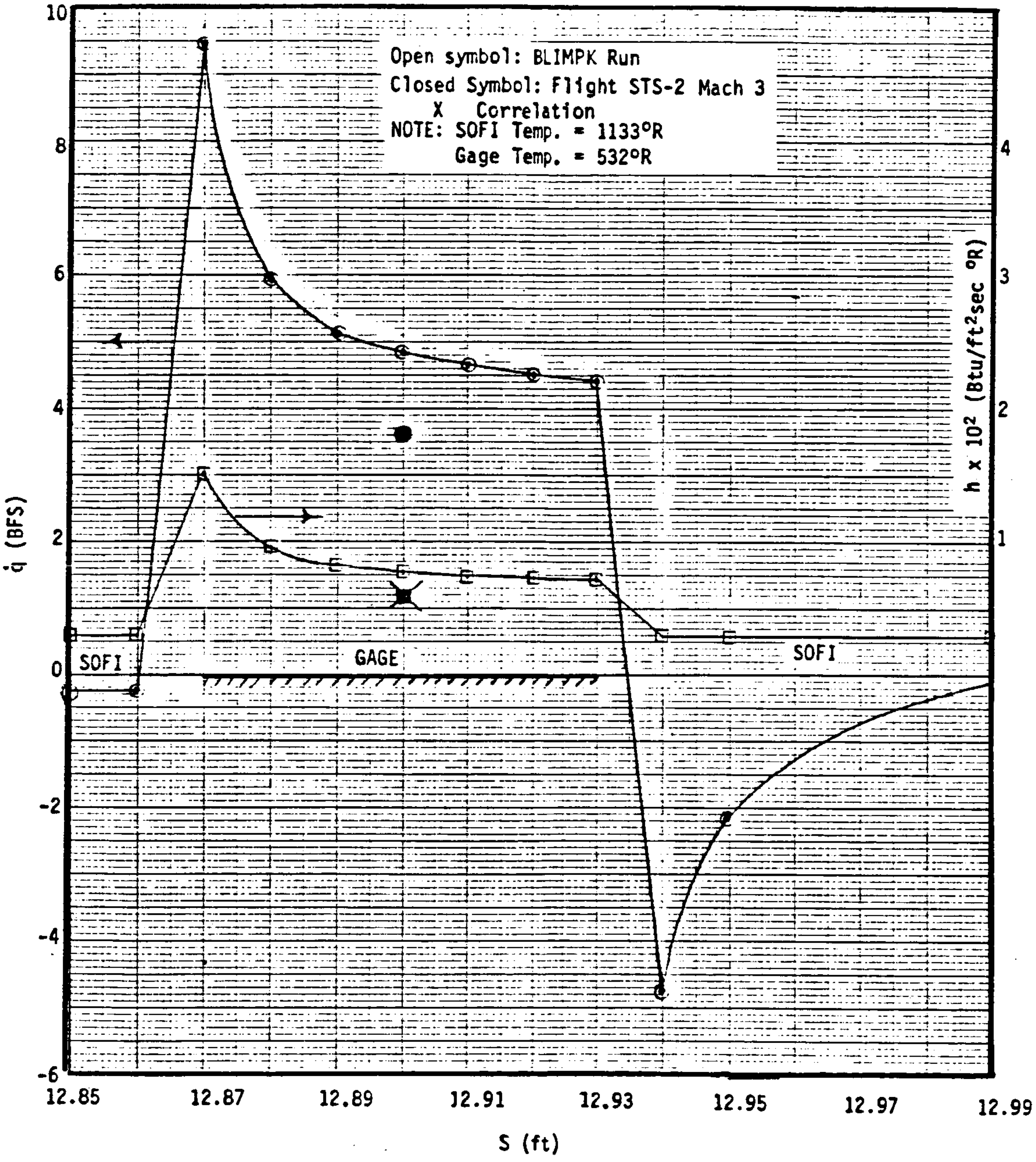

Fig. 3.39 BLIMPK Run for STS-2 ET Gage 9005 (Island 1: Located on ET LO_2 Tank Bottom Center Line) Showing the Effects of Temperature Mismatch

C-2

ORIGINAL PAGE IS
OF POOR QUALITY

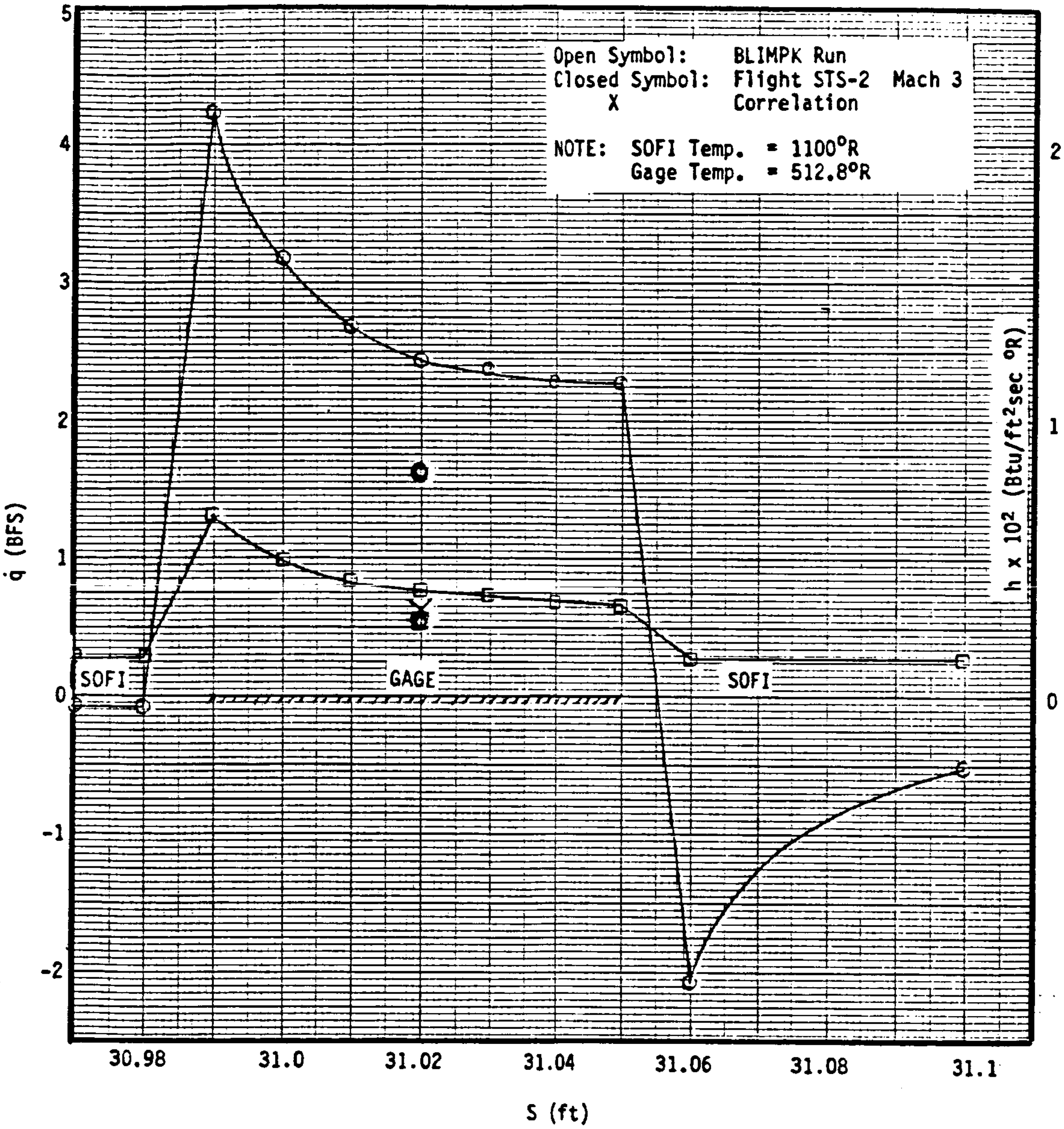

Fig. 3.40 BLIMPK Run for STS-2 Gage 9008 (Island 5: Located on ET LO_2 Tank Bottom Center Line) Showing the Effects of Temperature Mismatch

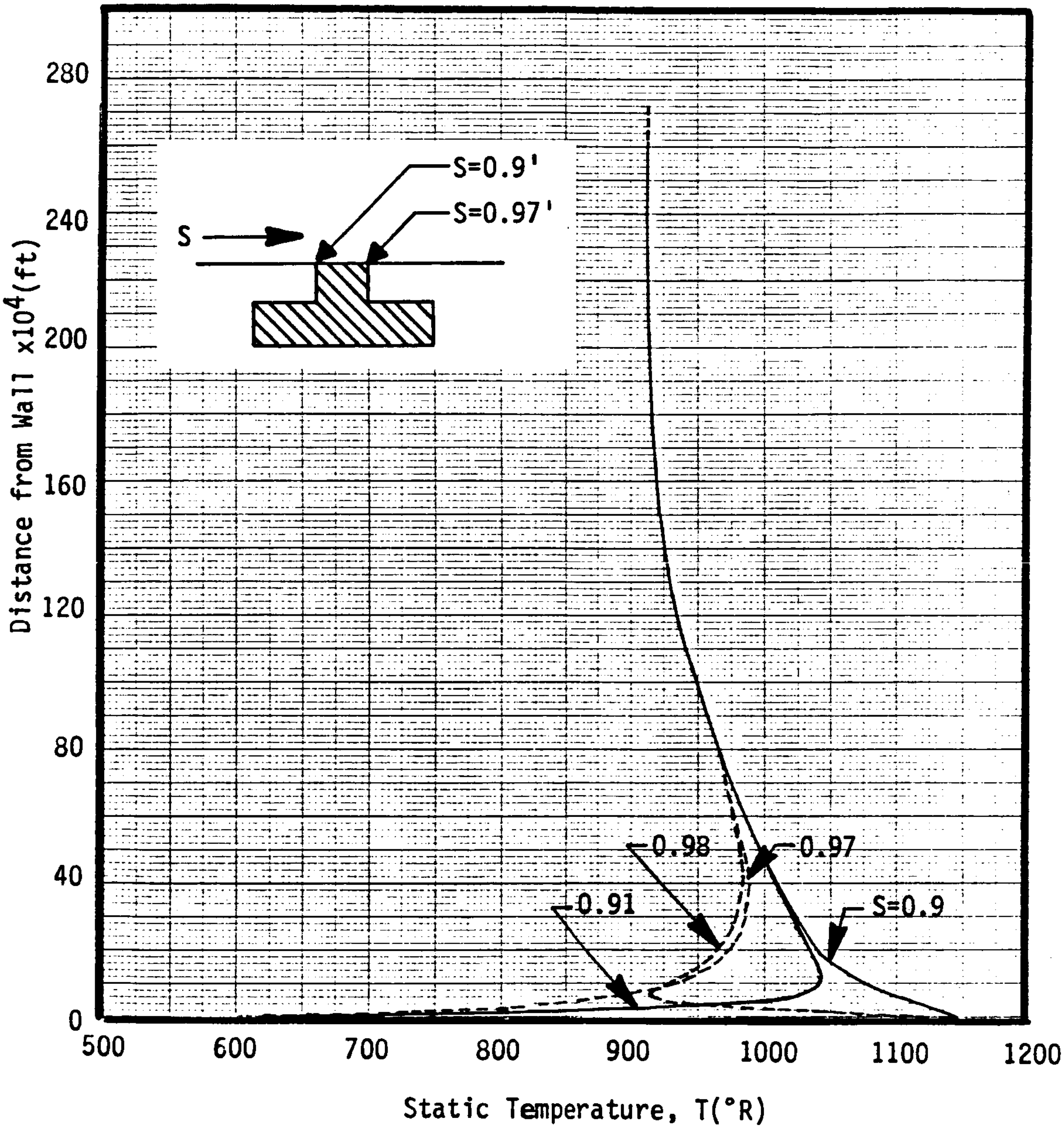

Fig. 3.41 Static Temperature Profile Across the Boundary Layer near Gage 9001

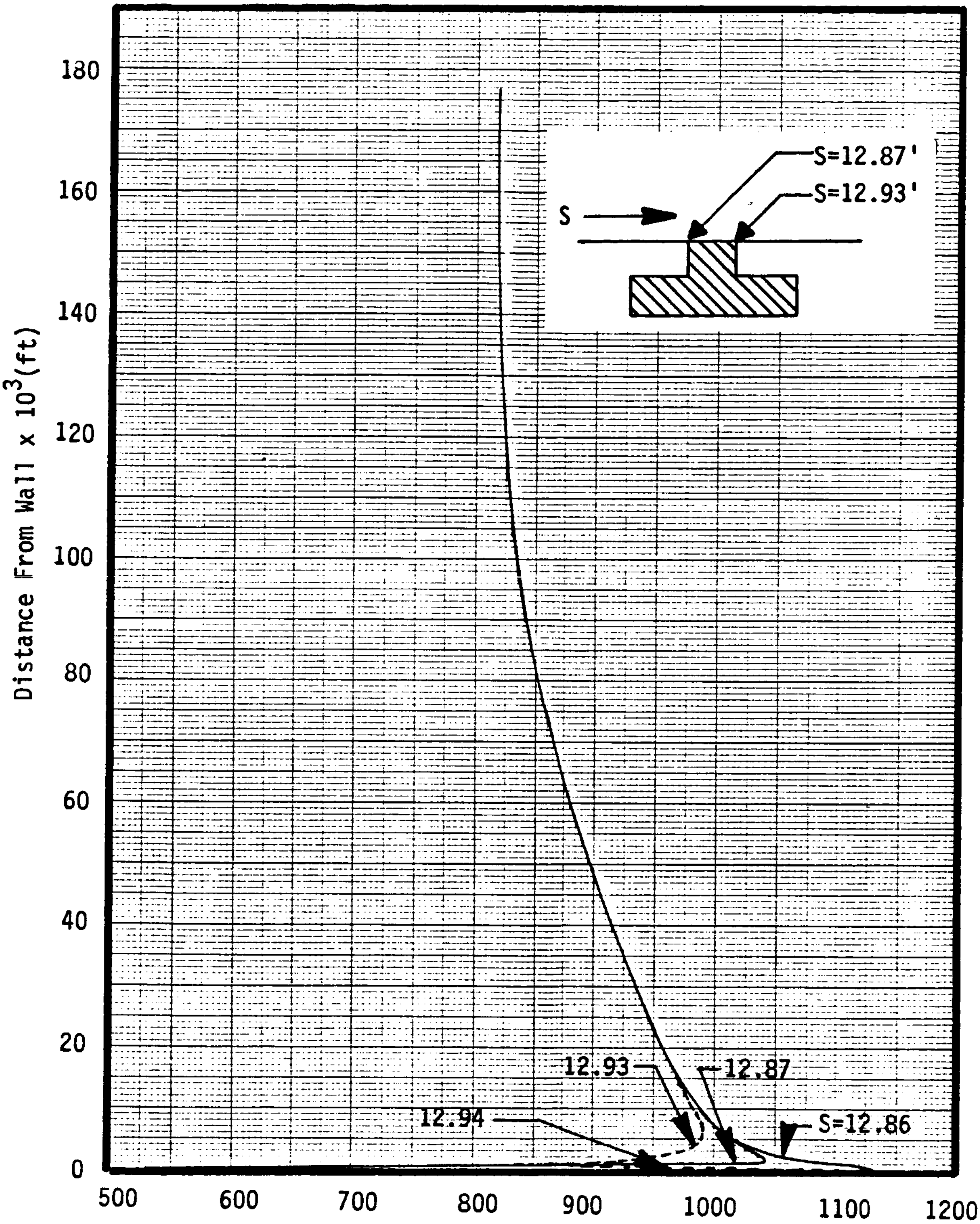

Fig. 3.42 Static Temperature Profile across the Boundary Layer near Island 1 (Gage 9005)

temperature at the wall, $T_W = 1144^oR$. As the flow passes to the edge of the cold gage, i.e., at S = 0.91 ft., the temperature gradient at the wall changes drastically so that the wall temperature is 603^oR, thus giving rise to the very high heating rate and heat transfer coefficient in Fig. 3.38. As the flow passes toward the rear edge of the gage, the boundary layer starts to adjust to the temperature mismatch, and the effect of this adjustment is felt in the temperature distribution at points farther and farther away from the wall inside the boundary layer. This is evident from the temperature distribtuion at S = 0.97 ft. (Fig. 3.41), which is the rear edge of the gage. As the flow passes further from the cold gage to the hot wall again, the change in the temperature gradient is very drastic also, as seen from curve at S = 0.98 ft. This effect shows up as a drastic cooling effect, as seen in Fig. 3.38. Finally, the effect of the temperature mismatch diminishes very rapidly, as the flow passes downstream of the gage. This is also seen in Fig. 3.38. Similar effects were oserved in the boundary layer profiles of the static temperature for the Island 1 gage, as observed in Fig. 3.41. Figure 3.38 shows that the Westkaemper correlation and BLIMPK are a little lower than flight mesurements in the case of Gage 9001. This may be due to some geometric interference effects existing in the flight measurements for Gage 9001. The last two plots for Islands 1 and 5 (Figs. 3.39 and 3.40) show that the Westkaemper correlation and flight are in good agreement, whereas BLIMPK results are a little higher than both flight and correlation. It should be noted that in all these calculations, the existence of a phenolic strip and SLA located around each metallic gage was neglected. Inclusion of the details of the total island material might slightly improve the above comparisons.

3.3.2.2 PLUME-INDUCED HEATING

While comparing the measured heating rates with predicted heating rates for the acreage islands located in the aft portion of the ET, it was found that the predicted values were consistently lower than those measured, (see Figs. A.26a - A.26e as examples). The measurements were quite significant at t = 0 sec. and the heat-transfer distribution beyond about 95 secs. did not follow an aeroheating trend. Based on both total and radiation measurements taken on the aft LH_2 tank and on the SRBs, it was concluded that the thermal environment during first stage flight for the aft portion of the ET was a combination of plume radiation and either aerodynamic convective heating or plume-induced convective heating. Therefore, to properly use the flight data obtained from the total calorimeters, the incident radiation to the gage sensor must be determined throughout the flight and then subtracted from the gage reading to determine the convective component of the environment. Furthermore, the resulting heat-transfer values are categorized as being due either to convective aeroheating or to convective base heating resulting from plume gas recirculation.

Six surface gages, 9029, 9027, 9030, 9028, 9031, and 9032, were identified as containing plume-induced heating contributions in the heat-transfer measurements. This plume-induced heating may be divided into three parts, (1) main plume radiation, (2) plume convection (baseflow recirculation heating), and (3) local gas radiation.

Since there were no radiation measurements made on the LH_2 barrel section, where the above gages are located, the trends for radiation were derived from the radiation measurements made by gages 9213, 9211, and 9212, all located on the tank base. Depending on the LH_2 gage under consideration which experiences plume-induced heating, the closest radiation gage on the tank base was examined to derive the trend due to radiation from the SSME and SRB main plumes. A typical radiation history is given in Fig. 3.43 for gage 9013 in STS-7 flight. This time-history contains SOFI outgas attenuation, local gas radiation due to recirculating gas, and a solid rocket motor shutdown spike in addition to the main plume radiation. In order to quantify the contribution due to radiation to the various gages previously listed, the measured heating rate histories for each gage in the OFT flights were examined in a composite manner and the sea-level main plume radiation value was determined. The distribution of radiation with flight time was derived by taking a ratio of the sea-level values of the composite set and the measurement from the adjacent radiation gage, and finally, multiplying the factor with the measured radiation values.

At a certain time in flight, the flow separates on the ET surface because of the widening of the plumes with altitude, and the plume gas recirculates in the separated regions. The time at which plume gas recirculates on the aft LH_2 section containing the above gages can be determined by examining the radiation gages on the base adjacent to the gage under consideration. The recirculating gas also radiates in the separated region giving the extra radiation spike shown in Fig. 3.43. As the chamber pressure drops off with flight time, the plumes become weak and no longer provide the high adverse pressure gradient needed to separate the boundary layer flow; consequently, the recirculation is weak and the extra radiation drops off as shown in Fig. 3.43. The magnitudes of the plume convective heating and local gas radiative heating to the gage under consideration are determined from the total heating and radiation gages on the base located adjacent to the gage. The plume convective heating values are obtained by subtracting radiation from total heating measurements, whereas the local gas radiation is obtained by subtracting the faired radiation value from the total radiation measurements, as shown in Fig. 3.43. The magnitudes of the three plume-induced heating contributions for the above gages are summarized in Table 3.3, and plotted in Figs. 3.44 - 3.49.

Based on the analysis of various gages in this section of the tank, the plume-induced heating corrections were applied to all the gages located aft of X_T = 2000 in. on the tank. This location is

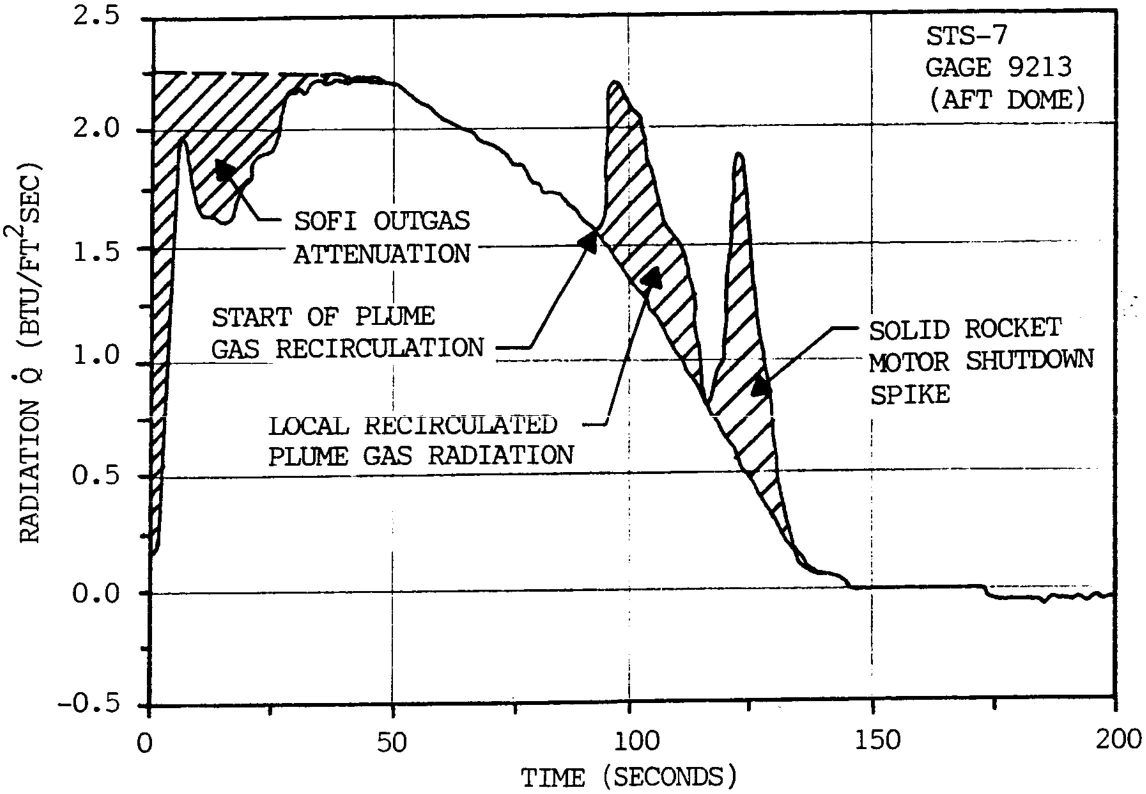

Fig. 3.43 Base Heating Radiation History

Table 3.3 BASE HEATING ENVIRONMENT FOR ET AFT INSTRUMENTATION ISLANDS

TIME FROM LIFTOFF (SECONDS)	HEATING RATE, BTU/FT.^{2}SEC.								
	ISLAND #32 (T07R9029A)			ISLAND #33 (T07R9027A)			ISLAND #34 (T07R9030A)		
	QR* M.P.	QR* L.G.	Q_c^*	QR M.P.	QR L.G.	Q_c	QR M.P.	QR L.G.	Q_c
0	0.40			0.50			0.60		
20	0.40			0.50			0.60		
40	0.38			0.49			0.58		
60	0.35			0.46			0.55		
80	0.32			0.42			0.52		
						AERO			AERO
94	0.29	0		0.38	0	2.0	0.50	0	2.91
96	0.28			0.38	0.14	2.16	0.48	0.14	3.41
98	0.28		AERO	0.37	0.26	2.28	0.47	0.26	3.78
100	0.27	0.37	0.95	0.36	0.37	2.34	0.46	0.37	4.01
102	0.27	0.44	1.92	0.36	0.44	2.30	0.46	0.44	4.0
104	0.26	0.42	2.50	0.35	0.42	2.21	0.45	0.42	3.89
106	0.26	0.38	2.81	0.35	0.38	2.08	0.45	0.38	3.71
108	0.25	0.33	2.92	0.34	0.33	1.95	0.44	0.33	3.48
110	0.25	0.27	2.85	0.34	0.27	1.80	0.44	0.27	3.25
112	0.25	0.20	2.65	0.33	0.20	1.63	0.43	0.20	3.0
114	0.24	0.13	2.36	0.33	0.13	1.46	0.42	0.13	2.75
116	0.24	0.05	2.0	0.32	0.05	1.35	0.42	0.05	2.46
120	0.22		1.0	0.30			0.40		
130	0.18			0.27			0.37		

* M. P. Main Plume
L. G. Local Gas
C Convective

Table 3.3 (Continued)

TIME FROM LIFTOFF (SECONDS)	HEATING RATE, BTU/FT.^{2}SEC.								
	ISLAND #35 (T07R9028A)			ISLAND #36 (T07R9031A)			ISLAND #37 (T07R9032A)		
	$QR_{M.P.}$	$QR_{L.G.}$	Q_c	$QR_{M.P.}$	$QR_{L.G.}$	Q_c	$QR_{M.P.}$	$QR_{L.G.}$	Q_c
0	1.1			0.80			0.75		
20	1.08			0.78			0.74		
40	1.03			0.75			0.70		
60	0.96			0.72			0.66		
80	0.87			0.67			0.61		
			AERO			AERO			AERO
94	0.81	0	3.47	0.63	0	3.15	0.58	0	2.62
96	0.80	0.18	4.17	0.62	0.22	3.94	0.57	0.18	2.90
98	0.79	0.35	4.64	0.62	0.43	4.40	0.56	0.35	3.14
100	0.78	0.50	4.87	0.61	0.63	4.65	0.55	0.50	3.26
102	0.78	0.61	4.89	0.61	0.76	4.68	0.55	0.61	3.25
104	0.77	0.59	4.80	0.60	0.73	4.60	0.54	0.59	3.17
106	0.76	0.54	4.63	0.59	0.65	4.43	0.53	0.54	3.05
108	0.75	0.46	4.39	0.58	0.55	4.20	0.53	0.46	2.92
110	0.74	0.37	4.10	0.58	0.45	3.91	0.52	0.37	2.75
112	0.73	0.28	3.74	0.57	0.34	3.55	0.52	0.28	2.60
114	0.72	0.18	3.35	0.56	0.22	3.17	0.51	0.18	2.45
116	0.70	0.08	2.91	0.55	0.10	2.75	0.50	0.08	2.28
120	0.67			0.54			0.48		
130	0.63			0.50			0.45		

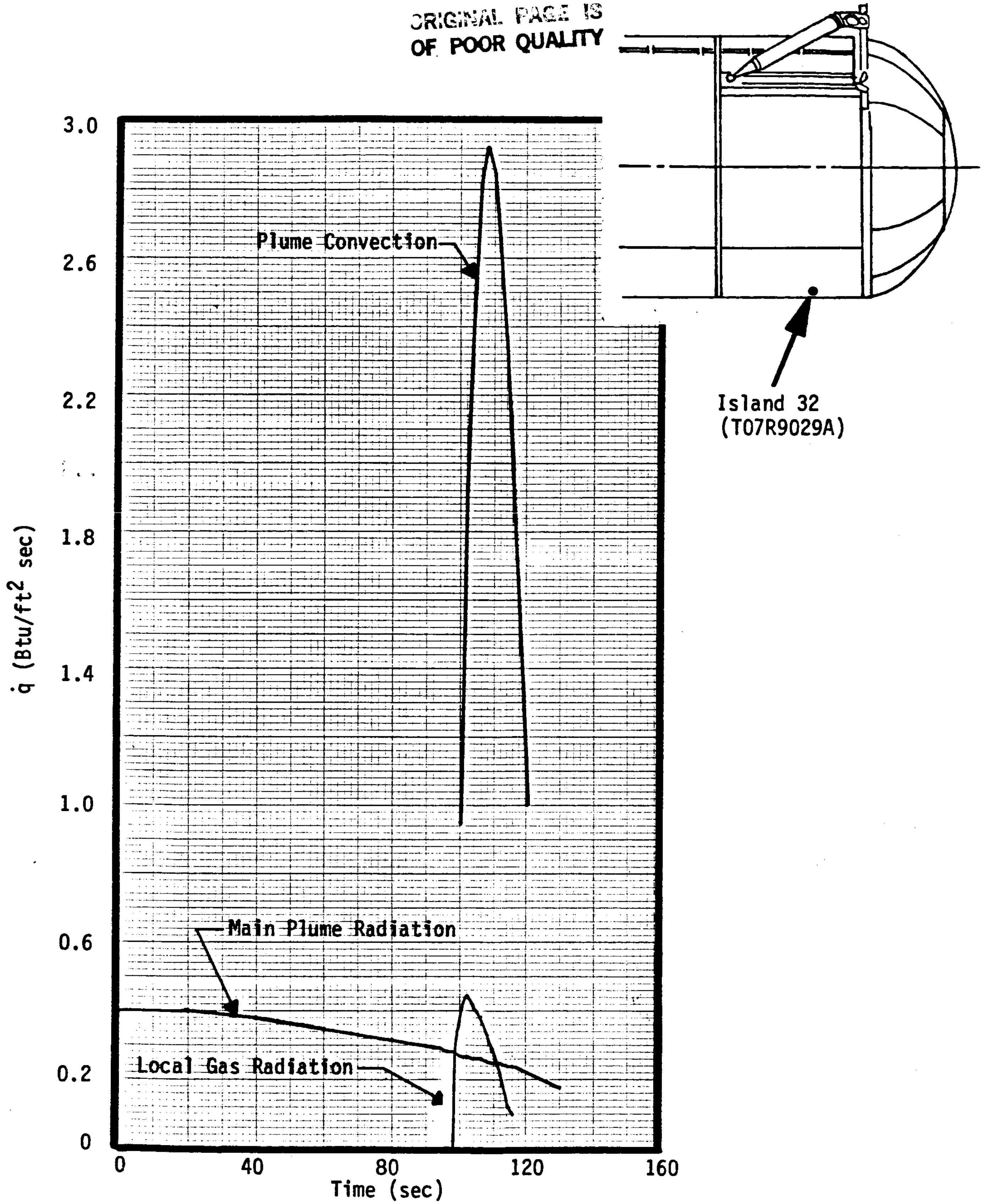

Fig. 3.44 Plume-induced Heating Time Histories for Gage 9029 (Island 32)

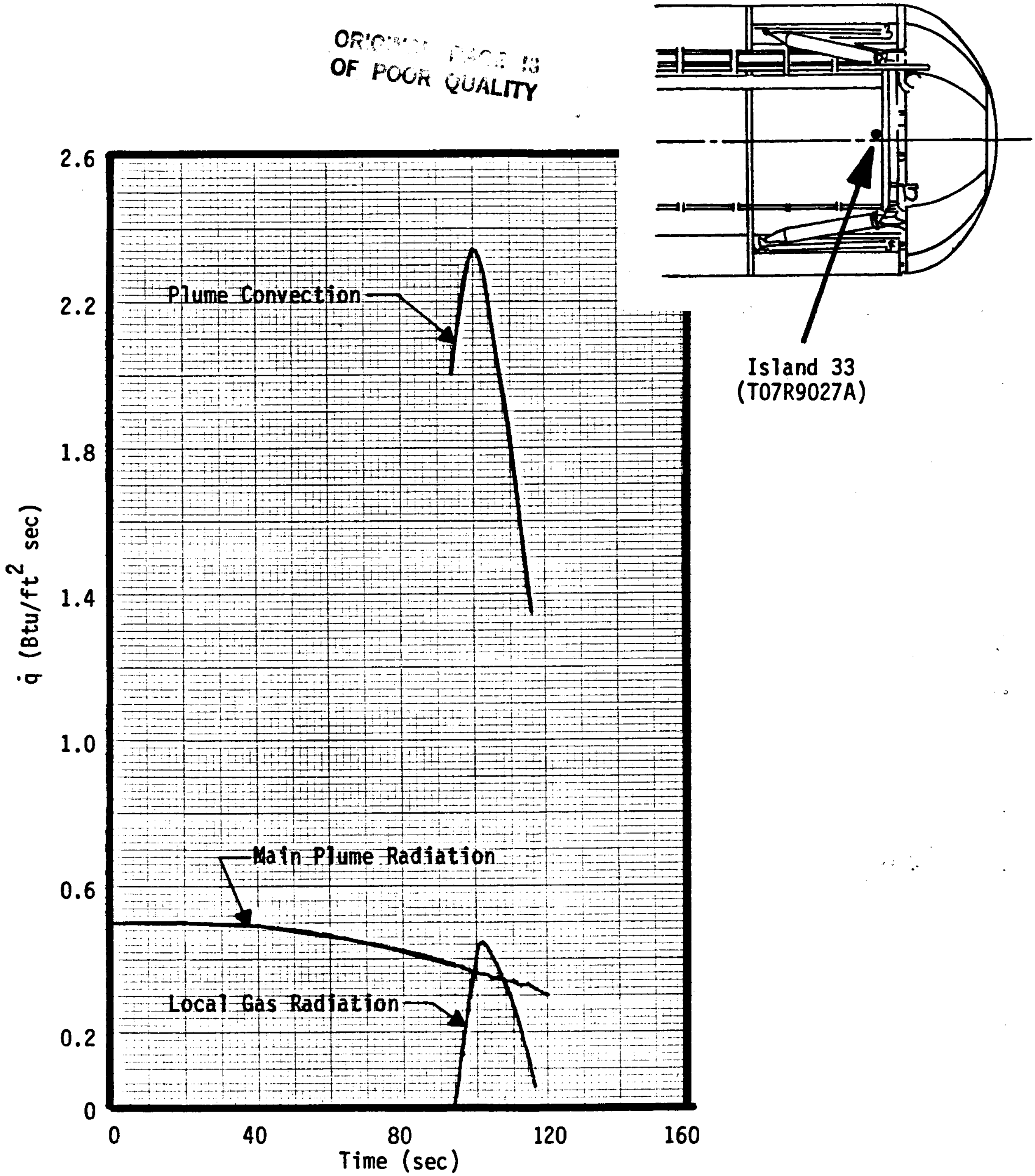

Fig. 3.45 Plume-induced Heating Time Histories for Gage 9027 (Island 33)

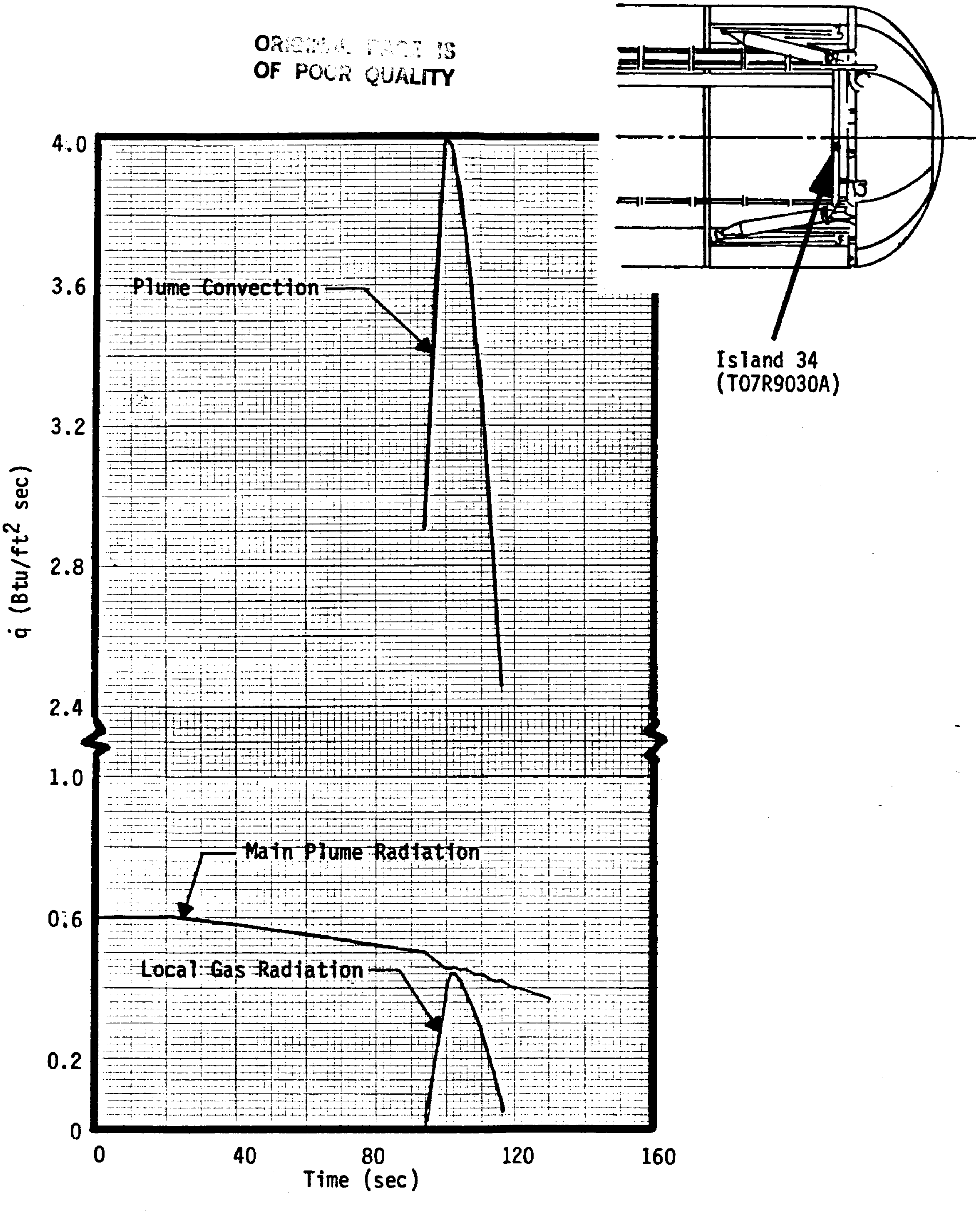

Fig. 3.46 Plume-induced Heating Time Histories for Gage 9030 (Island 34)

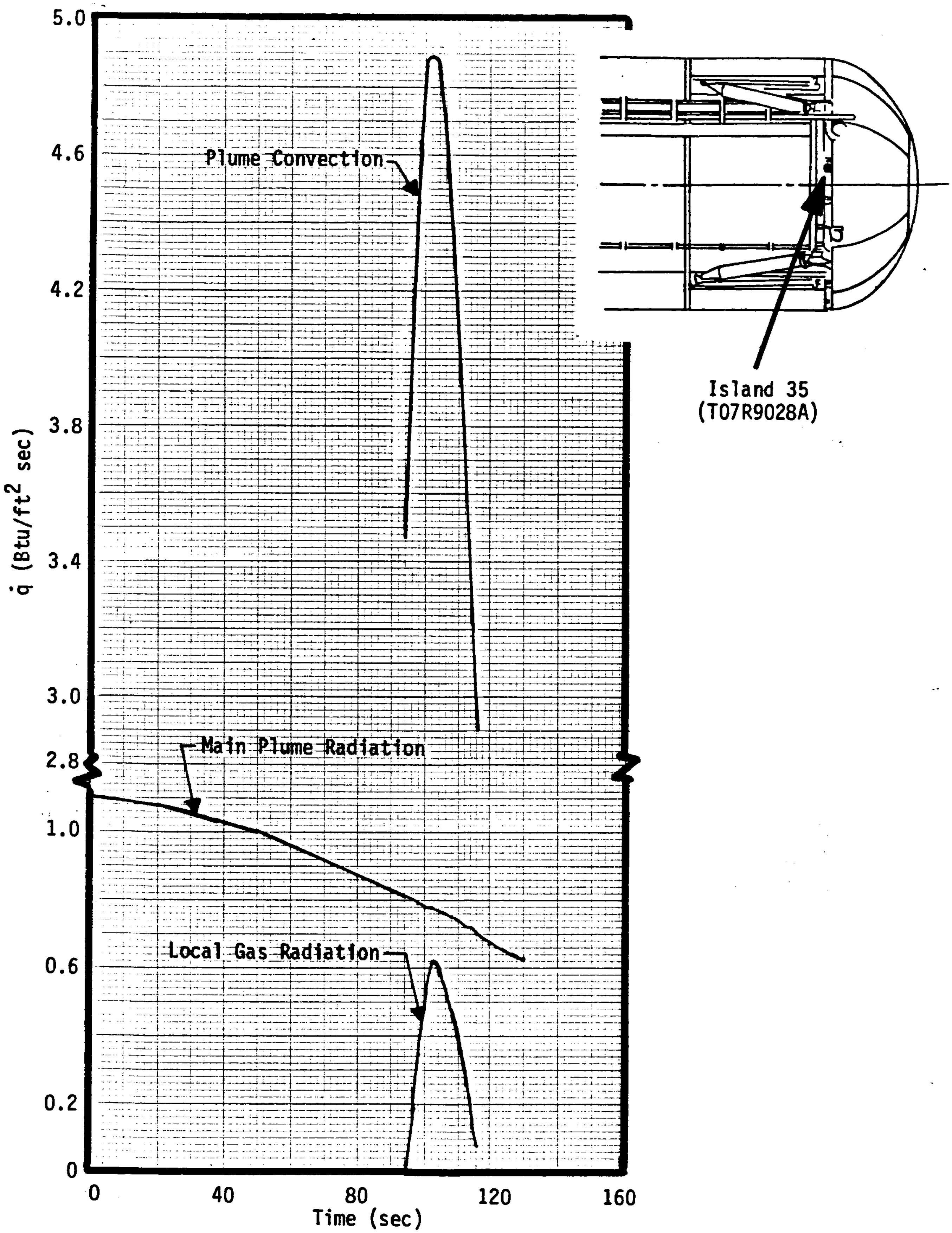

Fig. 3.47 Plume-induced Heating Time Histories for Gage 9028 (Island 35)

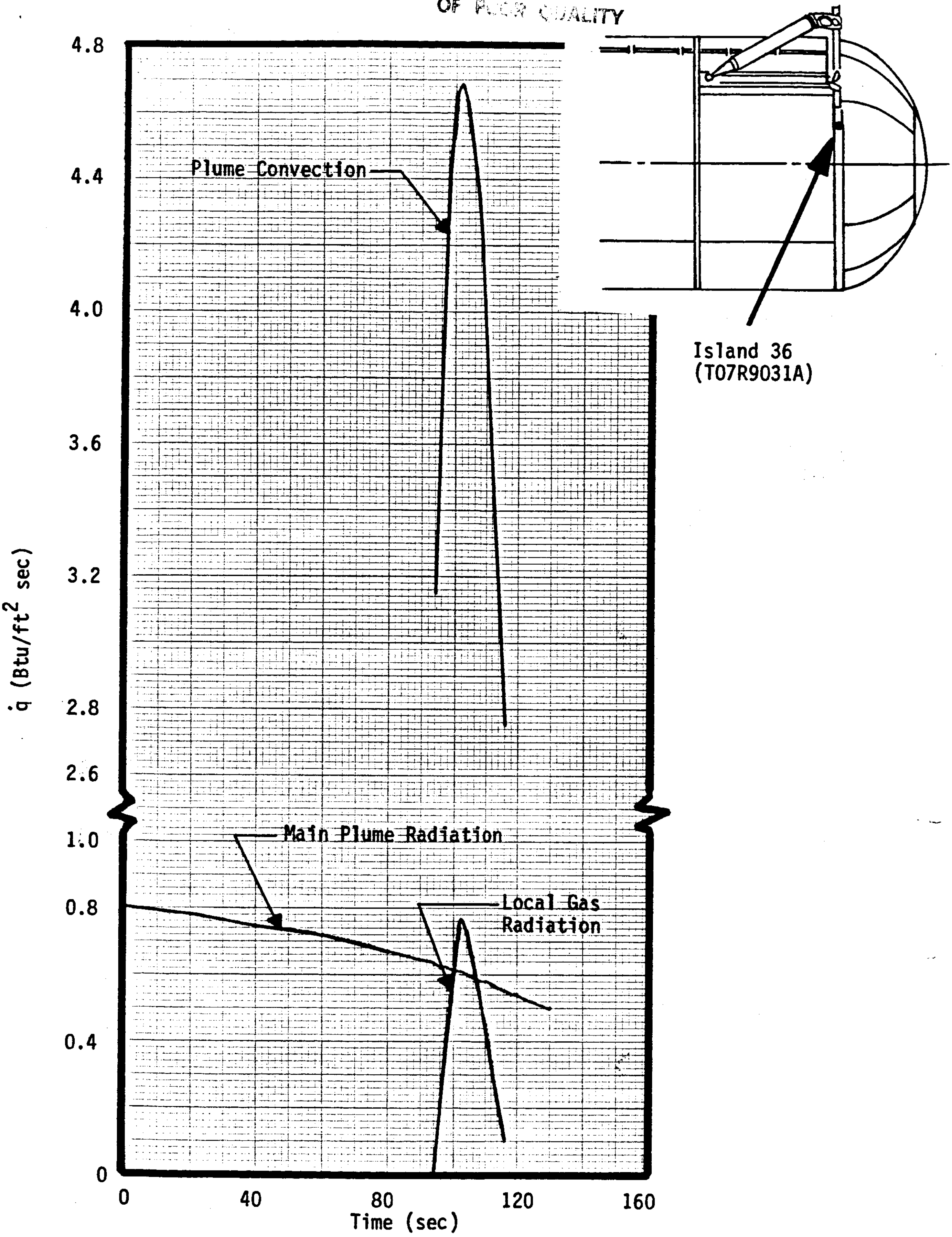

Fig. 3.48 Plume-induced Heating Time Histories for Gage 9031 (Island 36)

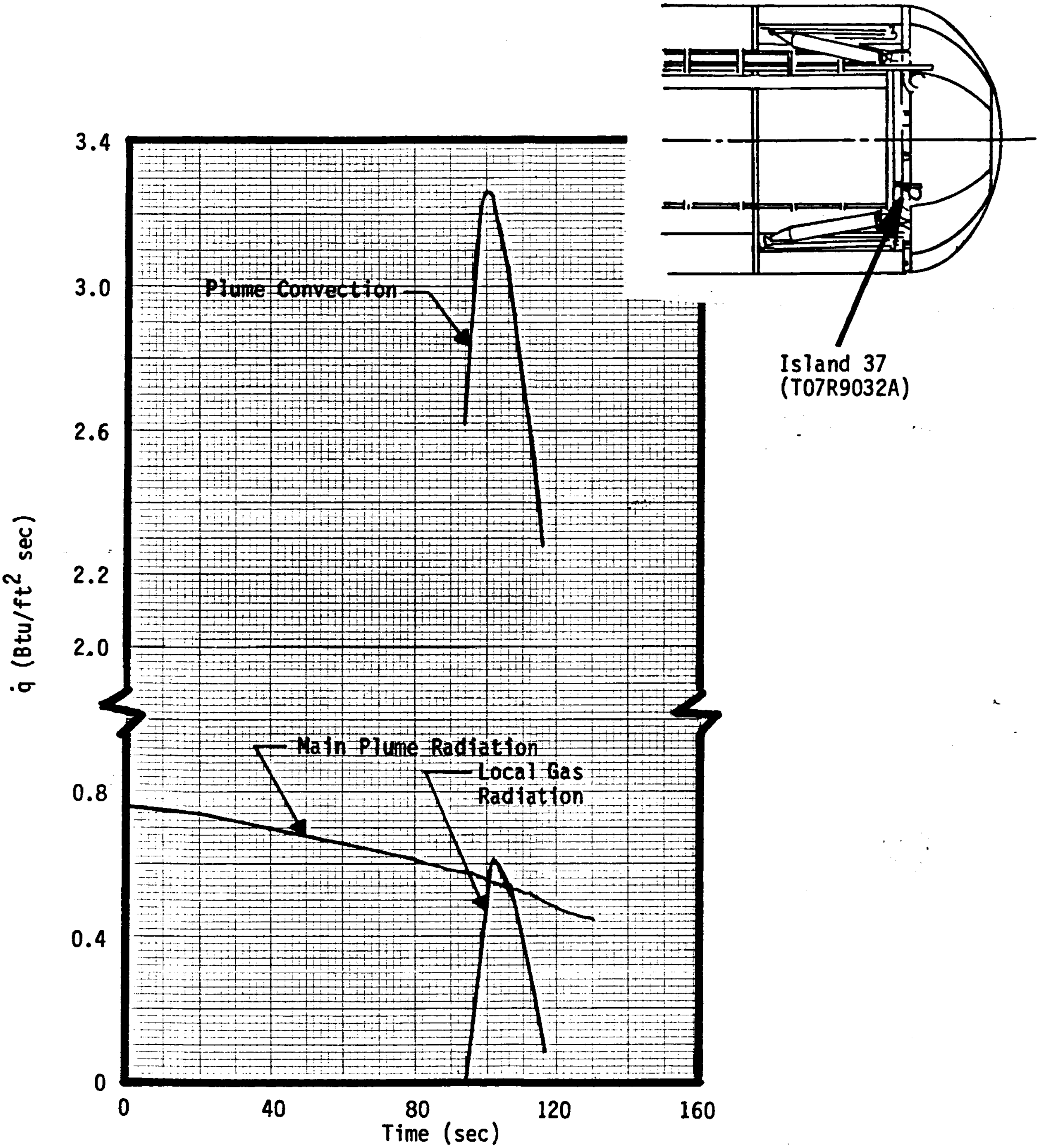

Fig. 3.49 Plume-induced Heating Time Histories for Gage 9032 (Island 37)

approximately 58 in. ahead of the LH_2 barrel/aft dome interface. Examples of these corrections will be given in the flight data analysis later.

The flight code was modified to correct the plume-induced heating rates. The hot-wall convective aeroheating was equated to zero for trajectory times lying between the time when base recirculation begins and the time when staging occurs. The main plume radiation was subtracted from the measured heating rates for all time according to the distribution given in Table 3.3. No attention was given during this study to the correction for the measured heating rates beyond SRB staging since the measured heating rates during this period were quite small in magnitude.

3.4 FLIGHT AEROTHERMAL ANALYSIS

This subsection presents discussions of the results of the OFT post-flight aerothermal data evaluation. This analysis points out the limitations of the wind tunnel h_i/h_u data base and the deficiencies in the aeroheating methodology. The results of the flight-reduced data provide another important data base, obtained solely from flight measurements.

3.4.1 TURBULENT FLOW

This section concentrates on the analysis of the turbulent flight data.

3.4.1.1 DATA ANALYSIS

40 Degree Cone

Gage T07R9001A: It was pointed out in Ref. 1 that the wind-tunnel data were transitional in the interaction region on the 39.4 deg. nose cone. As a result, the interference factor data base derived from the wind tunnel tests such as FH-15 (AEDC) and FH-16 (Ames) was not adequate for flight prediction, and was not used for prediction purposes. In order to understand the interference flowfield and the fact that there is influence of the $30^{\circ}/10^{\circ}$ cone on the pressure measurement gage 9062, the wind tunnel measurements along with theoretical computations were examined. The first case examined was the $10^{\circ}/39.4^{\circ}$ biconic configuration for which pressure data was available from the FH-13 test at $M_{\infty} = 4.5$. The Kutler code (inviscid) (Ref. 18) was run for the above configuration. The results in Fig. 3.51 show that the pressure peak occurs at the compression corner for an inviscid flowfield (Kutler code), whereas the peak measurement occurs somewhat downstream of the calculated peak. This discrepancy may be attributed to boundary layer displacement effects due to the boundary layer growth on the 10° cone and subsequent separation at the compression corner. In order to compare the pressure magnitudes on the 39.4° cone, a 39.4° cone value was obtained from NACA 1135 tables and was also plotted on Fig. 3.51. It is seen that there is no difference in the pressure levels on the 39.4° cone between the single-cone and biconic configurations. In other words, the effect of the 10° cone

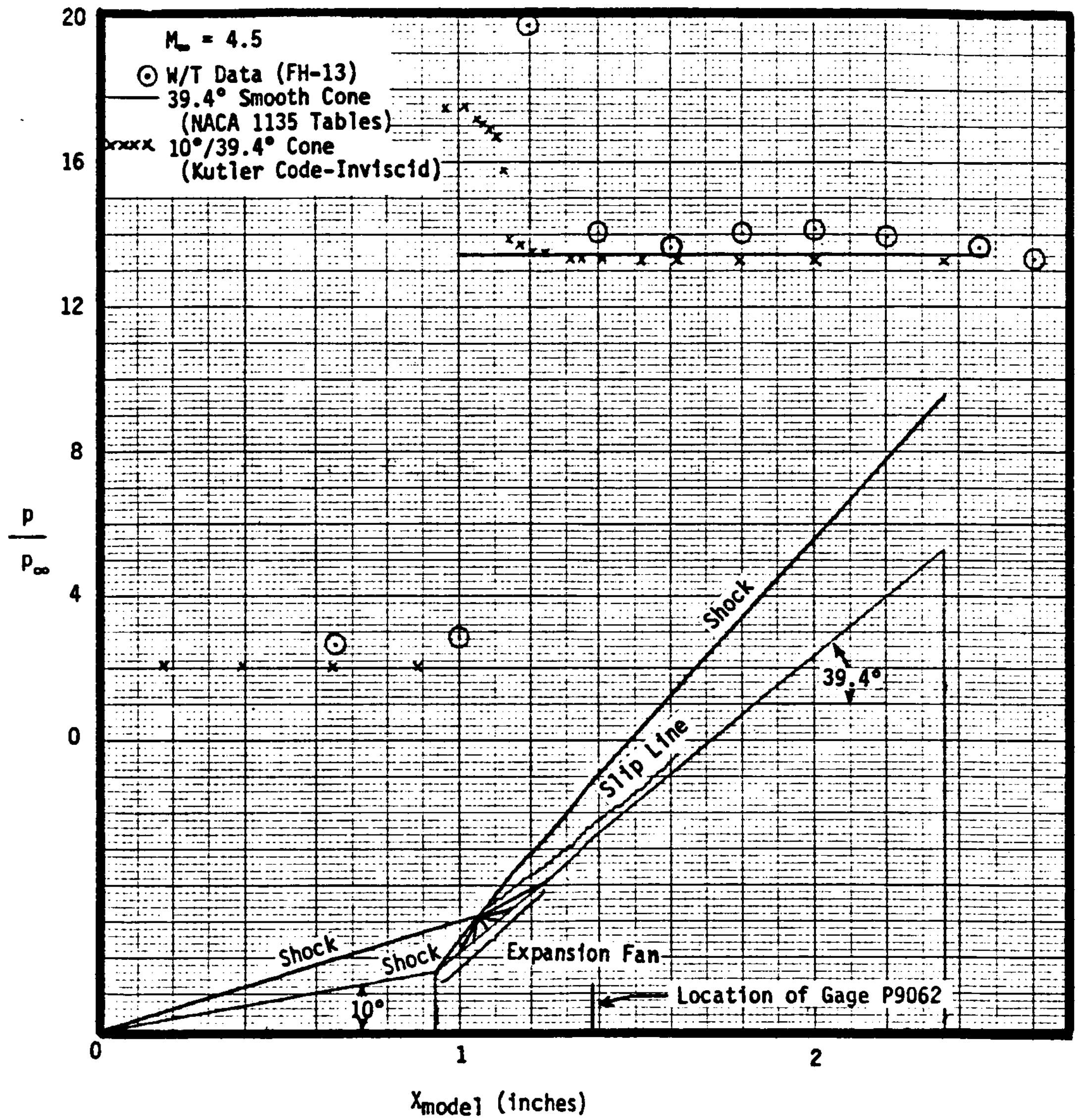

Fig. 3.50 Flowfield on a 10°/39.4° Biconic ET Nose Configuration

ORIGINAL PAGE IS
OF POOR QUALITY

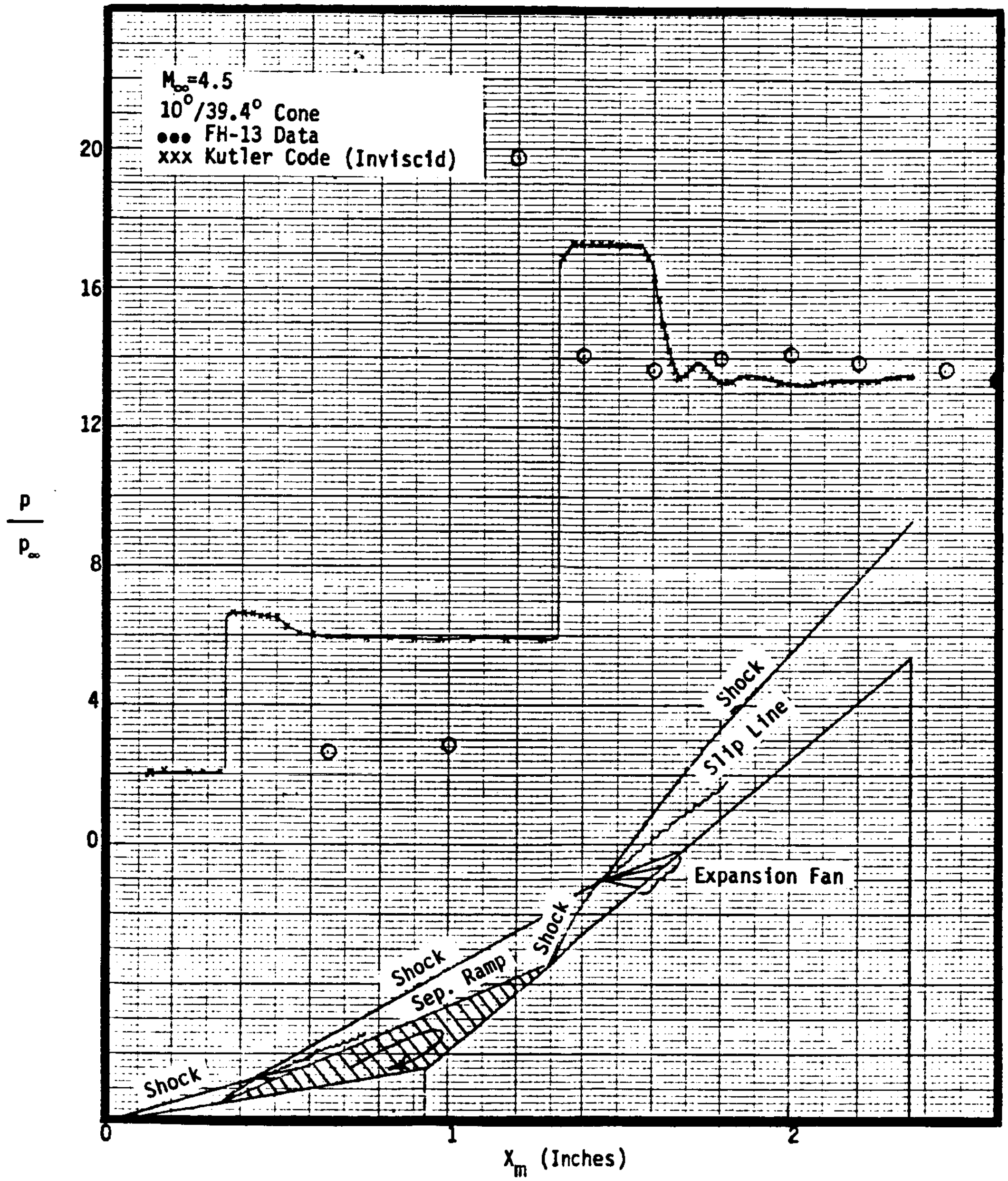

Fig. 3.51 Comparison of Pressure Ratio Between Measured Data and Theory (with Separation)

tip is felt only for a short distance downstream of the compression corner, where the flow expands to the 39.4^{o} cone value. However, since the pressure gage lies very close to the biconic juncture, it is expected to experience some interference effects at this Mach number. It is also felt that the same would be valid for other Mach numbers such as 3, 3.5 and 4. In order to take into account displacement effects, an approximate separation ramp (as shown in Fig. 3.51) was assumed at the compression corner, and the Kutler code was run. The computed results show that the assumed ramp started too far forward on the 10^{o} cone and that the ramp angle was too high. It also shows that the reattachment was too far back on the 39.38^{o} cone and the flow turning angle was smaller to produce a weaker recompression shock. Since the objective of the study was to establish the fact that there were interference effects due to the 10^{o} cone on pressure Gage 9062, no more runs were made to fine-tune the calculations. Moreover, the viscous flowfield over a compression corner is a separate study in itself and is beyond the scope of this report. No calculations for 30^{o}/10^{o}/39.38^{o} triple-cone configurations were made, since no wind tunnel pressure measurements are available on these configurations. However, it is expected that interference of the 30^{o}/10^{o} double-cone would exist on the 39.38^{o} cone at all the flight Mach numbers. As described in Ref. 19, the h_i/h_u prediction data base (Ref. 1) was modified based on STS-1 flight data. Before changing the data base, temperature mismatch effects based on the correlation (Ref. 15) described earlier in section 3.3.2.1 were factored out of the data. The BLIMPK run for Gage 9001 (Fig. 3.38) at $M_\infty = 3$ (STS-2) shows that BLIMPK underpredicted the flight data. This is attributed to nose interference effects. The interference factors were calculated from STS-1 as a function of freestream Mach number and were used for successive flights assuming no dependence on α, β combinations. The h_i/h_u dependence on α and β based on all the OFT flights, will be discussed later.

Another important criterion to be considered in these discussions is the transition criterion. One popular criterion that has been used in the Shuttle program is the one developed by the Douglas Corporation, i.e. flow is laminar for $Re_\theta/M_L \leq 150$, transitional for $150 \leq Re_\theta/M_L < 150\sqrt{2}$ and turbulent for $Re_\theta/M_L \geq 150\sqrt{2}$. While examining the preliminary flight h_i/h_u computations for Gage 9001, it was discovered (Fig. 3.52) that some of the h_i/h_u values around $M_\infty = 4$ were too high. As a matter of fact, sharp peaks occurred for STS 4, 5 and 7 around $M_\infty = 4$ (Fig. 3.52). In order to resolve this problem, the data reduction procedure was examined. Figure 3.53 gives plots of $\dot{q}_u$ vs. time for both turbulent and laminar flows. Also put on the plots is the $Re_\theta/M_L = 150$ transition criterion. Using this criterion, the flow is transitional for $100 < t < 107$ secs. for the STS-4 flight. Since the laminar values of $\dot{q}_u$ are quite small compared to the turbulent values beyond t = 107 secs., the unreasonably high values of h_i/h_u result. It should be noted that this criterion was developed for flat plate

ORIGINAL PAGE IS
OF POOR QUALITY

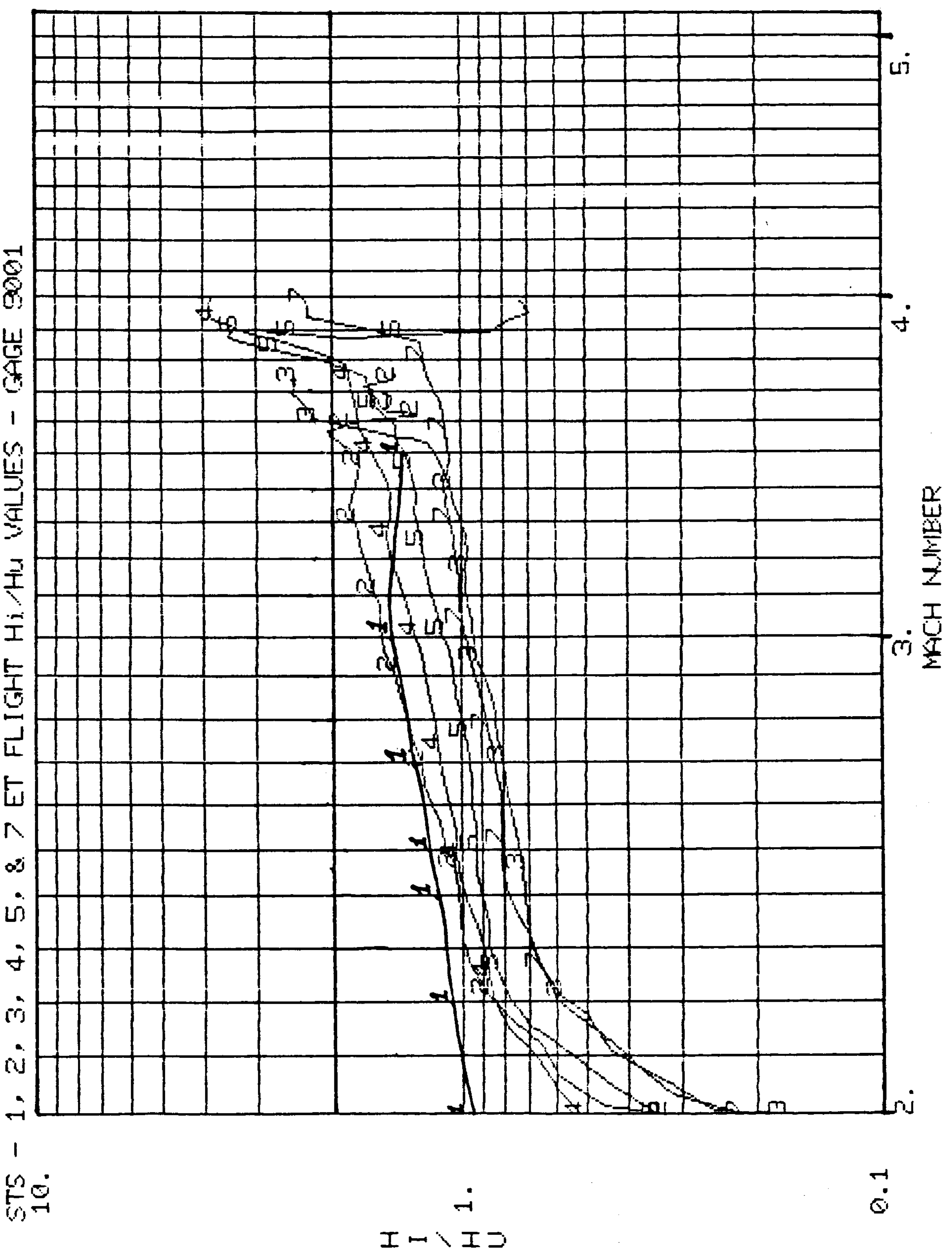

Fig. 3.52 Flight-derived h_i/h_u vs. M_∞

undisturbed flow and thus, may be inappropriate for use in an interference region such as Gage 9001.

Another transition criterion developed by Hung (Ref. 20) using Shuttle ET model test data states that flow is transitional in a disturbed flow region for $10^5 \leq Re_2^* \leq 10^6$, where "*" denotes Eckert reference conditions and the subscript "2" refers to post-shock conditions. Since the post-shock conditions are not easily definable in a complex shock interaction region, the pre-interaction conditions were used. Using this criterion, the flow becomes laminar (Fig. 3.53) at t = 126 secs. In this methodology, it is assumed that the flow is kept turbulent all the way up to the laminar interface for Gage 9001.

Using the above criteria, the RATE1 code (Ref. 13) was run to predict heating rates and interference factors for all the STS flights. The $\dot{q}$ vs. t plots and h_i/h_u vs. M_∞ plots are given in Fig. A.1b - A.1f comparing flight data, corrected flight (corrected for temperature mismatch) data and hot-wall predicted data for heat transfer and comparing corrected flight data with predicted data for h_i/h_u. The heat transfer comparisons are reasonable for all the flights. It is also noticed that for flights STS-3, 4, 5 and 7, the peak measurements are slightly to the right of the predicted peaks. It should be pointed out here that all these predictions were based on the h_i/h_u data base derived from STS-1. h_i/h_u is dependent on α , β combinations and would provide slightly different heat-transfer rate time history with the inclusion of this

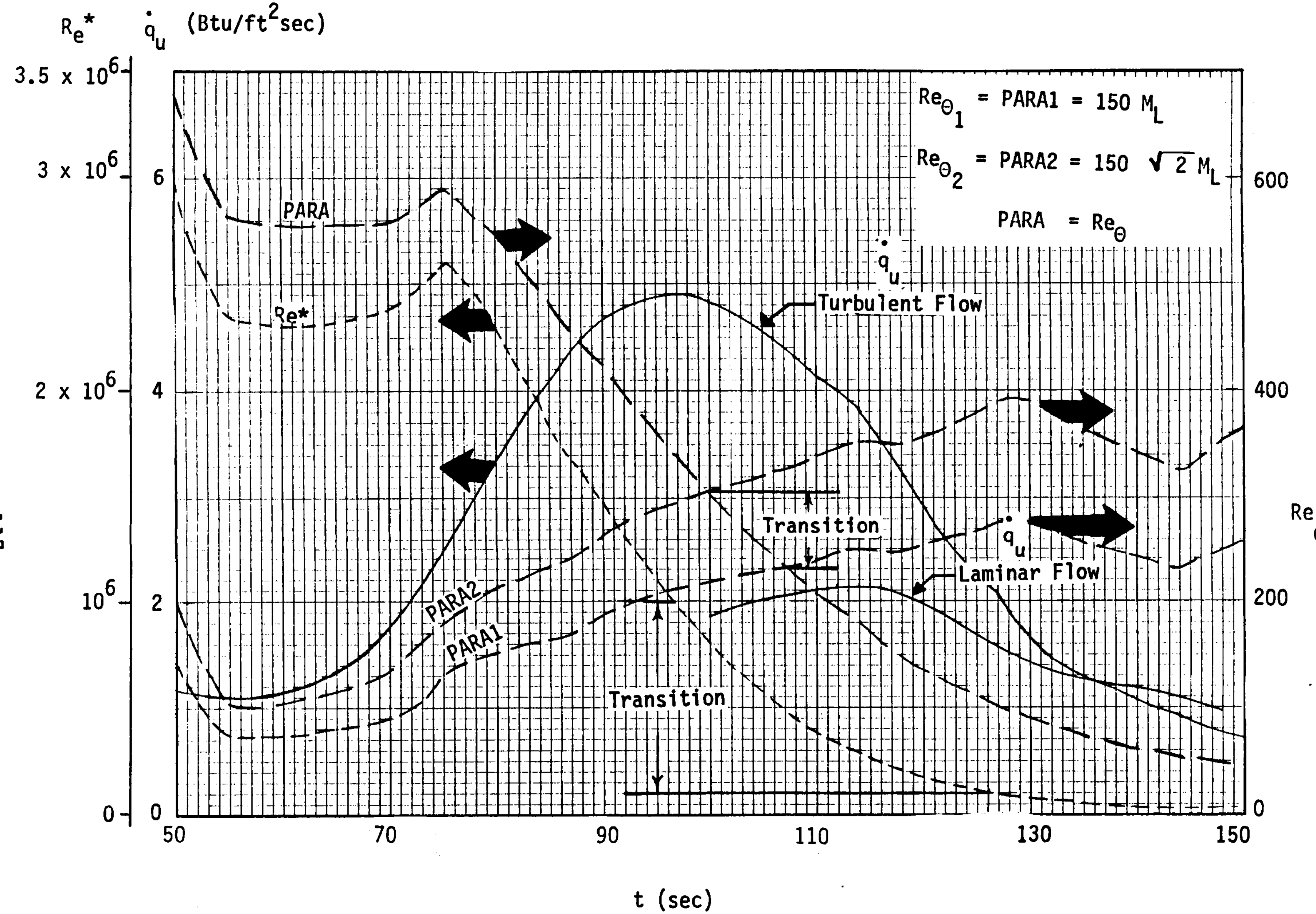

Fig. 3.53 Application Of Transition Criterion For Gage 9001.

h_i/h_u dependence on attitudes. Similar observations are made in the h_i/h_u vs. M_∞ comparison plots. Even after the adjustment in the transition criterion discussed above, small uncertainties in h_i/h_u remain around $M_\infty = 4$. The sudden "dip" in the h_i/h_u curve for $M_\infty < 2$ is due to the assumption that the cold wall values of heating rates were assumed to be zero, whenever $|T_{aw} - T_w| \leq 20^o$. In order to examine all the OFT flight data in a composite manner, the heat-transfer plots were assembled in Fig. 3.16 in the subsection 3.2 and the h_i/h_u vs. M_∞ plots for the six OFT flights are given in Fig. 3.52. The variation of h_i/h_u from flight to flight may be attributed to trajectory attitude effects.

As far as the pressure comparison is concerned, it had been noticed for STS-1 flight in Ref. 1 that in the detached shock regime, the pressure comparison was poor. Thus, the pressure math model for Gage 9001 needed to be changed in the Mach number range $1 \leq M_\infty \leq M_{attachment}$. Figure 3.54 plots the C_p data for all the STS missions in the above Mach number range. It is observed that the data collapsed in an orderly fashion showing the effects of attitudes to be minimal from flight to flight. A parabolic curve was faired through the data band and used in the prediction procedure. Since the flowfield is affected by interference which, in turn, is a function of attitude, it leads one to believe that the interference in the above Mach number range is minimal. Figure 3.55, on the other hand, shows the C_p variation with Mach number in the range $1 \leq M_\infty \leq 4$. Again, it is seen that C_p is virtually

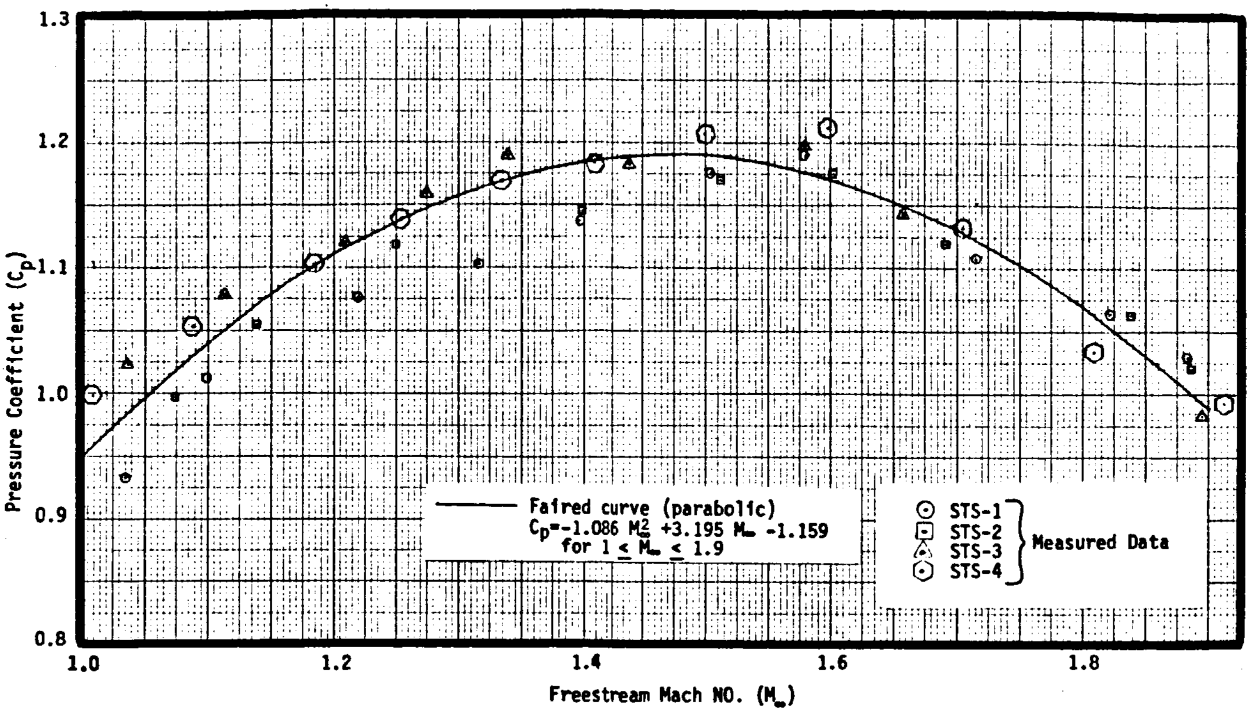

Fig. 3.54 Variation of Measured C_p with M_∞ for $1 \leq M_\infty \leq 1.9$ for Gage 9062

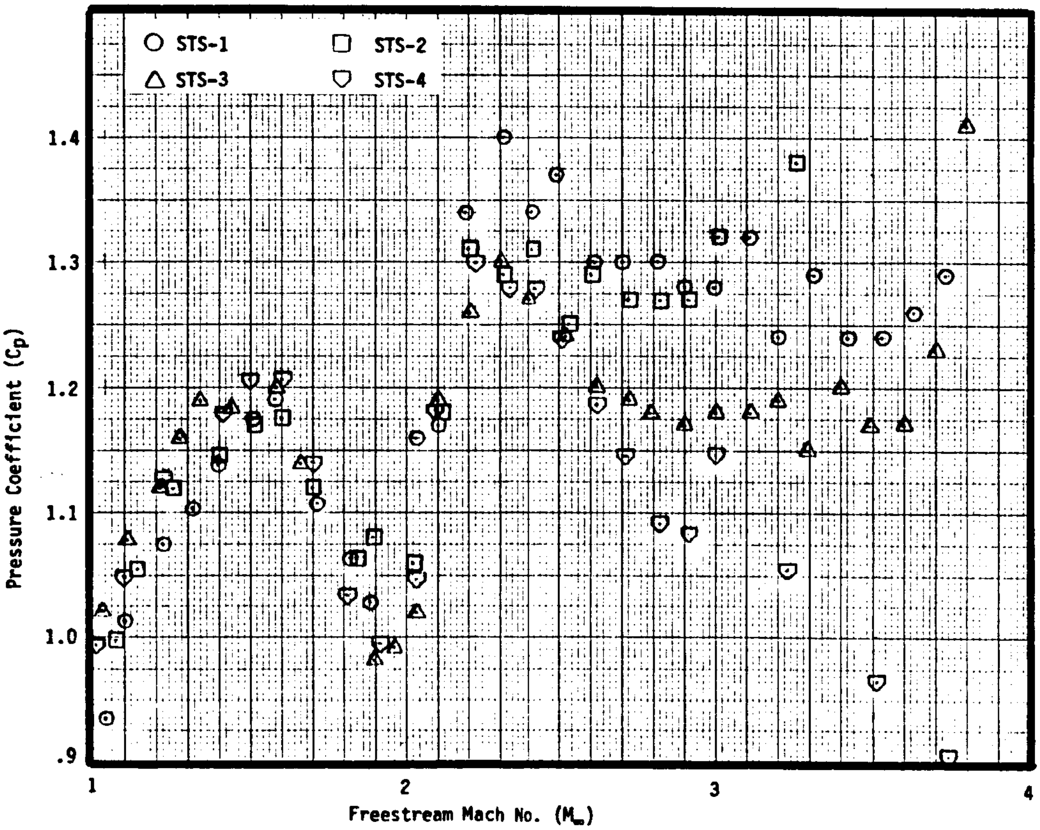

Fig. 3.55 Variation of C_p with M_∞ for $1 \leq M_\infty \leq 4$ for Gage 9062

independent of the trajectory attitudes in the Mach number range $1 \leq M_\infty \leq M_{attachment}$, whereas the C_p dependence on the trajectory is obvious beyond $M_\infty = 1.9$. The prediction of pressure in the interference region such as Gage 9001 location was accomplished by using the above correlation in the lower Mach number range, whereas the well-established correlation given below was used for Mach numbers in the attached regime for turbulent flow,

$$h_i/h_u = (p_i/p_u)^{0.8} \qquad (3.4)$$

From Eq. 3.4, p_i has been calculated and plotted in Figs. A.1a - A.1e in Appendix A. It is seen that the theory-data comparison is quite reasonable for all the OFT flights. This gives another indication that the h_i/h_u reduced from flight data and using all the applicable correlations are sound values.

LO_2 Tank Section

Gages 9004 (Island 2), 9005 (Island 1), 9007 (Island 6), 9008 (Island 5), and 9010 (Island 8): These gages are located on the ET ogive which is the undisturbed section of the tank. The flow on the ogive is processed through a 39.38° cone shock emanating at the 10°/39.38° cone junction on the ET nose and is then expanded around the ogive where the flow accelerates. Although the flow does not experience any interference on the ogive, the heat-transfer measurements contain temperature mismatch effects, SOFI (Spray-On-Foam-Insulation) roughness/waviness effects, rough surface-smooth island effects, and island geometry effects. It is hard to separate the above effects. These were not present on the wind-tunnel models, which were thin-skin smooth models with thermocouple measurements. This problem becomes much more difficult in the interference regions. Thus, the flight data will have to be looked at in a statistical fashion so that the flight-derived data base may be used to update the wind tunnel data base and applied for design and pre-flight assessment purposes.

The flight measured heating rates were processed by the ETFLIT computer code (Ref. 21) by utilizing the temperature mismatch correction described in detail in the previous subsection. No temperature mismatch correction was considered for $0 \leq t \leq 70$ sec., because there is negligible aerodynamic heating during this period, and the gage and upstream surface temperatures are approximately the same. Since it was observed that the TPS surface temperature closely tracks the recovery temperature (T_{aw}), the temperature mismatch factor is a constant only dependent on location but independent of flight trajectory and flight time up to approximately 100 sec. into the flight trajectory. It should be noted, however, that T_{W_1} is assumed to be equal to T_{aw} until the SOFI ablation temperature is reached and is equal to the SOFI ablation temperature when $T_{W_1} > T_{Ablation}$. The temperature mismatch factors are listed in Table 3.4 for the above flight gages.

As far as prediction is concerned, the methodology developed in Ref. 1 and briefly described in Subsection 3.3.1 was closely followed by using the MINPRE (Ref. 11) and RATE1 (Ref. 13) computer codes. The roughness/waviness factors and roughness-smoothness factors used in the prediction were derived from charts and tables in Ref. 1. In order to check the surface pressures measured on Gages 9064 (Island 2), 9065 (Island 1), 9066 (Island 6), and 9067 (Island 5), theory data comparisons were made in Figs. A.2 - A.5. These comparisons establish the validity of the inviscid pressure distribution at the boundary layer edge. The pressure comparisons show that the prediction is quite good beyond 60 to 70 sec. It should be noted that the pressure correlation developed for the 40 deg. cone gage described earlier for Mach numbers $1 \leq M_\infty \leq M_{attached\ flow}$ was used in the above comparisons. This cone value of pressure is ramped down to the ET shoulder value following a Newtonian correlation given in Ref. 1. However, the ET shoulder value in this correlation is not very accurate for $M_\infty < 2.5$. As a result, for $M_\infty < 2.5$, the pressure predictions for the gages near the shoulder (Islands 6 and 5) will have higher discrepancies when compared with measurements in this Mach number range. This is clearly observed in Figs. A.2 - A.5. Since peak heating is at a higher Mach number range than $M_\infty = 2.5$, the above inaccuracies are not a concern for design applications.

For a transition criterion for the undisturbed gages, a value of $Re_\theta / M_L = 150\sqrt{2}$ obtained from the literature for smooth flat plates was initially used for triggering transition and a value of 150 for complete transition from turbulent to laminar flow. However, since the flow over the ogive experiences a trip at the

$10^\circ/39.38^\circ$ cone juncture and the SOFI on the tank surface adds to the turbulence, the above criterion makes the flow become fully laminar much earlier than observed in flight measurements. Consequently, another transition criterion by Hung (Ref. 20) applicable for disturbed flow areas was examined.

In order to simplify this criterion it was found that $Re^* = 3 \times 10^5$ gave a reasonably good match between laminar theory and flight data for undisturbed flow regions. It was further assumed that the reference quantities in the expression for Re^* be evaluated by using the pre-shock or pre-interaction conditions in case of disturbed boundary layers.

TABLE 3.4

Temperature Mismatch Factor in 70 to 110 sec. Time Range

Westkaemper Correlation

Gage No.	Factor
9004	2.062
9005	2.062
9007	2.27
9008	2.27
9010	2.36

Since transition generally occurs around 125 sec. for the ET and small inaccuracies in the transition times do not affect peak heating, which is responsible for TPS design, a rigorous transition analysis was not used in the flight data analysis.

MINPRE and RATE1 were run back to back to predict the interference factor and heating rate as a function of trajectory time. Figures A.2 - A.5 plot the prediction vs. temperature mismatch - corrected flight data and compare predicted and calculated interference factors as a function of freestream Mach number. The general observation for all the LO_2 tank DFI gages is that the predictons code somewhat overpredicts the corrected heating rate flight data. This may be attributed to the temperature mismatch correction being a little too high. A more extensive BLIMPK analysis using the temperature variation on the various materials on the surface in the vicinity of the measuring gage is necessary to accurately model the temperature mismatch. The other errors may be in the calculation of roughness/waviness factors and rough surface-smooth island factors. The roughness/waviness factor is based on nominal sand roughness of the SOFI, whereas in actuality, this could vary from flight to flight. The rough surface-smooth island factor is derived on the basis that while the flow passes from rough SOFI surface to smooth island surface, the boundary layer tries to adjust to the smooth wall thus giving rise to a factor such as this. According to this, the total roughness factor is given by the following equation:

$$\frac{h_i \text{ Smooth Island}}{h_u \text{ Smooth Surface}} = \left(\frac{h_u \text{ Rough/Wavy}}{h_u \text{ Smooth Surface}}\right) \cdot \left(\frac{h_i \text{ Smooth Island}}{h_u \text{ Rough/Wavy}}\right) \qquad (3.5)$$

Typically, this total factor is of order one in the peak heating region, indicating that, at least, during this timeframe, the roughness has minimal effect on aeroheating. In any event, the uncertainties, if any, in the factor are thought to be of less magnitude than the temperature mismatch correction applied to measured heating rates. Similar trends are noticed in the h_i/h_u vs. M_∞ plots given in the above figures. Predicted values of h_i/h_u in the Mach 2.5 - 4 range is around unity or a little higher, whereas the flight-reduced values of h_i/h_u are almost consistently somewhat less than prediction. Some high "peaks" around $M_\infty = 4$ are a result of the assumption of the transition criterion. Perhaps the flow remains turbulent even longer than calculated.

Another interesting way of examining the measured heat-transfer is in a composite manner in which all the flights are examined on the same plot. The hot-wall heating rates from all the flights have already been compared with each other in Figs. 3.16 and 3.17. The differences among the various missions may be attributed to trajectory H-V profiles and attitude differences. From these plots, Gage 9005 (Island 1) STS-3, Gage 9008 (Island 5) STS-5, Gage 9004 (Island 2) STS-4, and Gage 9010 (Island 8) STS-4 seem to be the ones which are erratic in all the flight measurements. In order to examine these a little further, the measured heating rates on the $\theta_T = 180$ ray at $M_\infty = 3$ and 3.5 were plotted in Figs. 3.56 and 3.57. These plots also include Gages 9001 and 9017 measurements which were made on the ET nose and intertank

ORIGINAL PAGE IS
OF POOR QUALITY

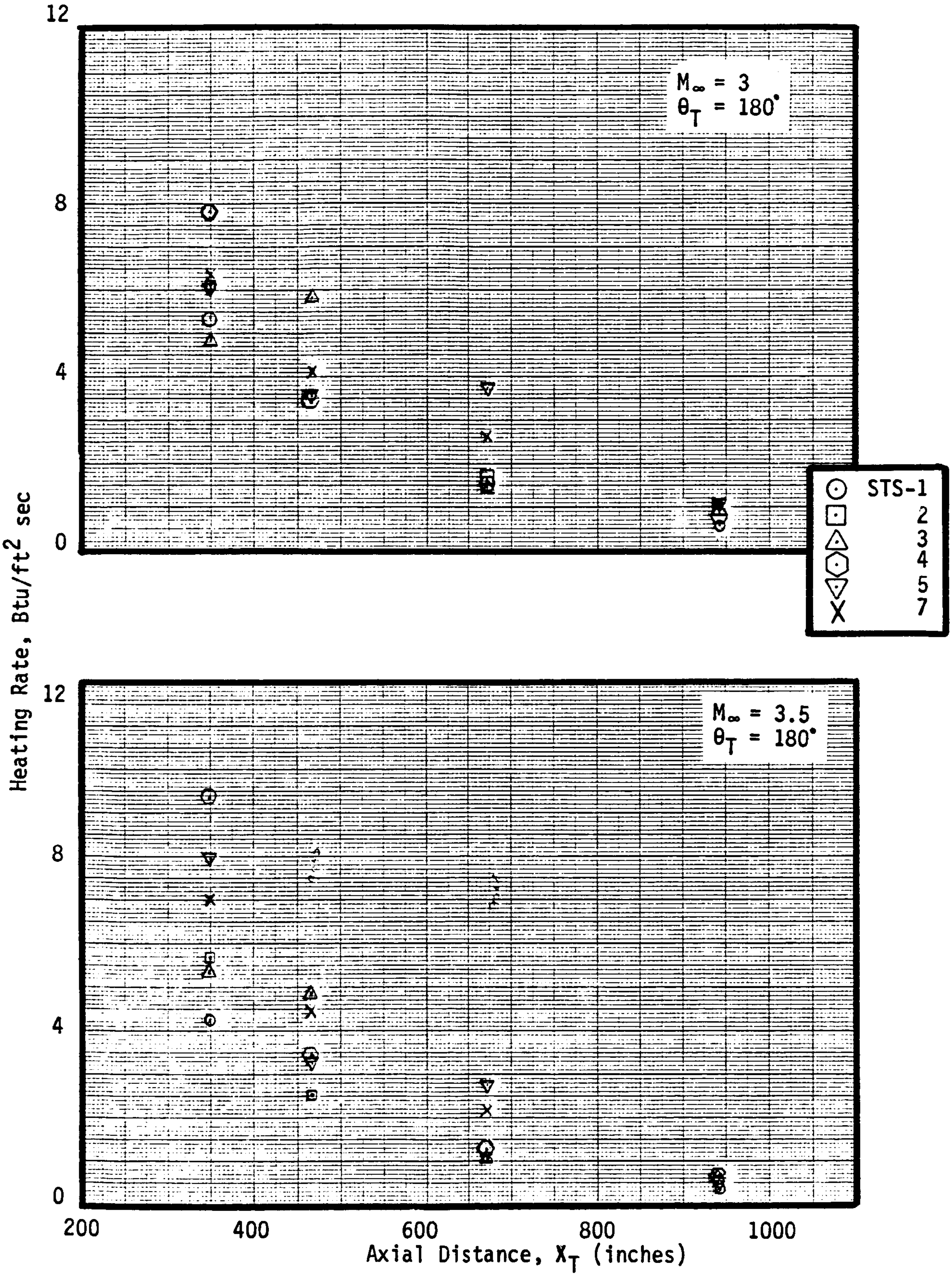

Fig. 3.56 Distribution of "Uncorrected" Flight Heating Rate Measurements at $\theta_T = 180°$

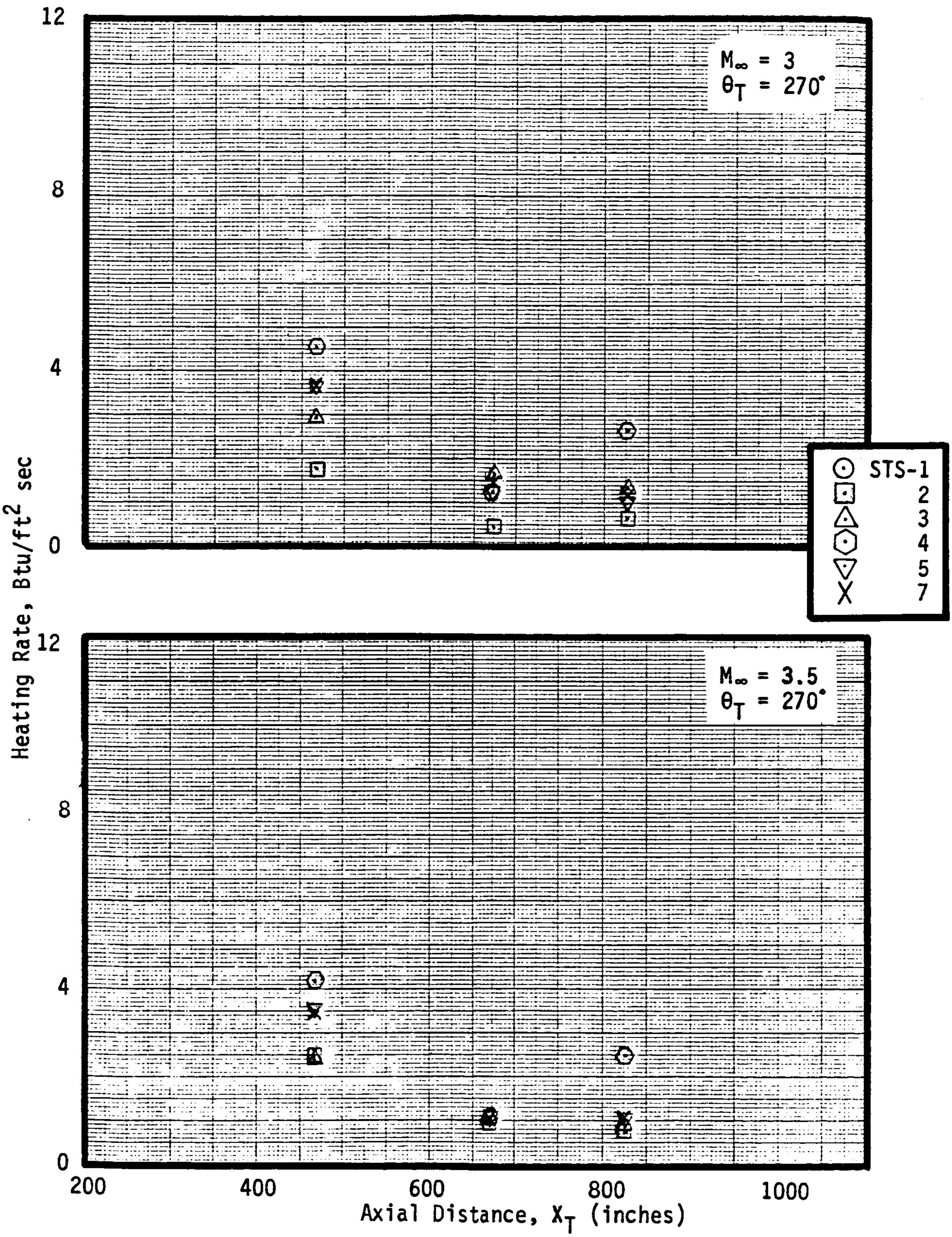

Fig. 3.57 Distribution of "Uncorrected" Flight Heating Rate Measurements on θ_T=270°

region, respectively, for establishing trends. Again, the two measurements on the $\theta_T = 180^o$ ray seem to stand out. In order to examine the effects of trajectory α , β (attitude) only on the heating rates, the heat-transfer coefficients were divided by h_{ref} (i.e. heating for a one-foot radius sphere) and plotted in Figs. 3.58 and 3.59 for $M_\infty = 3$ and 3.5, respectively. It is seen from these figures that with the exception of Gage 9005 in STS-3 and Gage 9008 in STS-5 both at $M_\infty = 3$ and 3.5 which are reading too high (as much as a factor of 2), the rest of the undisturbed gages on $\theta_T = 180^o$ seem to be reading correctly. This fact is confirmed by examining the trajectory plots in Fig. 3.10, where STS-2 flew at $\alpha \simeq 5^o$ in the peak heating range as compared to STS-3, 4, 5 or 7 which flew up to approximately $\alpha = 2^o$ and consequently, STS-2 should measure higher h_u/h_{ref} compared to the last four flights. Since STS-3 and STS-5 measured higher for these gages, these measurements are not believable. A similar explanation is valid for the measurements (Figs. 3.60 and 3.61) made in STS-4 flight on Gage 9010, located on the $\theta_T = 270^o$ ray. The derived interference factors for all the LO_2 tank gages were plotted in a composite manner on Figs. B.2 - B.6 in Appendix B. Islands 1 and 5 on $\theta_T = 180^o$ in Figs. B.3 and B.5, respectively show that STS-3 and STS-4 measurements were erroneous. The same is true for Island 8 on $\theta_T = 270^o$ in STS-4 flight. From such an analysis, measurements made on Gage 9004 (Island 2) in STS-4 could not be dismissed. Thus, out of a total of 25 measurements made on the LO_2 tank, the above 3 should be thrown out from the analysis.

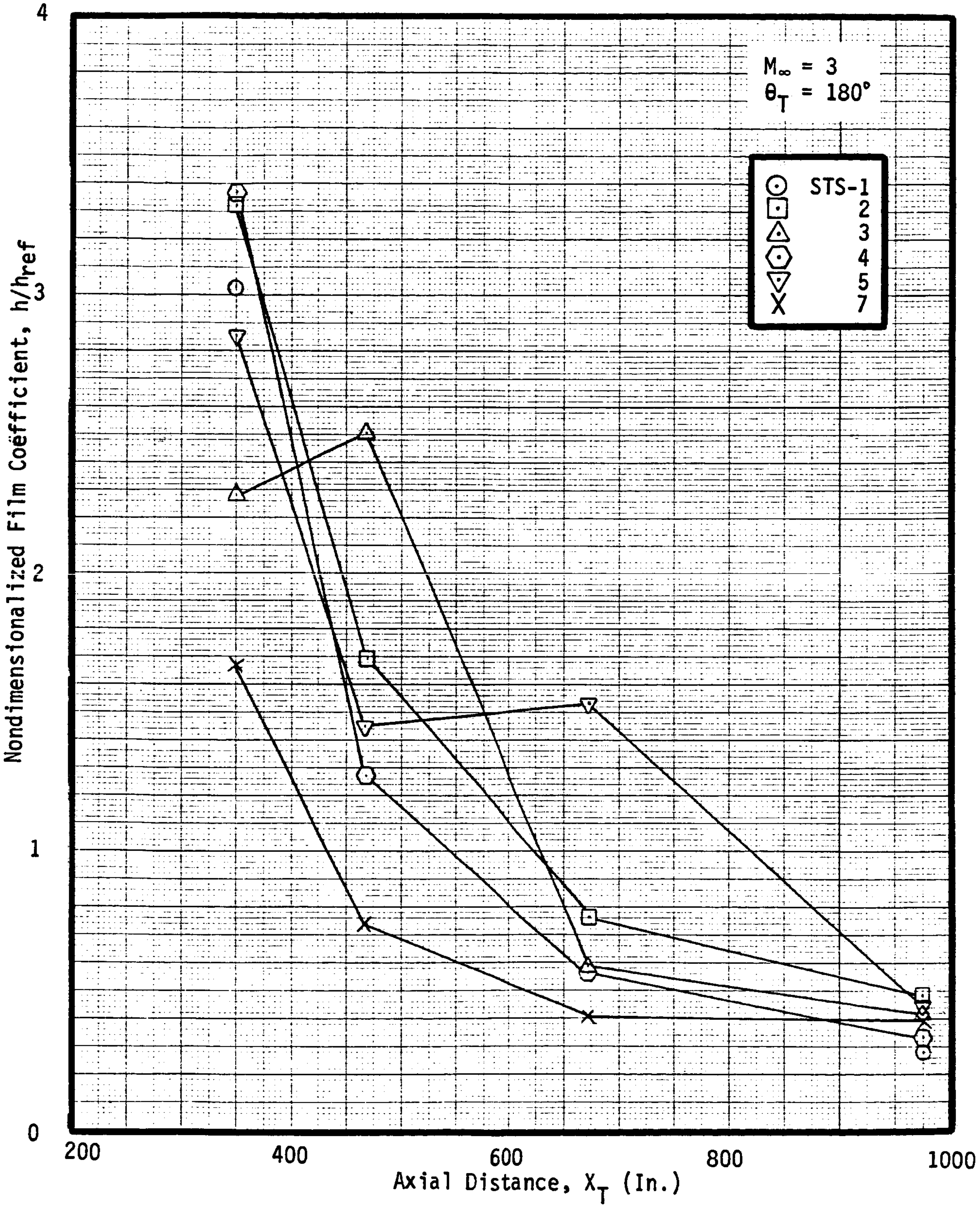

Fig. 3.58 "Uncorrected" Film Coefficient Distribution on $\theta_T = 180°$

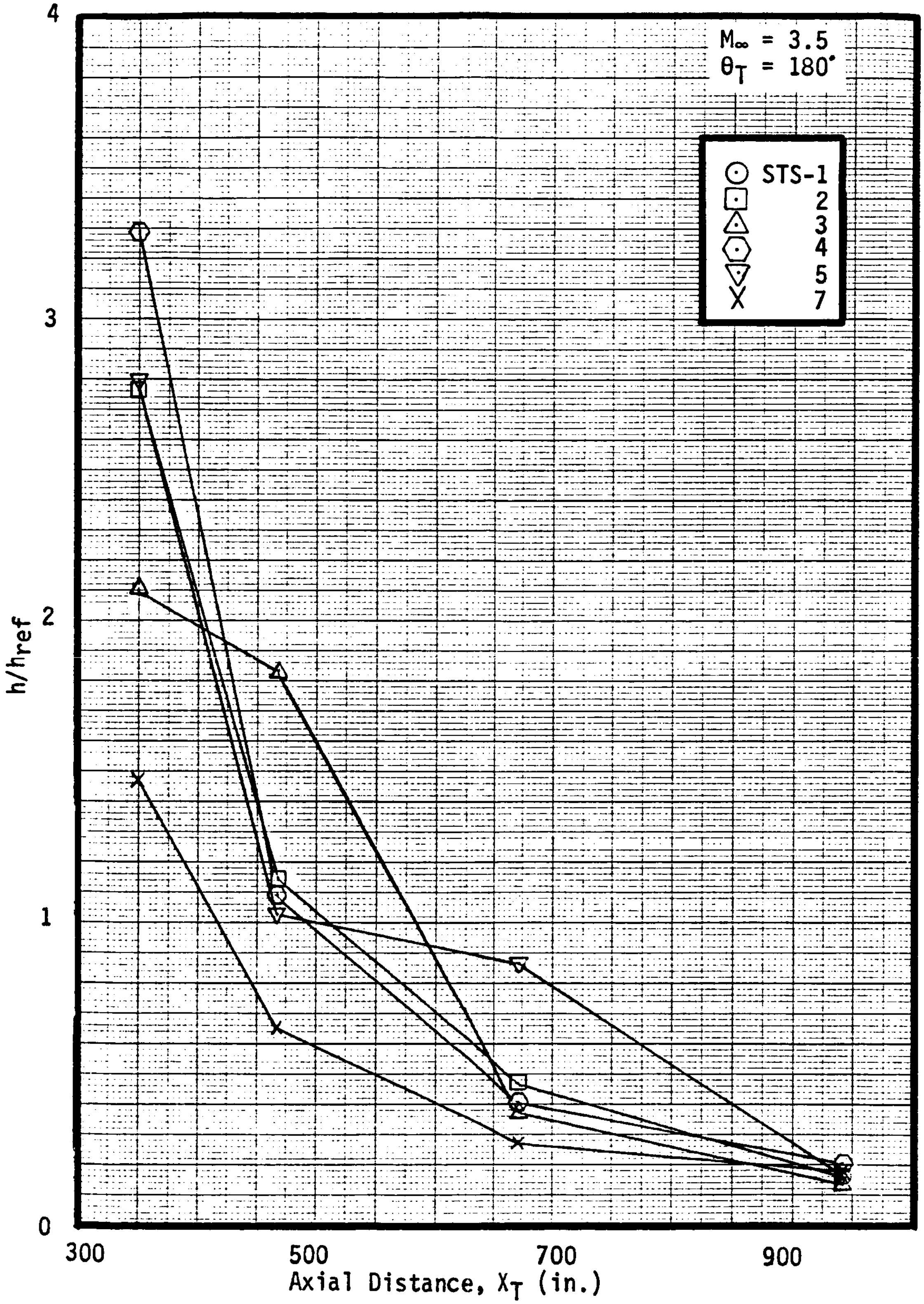

Fig. 3.59 "Uncorrected" Film Coefficient Distribution on $\theta_T = 180°$

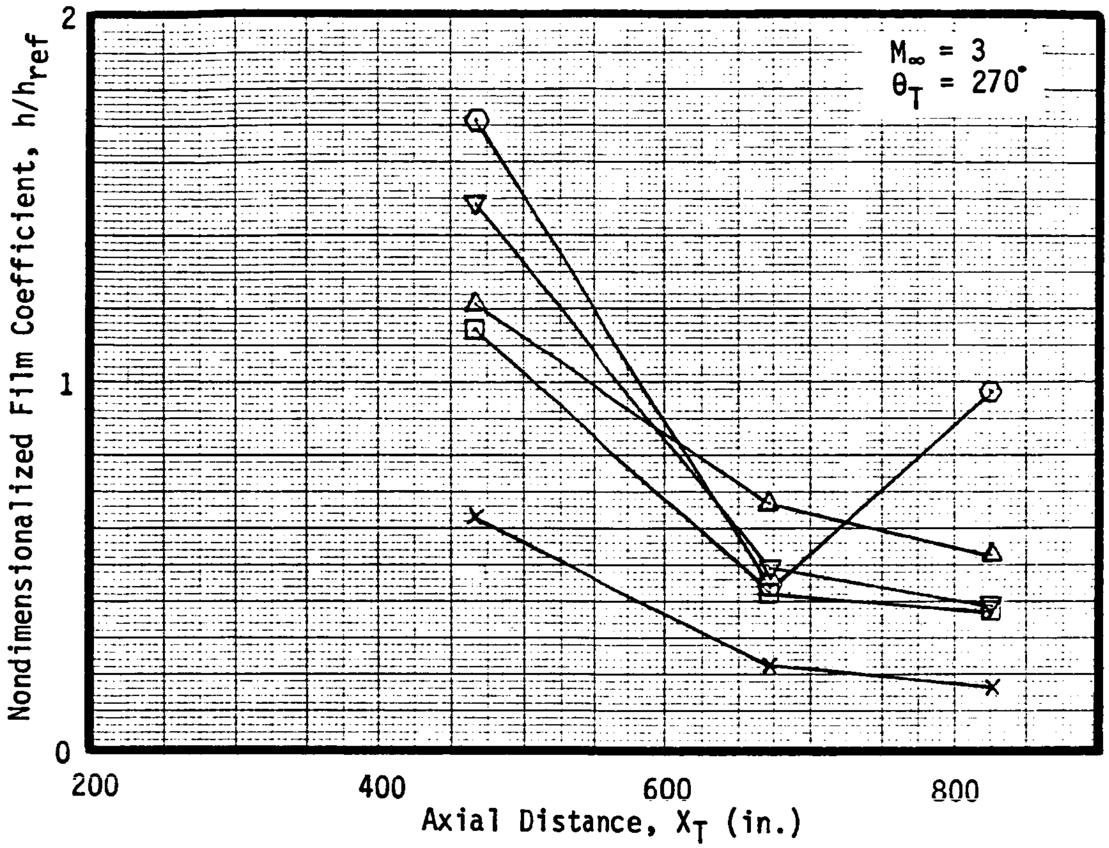

Fig. 3.60 "Uncorrected" Film Coefficient Distribution on θ_T = 270°

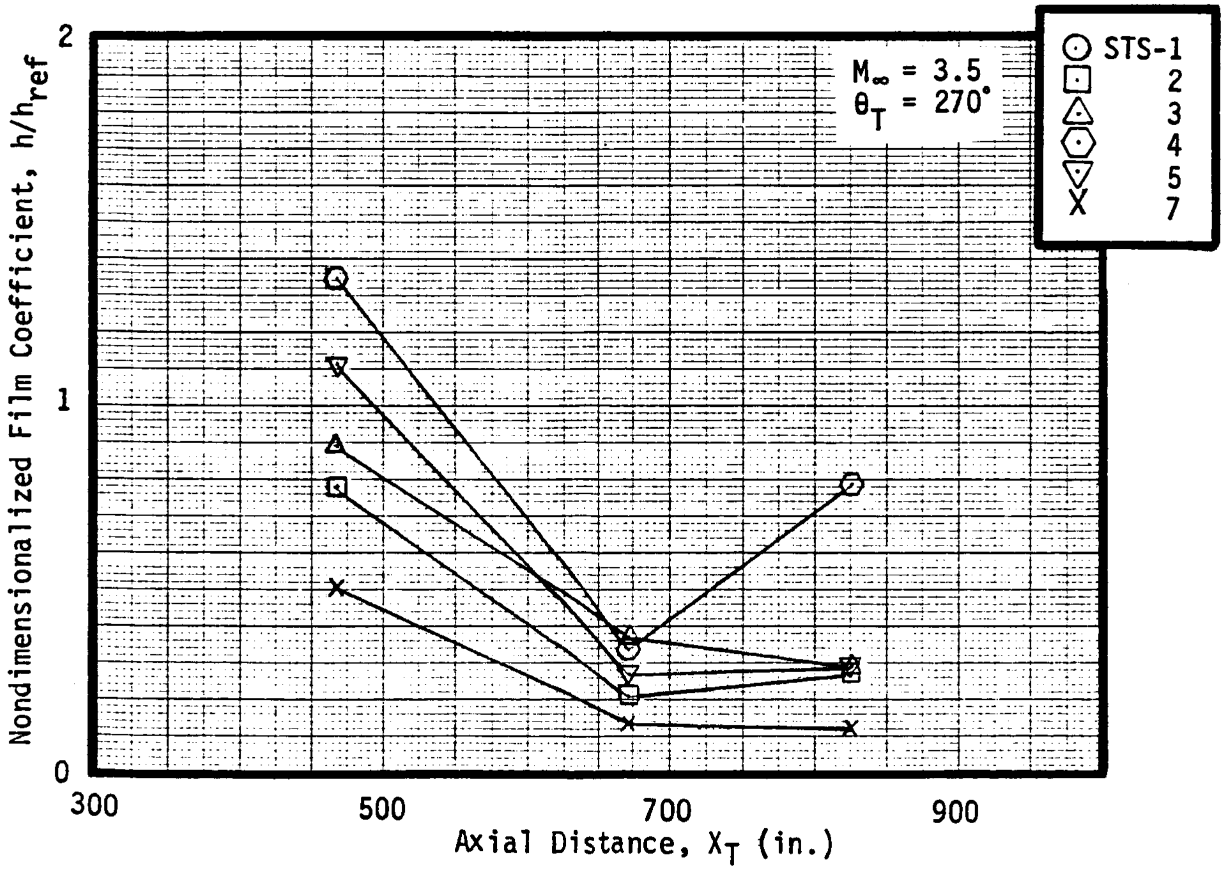

Fig. 3.61 "Uncorrected" Film Coefficient Distribution on θ_T = 270°

Intertank Section

<u>Gage 9011 (Island 18):</u> This gage is located in front of the LO_2 feedline fairing in the intertank section of the ET, and experiences interference from the fairing. It is observed by examining the hot-wall heating rate comparison plots for all the OFT missions that STS-1 and 2 were more benign than the rest of the flights. Of course, this is consistent with the H-V profiles of various STS flights. The predicted $\dot{q}_i$ environments, based on the undisturbed $\dot{q}$ math model and h_i/h_u data base, are plotted in Figs. A.7a - A.7e. It is seen that the predictions are quite a bit lower than flight. The same observations are made in the h_i/h_u comparisons in the above figures. It should be noted that the contributions due to temperature mismatch, geometric stringer factor, and island factor were not considered in these comparisons. It was assumed to contain no temperature mismatch effects, since the effective running lengths for such high interference regions may be considered small in the correlation Eq. 3.31 thus giving correction factors close to unity. No geometric island and stringer factors were included, since the island, although located between stringers, is blended into the surface and no significant cross-flow exists. The plots comparing pressure measurements on this island and the pressures derived from the interference factor data base are also given in Figs. A.7a - A.7e. Again, it is observed that the predictions are lower than measured pressures in all the flights.

Another test (IH-97A) (Ref. 22) was run in Tunnel A at AEDC, simulating the exact α , β profiles in STS-1 through STS-4 flights. The reduced h_i/h_u's have been plotted against prediction and flight in Appendix C. It is observed that the new data are more in line with prediction than with the flight data. All these seem to suggest that temperature mismatch should be considered in reducing the flight data.

A composite set of flight-derived h_i/h_u data are plotted in Fig. B.7 as a function of Mach number. The differences observed in this plot from flight-to-flight may be attributed to attitude differences. The sharp "peaks" occurring in the plots around Mach 4 are attributed to laminar values of h_u in the denominator of h_i/h_u, suggesting that the transition from turbulent to laminar flow occured later in flight.

<u>Gages 9013 (Island 173), 9018 (Island 172) and 9019 (Island 171):</u> These gages are located very close to the ET top center-line back-to-back with gage 9019 in the most forward position. These gages are placed on a long island located slightly ahead of the bipod and are designed to measure orbiter shock impingement heating on the ET intertank. This island also contains a pressure gage (Gage 9071) located between calorimeter Gages 9018 and 9013 but closer to Gage 9013 than 9018.

Examination of the predicted heating rates with measured rates for Gage 9013 in Figs. A.8a - A.8f shows that with the exception of STS-5, the comparison is quite good. No temperature mismatch has been considered for any of the gages located on the intertank, LH_2 tank, and protuberances. The stringer factor was taken to be 1.33 for all Mach numbers. Similar conclusions are made after examining the h_i/h_u vs. M_∞ plots in the above figures. The pressure comparisons between the Gage 9071 measurements and prediction show that, for STS-1 thru 4, the comparison is good. However, for STS-5, the prediciton is higher than flight. The heating measurements are high compared to prediction in STS-5, possibly because the heating peak is quite close to this gage. Obviously, this peak was not picked up in the wind tunnel data base. It is unfortunate that the IH-97A test which tested the ET model at exact attitudes as in flight did not test beyond STS-4 (see Appendix C). Even for the first four flights, the comparison between either the math model or flight data with IH-97A test data is not very good. The composite h_i/h_u plots in Fig. B.9 for Gage 9013 shows clearly that STS-5 h_i/h_u vs. M_∞ is completely different from the rest of the flights. The reason for lesser pressure discrepancies between STS-5 flight and prediction is not very clear since the flight-derived h_i/h_u's should yield high interference pressures.

The middle gage on this island, Gage 9018 (Island 172), measured hot-wall heating rates, which could be basically put into two groups, as seen in Figs. A.13a - A.13f. STS-1, 3, and 5 measured higher heating rates than the rest of the three flights. It was pointed out in Ref. 1 that the prediction for STS-1 was quite a bit lower than measurements. It was then thought that the "peak" heating values were not picked up by the wind tunnel data base thus yielding such discrepancies. Consequently, the data base for Gage 9018 was changed in Ref. 19 and was used in the predictions for the rest of the STS flights. The consequence of this was that those three high heating flights were reasonably modeled by the new data base, whereas the other three were overpredicted to a considerable extent. The same conclusions are made from individual h_i/h_u vs. M_∞ plots in the above figures. The composite flight-derived h_i/h_u vs. M_∞ plots in Fig. B.14 show that STS flights 2, 4, and 7 are low, STS 1 and 5 are high, and STS-3 goes from a low level to a high level around $M_\infty = 2.7$. This indicates that the shock may have moved across the gage in STS-3.

The forward gage on the island, Gage 9019, measured heating rates equal to the level experienced by the aft gage, 9013 (see Fig. 3.21). The STS-4 measurement seems to be high compared to the rest of the flights. This is also clear from the hot-wall heating rate comparison plots in Figs. A.14a - A.14f. The flight is somewhat underpredicted in flights STS-2 and 5 and quite substantially underpredicted in STS-4. The secondary peaks appearing in the flight measurements may be due to the shock off the LO_2 forward feed-line fairing located to the right and forward of this island. The same conclusion is reached from the plots of h_i/h_u vs. M_∞ in the above figures. The composite h_i/h_u vs. M_∞ plots in Fig. B.15 show more consistency than the rest of the two gages, described above. However, STS-4 seems to be a bit higher than the rest of the flights.

A special and more detailed analysis is given later for the entire Island 17 in order to shed more light on the validity of the above measurements.

<u>Gages 9014, 9015 and 9016:</u> These gages are located on the left side of the tank around the SRB/ET fitting ahead of the bolt catcher. All these gages are affected by the SRB shock interference. Although Gages 9014 (Island 16) and 9016 (Island 14) are symmetrically placed with respect to Gage 9015 (Island 15), the interference flow is not necessarily symmetrical because of angle-of-attack effects.

For Gage 9015, the composite measured heating rate plots in Fig. 3.20 show that the peak heating rate generally went up as the STS flight got "hotter". As on the top center-line (Island 17), this island is in a strong interference heating zone caused by the SRB nose shock impingement on the ET. The prediction was compared with measured heating rates in Figs. A.10a - A.10f. Generally, the math model somewhat underpredicted the flight data. The IH-97A test (Appendix C) also showed that the h_i/h_u's are generally higher than prediction based on the previous data base and are quite close to the flight-reduced h_i/h_u's. Pressure Gage 9070, located on Island 15, showed in the above figures that the prediction was higher than measurement in all flights. The predicted surface pressures were calculated from the interference factors in the following way:

$$p_i = (p_i/p_u) \cdot p_u \qquad (3.5)$$

where

$\frac{p_i}{p_u}$ = Interference pressure ratio calculated from a correlation of the form $p_i/p_u = (h_i/h_u)^n$

with

n = 1.25 for turbulent flow
= 0.77 for laminar flow

p_u = Undisturbed pressure calculated by a correlation derived from the MOC calculated pressures, documented in Ref. 1.

If one uses the flight-measured pressure values to calculate h_i/h_u from Eq. 3.7 and then uses that result with a calculated q_u to obtain hot-wall heating rates, the levels of heating would come close to the levels of prediction in Figs. A.10a - A.10f. In order to check the trends for h_i/h_u with freestream Mach number, flight-derived h_i/h_u for all the flights were plotted in Fig. B.11 in the Mach 2-4 range. The consistency of h_i/h_u variation is clear. The small differences between the curves may be attributed to α, β variations and other confounding effects in different flight trajectories. The analysis of Gage 9015, which is strongly affected by shock interference, shows that the flight environments are consistently being underpredicted by the existing math model. These discrepancies are thought to be in the $(h_i/h_u)_{geometry}$ data base, the surface roughness and stringer factors, and the omission of temperature mismatch corrections in the flight data reduction. Based on experience with the levels of the first three items and also on the flight pressure analysis described before, most of the uncertainties in the theory-data comparison in Figs. A.10a - A.10f are thought to be in the omission of the temperature mismatch in the data reduction. However, this was not observed for Island 17 as described before. A possible explanation for such differences is that the effective running lengths used in the correlation, Eq. 3.3, for the two Island measurements may be different; the differences could be in the shock impingement locations relative to the DFI Island locations. The precise effects of shock impingement on thermal mismatch are not currently known.

Even though Gage 9014 (Island 16) measured heating rates quite a bit below Gage 9015, as seen in Fig. 3.20, the nature of underprediction, as evidenced from Figs. A.9a - A.9e, is similar to Gage 9015. The composite h_i/h_u vs. M_∞ plots from all the six flights are given in Fig. B.10. Again, the consistency in the h_i/h_u vs. M_∞ relationship is clear.

However, the story is quite different for Gage 9016 (Island 14). The STS heating rate comparison plots in Fig. 3.20 show that STS-1, 5 and 7 measured high, whereas STS-2, 3, and 4 measured low. As a matter of fact, the low measurements are of the same order as the measurements of Gage 9014 located on the other side of the ET/SRB attach. As far as comparing with prediction (Figs. A.11a - A.11e), the differences between prediction and measurements are of the same order as Gages 9014 and 9015 for STS-2, 3, 4, and are tremendous for STS-1, 5, and 7 flights. The same observations are made in h_i/h_u vs. M_∞ comparisons given in the above figures. The composite h_i/h_u vs. M_∞ plots in Fig. 8.12 show that although h_i/h_u

correlates with Mach number in the Mach 2 to 4 range, there is a distinct separation between the above two groups of flight. The ratio between the two groups is of the order of 2.5 to 3, and cannot be explained by any conventional wisdom. The IH-97A test, which simulated at least the STS-1 flight condition of the three flights exhibiting high readings in flight, did not yield h_i/h_u values as high as flight, but instead close to the existing h_i/h_u data base. The discrepancies for the Island 14 measurements are dealt with in some detail in a latter subsection.

The analysis of the strong shock interference regions shows that the flight environments are consistently being underpredicted by the existing math model. The deficiencies could be in the prediction of surface roughness, stringer factor, and the omission of temperature mismatch factor in interference heating measurements. It is suggested that the uncertainties in the first two items are nowhere near the underprediction. So every indication points towards inclusion of temperature mismatch.

<u>Gages 9017 and 9022:</u> These gages are located on the bottom centerline of the intertank. The composite heating rate plots for Gage 9017 (Island 12) which compared the measured heating rates for all the flights in Fig. 3.20a show that the magnitudes of heating rates are benign. Since the wind tunnel data base for this region was very sparse, the h_i/h_u data base was updated in Ref. 19 based on the STS-1 flight measurements. Figures A.12a - A.12e compare hot-wall heating rates and h_i/h_u vs. M_∞ from flight with

prediction. The heating peaks are seen to be somewhat underpredicted from flight STS-2 on and are located slightly to the left of the measured peaks. The IH-97A test data (Appendix C) did not uncover anything new, but basically agreed with the original wind tunnel data base. The composite set of derived h_i/h_u vs. M_∞ plots is plotted in Fig. B.13.

Since the data base had been changed based on STS-1 flight, it did not account for α, β effects. This might explain the shifting of the peaks in prediction. Also, since this is a weak interference region mainly caused by the "wrap-around" effects of the SRB shocks, temperature mismatch that has not been considered in the above analysis may exist.

Gage 9022 is located behind Gage 9017. Examination of the composite heating rates for various flights in Fig. 3.23 shows that with the exception of STS-1, the flight heating measurements are benign. Again, the h_i/h_u data base was changed based on STS-1 flight. The result was that the rest of the five flights were consistently overpredicted as seen in Figs. A.16a - A.16f. The same was observed in the h_i/h_u vs. M_∞ comparison in the above figures. There was also a pressure measurement on Gage 9072, located on this island. Because of the changed data base described above, the predicted pressures are consistently higher than measured values in Figs. A.16a - A.16f. The IH-97A test data (Appendix C) shows that there is inconsistency between flight and test data, and that the test data was lower than the flight-reduced data. The deficiencies may be due to temperature mismatch effects. The composite flight-derived h_i/h_u vs. M_∞ plots for all flights (Fig. 3.18) show that with the exception of STS-1, the h_i/h_u levels are at a value of 2 at Mach 3 and 4.

Gage 9021 (Island 20): This gage is located behind the bolt catcher. The composite measured heating rate plots in Fig. 3.2 show that after around 90 secs. into the flight trajectory, aeroheating seems to stop and a different trend in the heating rate begins. This is evident from the comparison of data with prediction in Figs. A.15a - A.15e for $\dot{q}$ vs. t plots and for h_i/h_u vs. M_∞ plots. The IH-97A test (Appendix C) suggests the same kind of inconsistency between flight and wind tunnel data. The composite set of flight-derived h_i/h_u is given in Fig. B.17.

The reason for the above inconsistency may be due to the "wake-like" nature of the flowfield existing behind the bolt catcher, which is hard to scale from tunnel to flight. Moreover, since the heating rates are quite benign in this region, any small errors as a result of scaling will have minimum impact on design.

LH_2 Barrel Section

Gages 9020 (Island 27) and 9023 (Island 26): These two gages are located behind the bipod on the LH_2 barrel section. Both of these gages are affected by the orbiter shock impingement and the interference of the bipod. Examining the composite measured heating rate plots from flights 4 thru 7 (Fig. 3.23b) shows that the measurements are quite consistent in nature. It is also seen that in the subsonic regime, there appears to exist in both of the gages some heating caused by possible instrumentation error due to the "coldness" of the LH_2 tank.

Figures A.17 - A.18 give comparison of flight heating rates with prediction. It should be noted that the above instrumentation errors have not been taken out of the flight data before comparing with the convective prediction. It is seen that the flight is underpredicted to some extent for both the gages. The above figures also compare h_i/h_u vs. M_∞ derived from flight with prediction. Again, similar observations as above are made. The IH-97A test data in Appendix C shows that for STS-4 flight conditions, this test compares well with the previous data base for Gage 9020 but underpredicts somewhat for Gage 9023.

The flight-derived h_i/h_u vs. M_∞ for both of these gages are given in Figs. B.16 and B.19. The consistency of these curves is quite good. The small differences in these curves may be attributed to attitude effects.

Gages 9025 (Island 29) and 9026 (Island 28): These gages are located on the mid-body region of the LH_2 barrel and are affected by the mid-body interference effects. The composite measured heat-transfer rate plots in Figs. 3.24 show that gage 9025 failed in STS-2, 3 and 5 flights. It is not obvious from the STS-4 and 7 plots whether there was influence of the main plume radiation on the measurements or there existed the same kind of instrumentation error, described above. It is seen from Figs. A.19a - A.19e that the flight measurements are underpredicted to some extent. However, the nature of heat-transfer rate distribution in the 80 to 100 secs. range does not seem to be due to aeroheating, but due to something else. The h_i/h_u vs. M_∞ plots in the above figures show similar discrepancies between flight and prediction. The flight-derived h_i/h_u vs. M_∞ plots in Fig. B.20 show that the interference factor ranges from a value of 1 to 2.

Gage 9026 on the other hand, is located on an island on the bottom centerline of the mid-body section. This island also contains a pressure gage, 9074. The composite heating rate plots in Fig. 3.24 show that there was gage failure in STS-2 and that STS-4 measurements are much higher than the rest. This is clear from the comparisons of flight data with prediction in Figs. A.20a - A.20f. It is not clear from these measurements whether main plume radiation or plume-induced convection affected this particular gage. The h_i/h_u vs. M_∞ comparisons in the above figures show similar discrepancies between flight and prediction as in the heating rate comparisons. The pressure measurements in STS-2 and 3 flights given in Fig. 33 are erroneous; however, STS-4, 5, and 7 measurements seem to be in reasonable agreement with prediction. The flight-derived h_i/h_u vs. M_∞ plots are given in Fig. B.21, where it is observed that STS-4 flight is distinctly different from STS-3, 5, and 7 flights.

Gages 9027 (Island 33), 9028 (Island 35), 9030 (Island 34) and 9032 (Island 37): All these gages are located close to the top centerline and near the aft structural ring frame of the LH_2 tank. These gage locations not only are in an interference region, but also experience strong plume-induced heating effects. The plume-induced heating components for these gages have been categorized in Fig. 3.45.

The composite measured heating rate plots for Gage 9027 in Figs. 3.25 show that it measured too low in STS-3 flight. Apart from this flight, the rest of the flights seem to be quite consistent. The effects of plume-induced heating contribution to the measurements have been discussed earlier in the last subsection. Subtracting the plume-induced radiation component given in Fig. 3.45 from the measurements and noting the time when aeroheating stops and plume-induced recirculation begins, the corrected flight heating rates have been plotted against prediction in Figs. A.21a - A.21e. With the exception of STS-3, the comparison is quite reasonable for the OTS configuration. However, after the SRB separation, discrepancy between the data and prediction is observed. Similar observations are made in the h_i/h_u vs. M_∞ plots in the above figures. The IH-97A test data (Appendix C) did not help in clearing this inconsistency. The flight-derived h_i/h_u vs. M_∞ plots given in Fig. B.22 show consistency in their trends with the exception of STS-3 flight.

As far as Gage 9028 is concerned, the composite heating rate plots in Fig. 3.25 show that STS-3 and STS-5 seem to have measured too low and too high, respectively. Both heating rate and h_i/h_u predictions in Figs. A.22a - A.22e show that all the flights with the exception of STS-3 are being underpredicted. The IH-97A test which simulated the exact flight attitudes yielded h_i/h_u's generally higher than the previous data base. However, inclusion of this new h_i/h_u data base will not necessarily predict right magnitudes of heating rates for all the flights. Such discrepancies may be attributed to inadequate simulation of flight in the tunnel. The flight-derived h_i/h_u vs. M_∞ plots are given in Fig. B.23.

Similar observations are made for Gages 9030 and 9032. The composite heating rate plots (Fig. 3.25) for both gages show that flights STS-3 and 4 recorded erroneous data. The comparisons between flight data corrected for plume-induced heating and prediction (Figs. A.24 and A.25) show some underprediction. The same observations are made in the h_i/h_u vs. M_∞ comparisons. Pressure measurements made on Gage 9076 located on Island 34 (containing Gage 9030) and plotted against prediction in Figs. A.24a - A.24e show approximate correlation. The IH-97A test data in Appendix C shows that the h_i/h_u levels are consistent with the previous data base for both gages. The flight-derived h_i/h_u vs. M_∞ in Figs. B.25 and B.27 seem to be consistent with the exception of STS-3 and -4 flights.

<u>Gages 9029 (Island 32) and 9031 (Island 36)</u>: Gage 9029 is located in the bottom centerline ahead of the LH_2 barrel/aft dome

interface, whereas Gage 9031 is located close to the side centerline slightly ahead of the interface. The composite heating rate plots for Gage 9029 in Fig. 3.24 show that with the exception of STS-3, there is good consistency of heating rate histories. It is seen more readily than before that the plume-recirculation heating is more distinct and happens around 100 secs. into the flight trajectory. Comparison of the measured heating rates corrected for plume-induced heating with prediction in Figs. A.23a - A.23e shows that the flight measurements are consistently being underpredicted. The same conclusion is made from the h_i/h_u vs. M_∞ comparisons. The IH-97A test h_i/h_u results (Appendix C) compare well with those in the existing data base. Some of the pressure measurements (Gage 9075) taken on Island 32 seem to be erroneous (Fig. 3.33) since the pressure either does not decay with trajectory time in the right fashion or asymptotically approaches a non-zero value (positive bias) at large times. The flight-derived h_i/h_u's are plotted in Fig. B.24 which shows that with the exception of STS-3, the rest of the flights yield consistent h_i/h_u - Mach number relationships all the way up to the time when plume-induced recirculation begins.

The composite measured heating rate plots (Fig. 3.24) for Gage 9031 show that with the exception of STS-2 and 3, the rest of the measurements are consistent in nature. The comparison of data with prediction for h_i/h_u vs. M_∞ in Figs. A.25a - A.25e shows that the math model somewhat underpredicts the flight-corrected data. The IH-97A test data (Appendix C) shows that the test h_i/h_u's are somewhat higher than the previous data base. The flight-derived h_i/h_u vs. M_∞ plots in Fig. B.23 are quite consistent with the exception of flights 2 and 3.

Protuberance Gage Locations

Gages 9012 and 9038: These gages are located on the LO_2 feedline fairing side and top, respectively. The composite measured heating rate comparisons in Fig. 3.2a show that the time histories are quite consistent with the exception of STS-2 and STS-1 for Gages 9012 and 9038, respectively. This is clearly seen by examining the comparisons of prediction with measured data in Figs. A.27 and A.28 for both gages. It should be noted that the old data base was derived from α, β = 0^o condition in the IH-51B test (Ref. 23) and was considered to be a function of the local Mach number upstream of the fairing. The same conclusions are made from the h_i/h_u comparisons between prediction and flight in the above figures. As far as gage 9012 is concerned, the IH-97A (Appendix C) test yielded h_i/h_u's much lower than both the flight and old h_i/h_u data base. The flight-derived h_i/h_u vs. M_∞ plots in Fig. B.8 show reasonable consistency with the exception of STS-2. For Gage 9038, the comparison of flight and prediction shows that with the exception of STS-1, the flight data is being over-predicted by the math model. The IH-97A (Appendix C) test shows that the test h_i/h_u's are generally lower than flight. The flight-derived composite h_i/h_u vs. M_∞ plots in Fig. B.28 show that with the exception of STS-1, the rest are generally consistent, although there is more scatter in this set than those for Gage 9012.

Gage 9039: This gage is located on the right link of the bipod facing forward to the flow. Even though this gage is located on a cylindrical strut behind the orbiter nose, it does experience the effects of interference from the Orbiter. The composite measured heating rate plots in Fig. 3.26 show reasonable consistency among all the STS flights. Figures A.29a - A.29f compare hot-wall measured heating rates with prediction. In all cases, the math model overpredicts the data. The h_i/h_u comparisons in the above figures show the same trend. It should be noted that h_u in h_i/h_u is the flat-plate value. However, the math model used for the prediction models both h_i and h_u in h_i/h_u for a cylinder, but the procedure converts the h_i/h_u with respect to a flat-plate h_u to maintain consistency in the difinition of h_i/h_u and in the h_i/h_u vs. M_∞ plots for all the DFI locations. It is unfortunate that IH-97A test data (Appendix C) could not provide any data for this gage location because of instrument failure. The flight-derived h_i/h_u vs. M_∞ plots in Fig. B.29 show adequate consistency with the exception of STS-7.

Gage 9041: This gage is located on the bolt catcher and measures the hottest readings of all the gages located on the tank. The composite measured heating rate plots in Fig. A.26 show that the peaks occur around 120 secs. indicating that the flow is laminar. The comparisons of math model and measurements in Figs. A.31a - A.31f show generally an overprediction with the exception of STS-4 and 7 flights, where the measured values around the peaks were higher than prediction. Similar conclusions are made from the h_i/h_u vs. M_∞ comparisons in the above figures. Again, h_u in this h_i/h_u comparison is the flat-plate value on the tank surface. The IH-97A test (Appendix C) data seems to suggest that the h_i/h_u values are closer to the old math model than the flight-reduced data. This may be attributed to Reynolds number under-simulation in the tunnel. The flight-derived h_i/h_u vs. M_∞ in Fig. B.31 are quite consistent.

Gages 9042, 9045, 9046 and 9047: These four gages are located on the RH thrust strut, the aft diagonal strut, the LH vertical strut cable-tray and the cross-beam cable-tray, respectively. The composite measured heating rate plots are given in Fig. 3.27 for all the four gages. Since the wind tunnel data base for these locations was derived from only one freestream Mach number (M_∞ = 8) and one set of α, β ($\alpha = 0^\circ$, $\beta = 0^\circ$) conditions in Tests IH-33 and IH-43 at CALSPAN (Refs. 25 and 26), the flight data would really serve as the final data base. Some of the measurements for these gages are in error and are indicated in Table 3.1.

Since these gages are located on the forward faces of the struts, they do not experience the tremendous effects of plume-induced heating. Although some effects may exist, they are considered insignificant and have been ignored in this analysis. As reported in Ref. 19, the h_i/h_u data base for these gages was updated based on the STS-1 flight. Obviously, no α, β effects could be incorporated in the data base from only one set of flight measurements. The comparison of flight and predicted heating rates for Gage 9042 in Figs. A.32a - A.32f shows that underprediction persists. The same is true for the h_i/h_u vs. M_∞ comparisons given in the above figures. No IH-97A test data (Appendix C) exists for this gage to compare with flight. The flight-derived h_i/h_u vs. M_∞ plots in Fig. B.32 show reasonable consistency. Similar conclusions are made for Gage 9045 in the measured heating rate and flight h_i/h_u comparisons with prediction in Figs. A.34a - A.34f. The IH97A test data (Appendix C) measured lower than flight for the first four flights. No explanation exists at present to explain this anomaly. The flight-derived h_i/h_u data, however, is reasonably consistent, as seen in Fig. B.34.

As far as Gage 9046 is concerned, the comparison of flight data with predicted heating rates is good, as seen in Figs. A.35a - A.35f. The flight gages failed in STS-2, 5, and 7. The same observations are made in h_i/h_u vs. M_∞ comparisons in these figures. Again, the IH-97A test data (Appendix C) did not compare well with flight. The h_i/h_u data seems to drop off after about Mach 3, which suggests that the interference decreases with increasing freestream Mach number. This does not happen in flight. A pressure gage (Gage 9079) located near the calorimeter was connected in flight. However, the flight and prediction don't compare well, as seen in the above figures. The reason may be the pressure math model for this gage location. The flight derived h_i/h_u vs. M_∞ plots in Fig. B.35 are quite consistent with the exception of the flights for which the gages failed.

Gage 9047 failed in STS-5 flight and gave erroneous readings beyond 100 secs. in STS-2 (see Fig. 3.27). The h_i/h_u data base was modified based on STS-1 flight. The flight data comparisons with prediction in Figs. A.36a - A.36f show that there was considerable underprediction. The same trend was noticed in the h_i/h_u vs. M_∞ comparison plots. The IH-97A test (Appendix C), however, seemed to yield a h_i/h_u trend similar to flight. The pressure measurement on Gage 9079 did not compare well with the math model, as seen in the above figures. The discrepancies are similar to those observed before for Gage 9079. The flight-derived h_i/h_u vs. M_∞ plots in Fig. B.36 are reasonably consistent.

Gages 9040 and 9043: These gages are located on the cable-tray supports at the aft-section of the tank. The measurements were taken only on STS-5 and -7 flights and are consistent, as seen in Fig. 3.28. Gage 9040 failed in STS-7. The comparison of flight data with math model prediction is quite good, as seen in Figs. A.30a and A.33. The flight-derived h_i/h_u vs. M_∞ plots in Figs. B.30 and B.33 also appear to be reasonable.

3.4.1.2 SPECIAL ANALYSIS OF A FEW GAGES

A few gages located in the interference region of the ET surface exhibited unreasonable magnitudes and trends in the measured data. This section examines these data from a slightly different viewpoint in order to identify and discard anomalous data. The candidate gages examined were Island 14 (Gage 9016) and Island 17

(Gages 9013, 9018 and 9019).

A. Validity of STS 1-7 Data for Island 14

The following questions were addressed to determine the validity of measurements on Island 14.

A.1. Are both high and low measurements possible?

- No wind tunnel or flight data supports a factor of 3 difference in heating. The surrounding gages such as Gage 9015 (Island 15) and Gage 9014 (Island 16) show no such jump. Run 96 of IH-97B (Ref. 22) shows a slight jump, but the factor is less than 1.5 (See Fig. 3.62). The wind tunnel data for Island 16 in Fig. 3.63 shows a corresponding jump and the "jumped" readings agree with low (STS - 2, 3, and 4) Island 14 data.

- The sensors show a tendency to read high for a failed-but-still-reading gage. The laboratory tests show that such high factors are possible. Flight data analysis at other sensor locations also shows probable high readings.

From the above considerations it may be said that high readings for Island 14 are suspect.

A.2. Would a sweeping shock account for high readings?

Wind tunnel data shows symmetrical heating around the side centerline locations. It has been shown that Island 16 did not have high readings for STS-1, 5, and 7. Island 14 data, on the other hand, exhibited high readings during the entire turbulent heating regime. No sudden jumps in heat flux are present. Therefore, the sweeping shock scenario may be considered invalid.

INTERTANK DF 1 OTS CONFIGURATION
HU FROM TEST DATA
MODEL S-B GAGE 5036
DFI SENSOR TO7R9016
X/L = .333 PHI = 251.40
MACH NO. 4.02 TLM = 0

ISLAND 14 RUN 96

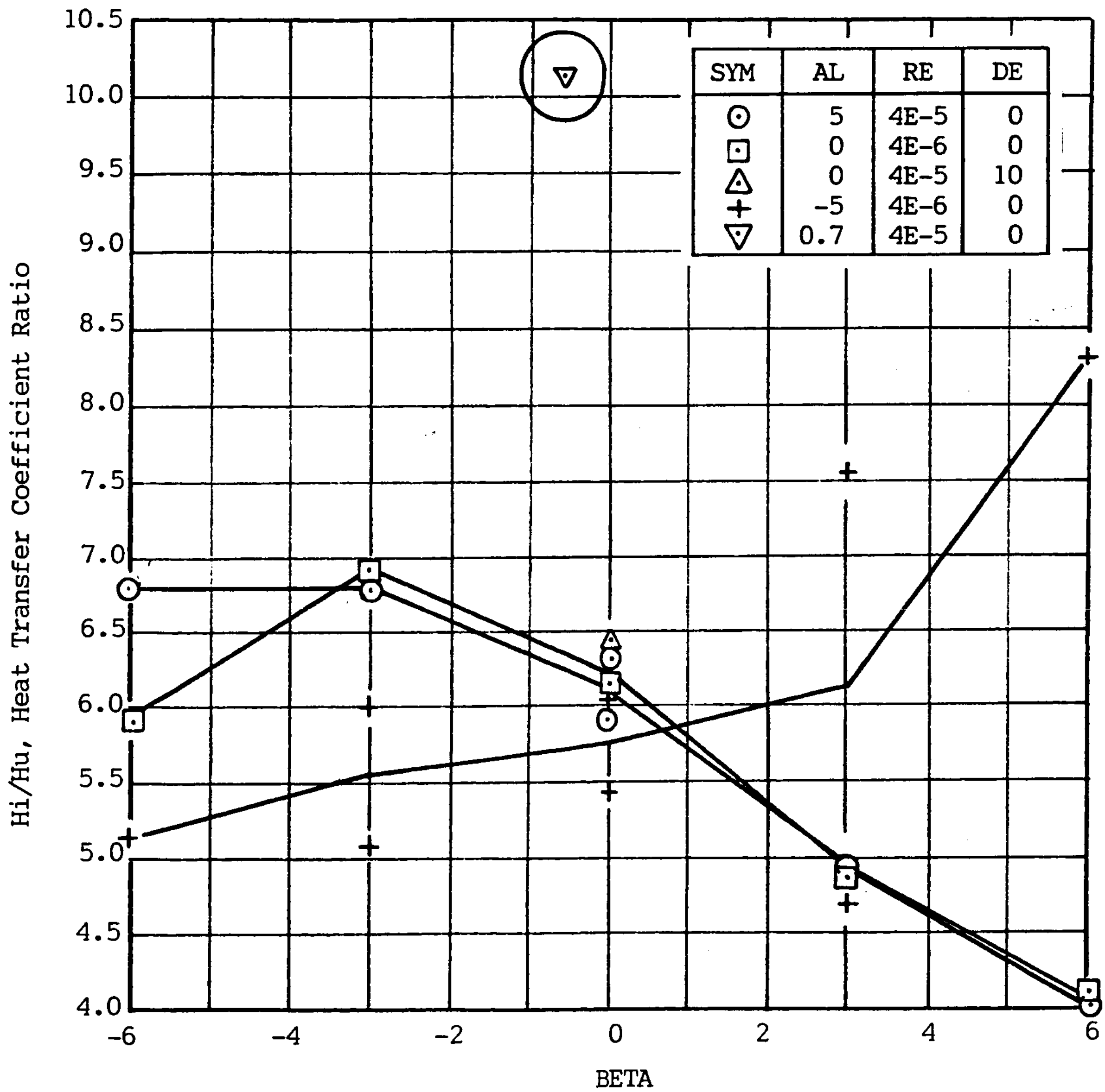

Fig. 3.62 Hi/Hu Data Base for Island 14

Intertank DFI   OTS Config.
H_U From Test Data
Model S-B Gage 5038   DFI Sensor T07R9014
X/L =.333   PHI = 288.60
Mach No. 4.02   TLM = 0

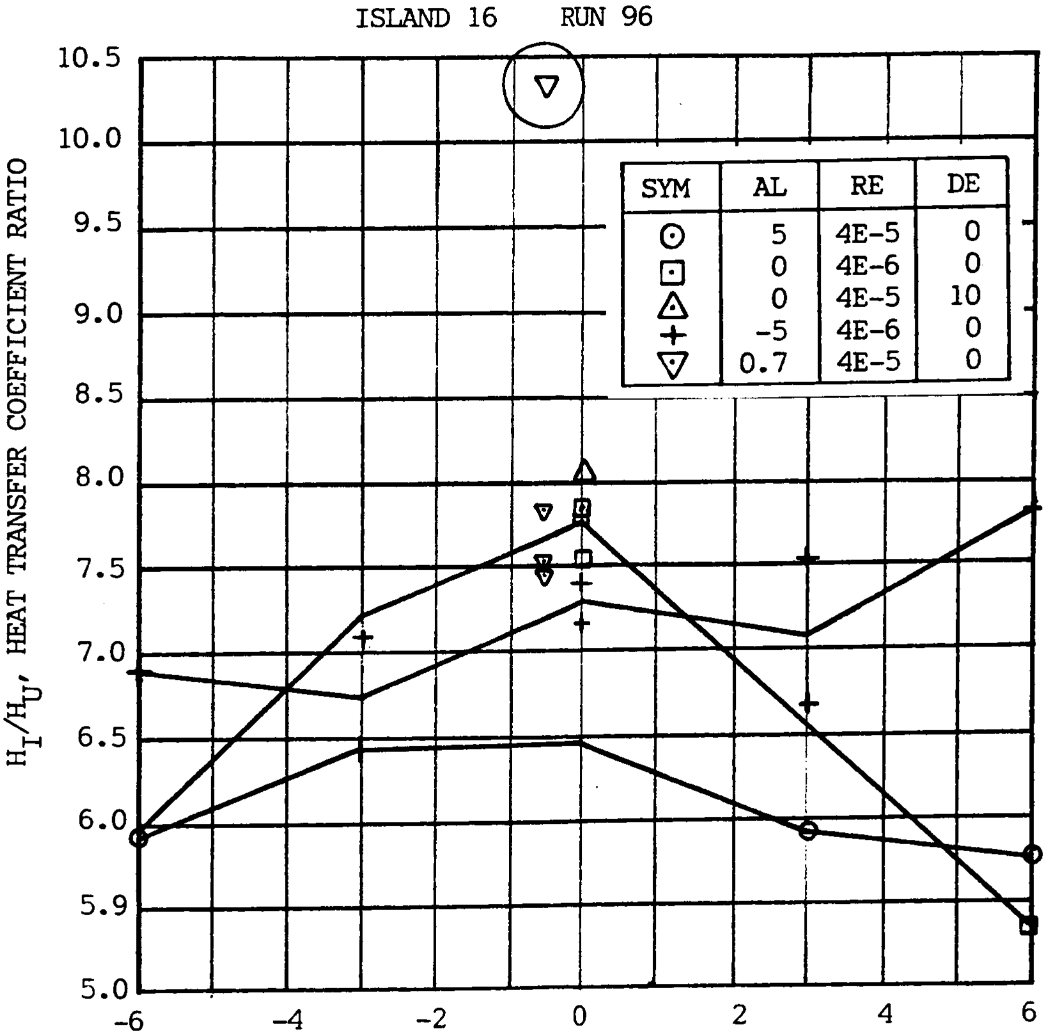

Fig. 3.63 H_i/H_u Data Base for Island 16

A.3. Are high readings early in flight possible?

It is seen that at 80 secs. heating is inordinately high for STS-1, 5, and 7. The required h_i/h_u has to approach 10 at $M_\infty = 2.3$ (t = 80 secs.). However, stagnating the flow behind the SRB conical shock at $M_\infty = 2.3$ would lead to a

$$\frac{h_i}{h_u} = \left(\frac{p_{t_2}}{p_\infty}\right)^{0.8} = 4.7$$

Thus, high readings at 80 secs. are considered unreasonable.

A.4. Do pressure data support high readings?

Wind tunnel pressure measurements from Test IH-11 (Ref. 24) provide pressure data for side centerline. This data supports the Island 15 measurements. No conceivable mechanism exists for getting higher local pressure at the Island 14 location. Therefore, high readings are felt to be improbable.

A.5. Do flight data at BSM firing support high or low readings?

The heating "spikes" occurring because of the BSM plume impingement shows interesting trends. The six figures (Figs. 3.64 - 3.69) show unreasonably high readings on Island 14. Therefore, the majority of plume impingement data implies that high readings are erroneous.

A.6. If high Island 14 data for STS-1, 5, and 7 were discarded, would the data look better?

Low data from STS-2, 3, and 4 for Island 14 superimposed on the entire Island 16 data set plotted in the form of

ORIGINAL PAGE IS OF POOR QUALITY

STS-1
@ TIME = 133 sec
α = 3.7
β = .6

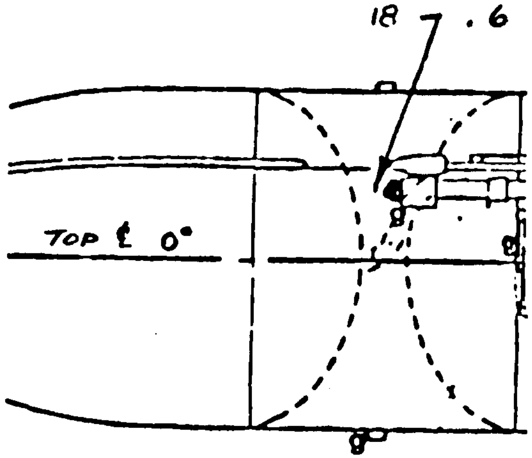

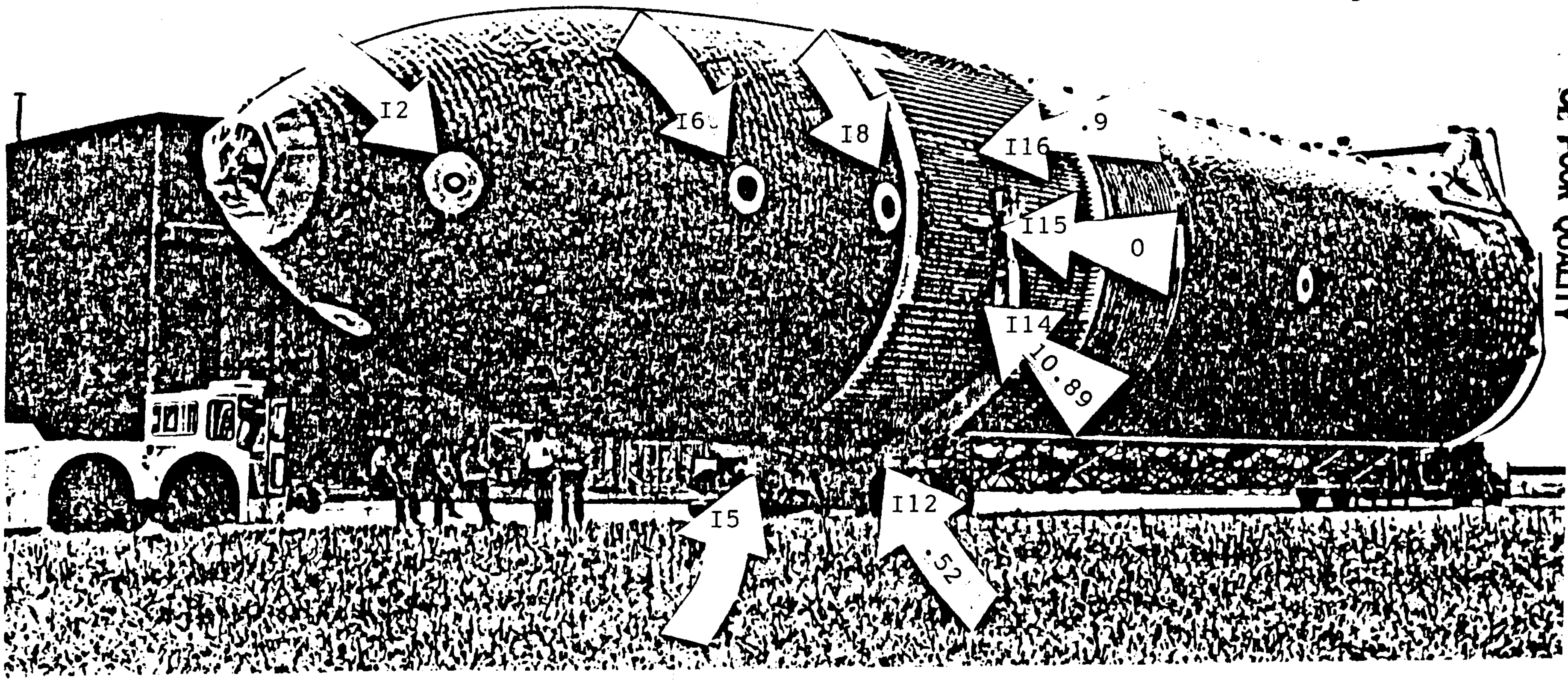

Fig. 3.64

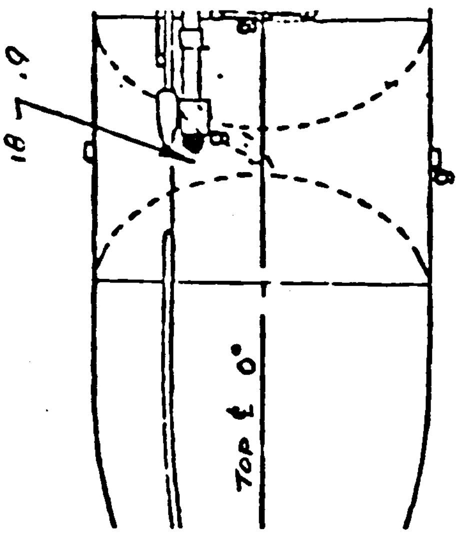

STS-2
@ TIME = 132 sec
α = 4.2
β = .9

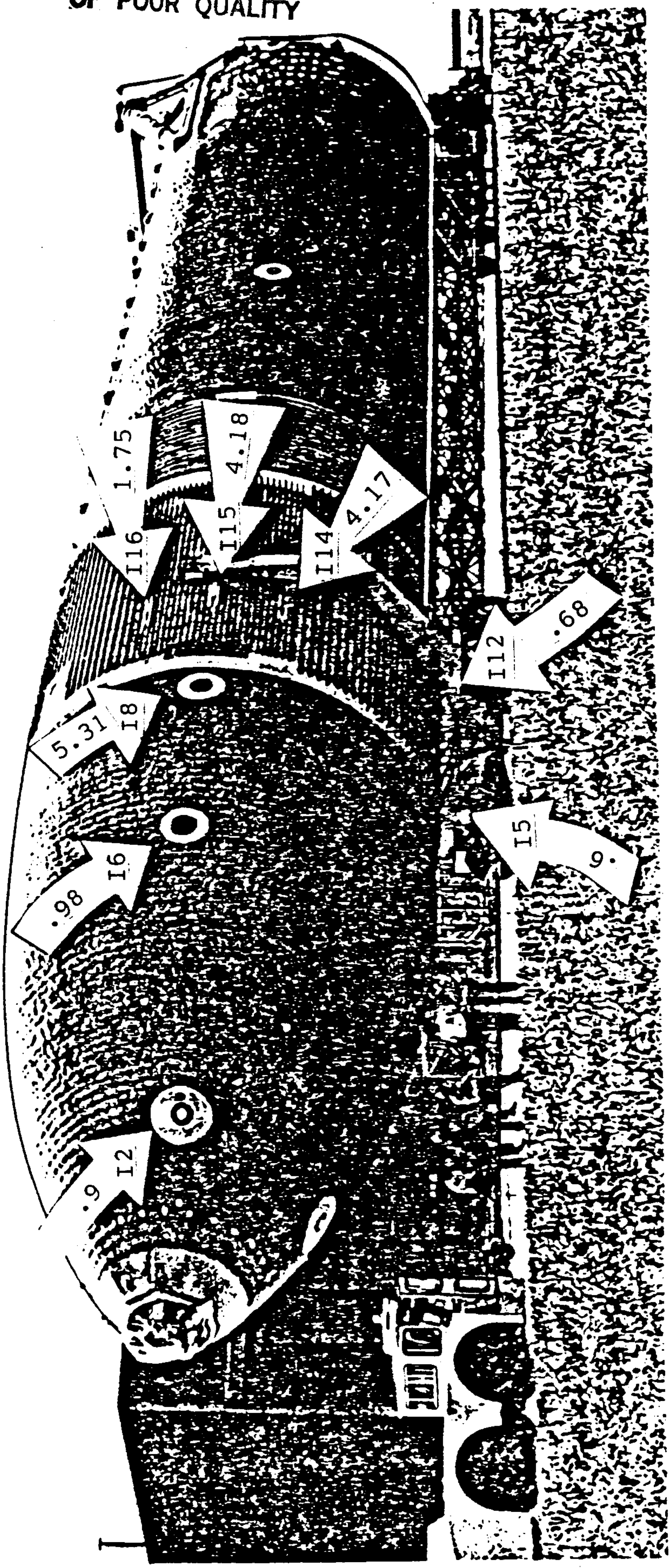

Fig. 3.65

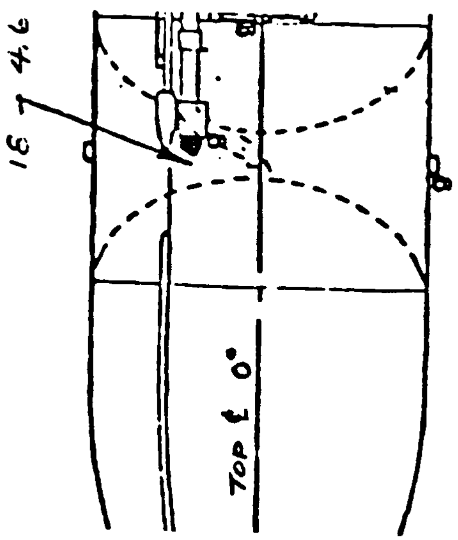

STS-3
@ TIME = 130 sec
α = -.4
β = .8

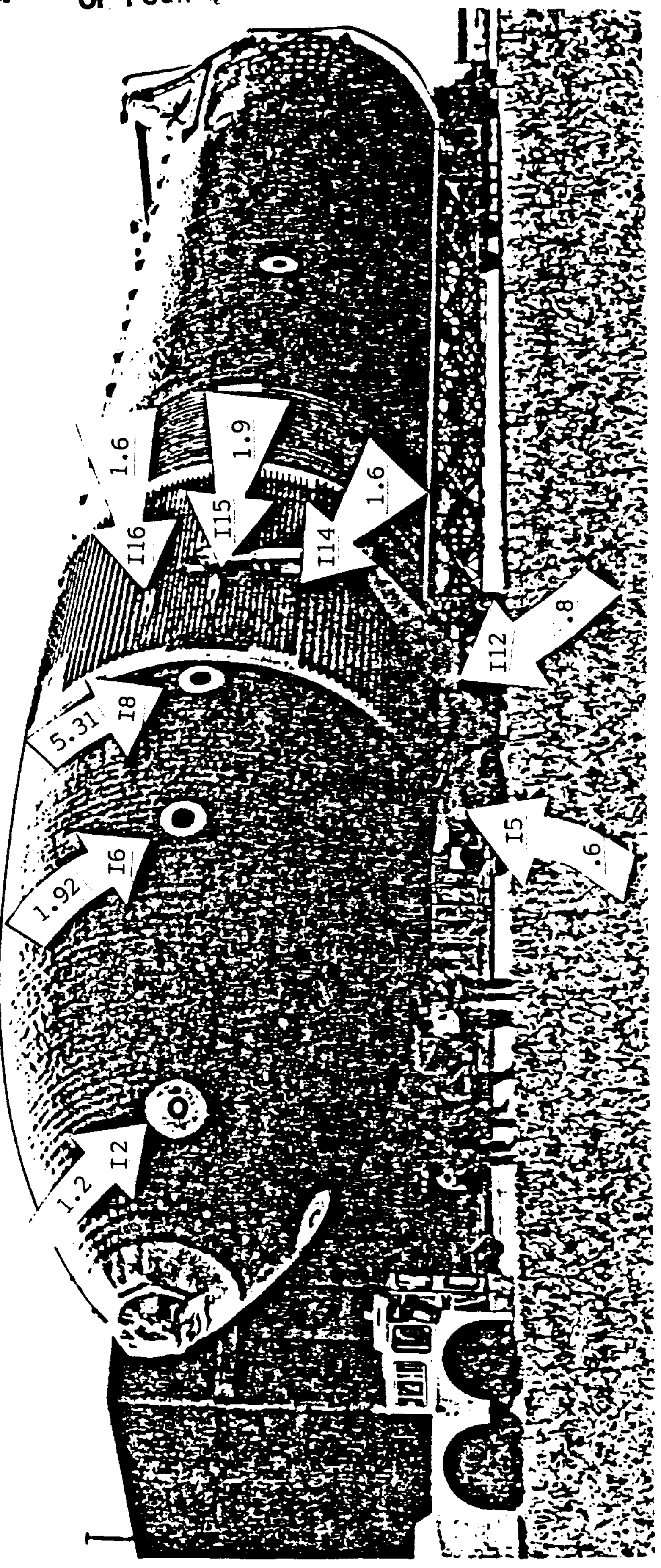

Fig. 3.66

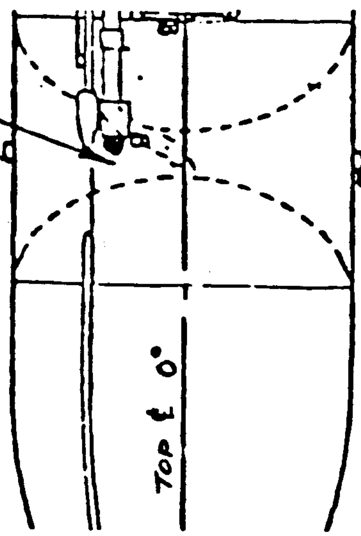

STS-4
@ TIME = 134 sec
α = -2
β = .3

ORIGINAL PAGE IS
OF POOR QUALITY

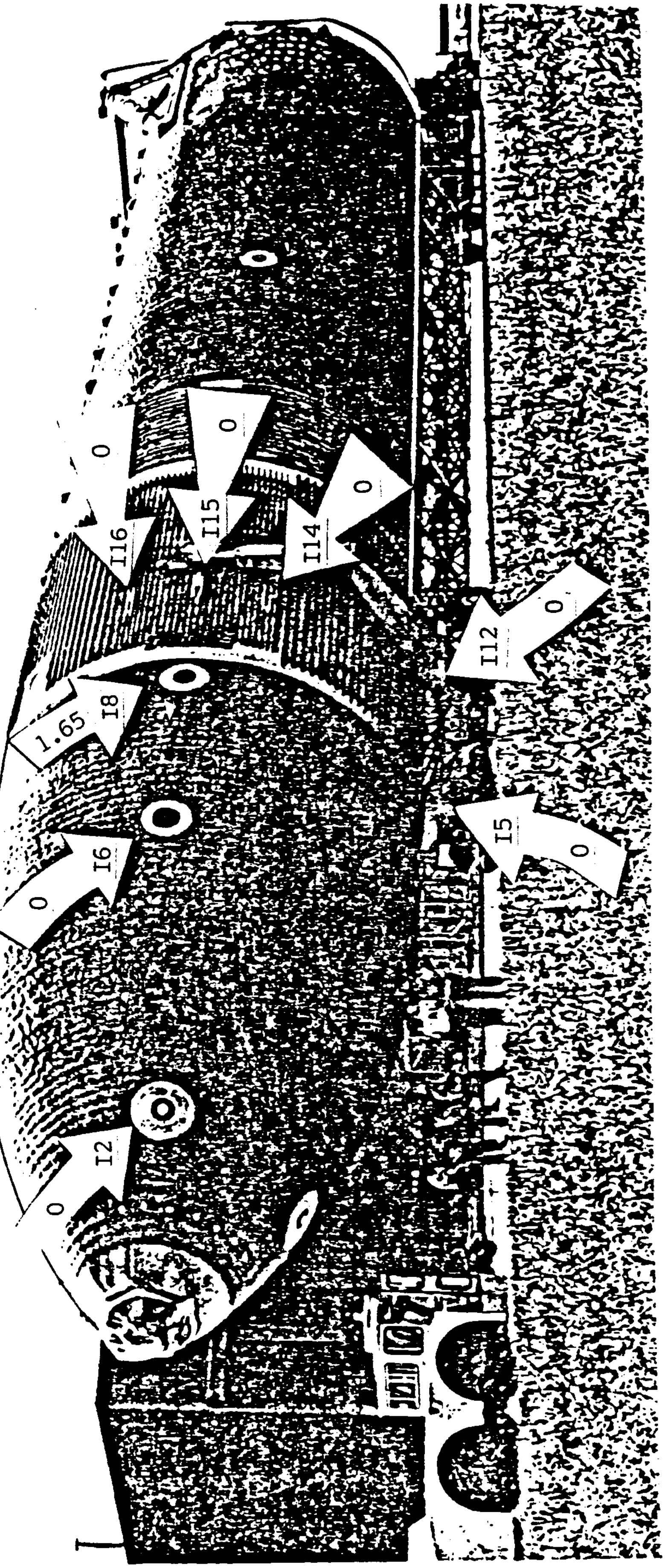

Fig. 3.67

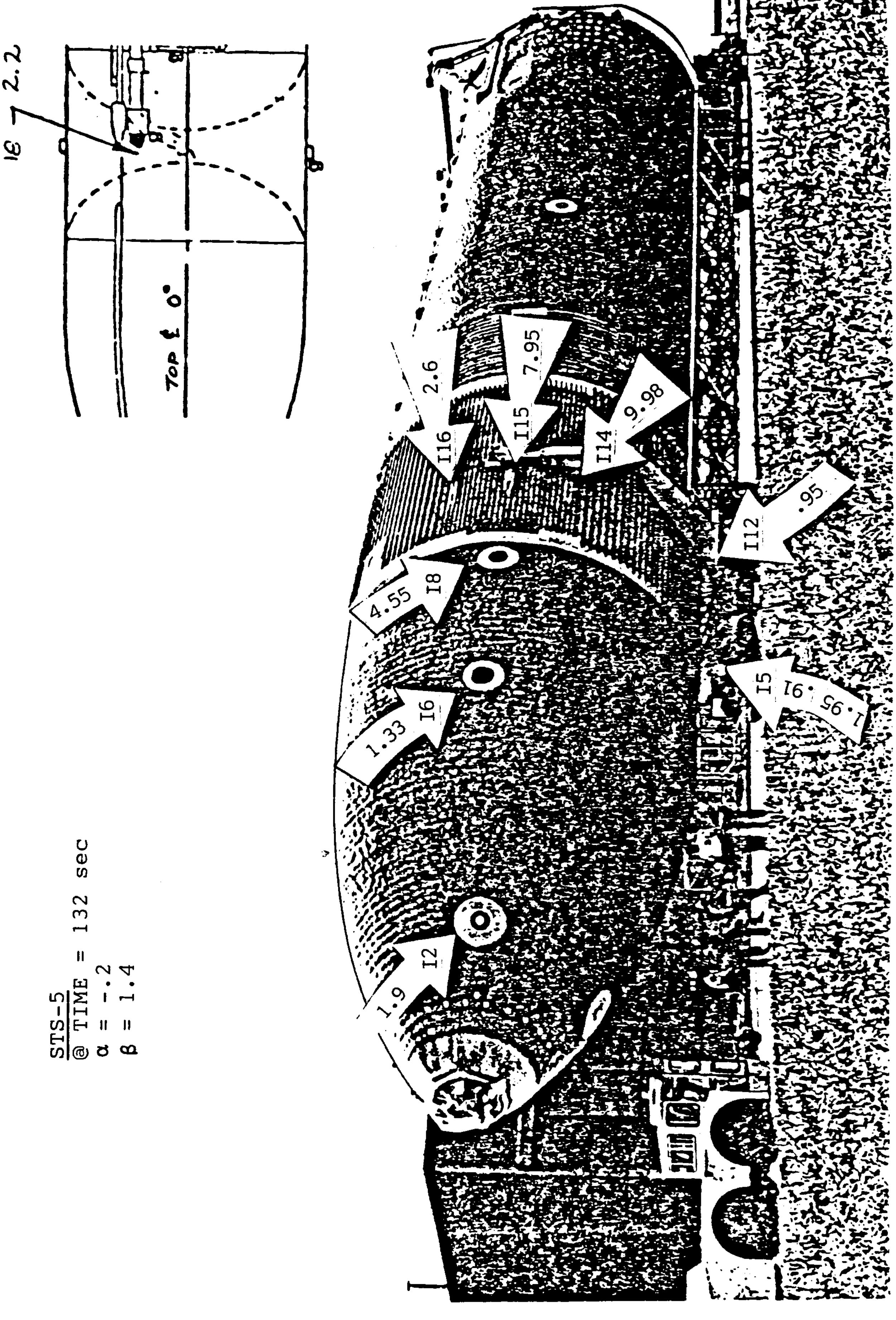
18
2.2
TOP ℄ 0°
STS-5
@ TIME = 132 sec
α = -.2
β = 1.4
1.9
I2
1.33
I6
4.55
I8
2.6
I16
7.95
I15
9.98
I14
.95
I12
I5
.91
1.95

Fig. 3.68

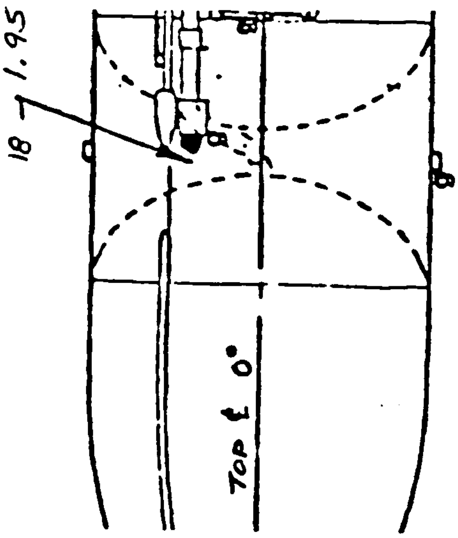

STS-7
@ TIME = 129 sec
α = -.1
β = .5

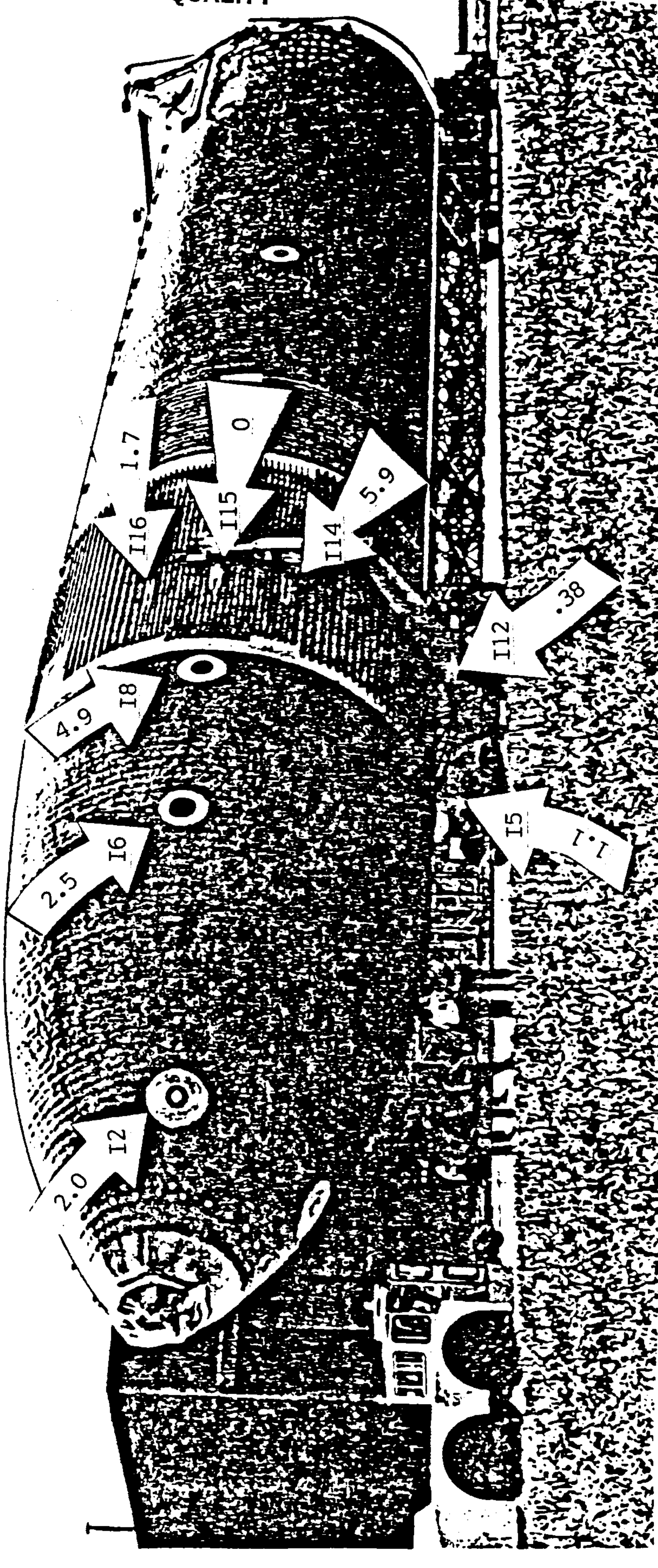

Fig. 3.69

St_∞ vs. Re_∞/ft in Fig. 3.70 looks to be an excellent match. The same conclusion would be reached by examining St* vs. Re* data plots for Island 14 and 16 in Figs. 3.86 and 3.88, respectively.

Based on the preponderance of evidence, the high measurements on island 14 for STS-1, 5, and 7 should be discarded as erroneous data due to faulty sensors.

B. Validity of STS 1-7 Data for Island 17

The heating measurements on the Island 17 location have been presented earlier in this report and were described to be partially valid. This analysis discussed the validity of the measurements of various gages on Island 17 in more detail by addressing the following questions.

B.1 Are both high and low measurements possible?

- From the aeroheating indicator plots in Fig. 3.2 we see that both the $\dot{q}_{max}$ ratio and the heating load ratio on a 1-ft radius sphere has a maximum value of approximately 1.4. It is further seen that heating increased with successive missions. This trend does not explain the measurement anomaly observed in Gages 9018 and 9013.

- No wind tunnel data supports a factor of 3 or more between the low and high measurements observed for STS-5 in both gage 9018 and 9013. These readings are suspect.

B.2 Would a sweeping shock account for high readings?

Gages 9018 and 9013 show high readings consistently in STS-5 (Figs. 3.72 and 3.73) during the entire heating regime thereby

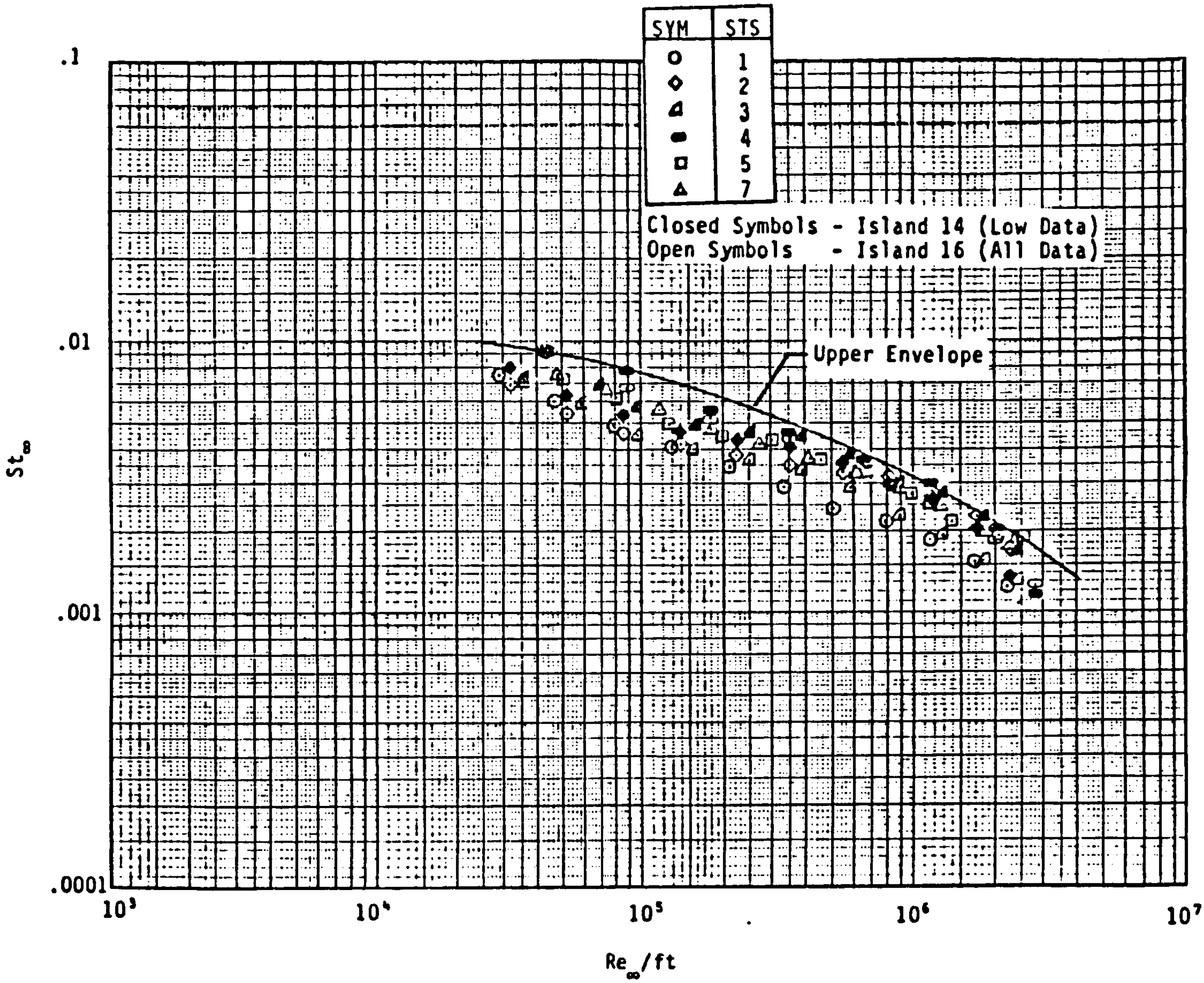

Fig. 3.70 Stanton number as a Function of Reynolds Number for all of Island 16 Data and the low Island 14 Data

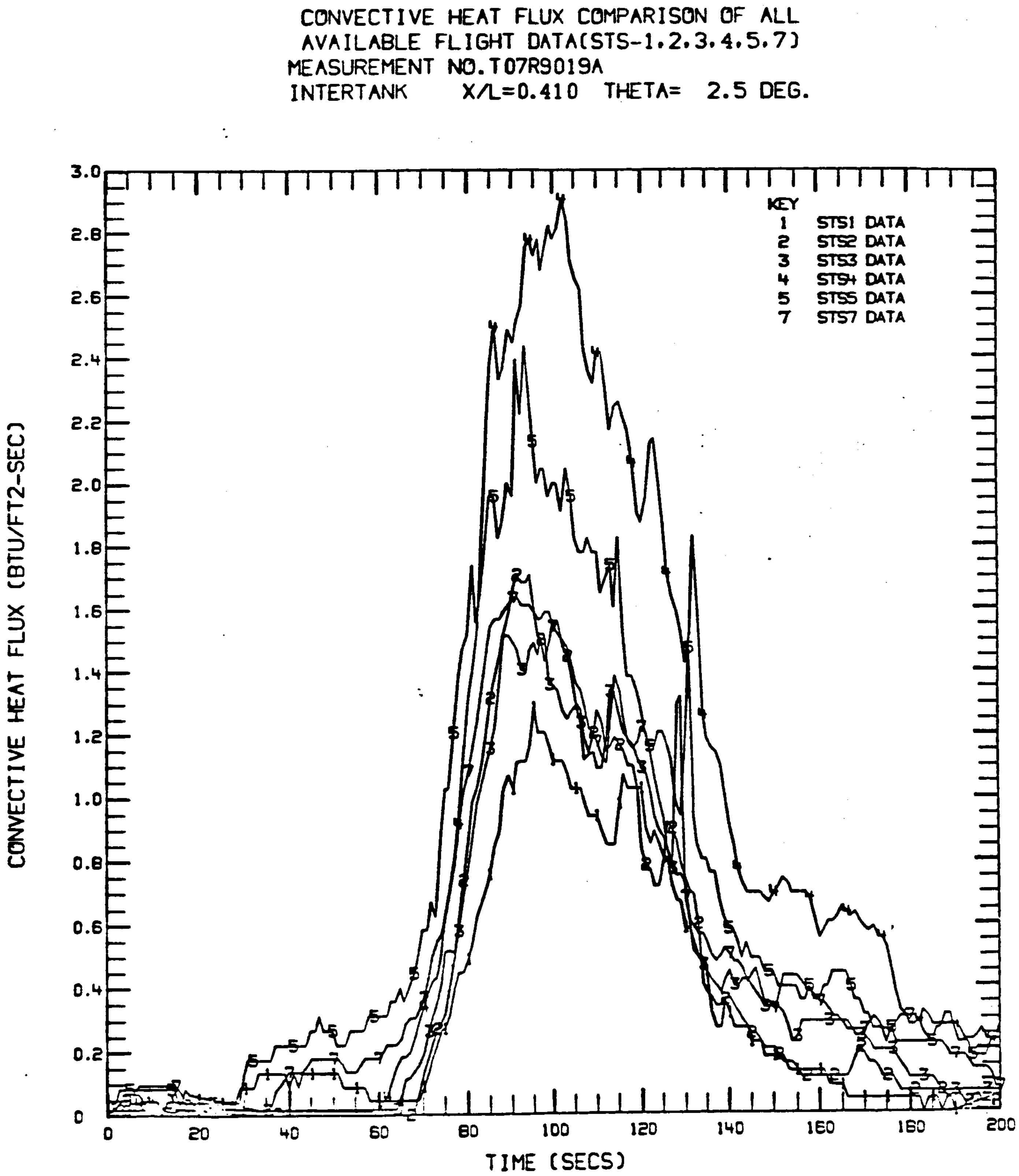

Fig. 3.71 Composite Heating Rate Plot for Island 17(1)

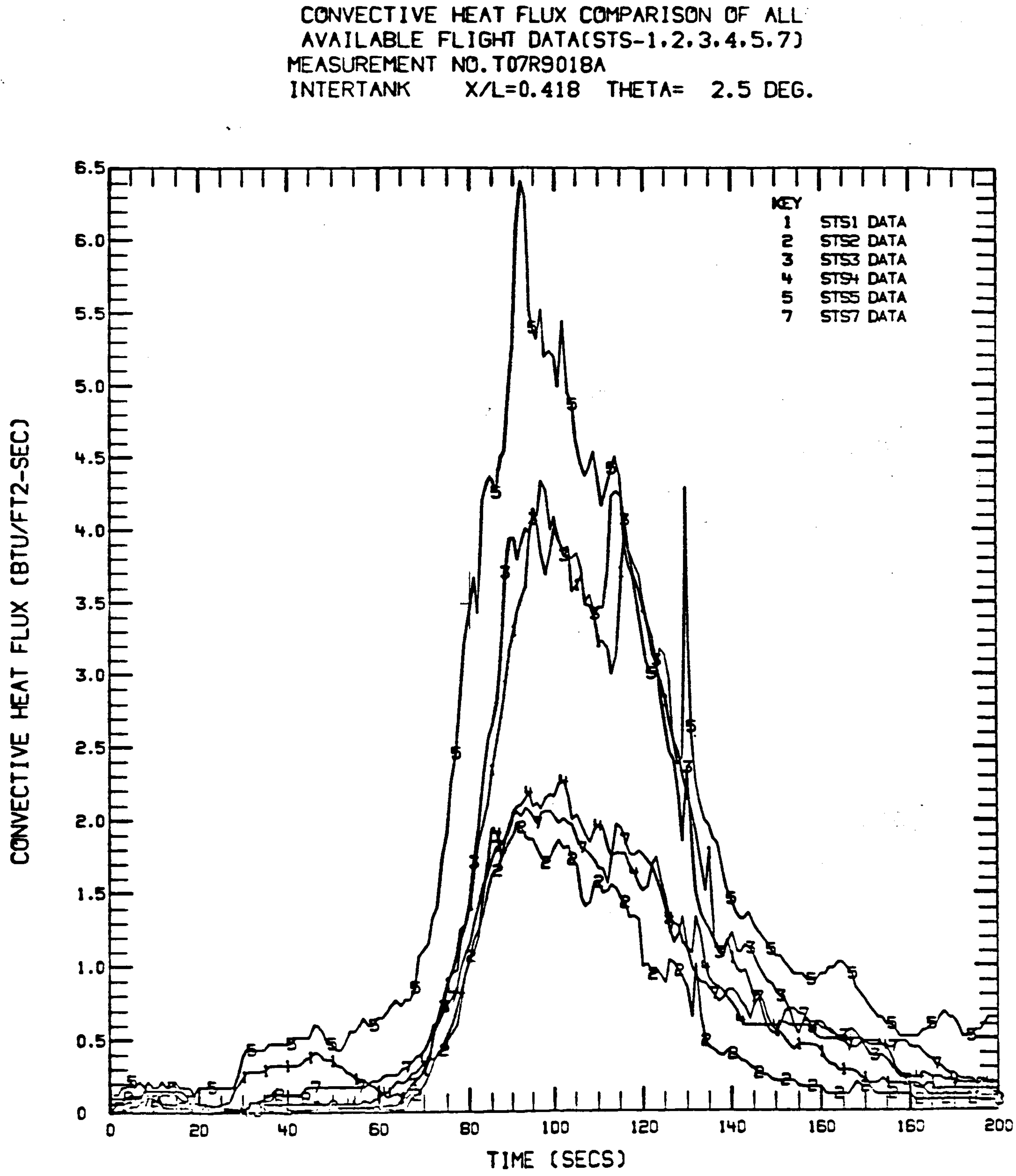

Fig. 3.72 Composite Heating Rate Plot for Island 17(2)

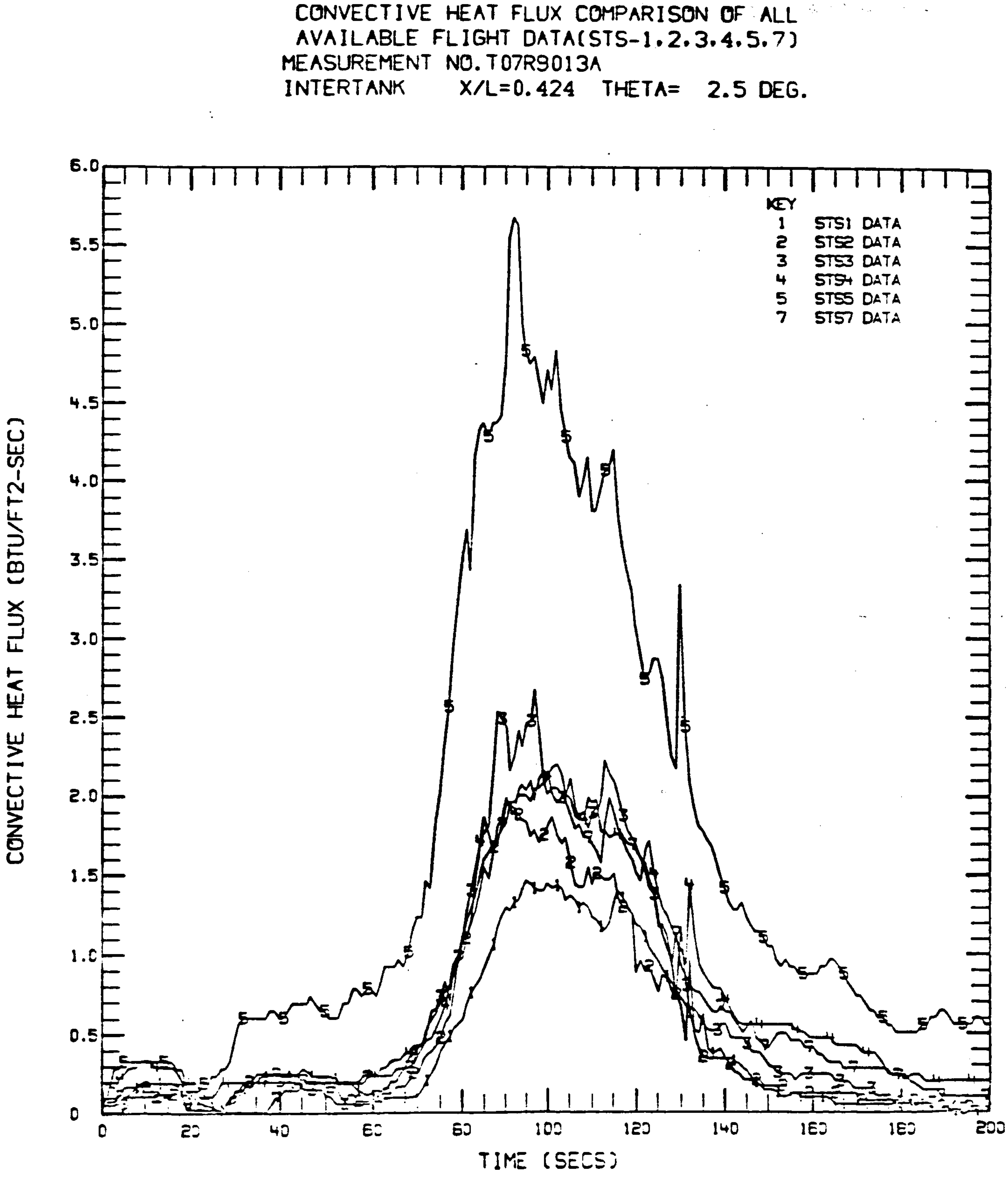

Fig. 3.73 Composite Heating Rate Plot for Island 17(3)

showing no jumps in heat flux because of shock-sweeping. The same was observed for Gage 9018 in STS-1 and 3 missions excepting a small jump at t = 120 secs. possibly because of sweeping of a shock from the LO_2 feedline fairing. Thus, a sweeping shock scenario is considered invalid.

B.3 Do pressure data support high readings?

A pressure gage (Gage 9071) located between Gages 9018 and 9013 measures very consistent pressure readings in all the flights except STS-7.

At t = 100 secs., for STS-7

$$\left(\frac{p_i}{p_u}\right) \text{(from flight)} = \frac{1.3 \times 144}{25.2} = 7.4$$

$$\left(\frac{h_i}{h_u}\right) \text{(from coorelation)} = \left(\frac{p_i}{p_u}\right)^{0.8} = 4.97$$

But, $\left(\frac{h_i}{h_u}\right)$ (from flight) = 11.9

for Gage 9018

The discrepancies will be even higher if we consider the peak heating rates. Therefore, STS-5 heating measurements both for Gages 9018 and 9013 are considered inaccurate.

B.4 Does "temperature mismatch" explain any of the high readings?

If there were temperature mismatch effects in the middle and aft gages for STS-5 because the shock impingement occurred aft of Island 17, then it should also affect the front gage. However, the measurements compare well with the wind tunnel data base, as seen in Fig. A.14e, indicating that no temperature mismatch correction of the magnitude required for STS-5 Gage 9018 is necessary. The same logic applies to the STS-1 and STS-3 measurement for Gage 9018.

B.5 If the high Island 17 data were discarded, would the data look better?

If one discards the high data from Gages 9018 and 9013 measurements in STS-5 and Gage 9018 measurements in STS-1 and 3 (Fig. 3.21), the rest of the data superimposed either in the St* vs. Re* correlation or the h_i/h_u vs. M_∞ correlation would be very consistent.

3.4.1.3 ANOTHER ANALYSIS APPROACH

Another accepted procedure in the literature is to correlate heat-transfer data with the use of Stanton number and Reynolds number. It was discussed before that the heat-transfer data obtained from the wind tunnel was correlated in terms of the ratio of heat-transfer coefficient to a reference value of heat-transfer coefficient vs. running length for undisturbed regions of the ET. The mathematical model derived from these measurements was used to calculate heat-transfer quantities in flight both for design and flight evaluation. In the interference regions of the ET, however, a dimensionless quantity called the interference factor was derived from the wind tunnel data and scaled to flight only as a function of freestream Mach number. In this situation it was assumed that the wind tunnel simulated (to a large extent) the Reynolds numbers experienced in flight at least in the peak heating regime. So, in order to explain possible deficiencies in the above methodology, another analysis was examined.

The measurements made in the OFT flights were correlated in the previous subsection in Figs. 3.56 - 3.61 for the ET ogive, but the data did not collapse at any of the freestream Mach numbers examined, the reason being that the effects of angle of attack were not taken out of the data. So, in order to collapse the heat transfer data on the ET ogive from various flights, flight Stanton number was correlated with Reynolds number. The rationale behind this effort in collapsing the data is to eliminate questionable measurements from the data base, increase confidence in the rest of the data, identify the various flow regimes, and define transition criterion based on flight measurements. There are various ways of correlating the heat transfer data in order to accomplish the above objectives.

One simple way of correlating the Stanton number data was to assemble and plot Stanton number vs. Reynolds number based on the freestream quantities. This was accomplished by the REMTECH personnel for all the DFI gages documented in Appendix D. In addition to the flight data in each plot, the wind-tunnel data from Test IH-97 were also plotted for comparison. It was pointed out in this work that this data did not consider the effects of angle-of-attack. The edge Stanton number was then correlated with edge Reynolds number. A composite plot for all the ogive Islands in STS-5 was accomplished using the edge quantities and reducing the Stanton number data on a flat plate basis, as shown in Fig. 3.74. A similar effort was undertaken for the same flight using reference "star" quantities to generate Fig. 3.75. Also plotted in the above two figures are calculations based on Spalding-Chi theory. The theoretical curves do not collapse in the correlations using edge quantities, whereas they collapse better in the correlations using the "star" quantities. It should be noted here that the flight data plotted both in Figs. 3.74 and 3.75 have been corrected for temperature mismatch.

The "star" quantities for Stanton number and Reynolds number were calculated for all the gages in all the DFI flights. The measured data for some of the gages observed to be outside the band of plotted data were suppressed. The peaks around the BSM firing period were also suppressed from the data by eliminating a few seconds of the data and fairing the data. The data was plotted up to 180 secs. into the flight. The resulting composite set of $St^*/N_T^{**.2}$ vs. Re^* (N_T = Turbulent Multiplication Factor) curves is given in Fig. 3.76. In Fig. 3.77, however, only the data pertaining to Islands 1 and 2, both located at X_T = 467.4 in., were plotted. This was done to take out the N_T dependence of the Stanton number data, since N_T depends strongly on the X_T location and weakly on α, β effects. A similar plot (Fig. 3.78) was made for Islands 5 and 6 located at X_T = 672.5 in. In both of these figures, the data trend is similar. The scatter in the laminar regime

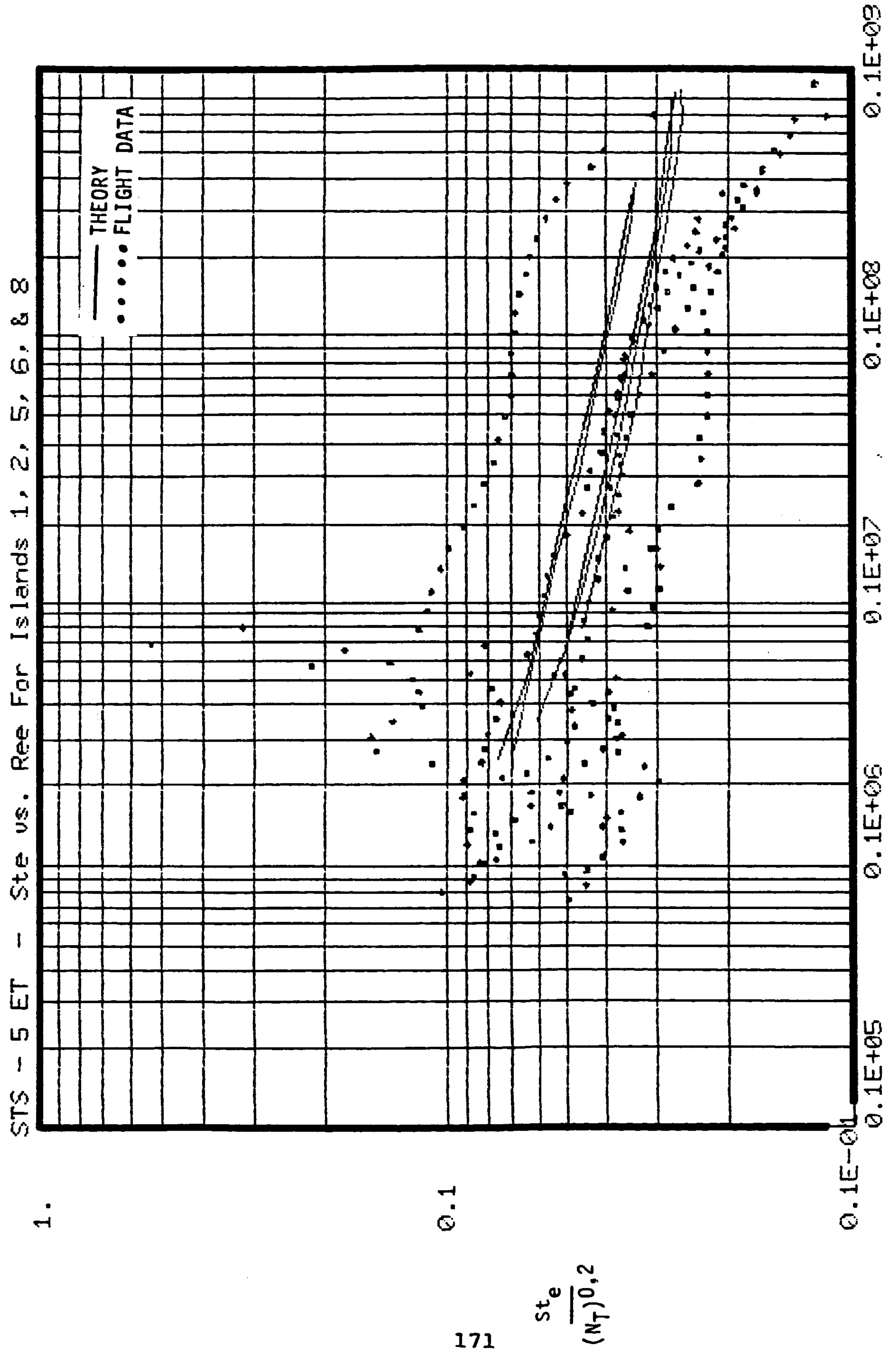

Fig. 3.74 Composite Flat Plate St_e vs. Re_e Plot For ET Ogive Islands In STS-5 Flight

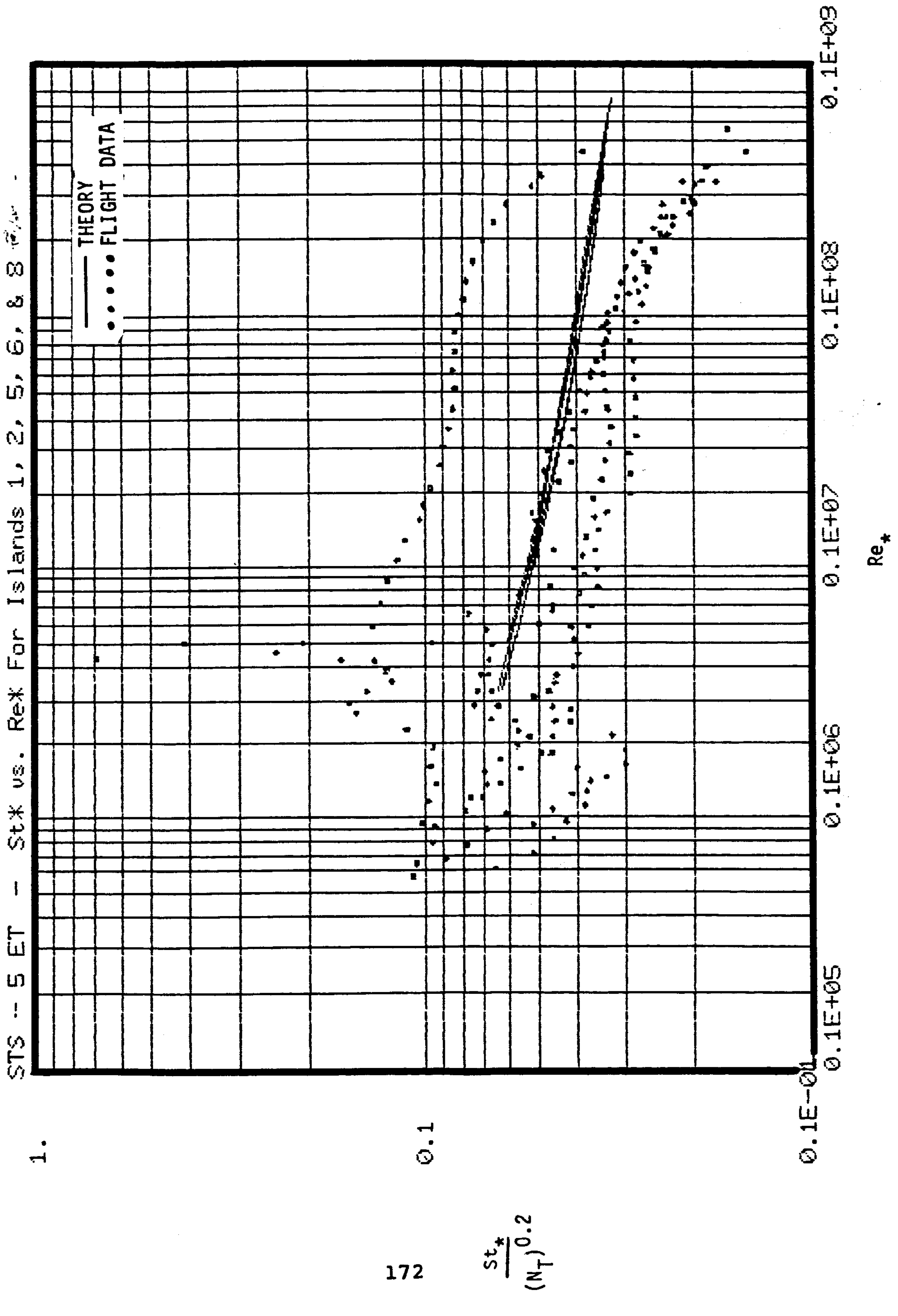

Fig. 3.75 Composite Flat Plate St* vs. Re* Plot For ET Ogive Islands In STS-5 Flight

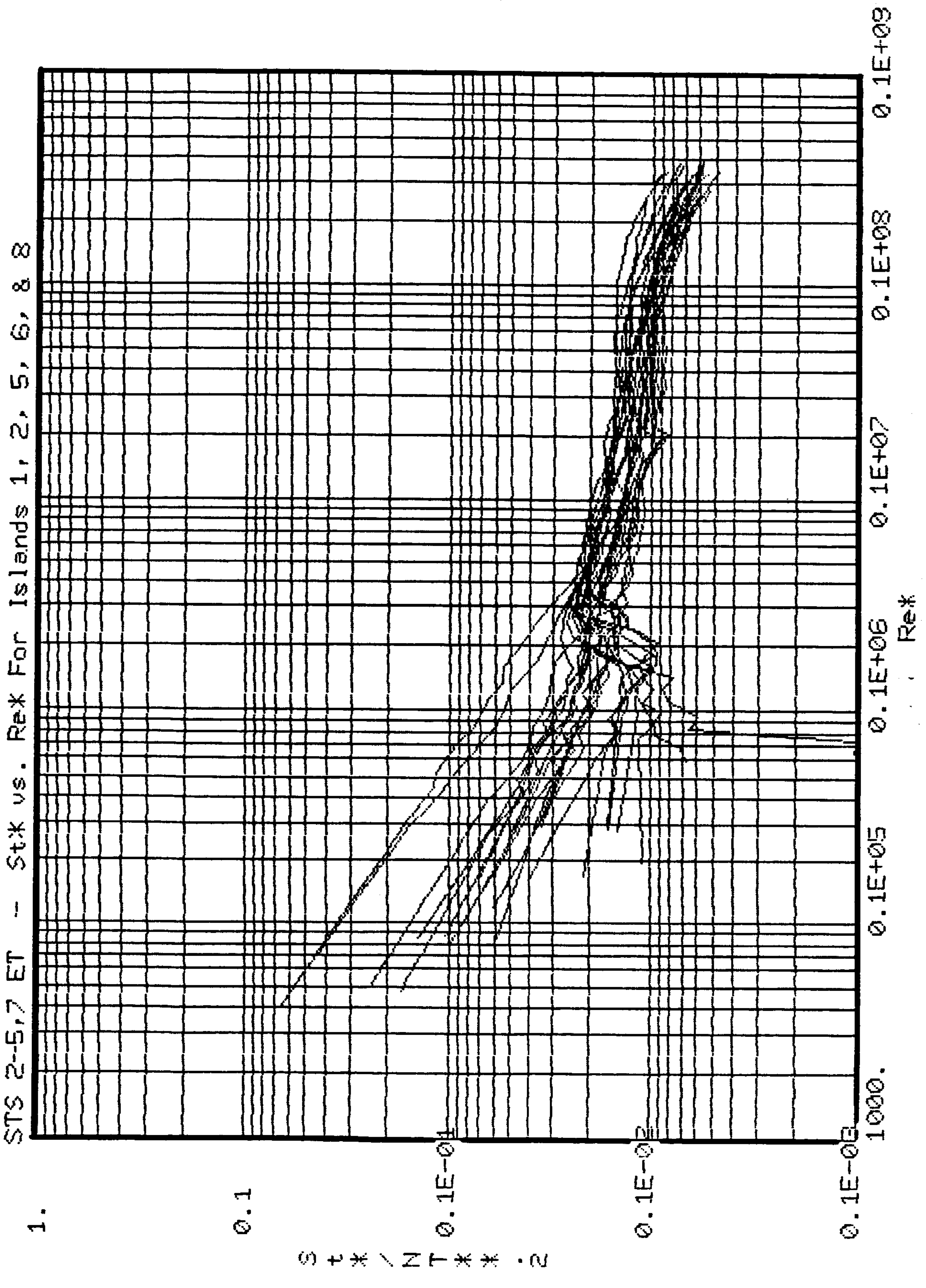

Fig. 3.76 Composite Flat-Plate St* vs. Re* Plots for All but Questionable LO_2 Gages for All STS DFI Flights

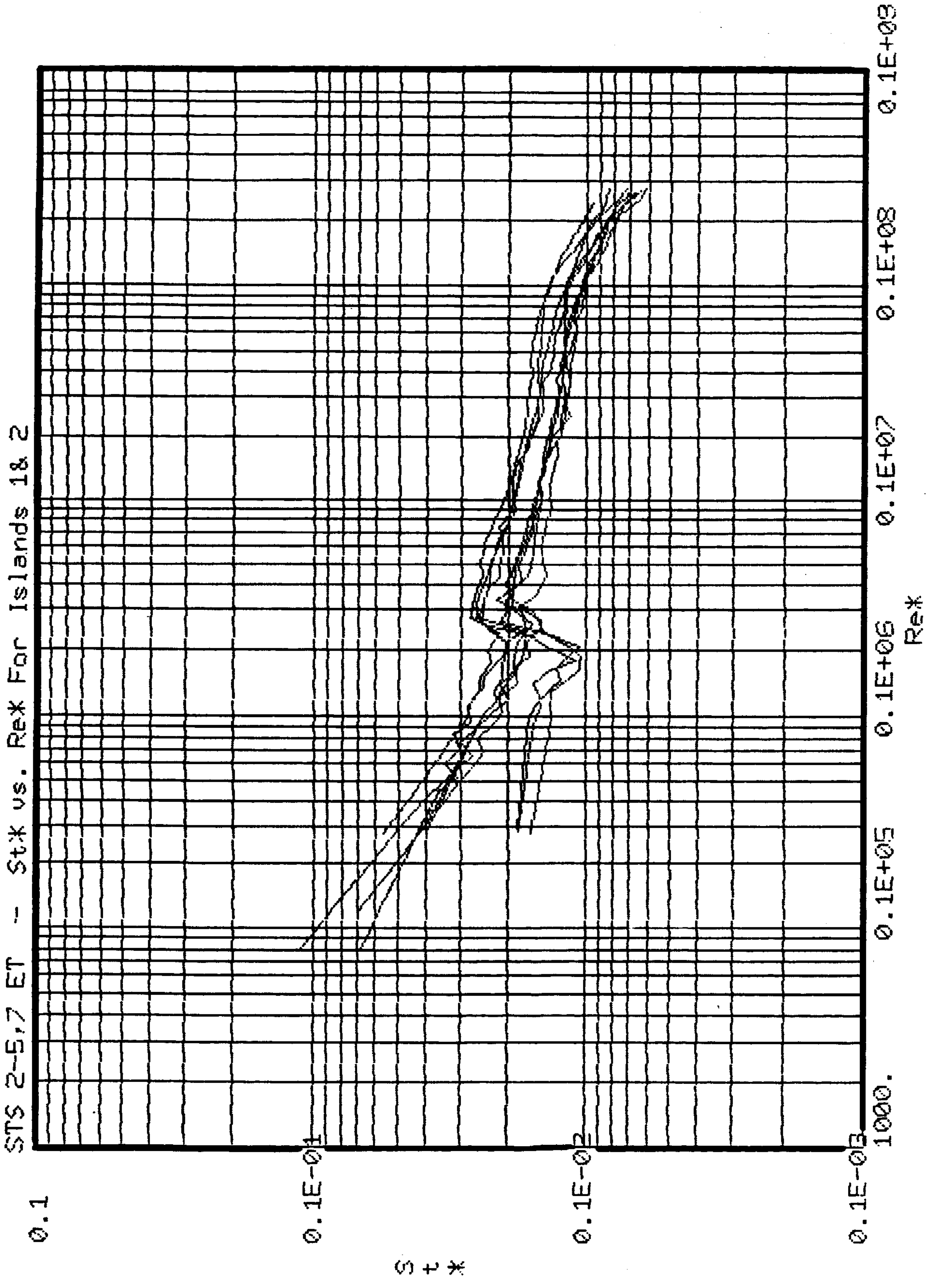

Fig. 3.77 Composite St* vs. Re* Plots for All LO_2 Gages Located at X_T = 467.4" for All STS DFI Flights

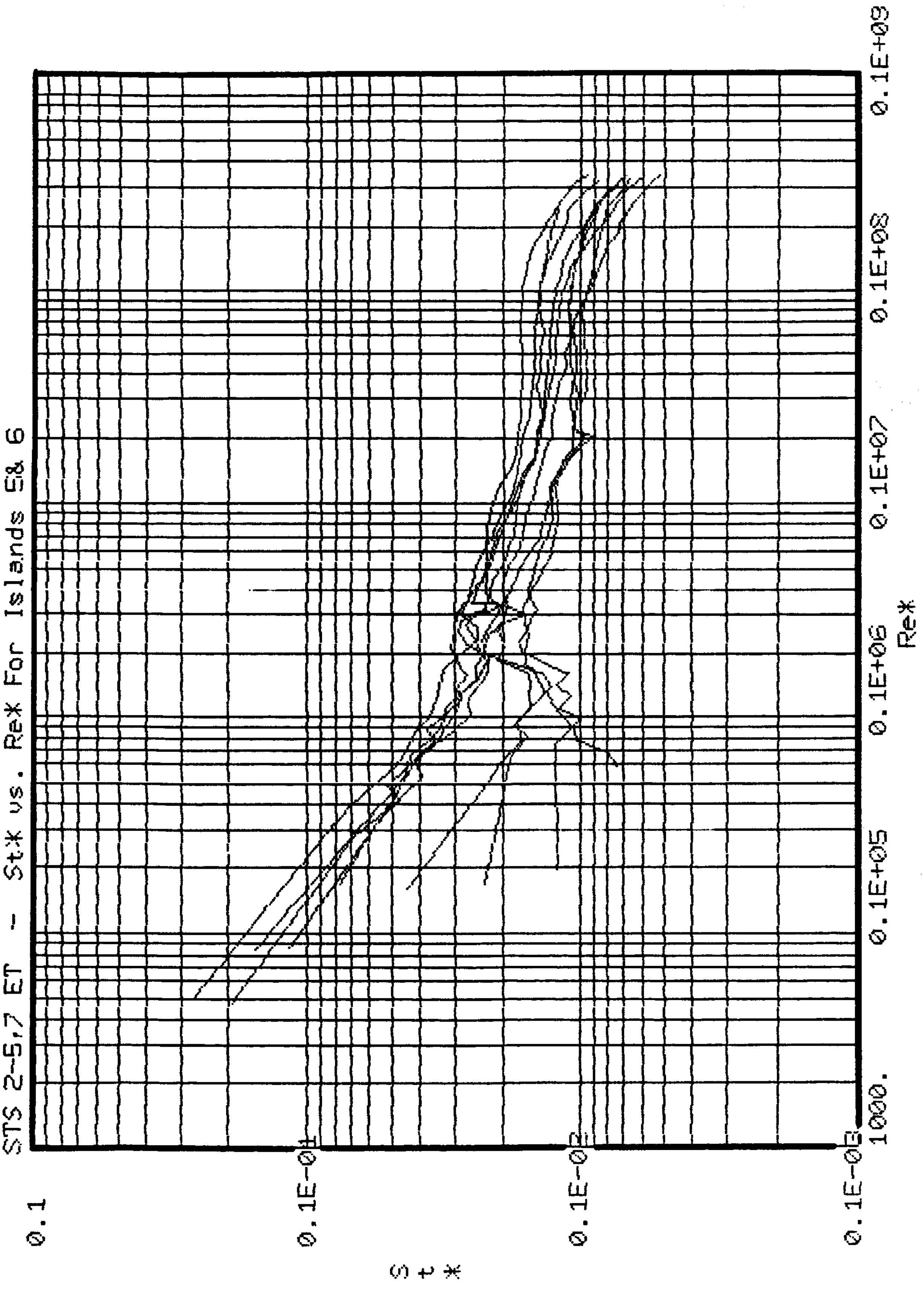

Fig. 3.78 Composite St* vs. Re* Plots for All LO_2 Gages Located at X_T = 672.5" for All STS DFI Flights

is much more than in the turbulent regime mainly because of inaccuracies of the heat-transfer gages in measuring small (close to zero) heating rates in the laminar regime.

Figure 3.79 was prepared to summarize all the turbulent flight data on the LO_2 tank along with the Eckert turbulent and Spalding-Chi correlations. It is seen that the Eckert correlation brackets the data from the top and that the Spalding-Chi correlation more or less goes through the data. A least-square straight line (on a $\log_{10}$-$\log_{10}$ scale) curve-fit was made to all the data yielding a - 0.195 power and is observed to lie somewhat below the Spalding-Chi correlation. For comparing the flight data with the tunnel data, IH-97B test data was examined both for Mach 3 and 4 runs. The wind tunnel runs, made at Reynolds numbers approximately equal to 3.7 and 4 million per foot at Mach 3 and 4 conditions, respectively, show that the test St*-Re* data lie in a small band of Reynolds number and within the flight data band close to the Spalding-Chi correlation. For ease of understanding, the trajectory time range and Mach number range for all the flights are also provided under the x-axis of this figure.

Figure 3.80 was prepared to plot all the laminar heating data in one place. Stanton number was divided by N_L (Mangler factor) to the power 0.5 in order to reduce the data on a flat-plate basis. The Eckert laminar correlation was superimposed on the set of curves to examine the validity of the data. It is seen that the data scatter in the laminar regime is much more than in the

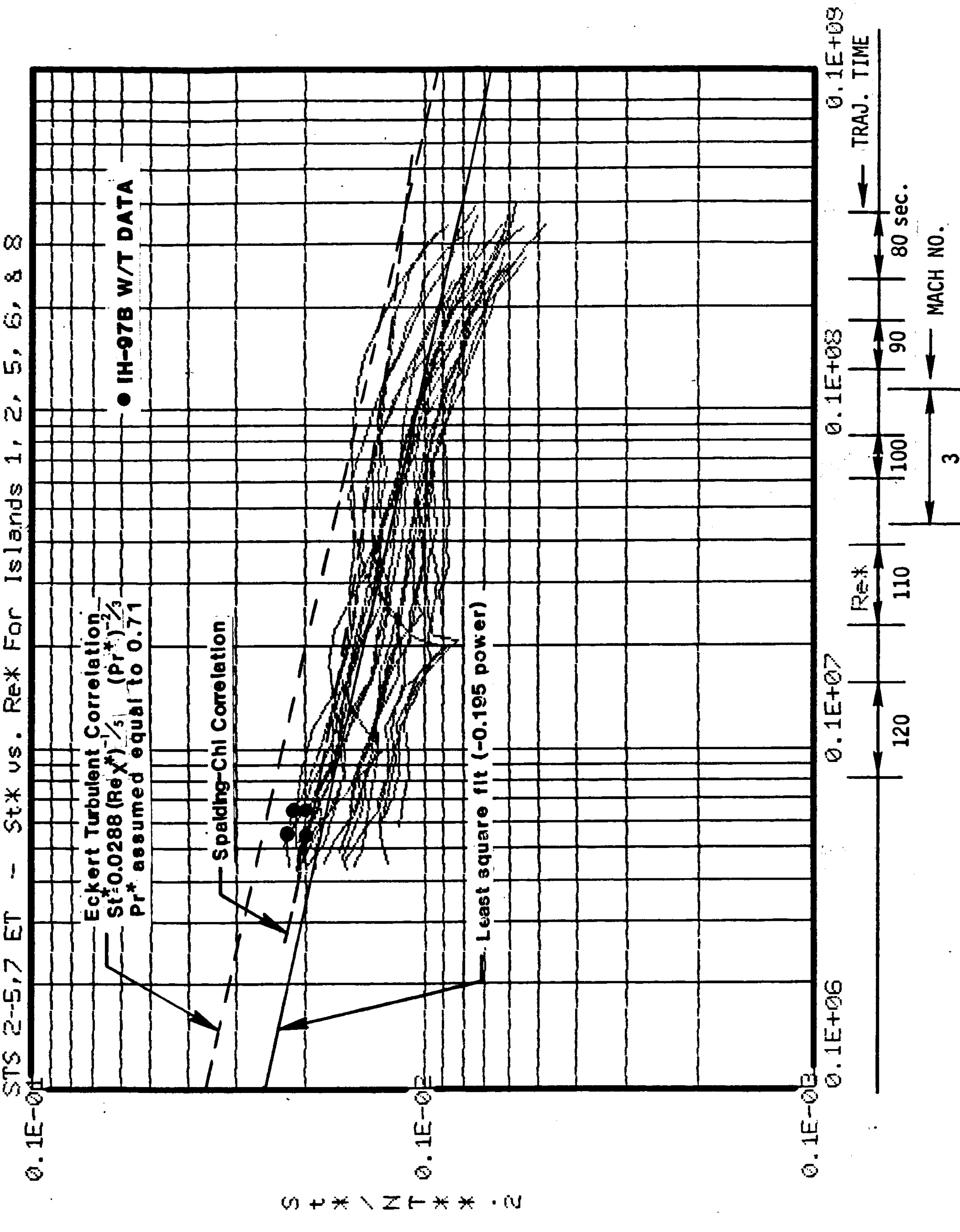

Fig. 3.79 Composite Flat-Plate Turbulent St* vs. Re* for All LO_2 Gages for All STS DFI Flights

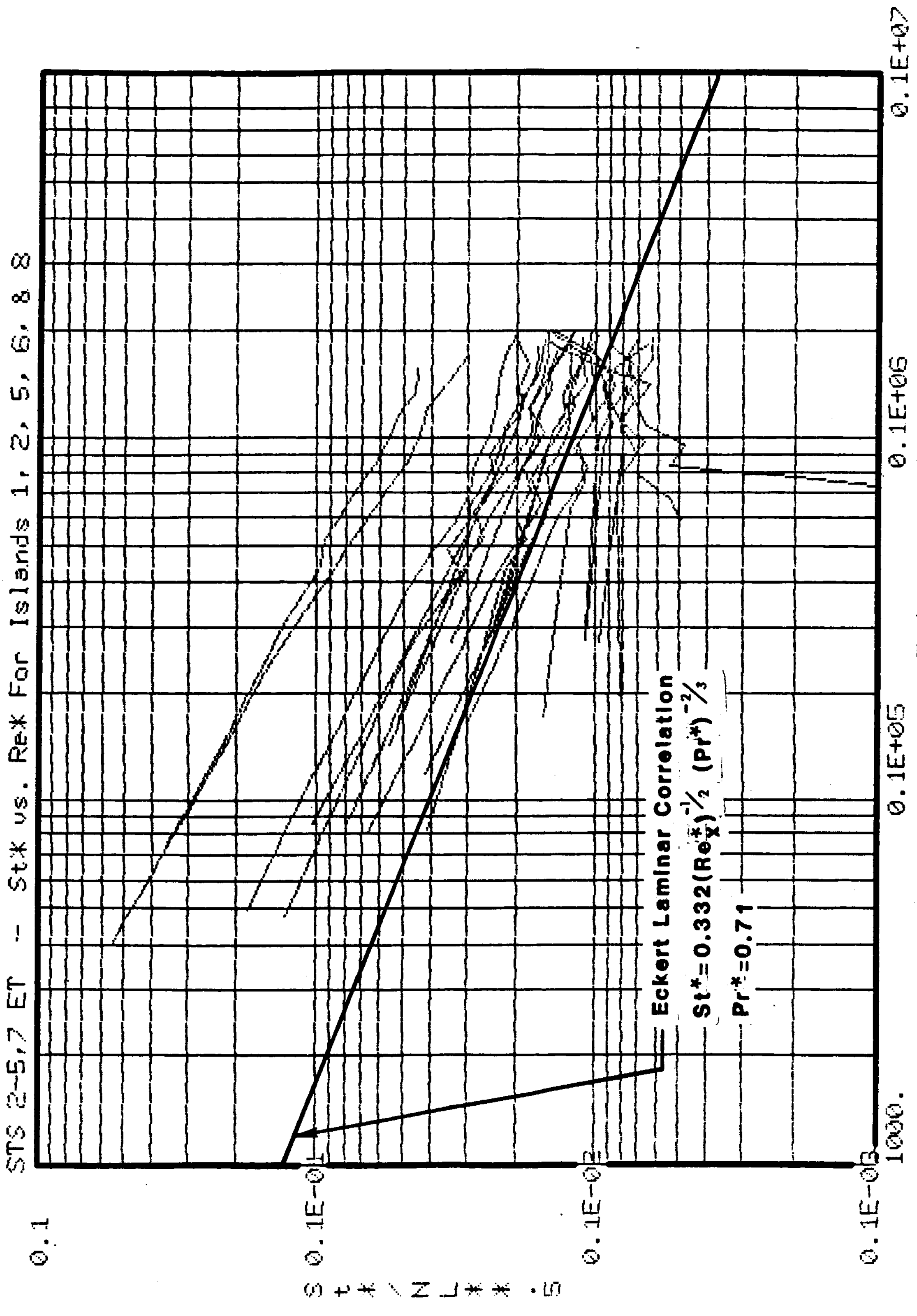

Fig. 3.80 Composite Flat-Plate Laminar St* vs. Re* for All LO_2 Gages for All STS DFI Flights

turbulent regime. The trend of the laminar data seems to suggest close to a 1/2 power relationship between St* and Re*.

In order to check the data spread from the least square curve-fit given in Fig. 3.79, Fig. 3.81 was prepared to reflect the $\pm$ percent deviation of the data in relation to the number of observed data points. The heat-transfer data was scanned for every 2 percent deviation from the least square fit for completing this plot. The same procedure was tried using 0.5 and 1 percent deviations from the curve fit and was found to yield a more erratic trend than the 2 percent case. It is seen that 74 percent of the data lies within a $\pm$ 20 percent band, whereas 92 percent of all the data lies within $\pm$ 30 percent of the least square fit. It is further seen that the error distribution is approximately Gaussian. For a Gaussian error distribution, $\pm 1\sigma$ spread in data gives a probability of error equal to approximately 68 percent, whereas a $\pm$ 2σ spread yeilds a probability of approximately 95 percent. The standard deviation, σ, of the data curve-fitted in Fig. 3.79 is 18 percent. Figure 3.81 shows that a 20 percent deviation yields a probabilty of error of 74 percent, which is somewhat higher than a $\pm 1\sigma$ deviation yielding a probability of 68 percent. A consistent observation is also made for $\pm 2\sigma$ deviation from the least square fit.

In order to examine the data spread from the standpoint of design application, an upper limit was taken from Fig. 3.79 and applied to the IVBC #3 design trajectory. A similar procedure was

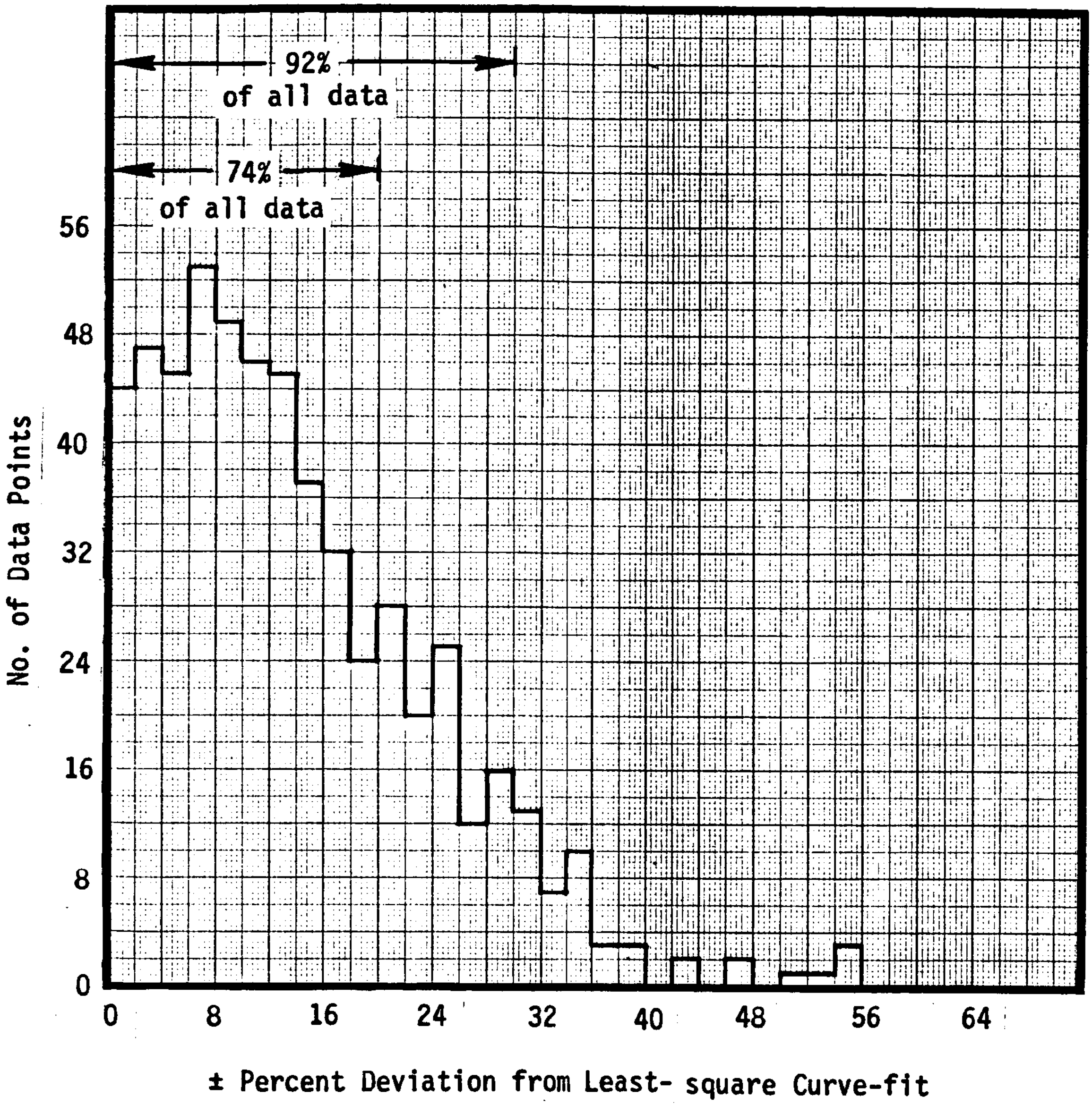

Fig. 3.81 Curve-fit Error Distribution of the STS DFI LO_2 Tank Heat Transfer Data

followed for the lower limit. Both procedures were applied to the Island 1 location on the ET ogive. The results were plotted in Fig. 3.82 in relation to the IVBC #3 design environment for Rockwell Body Point 71250 located very close to Island 1.

The next six plots are presented for some of the gages located in the strong interference regions on the ET. Figures 3.83 - 3.85 were prepared for Island 17, which contains three gages, all experiencing orbiter nose shock impingement heating. For gage 17(1), the data seem to lie in a band without showing any signs of transition up to t = 180 sec. However, for gage 17(3), one flight seems to be out of place, whereas for gage 17(2), the data is divided into two groups. All these observations for the Island 17 gages were already made from the composite h_i/h_u vs. M_∞ plots prepared before. The other group of islands 14, 15 and 16, which experience the left SRB nose shock, are examined next. As observed before in the composite h_i/h_u vs. M_∞ plots for Island 14, the data in Fig. 3.86 is divided into two groups. Also plotted on this figure are Eckert laminar and turbulent correlations applicable to undisturbed flow in order to show that interference is present throughout the flight regime. Figures 3.87 and 3.88 show the Stanton number correlation with Reynolds number for Islands 15 and 16, respectively. The sudden dips in these curves, also seen before in Fig. 3.86 for Island 14 in the range $10^5 < Re^* < 10^6$, refer to the transition from the OTS to OT configuration. The data appears to be quite consistent in the turbulent regime. The magnitudes of

ORIGINAL PAGE IS
OF POOR QUALITY

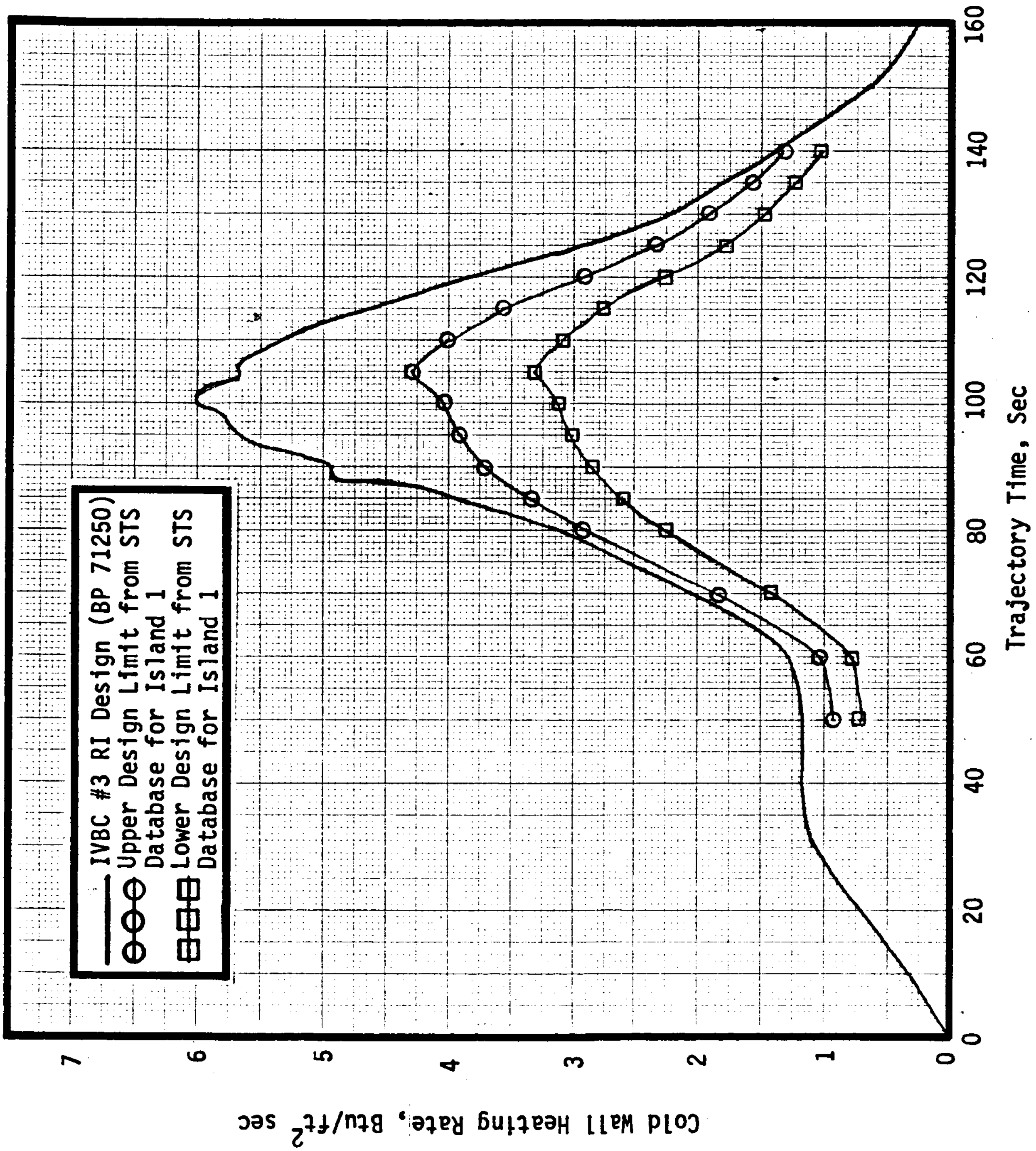

Fig. 3.82 Comparison of Cold Wall Heating Rates Between Design and Flight-derived Values

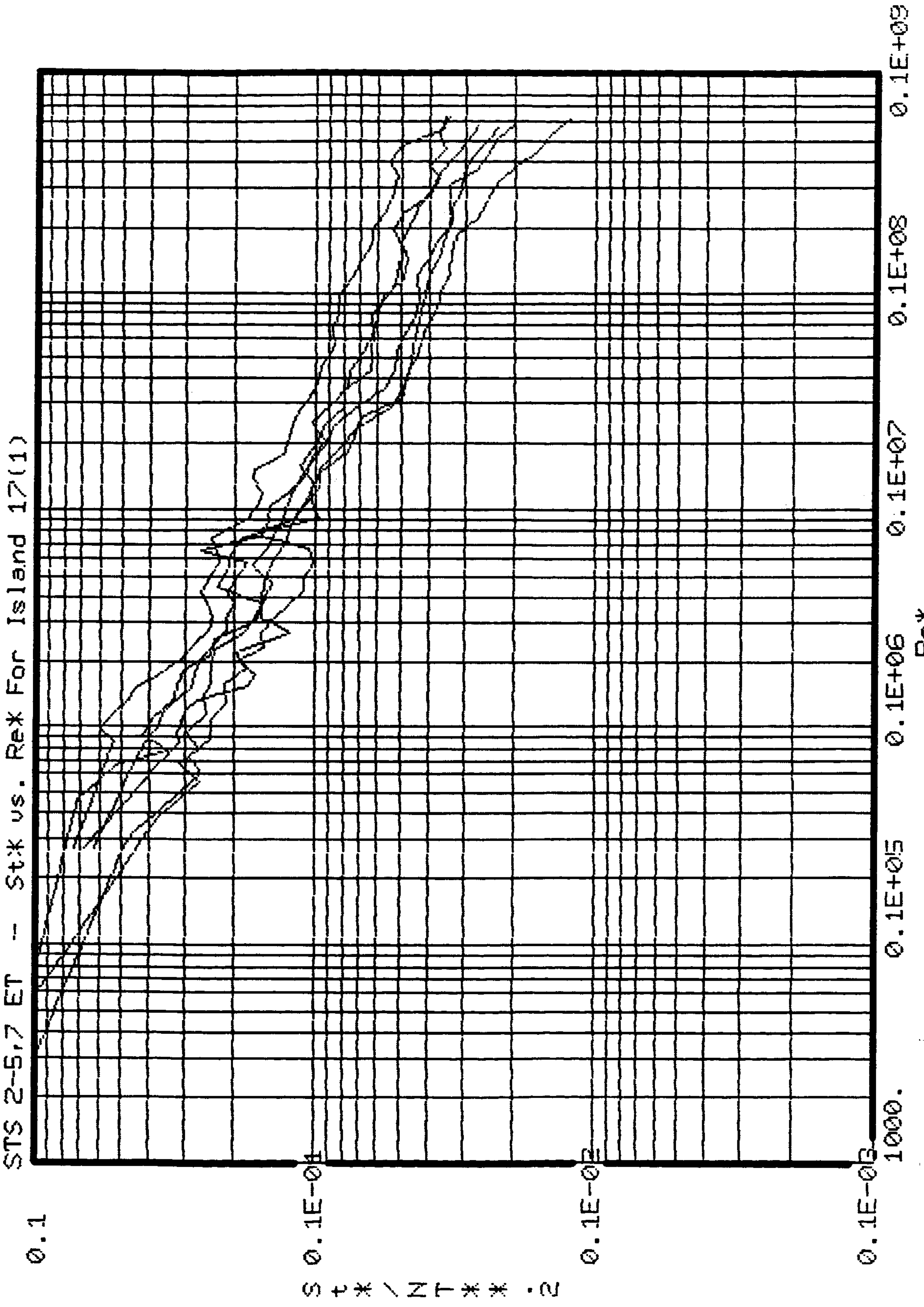

Fig. 3.83 Composite St* vs. Re* Plots for Island 17(1) for all STS DFI Flights

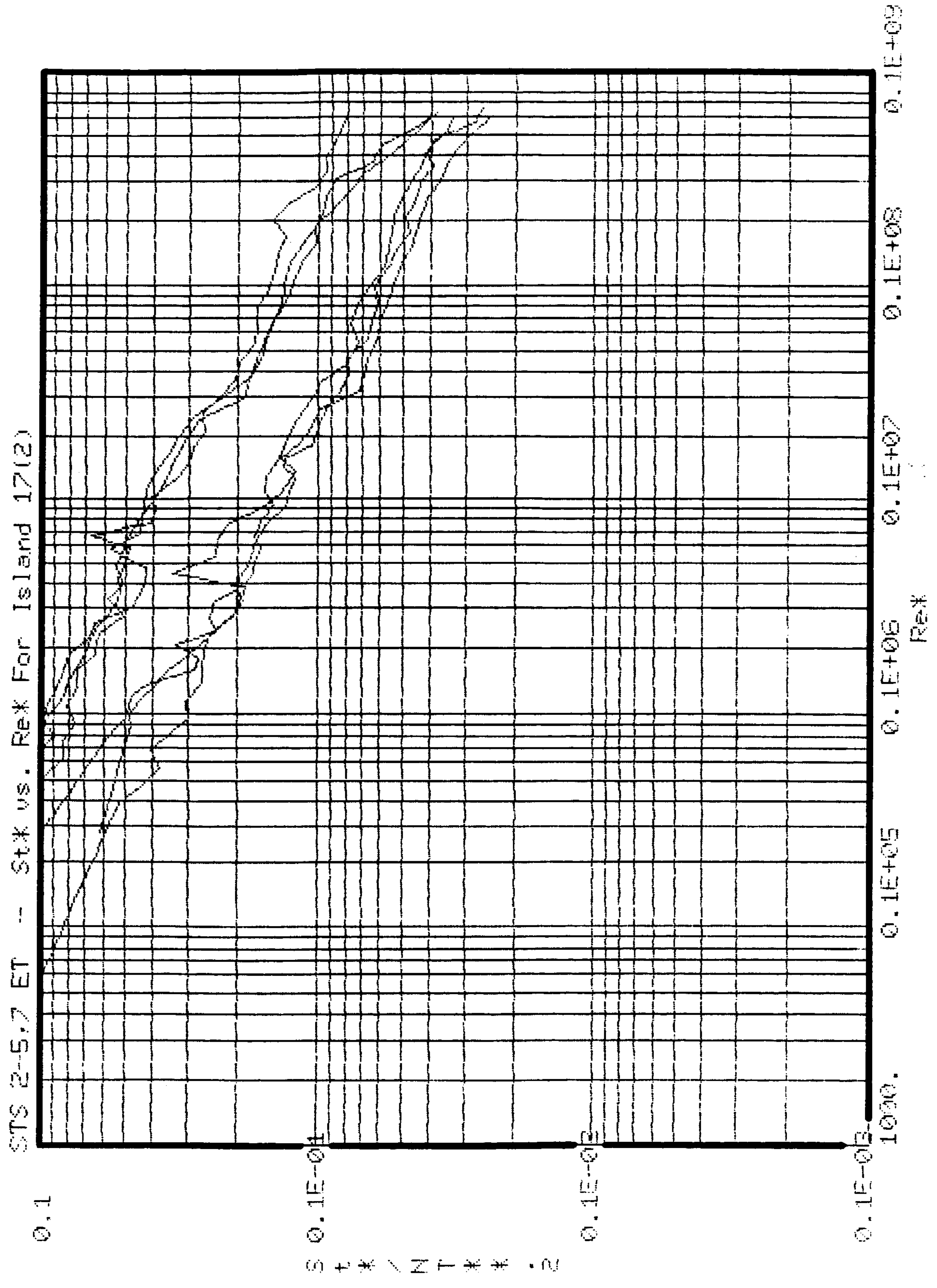

Fig. 3.84 Composite St* vs. Re* Plots for Island 17(2) for all STS DFI Flights

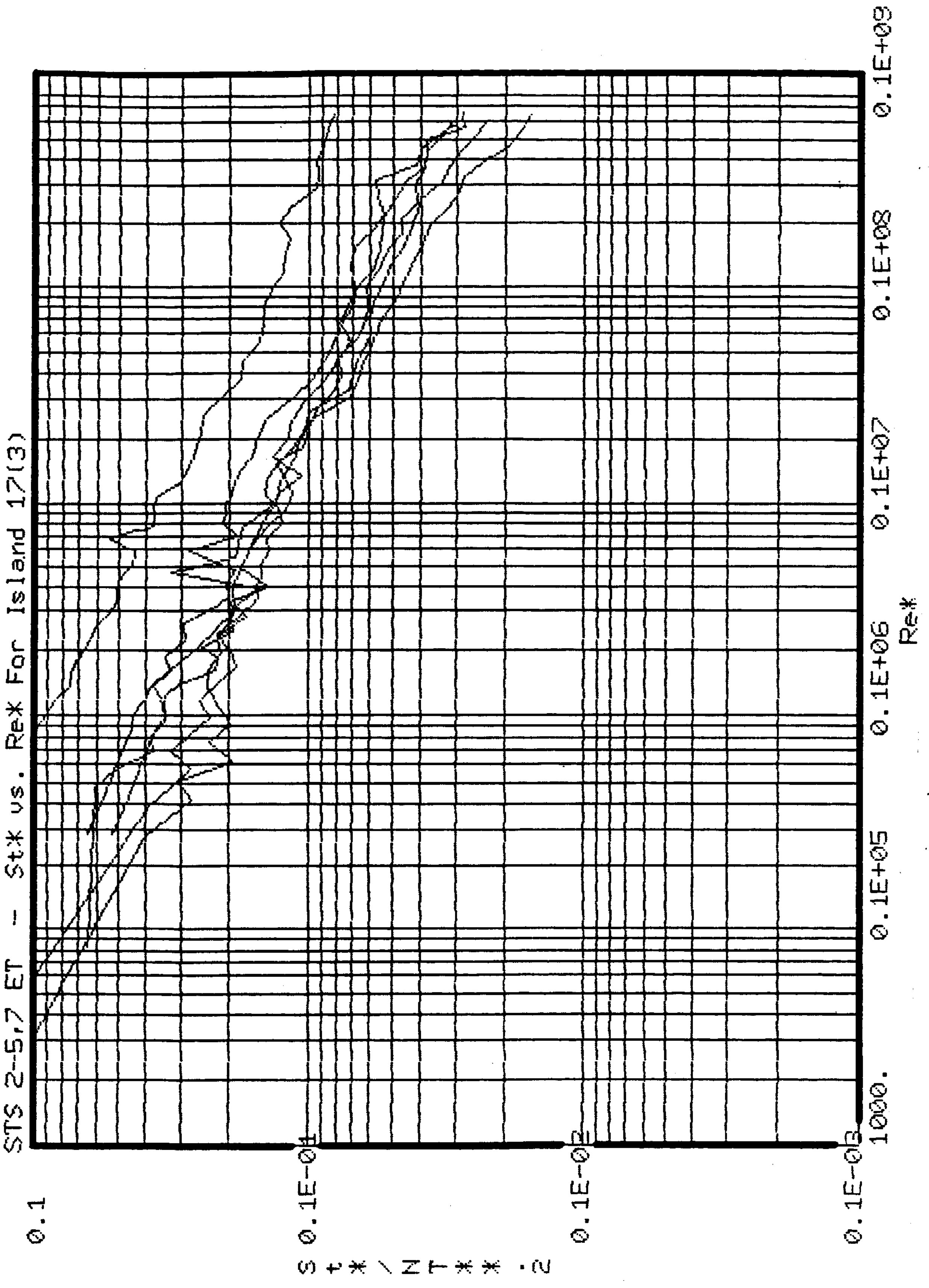

Fig. 3.85 Composite St* vs. Re* Plots for Island 17(3) for all STS DFI Flights

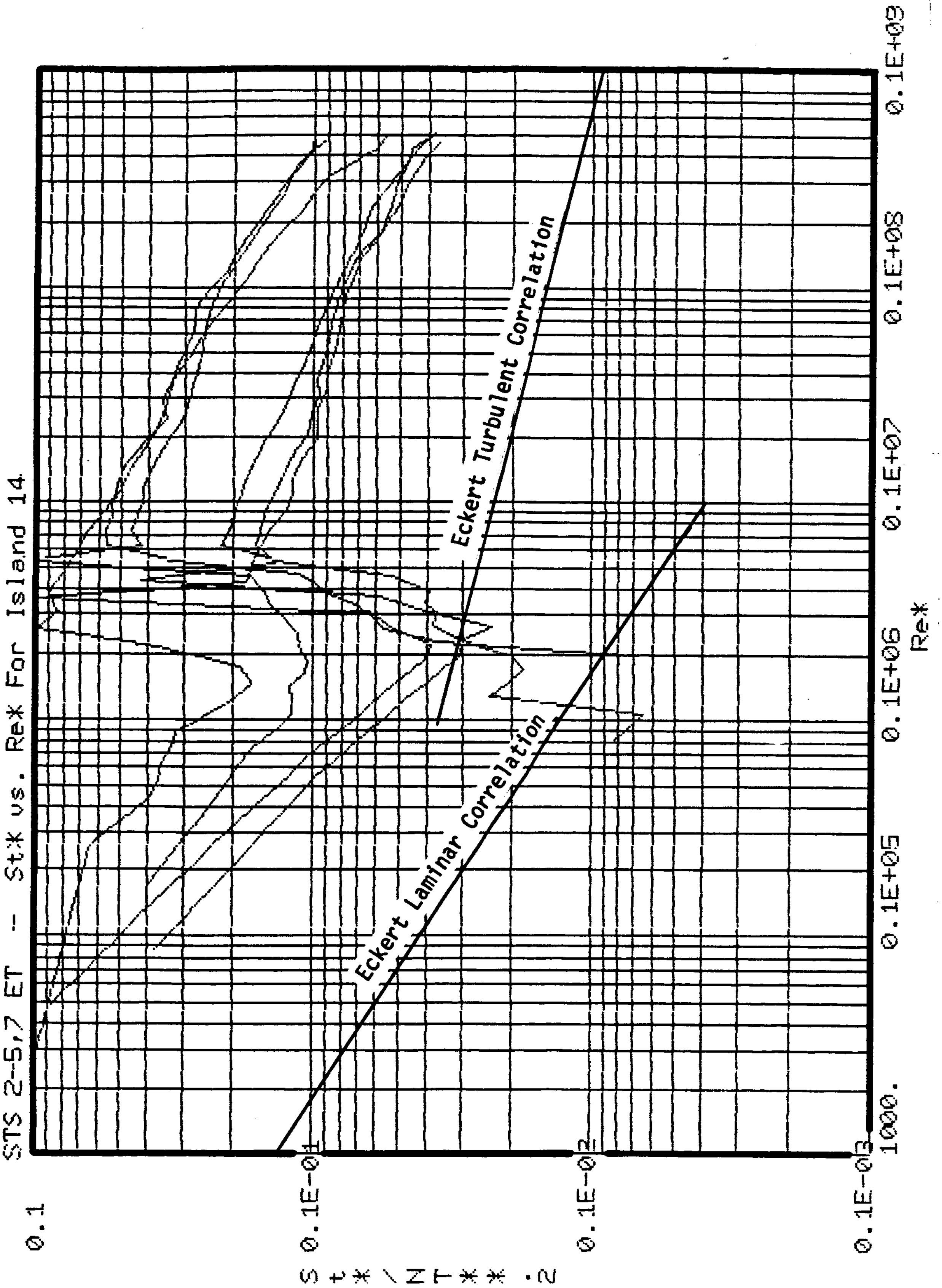

Fig. 3.86 Composite St* vs. Re* Plots for Island 14 for all STS DFI Flights

ORIGINAL PAGE IS OF POOR QUALITY

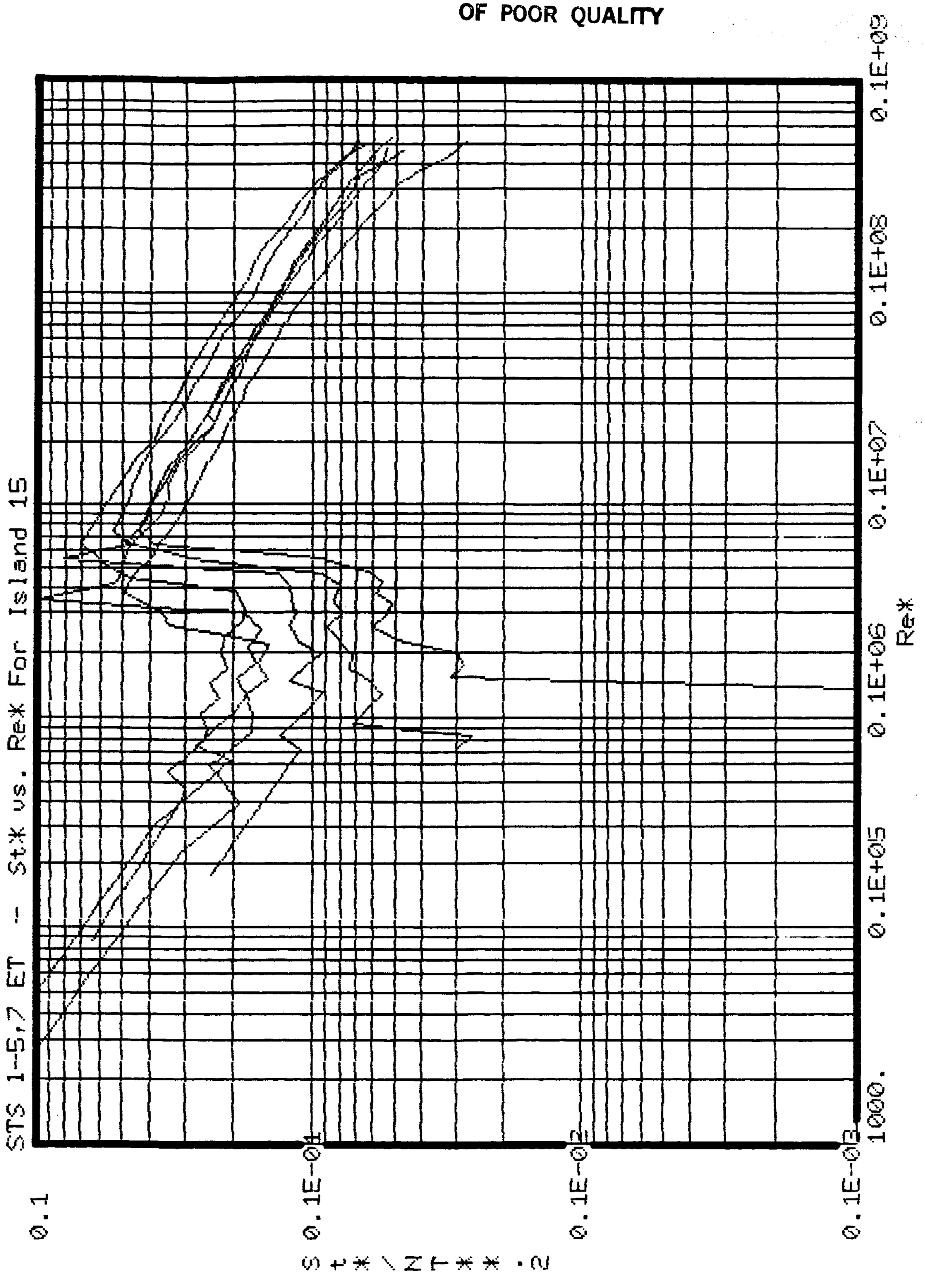

Fig. 3.87 Composite St* vs. Re* Plots for Island 15 for all STS DFI Flights

REMTECH INC.

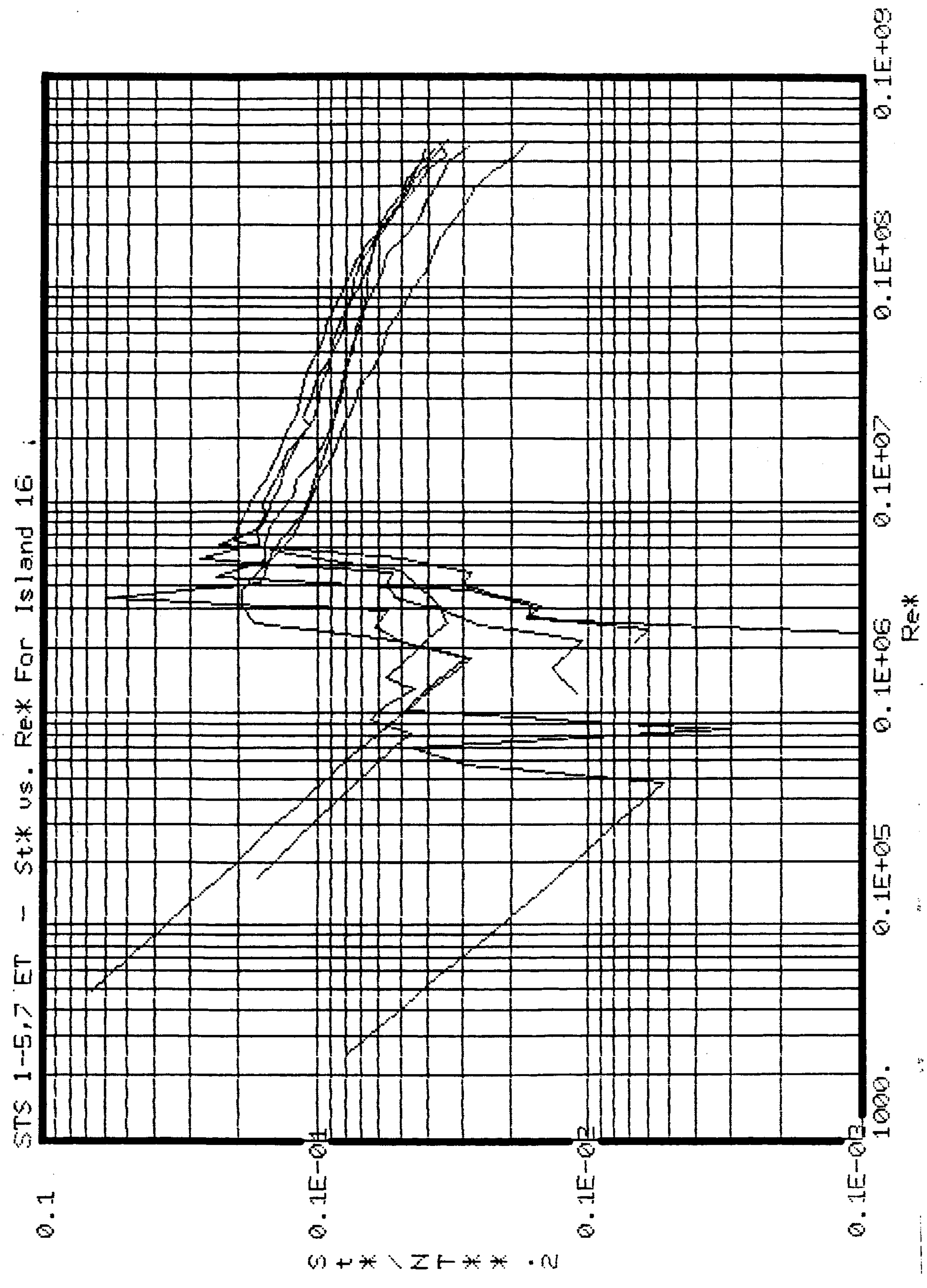

Fig. 3.88 Composite St* vs. Re* Plots for Island 16 for all STS DFI Flights

Stanton number in the turbulent regime for Island 15 in Fig. 3.87 are higher than for Island 16 in Fig. 3.88, indicating that interference is stronger for the Island 15 location. This, of course, has been observed in the analysis made earlier both in ground test and flight.

3.4.1.4 TRANSITION CRITERION ANALYSIS

The Orbital Flight Tests provided, for the first time, heat transfer measurements spanning the turbulent, transitional, and laminar regimes. It is clearly seen from the composite St* - Re* plots in Fig. 3.76 that the uncertainties in the laminar regime are much more than those in the turbulent regime. This may be attributed partially to the measurement inaccuracies in the laminar regime, since the gages were measuring very small magnitudes of heat transfer rates. However, the data trends in those regimes are clear from Figs. 3.79 and 3.80. The onset of transition from the turbulent side of the data is much sharper than the completion of transition to fully laminar flow, as seen in Figs. 3.76, 3.77, and 3.78. In order to observe the transitional regime in a clearer way, the X_T dependence was taken out by plotting St* vs. Re* at one X_T location without using a Mangler factor for reducing the Stanton number data to a flat-plate basis. Such plots are given in Figs. 3.77 and 3.78. It is clear from these plots that the onset of transition from the turbulent side occurs close to $Re^* = 3 \times 10^5$, whereas the end of transition to laminar flow occurs close to $Re^* = 2 \times 10^5$. However, the end of transition is not very well defined because of measurement uncertainties of the gages.

A similar procedure was attempted for observing turbulent-to-laminar transition for interference gage locations. However, a clear trend was not observed from the Island 17 plots in Figs. 3.83, 3.84 and 3.85. It appears that the flow remains turbulent longer in ascent flight. For Islands 14, 15, and 16, staging affected the flow pattern in a Reynolds number range close to the transition range given in the previous paragraph. Transitions, if any, are confounded in the measurements in this Reynolds number range, thus yielding no definite clue to the onset of transition.

3.4.2 Laminar/Rarefied Flow

Heating rates measured by gages on the 40° cone and LO_2 tank for second stage flight are shown in Figs. 3.17a, 3.17b, 3.19a, and 3.19b. This data shows a second pulse of significant heating near the end of second stage flight ($\approx$ 500 seconds) where the shuttle speed is near orbital velocity. A complete set of plots showing the data measured over the entire tank are given in Ref. 10. The heating on the nose during this second pulse is, however, the only data where heating levels are high enough to justify analyses.

The data measured on the ET 40° nose cone (Gage 9001) for all six DFI flights are shown in Fig. 3.89. Table 3.5 gives trajectory conditions and heat flux measurements at the time of MECO for each flight. The flow velocity at MECO was approximately the same (24,300 ft/sec) for all flights, but MECO altitudes varied from 348,858 to 387,104 feet.

An analysis of the data measured on the 40° cone at MECO time

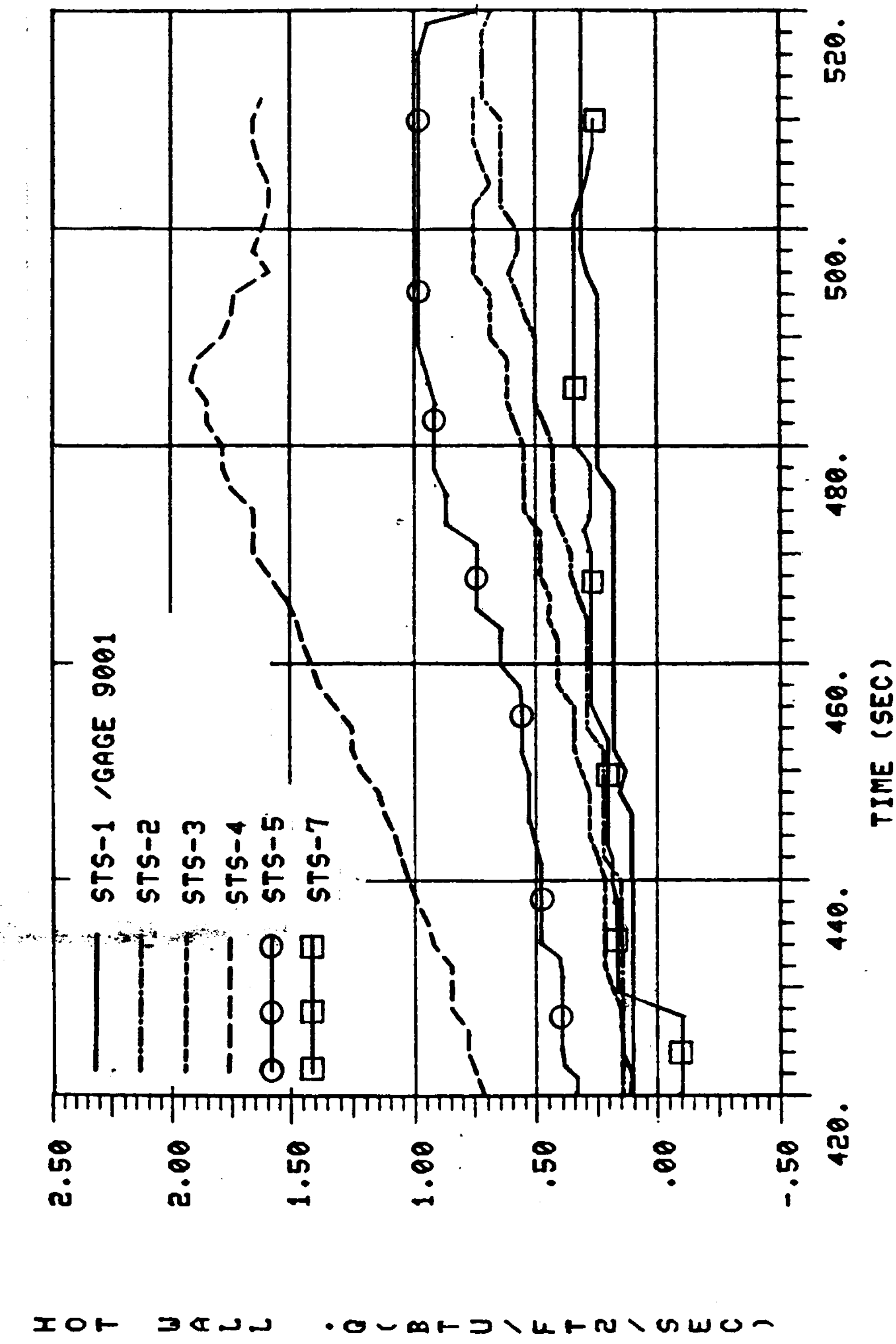

Fig. 3.89 ET Nose Rarefied Flow Heating Measurements

Table 3.5 MECO TRAJECTORY CONDITIONS AND MEASURED HEATING RATES ON THE 40° CONE (GAGE 9001)

Flight #	Time (sec)	Alt. (ft.)	U_∞ (ft/sec)	$\rho_\infty x 10^{10}$ (slugs/ft^3)	q (measured) (Btu/ft^2 sec)
STS-1	520	387,104	24,480	0.584	0.30
STS-2	514	384,734	24,410	0.683	0.62
STS-3	511	365,995	24,148	1.493	0.70
STS-4	512	348,858	24,128	3.367	1.60
STS-5	511	360,402	24,276	2.002	0.90
STS-7	500	361,072	24,139	1.807	0.35

is shown in Fig. 3.90. The measured data is compared with free molecular theory and the maximum values possible ($\rho_\infty U_\infty{}^3/2gJ$) for aerodynamic heating. The free molecular theory is given by the following equations.

$$q_{FM} = \alpha \sin 40^\circ \cdot \frac{H_r}{H_t} \frac{\rho_\infty U_\infty^3}{2gJ}, \left(\frac{Btu}{ft^2 sec}\right)$$

$$\frac{H_r}{H_t} = \sin^2 40^\circ + r \cos^2 40^\circ$$

$r = \sqrt{pr}$, (Pr = .71)

α = 0.9 (accommodation coefficient)

g = 32.17, ($lbm\text{-}ft/lbf\text{-}sec^2$)

J = 778, (ft-lbf/Btu)

ρ_∞ = free stream density, ($slug/ft^3$)

U_∞ = free stream velocity, (ft/sec)

The comparison of the measured data with the free molecular theory in Figure 3.90 shows that the flow is free molecular near the end of second stage flight. The comparison between free molecular theory and measurements shows excellent agreement.

A prediction technique referred to as the D^2-correlation method was developed and incorporated into a version of the MINIVER aeroheating computer code at REMTECH to predict heating in the rarefied flow regime. The trajectory and flow conditions for STS-3 flight from 400 - 510 secs. were input into this code and the calculated values of the heating rates are compared with measurements

REMTECH INC.

ORIGINAL PAGE IS
OF POOR QUALITY

SYMBOL	DESCRIPTION
⊙	$\frac{\rho_\infty U_\infty^3}{2gJ}$ (Calculated)
●	Measured on ET 40° Nose Cone
———	Free Molecular for 40° Cone (Calculated)

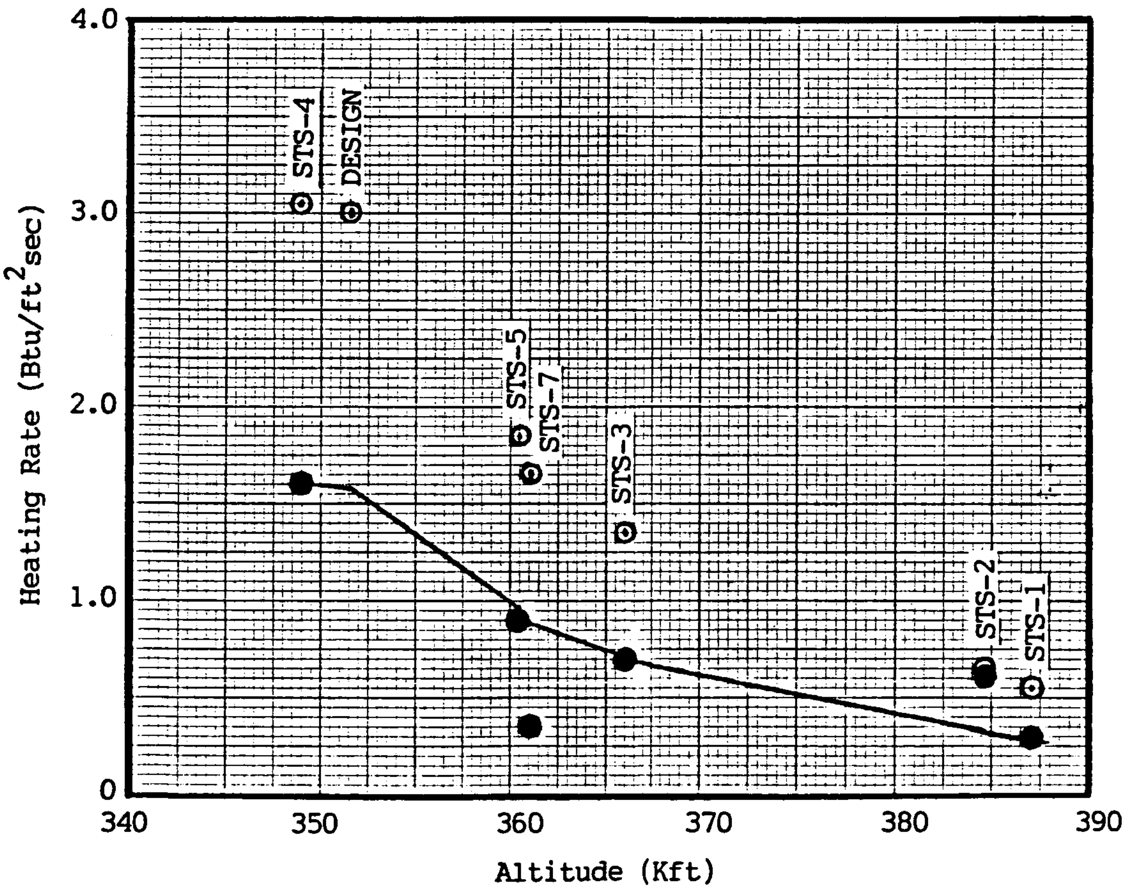

Fig. 3.90 Comparison of Measured and Calculated Heating Rates on 40° Cone Near/At MECO

in Fig. 3.91 the agreement between theory and data verifies that the D^2 method produces good results in this flow regime.

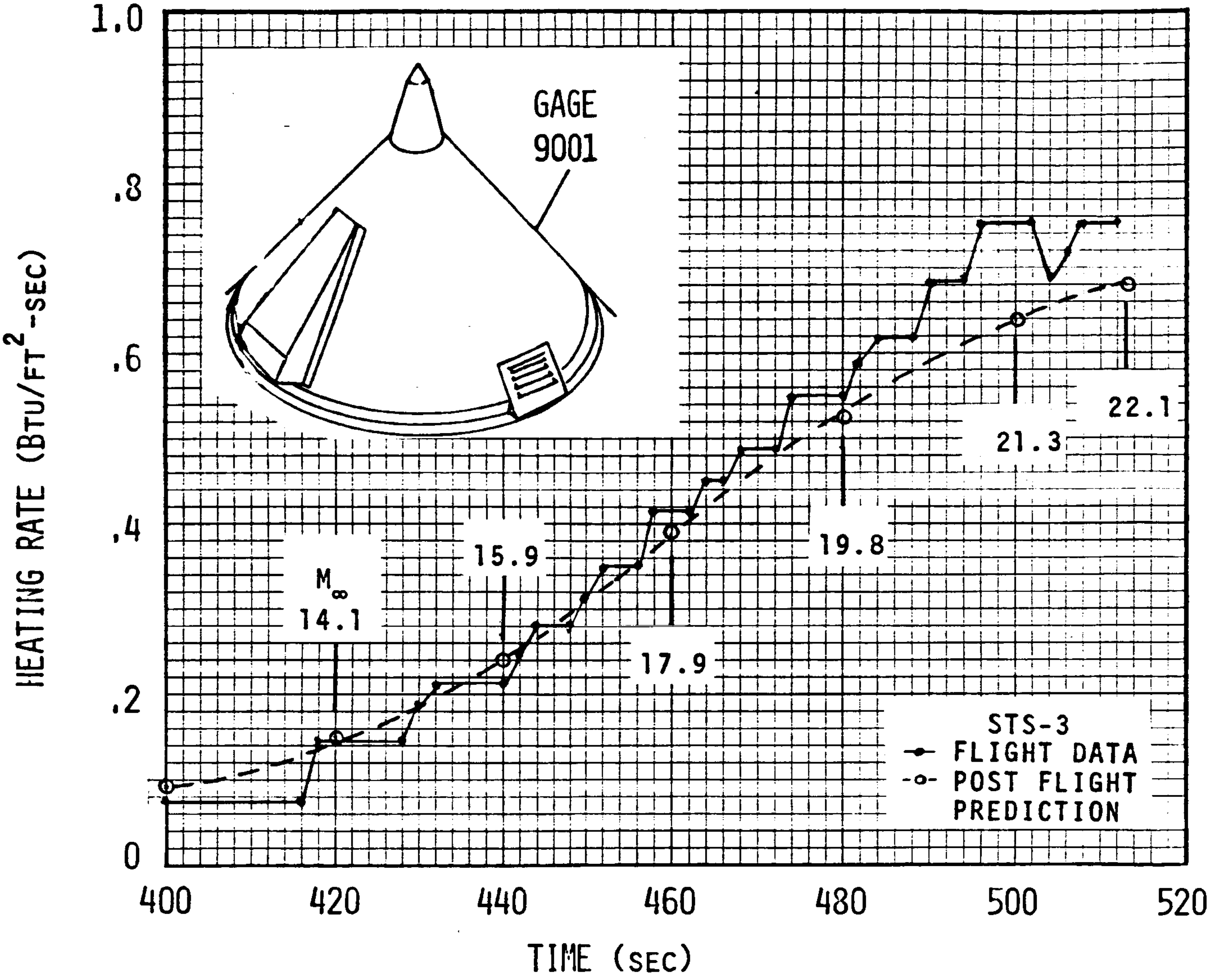

Fig. 3.91 Rarefied Flow Heating Rate Predictions Compared with Flight Data

Section 4.0

AEROTHERMAL MATH MODEL UPDATES

The OFT flight data evaluation provided the first opportunity of verifying the prediction math model with measurements from the full scale vehicle in flight. The math model was based on ground test data which simulated (to a large extent) the flight conditions in the tunnels. The scalability of this ground test data to flight is the subject of discussion in this section. The discrepancies between flight data (or flight-derived data) and wind tunnel data cannot necessarily be attributed to scale effects, but may be due to the deficiencies in various elements of the data reduction procedure. However, all the defieciencies may be "lumped" into one factor, called the scale factor, which encompasses various deficiencies in the flight data reduction methodology, the prediction procedure, and the shortcomings of wind tunnel flight simulation. The math model updates as applicable to both undisturbed and disturbed prediction methodologies are detailed below.

4.1 UNDISTURBED HEATING PREDICTION METHODOLOGY

No major updates are necessary in the prediction of undisturbed heating rates. Although small discrepancies remain in the comparisons of flight data and prediction data for the gages on the LO_2 tank section (see Section 3.3), they are not considered to be due to scale effects, but rather due to uncertainties in the various elements in the data reduction procedure, such as inaccuracies in temperature mismatch correction and roughness factor calculation.

However, based on the flight measured data, the pressure option in the supersonic detached flow regime was changed according to the equation given in Fig. 3.54. This modification has already been integrated with the MOC pressure option in the prediction. However, a problem remains in the calculation of entropy behind the detached shock. As a result, the heat transfer calculations based on correct pressure but inaccurate entropy still give reasonable levels of heating on the Gage 9001 and some of the gages on the LO_2 tank. Since the impact of such a discrepancy in the lower supersonic flow region on peak heating is minimum, no design concerns are apparent.

So far in the prediction procedure, no rigorous transition criterion has been developed. The well-known criterion that assumes the flow to become transitional at $Re_\theta / M_L = 150$ and fully turbulent at $Re_\theta / M_L = 150 \sqrt{2}$ was based on data from flat plate tests and is not strictly applicable to interference flow regions on the tank. It was observed from the flight measurements given in the previous section that flow makes transition from turbulent to fully laminar flow at $Re^* \simeq 10^5$ for Gage 9001 and $Re^* \simeq 3 \times 10^5$ for the rest of the gages. While this does not provide a strict rule for transition, it is reasonable for the present work. Moreover, the impact of such an approximation on design assessment is minimum. The OFT measurements, for the first time, provided transition criteria based on the analysis made earlier in this report. Even though the Re* value at which the beginning of transition from turbulent to laminar flow is much more definite from the previous analysis, the end of transition is not very clear because of inaccuracies in the heat-transfer measurements in the laminar range.

4.2 INTERFERENCE HEATING PREDICTION METHODOLOGY

As reported in Ref. 1, the interference heating prediction consisted of various elements. As described in Section 3, these elements are (i) intertank stringer factors, (ii) roughness/waviness factors, (iii) rough wall - smooth island factors, (iv) island geometric interference factors, and (v), most important of all, proximity geometric interference factors. If there are inconsistencies between flight and prediction, they are due the confounding nature of all these elements, which cannot easily be separated from each other. It is for this reason that scale factors need to be established for methodology updating.

4.2.1 HI/HU DATA BASE

Since the interference factor, h_i/h_u, is the basic element of the interaction region heating, it is important to update the h_i/h_u data base from the analysis of the IH-97 wind tunnel data and OFT flight data.

4.2.1.1 OFT STATISTICAL DATA BASE

In order to derive a statistical data base for h_i/h_u from the instrumented flight tests, STS-1 thru STS-7 missions were all examined. These sets of h_i/h_u take into account the corrections for plume-induced heating and thermal mismatch. First the h_i/h_u's were assembled for various cuts in Mach numbers and α, β combinations. These cuts were chosen to be within the (Mach, α, β) box available from the flight data. Various trials were made to scan the data from all the flights with various tolerances around the Mach number and (α, β) cuts for which h_i/h_u data were desired. These tolerances varied in the range $|\Delta M_\infty| = .1 \rightarrow .2$, $|\Delta \alpha| = .25 \rightarrow .5$ deg. and $|\Delta \beta| = .25 \rightarrow .5$ deg. Since the object of the analysis is to obtain a statistical data base, it is imperative that as big an ensemble of data as possible be used in the averaging process. The best results were obtained with tolerances for M_∞, α, and β as .1, .5, and .5, respectively.

The final tables are fully documented in Appendix E for all the OFT DFI gages. It is apparent from these tables that the peak values of h_i/h_u occur at certain (α, β) combinations. The tables also provide standard deviations and the number of values averaged to indicate the accuracy of the linear averaging process for various (α, β) cuts.

4.2.1.2 IH-97 WIND TUNNEL DATA BASE

Test IH-97, being the latest wind tunnel test program conducted, was designed to provide a data base superior to the old wind tunnel data base used in Ref. 1. This test was conducted in three different phases. The differences in the two wind tunnel data bases arise basically because of better Shuttle geometry simulation and the provision of stringers on the intertank in the IH-97 test.

The IH-97A phase of this test simulated the STS-1 thru STS-4 flight conditions in Tunnel A of the von Karman test facility at AEDC. Measurements were performed on gages located exactly at the same X/L and θ_T locations as on the flight vehicle. The (α, β) profiles in flight for each of the above missions were simulated in the tunnel as a function of flight freestream Mach number. The Reynolds number and wall-to-total enthalpy ratio were also approximately simulated, as shown in Figs. 4.1 and 4.2. The existing h_i/h_u data base used for flight prediction for many of the DFI gages was derived from extrapolation, interpolation, and judgement of the past wind tunnel test programs, whereas such approximations were removed from the current IH-97A test by simulating exact flight M_∞, α and β in the tunnel. Since this tunnel simulation is the best so far, this set of data should be better than any other existing data. In order to compare the quality of this data, plots given in Appendix C were made in which flight h_i/h_u, IH-97A test data, and the existing wind tunnel h_i/h_u data were compared. Much discussion about these comparisons has already been given in the previous section.

The IH-97B phase of this test was dedicated to making

REMTECH INC.

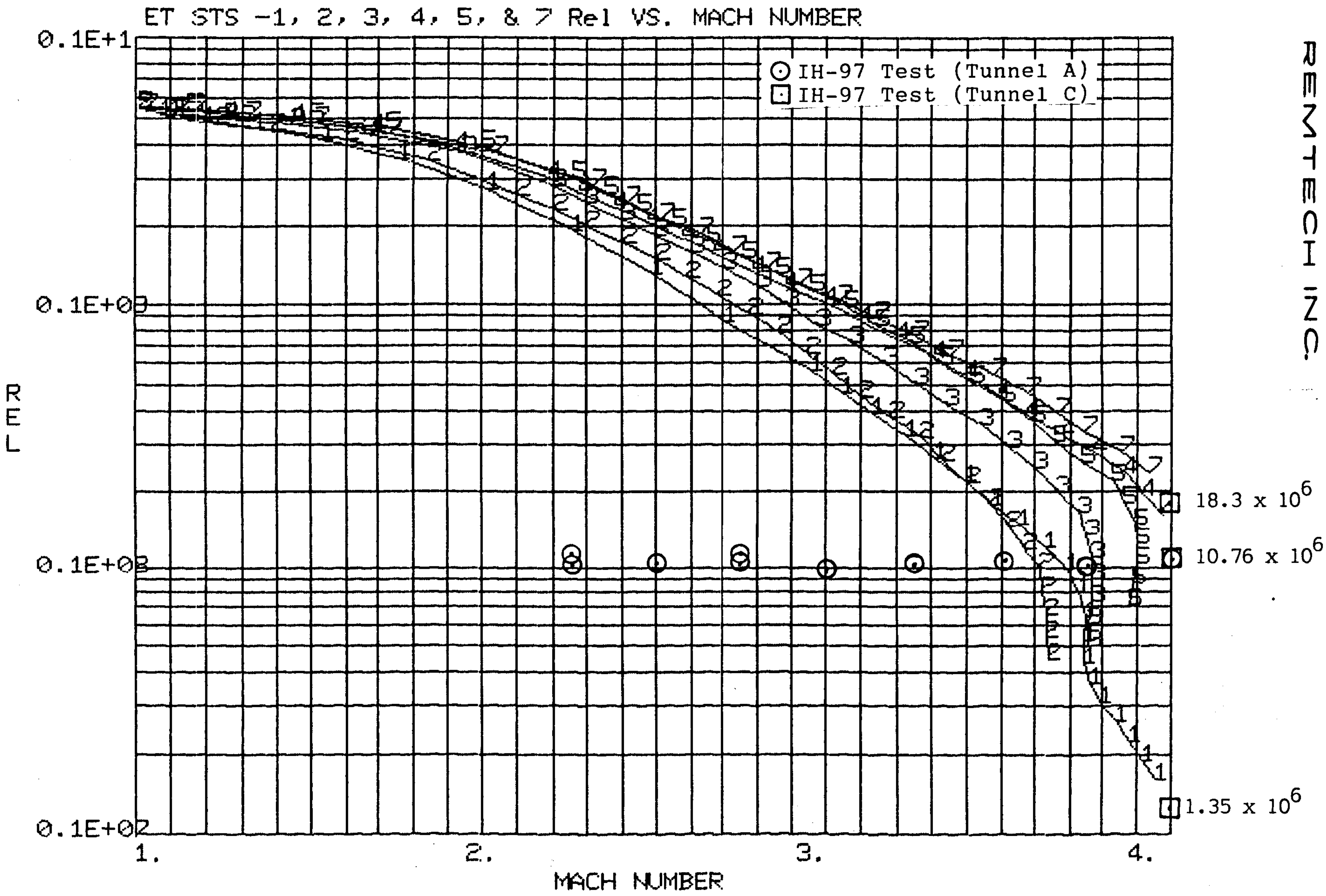

Fig. 4.1 Reynolds Number Simulation in Tunnels A & C

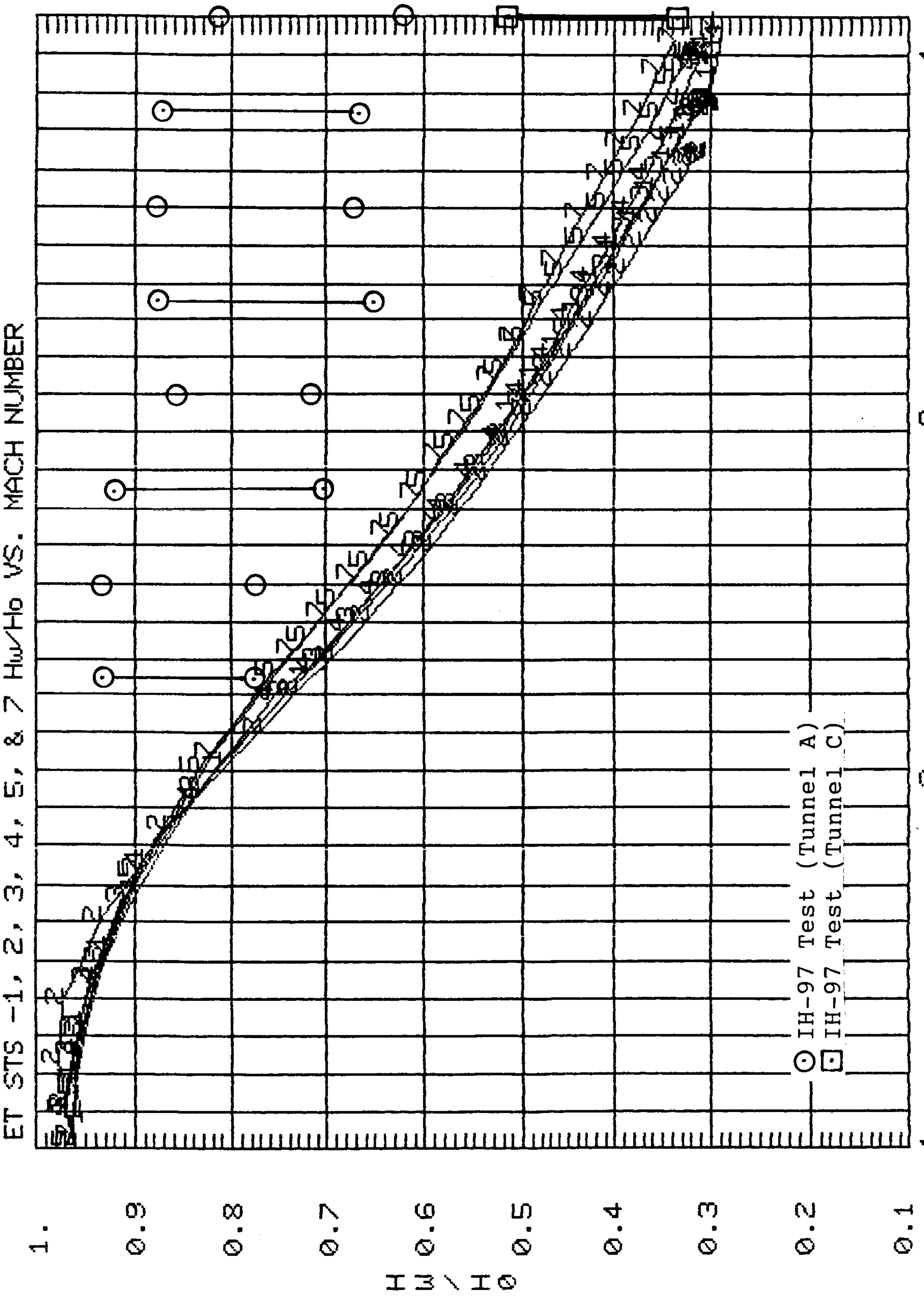

Fig. 4.2 . Enthalpy Ratio Simulation in Tunnels A & C

FLIGHT GAGE 9014 (ISLAND 16) $M_\infty = 3$, TEST IH-97B GAGE 5038

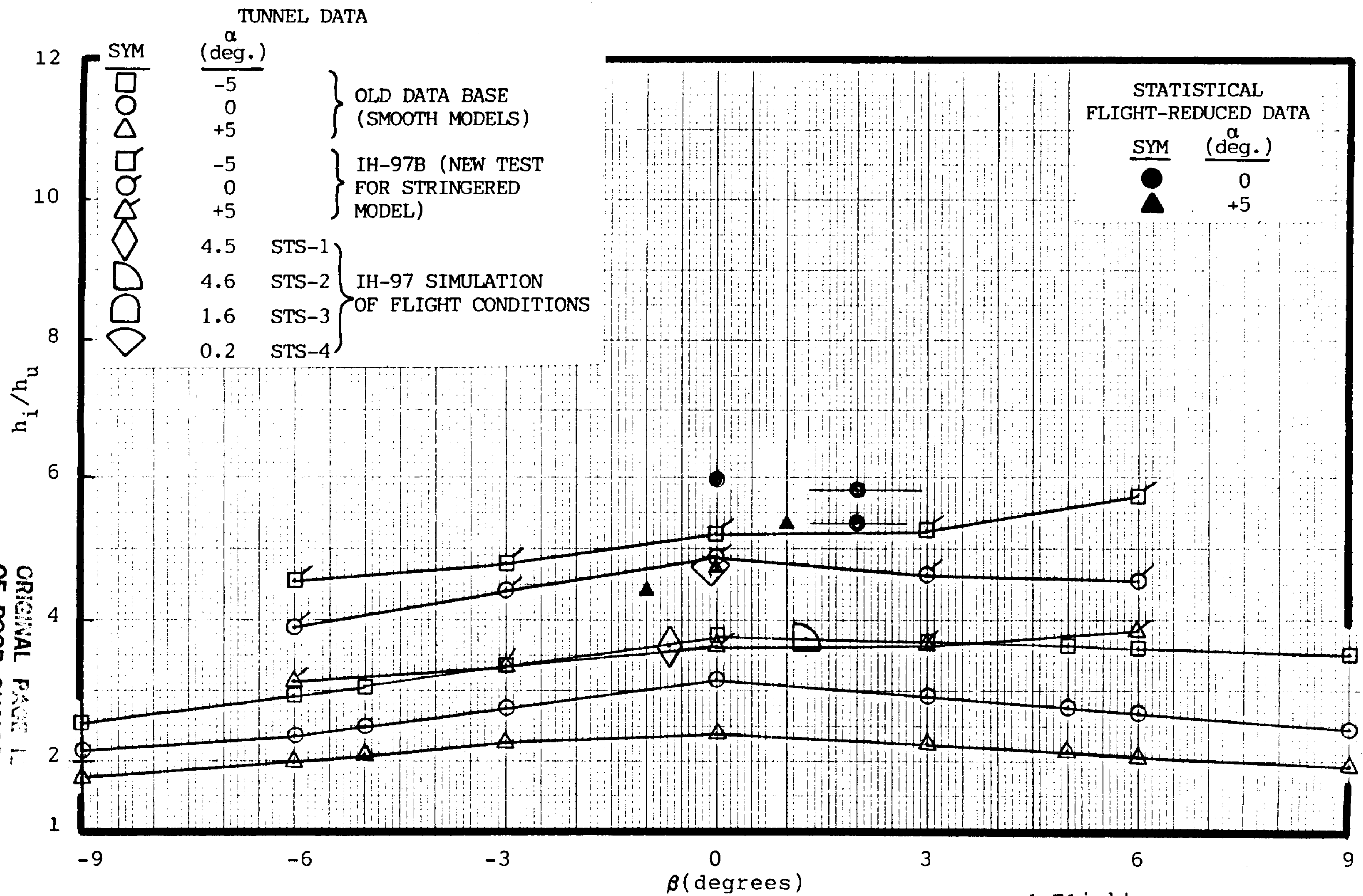

Fig. 4.3a h_i/h_u Data Base from Wind Tunnel and Flight

FLIGHT GAGE 9014 (ISLAND 16) $M_\infty = 4$, TEST IH-97B GAGE 5038

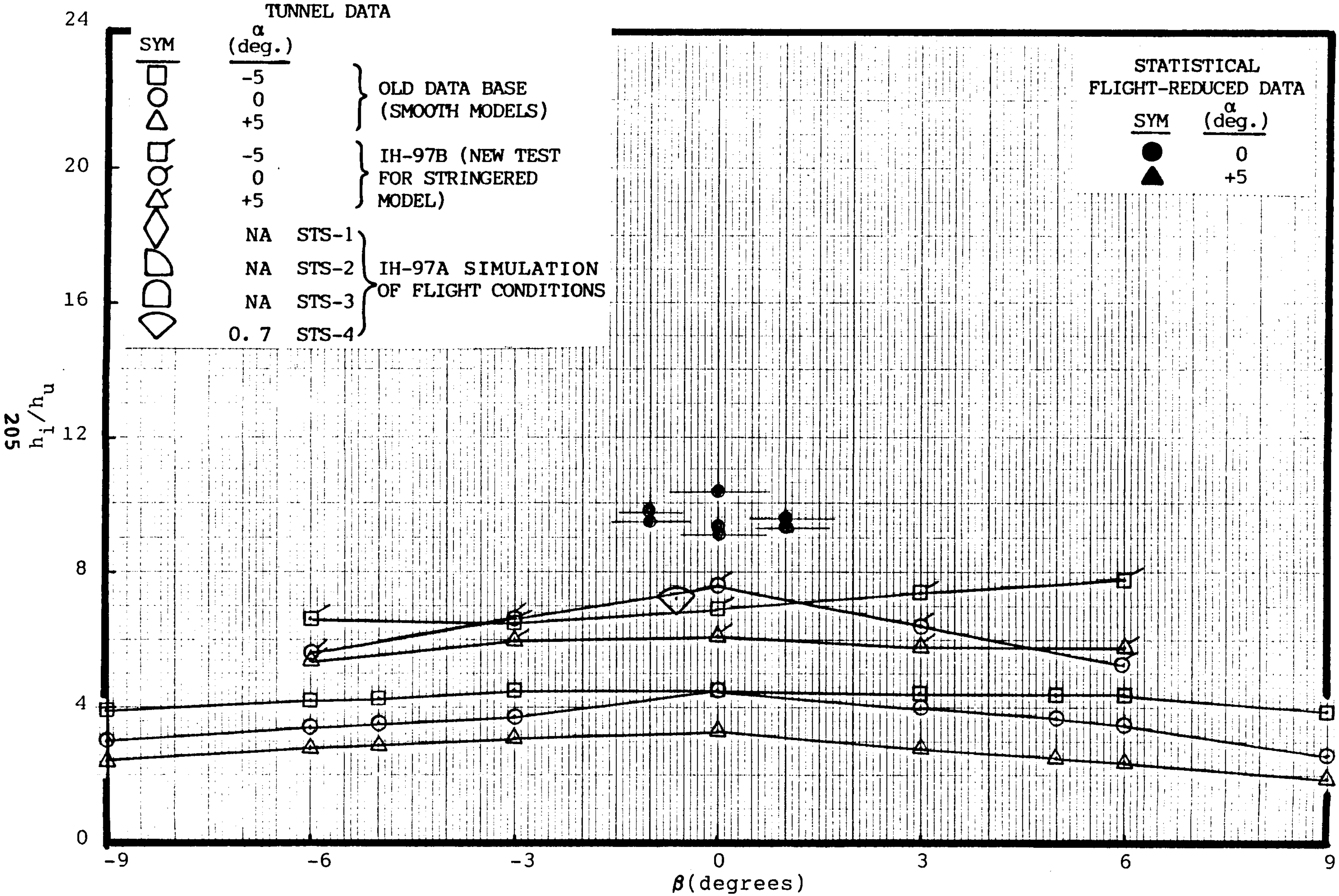

Fig. 4.3b h_i/h_u Data Base from Wind Tunnel and Flight

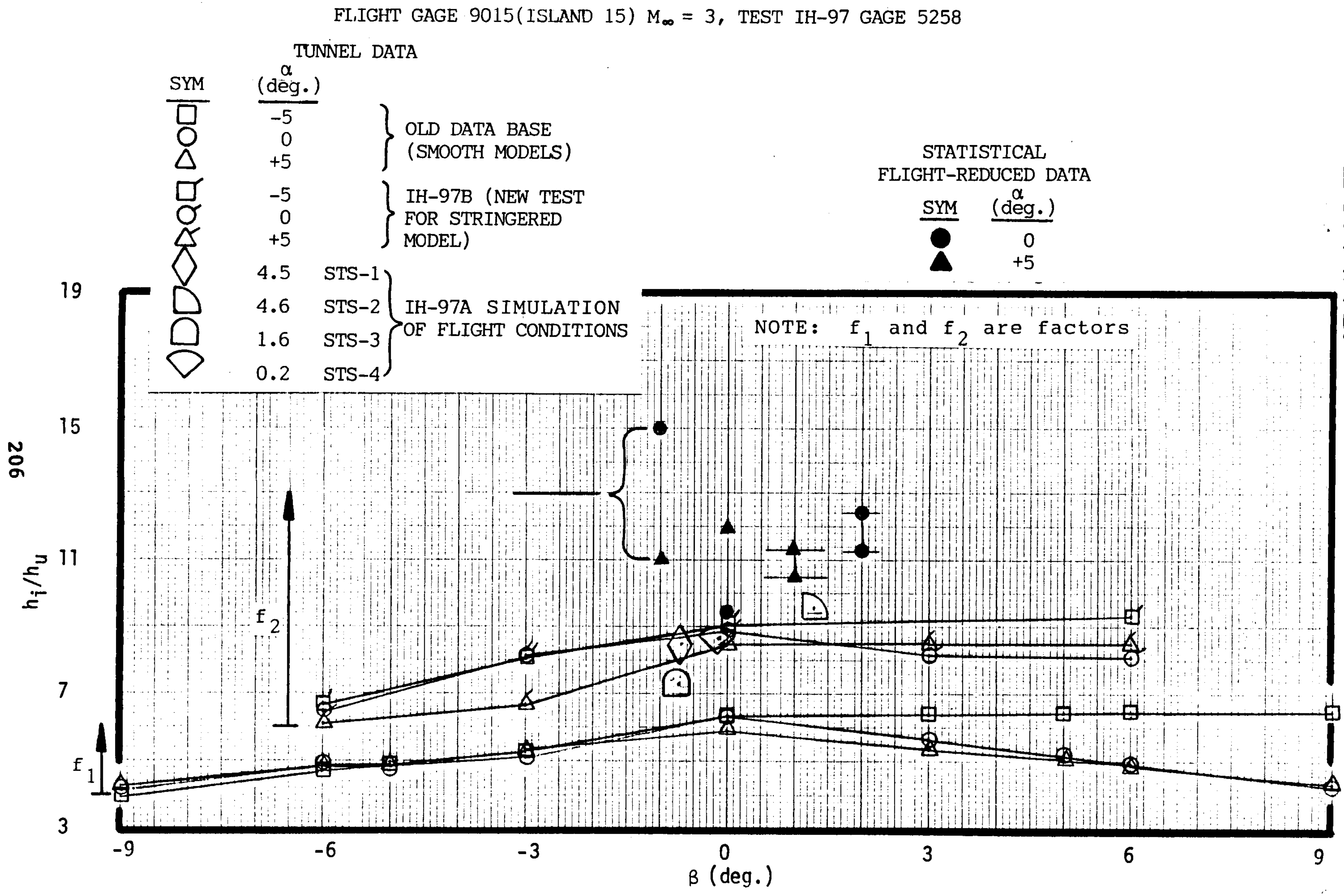

Fig. 4.4a h_i/h_u Data Base from Wind Tunnel and Flight

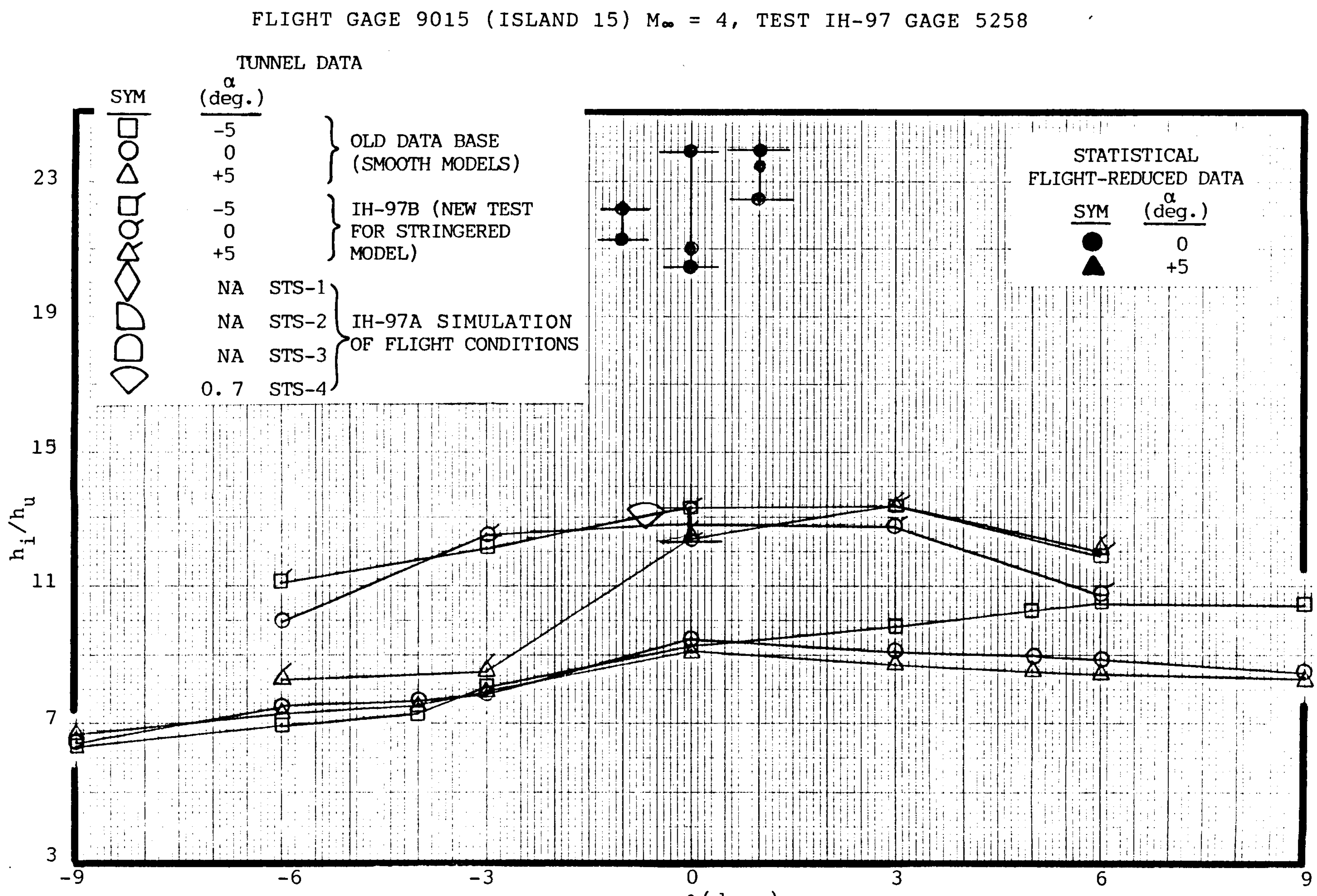

Fig. 4.4b h_i/h_u Data Base from Wind Tunnel and Flight

FLIGHT GAGE 9016 (ISLAND 14) $M_\infty = 3$, TEST IH-97B GAGE 5036

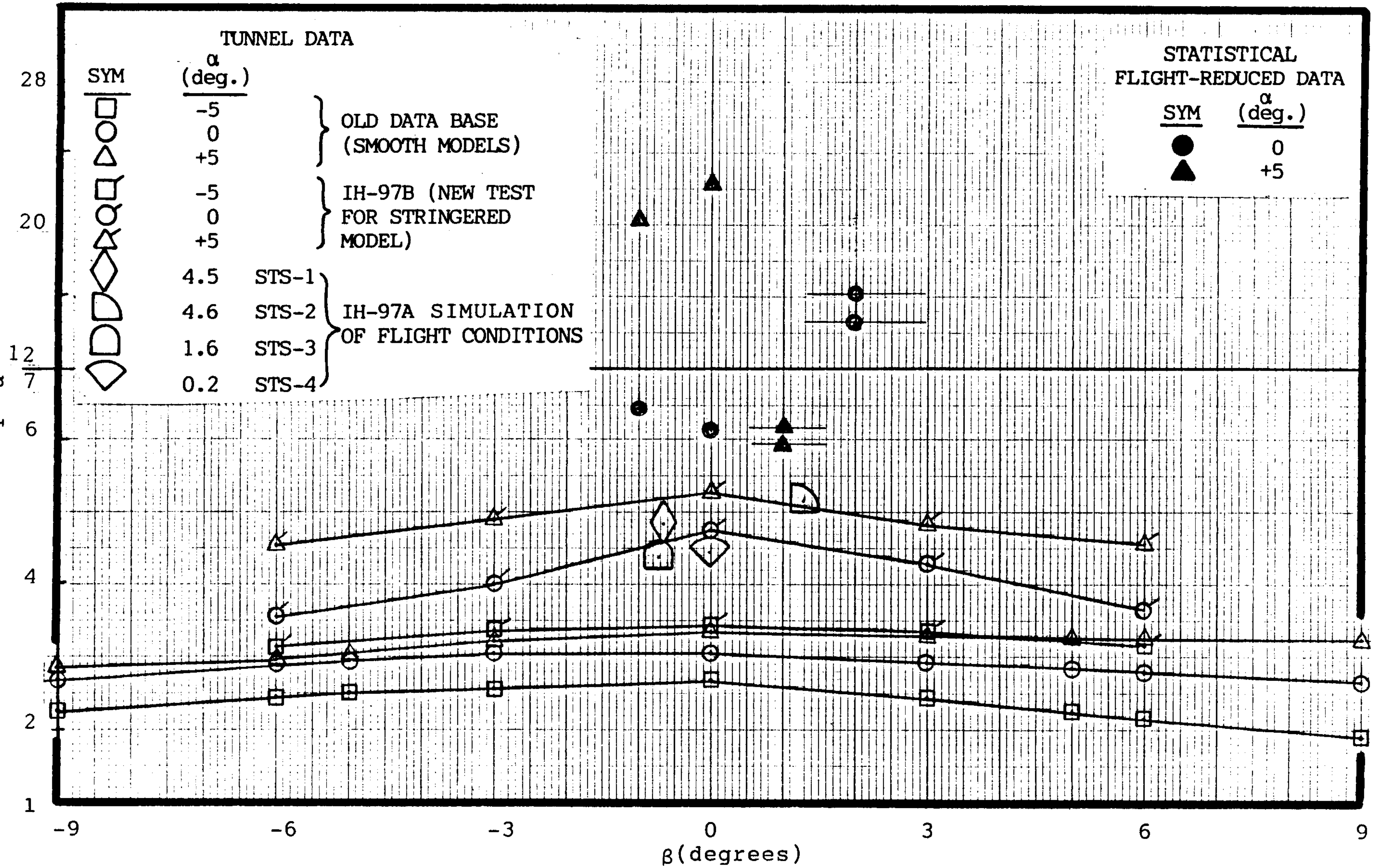

Fig. 4.5a h_i/h_u Data Base from Wind Tunnel and Flight

FLIGHT GAGE 9016 (ISLAND 14) $M_\infty = 4$, TEST IH-97B GAGE 5036

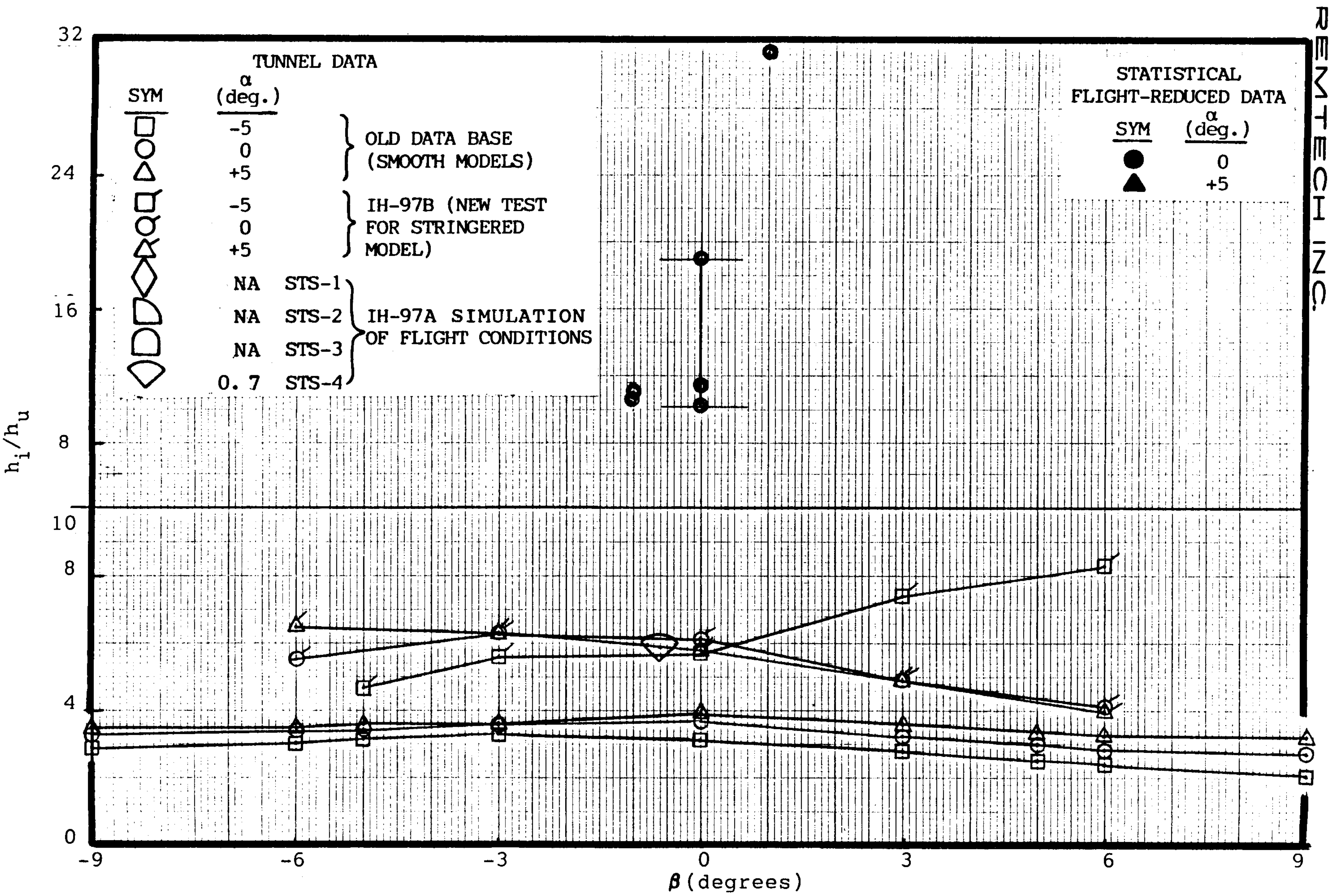

Fig. 4.5b h_i/h_u Data Base from Wind Tunnel and Flight

REMTECH INC.

FLIGHT GAGE 9019 (ISLAND 17(1)) M_∞ = 3, TEST IH-97B GAGE 5040

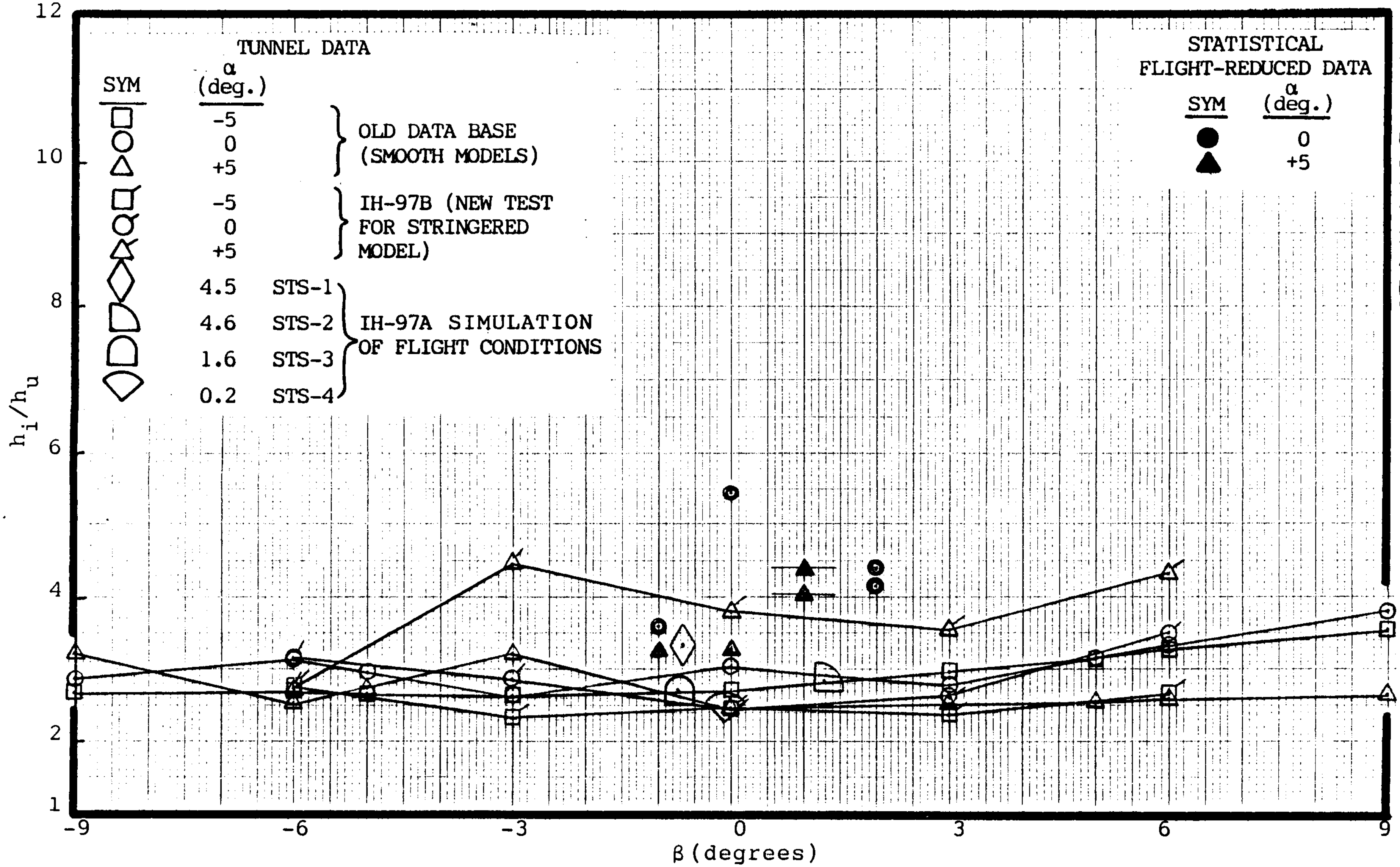

Fig. 4.6a h_i/h_u Data Base from Wind Tunnel and Flight

ORIGINAL PAGE IS
OF POOR QUALITY

FLIGHT GAGE 9019 (ISLAND 17(1)) M_∞ = 4, TEST IH-97B GAGE 5040

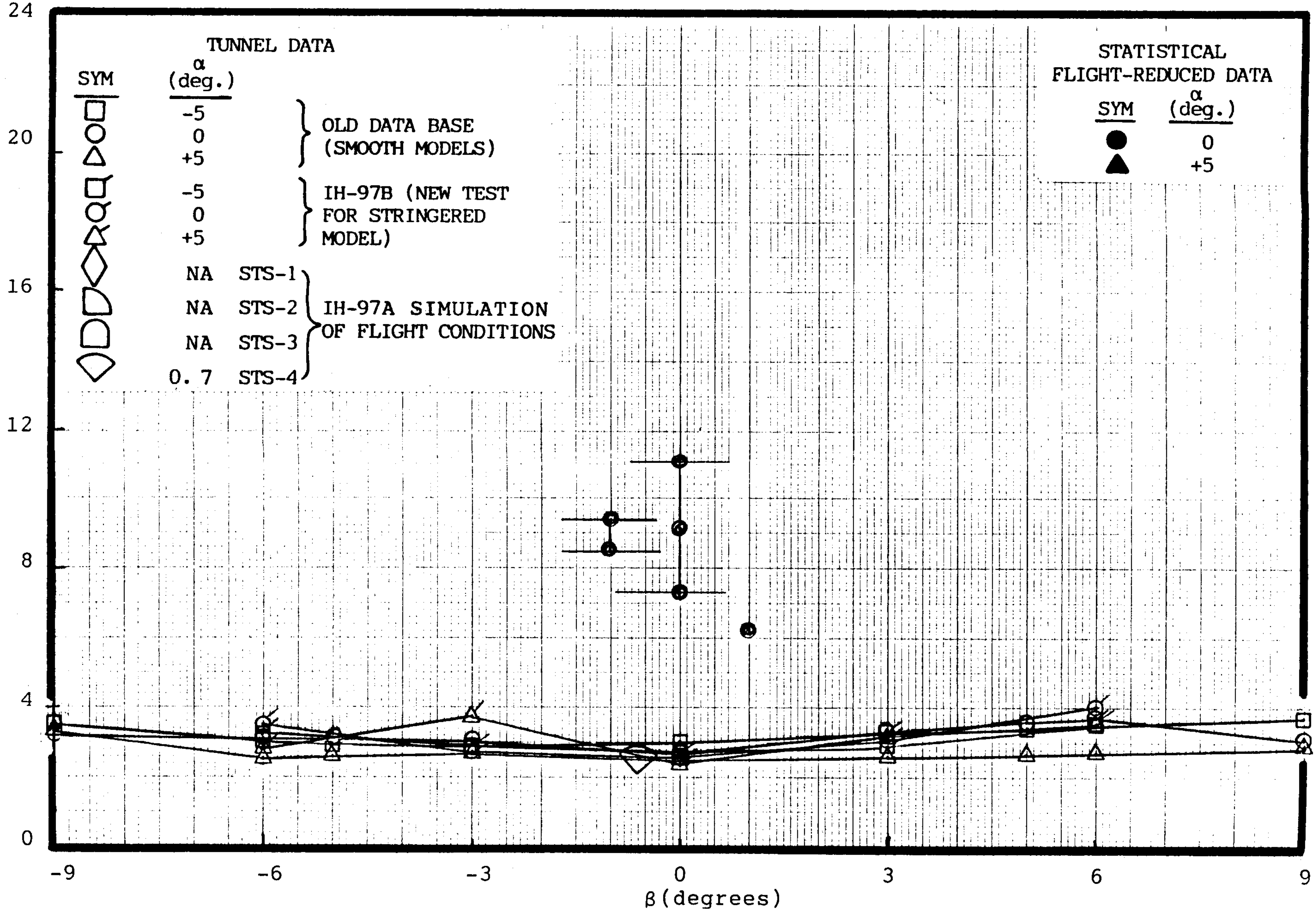

Fig. 4.6b h_i/h_u Data Base for Wind Tunnel and Flight

REMTECH INC.

FLIGHT GAGE 9018 (ISLAND 17(2)) M_∞ = 3, TEST IH-97B GAGE 5039

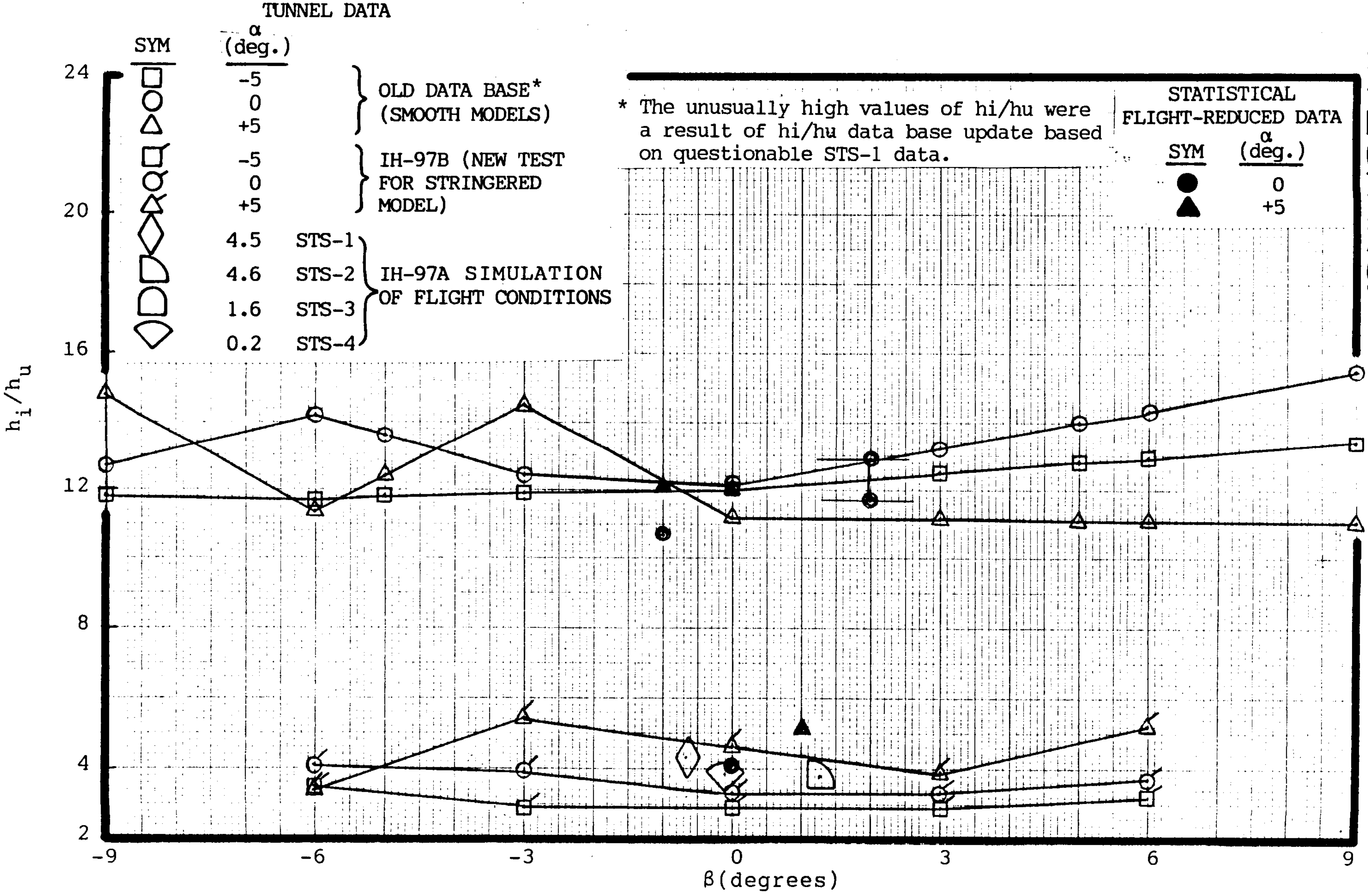

Fig. 4.7a h_i/h_u Data Base from Wind Tunnel and Flight

FLIGHT GAGE 9018 (ISLAND 17(2)) M_∞ = 4, TEST IH-97B GAGE 5039

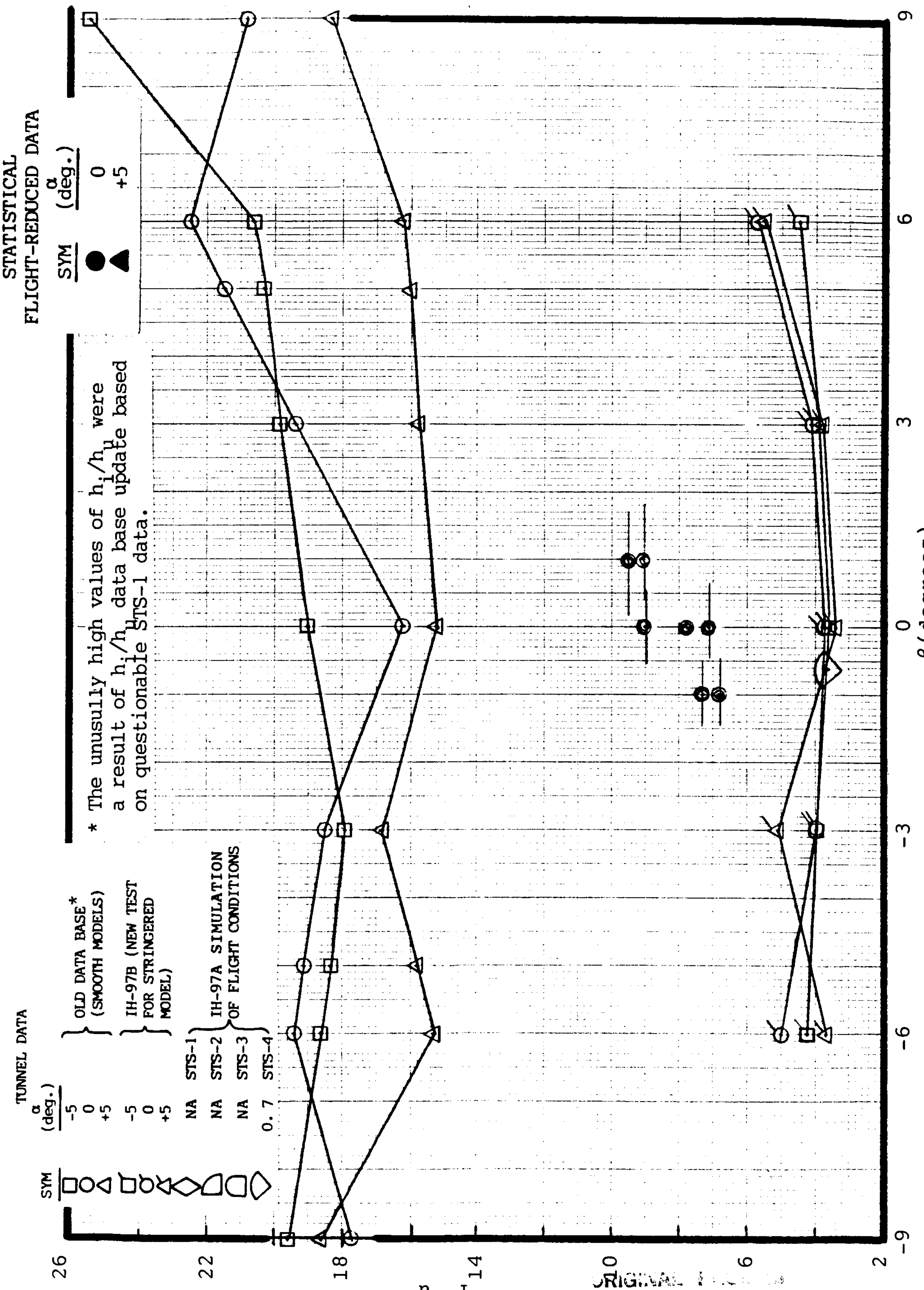

Fig. 4.7b h_i/h_u Data Base from Wind Tunnel and Flight

ORIGINAL PAGE IS OF POOR QUALITY

FLIGHT GAGE 9013 (ISLAND 17(3)) M_∞ = 3, TEST IH-97B GAGE 5041

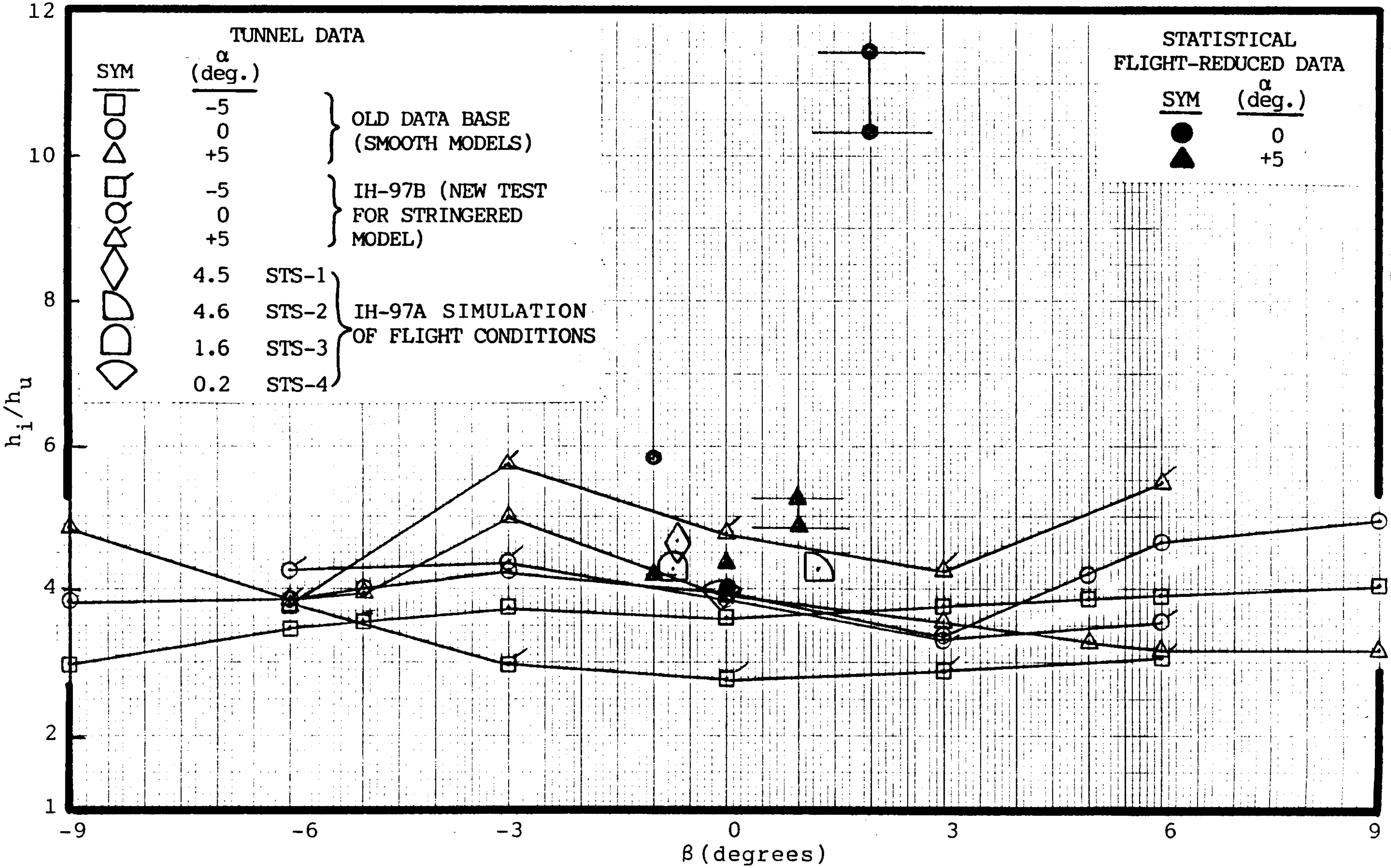

Fig. 4.8a h_i/h_u Data Base from Wind Tunnel and Flight

FLIGHT GAGE 9013 (ISLAND 17(3)) M_∞ = 4, TEST IH-97B GAGE 5041

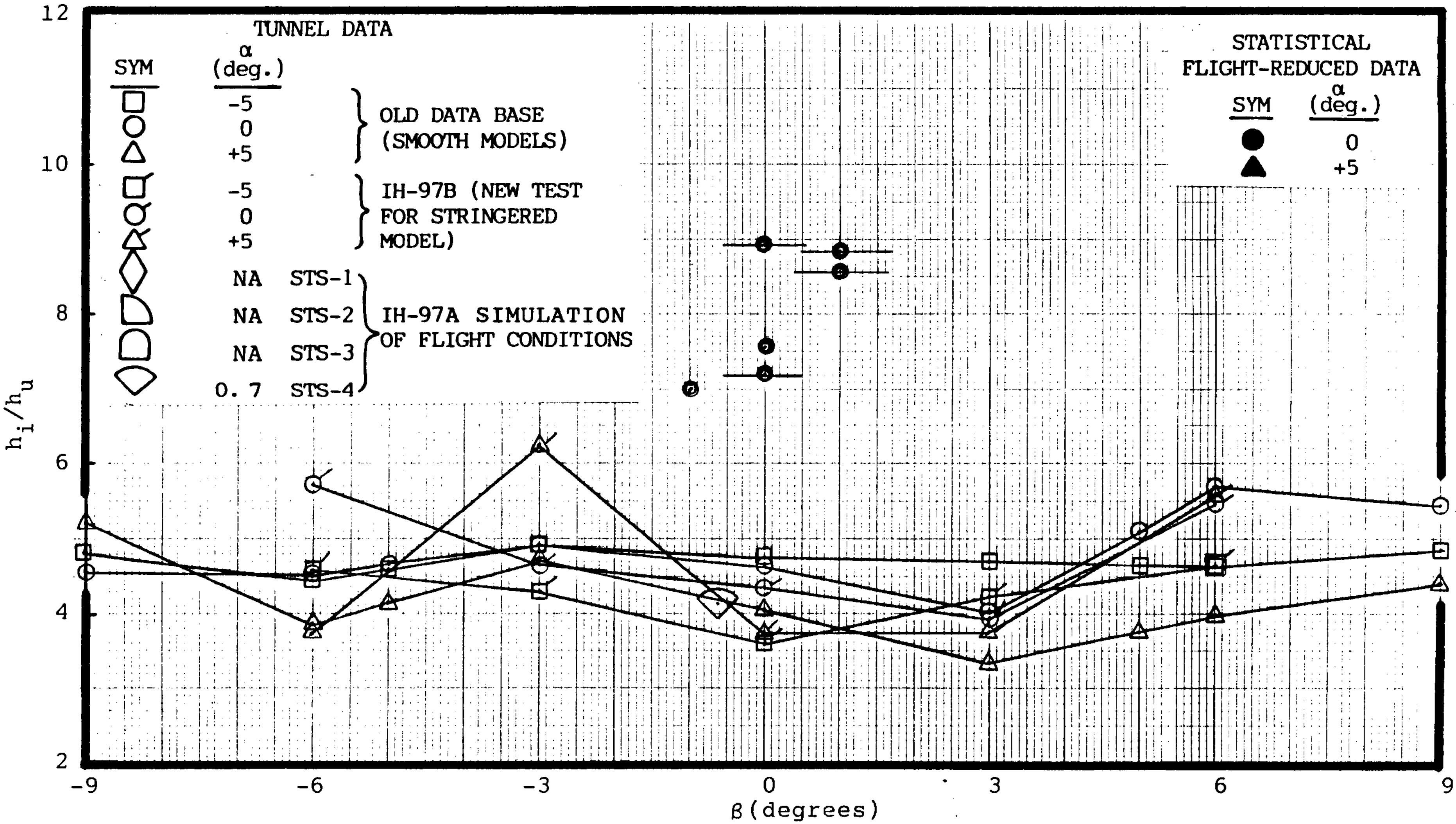

Fig. 4.8b h_i/h_u Data Base from Wind Tunnel and Flight

measurements in the old (α, β) box so that test data could be compared against previous test data. The α, β tested was in the range $-5^o \leq \alpha \leq +5^o$ and $-6^o \leq \beta \leq +6^o$. However, the DFI data base developed from the old test data was in the range $-5^o \leq \alpha \leq +5^o$ and $-9^o \leq \beta \leq +9^o$. The flight-reduced h_i/h_u's were obtained from a statistical analysis reported earlier as a function of M_∞ = 3 and 4 for each gage and h_i/h_u for a few important gages are plotted in Figs. 4.3 - 4.8. Also plotted on these figures is the test data for the stringered IH-97 model (Phases A and B) and the old data base as a function of α and β. It should be noted that in Fig. 4.7 unusually high values of h_i/h_u are present for Gage 9018. This is because of the h_i/h_u data base update (Ref. 19) made for Gage 9018 based on questionable data (now-proven) obtained in STS-1.

4.2.2 TUNNEL TO FLIGHT SCALING

In order to update the flight data base, a scaling procedure has to be utilized. It is quite clear that the flight prediction procedure is comprised of various elements which were developed from various sources other than the Shuttle model tests. Sources of uncertainties lie both in flight data reduction and flight prediction technique. The rationale behind scaling is to determine a flight factor encompassing all the above deficits and also approximations in the flight corrections for temperature mismatch and plume-induced heating.

4.2.2.1 SCALING PROCEDURE

The scaling procedure that will be described here is a version slightly different but along the same lines of the one described in Ref. 27. It has been described earlier that the IH-97 data base is considered superior to the old wind tunnel data base existing in Ref. 1. The differences in the two wind tunnel models basically comprise of better Shuttle geometry simulation in IH-97 test and the provision of stringers on the intertank. So by comparing the old data base with the IH-97 test, a factor can be calculated accounting for geometry differences between the test models.

At any (α , β) combination in the test matrix of the phase B, IH-97 test,

$$f_{1n} = (h_i/h_u)_{IH-97B} \Big/ (h_i/h_u)_{Old\ Data\ Base} \tag{4.1}$$

Taking an average over all α , β combinations for which both sets of data are available,

$$f_1 = \frac{\sum_{n=1}^{N} f_{1n}}{N} \tag{4.2}$$

There are two Mach numbers, M_∞ = 3 and 4, for which these two sets of data are available from the test programs.

It has further been described before that IH-97A phase of the test simulated the STS-1 thru STS-4 flight conditions as far as M_∞ , α and β are concerned. The enthalpy simulation was reasonable, but the Reynolds number simulation was only approximate.

Thus, a factor encompassing all these deficits and approximations in the flight correction factors such as temperature mismatch and plume-induced heating, may be lumped and calculated as follows:

At any M_∞, i.e., trajectory time,

$$f_{2n} = (h_i/h_u)_{Flight} \Big/ (h_i/h_u)_{IH\text{-}97A} \quad (4.3)$$

It was observed from calculations of total roughness factors in Eq. 3.5 that the magnitudes are roughly unity both at Mach 3 and 4. Consequently, those factors were not included in the overall scale factors. Taking an average of over all the STS flights for which IH-97A data are available,

$$f_2\,(M_\infty) = \frac{\sum_{n=1}^{K} f_{2n}}{K} \quad (4.4)$$

Knowing f_1 and f_2, the overall scale factor may be calculated at $M_\infty = 3$ or 4 by

$$\mathcal{F} = f_1 \cdot f_2 \quad (4.5)$$

4.2.2.2 <u>SCALE FACTOR EVALUATION</u>

In order to give details of evaluating scale factors using the procedure described above, DFI Gage 9015 was chosen. Figures 4.4a and 4.4b give h_i/h_u comparison of IH-97B and the existing data base for $M_\infty = 3$ and 4, respectively. These figures also contain h_i/h_u from the IH-97A simulation of STS-1 thru STS-4 flight conditions. Also plotted on these figures are the statistical values of h_i/h_u derived from the STS-1 thru STS-7 flights. It is clearly seen that IH-97B test data is higher than the old data base, and that the flight data is higher than IH-97B data. It is also seen that the IH-97A data lies in the IH-97B data band. The first observation is valid, since the stringer factors are not multiplied with the old data base. The factors, f_1 and f_2, as indicated in Fig. 4.4 are the correction factors needed to calculate the overall scale factor. It must be noted here that the evaluation of $f_2(M_\infty)$ is accomplished by using Eqs. 4.3 and 4.4, where the ratios of h_i/h_u in flight to that in the wind tunnel with exact Mach number and (α , β) simulation were calculated and averaged. The following table was prepared for flight freestream Mach numbers ranging from 2.5 to 4.

Table 4.1 - Calculations of f_1, f_2 and $\mathcal{F}$ for Gage 9015 (Island 15)

Factor	M_∞						
	2.5	2.75	3.0	3.25	3.5	3.75	4.0
f_1	---	----	1.46	----	---	----	1.36
f_2	1.07	1.24	1.39	1.59	1.615	1.33	1.68
$\mathcal{F}$			2.03				2.38

The blanks for f_1 in Table 4.1 may be filled by interpolating f_1 between Mach 1 and 3 and between Mach 3 and 4 values on a $\log_{10}$ - $\log_{10}$ scale. (f_1 at Mach 1 is assumed to be unity)

This procedure was applied to various DFI locations and scale factors were evaluated, and compared in Table 4.2 with those calculated for these DFI locations in Ref. 27. It is generally found that the current scale factors are somewhat lower than the ones

Table 4.2 CALCULATION OF SCALE FACTORS

M_∞	Island No.	Flight Gage	IH-97 Gage	Baseline W.T. Gage	Flight Gage		$\frac{(h_i/h_u)_{IH-97}}{(h_i/h_u)_{Base}}$		$\frac{(h_i/h_u)_{FLT}}{(h_i/h_u)_{IH-97}}$		W*	
					X_T	θ_T	Old Data	Current Data	Old Data	Current Data	Old Data	Current Data
3.0	14	9016	5036	----	937.4	251.4	1.530	1.40	3.750	2.07	5.74	2.90
	16	9014	5038	(843)844	937.4	288.6	1.550	1.57	1.250	1.30	1.94	2.04
	12	9017	5035	(751)752	948.5	180.0	0.800		2.211		1.77	
	15	9015	5258	824	956.2	270.0	1.440	1.46	1.320	1.39	1.90	2.03
	18	9011	5042	----	976.0	25.0	1.000		2.800		2.80	
	20	9021	5043	832	1030.1	270.0	1.340		0.948		1.27	
	23	9022	5044	753	1073.8	180.0	0.580		2.556		1.48	
	17-1	9019	5040	----	1084.4	2.5	1.190	1.11	1.460	1.47	1.74	1.63
	17-2	9018	5039	----	1098.5	2.5	1.220	0.30	2.143	1.78	2.61	0.53
	17-3	9013	5041	----	1110.4	2.5	1.140	1.02	1.470	1.17	1.68	1.19
4.0	14	9016	5036	----	937.4	251.4	1.500	1.81	5.340	1.82	8.01	3.29
	16	9014	5038	(843)844	937.4	288.6	2.300	1.77	1.170	1.30	2.69	2.30
	12	9017	5035	(751)752	948.5	180.0	1.000		1.460		1.46	
	15	9015	5058	824	956.2	270.0	1.540	1.36	1.950	1.68	3.00	2.28
	18	9011	5042	----	976.0	25.0	1.000		3.840		3.84	
	20	9021	5043	832	1030.1	270.0	1.350		0.550		0.74	
	23	9022	5044	753	1073.8	180.0	0.870		1.960		1.71	
	17-1	9019	5040	----	1084.4	2.5	1.210	1.06	3.030	3.21	3.67	3.40
	17-2	9018	5039	----	1098.5	2.5	1.070	0.24	4.340	1.86	4.64	0.45
	17-3	9013	5041	----	1110.4	2.5	1.040	1.03	2.530		2.63	

*NOTE:

$$W = \left[\frac{(h_i/h_u)_{IH-97}}{(h_i/h_u)_{Old\ W.T.\ Data\ Base}}\right]_{\text{All } \alpha\text{'s and all } \beta\text{'s}} \cdot \left[\frac{(h_i/h_u)_{Flight}}{(h_i/h_u)_{IH-97}}\right]_{\alpha,\beta}$$

calculated before. Since the previous scale factors have already been used in the redesign of SLA (Super Light Ablator) on the ET, they are conservative and pose no danger of underdesign.

Finally, one word of caution must be given about the flight scale factors evaluated by the procedure given here and documented in Table 4.2. It has been pointed out repeatedly in the text that temperature mismatch effects for the interference measurements have been assumed to be unity, whereas, in reality, these may be higher than unity, as in the case of undisturbed measurements on the ET. In fact, a computer code called ETCHECK was written by the REMTECH personnel (Ref. 28) where scale factors for the interference regions were assumed to be unity after considering approximate temperature mismatch factors in these regions and correcting the flight-measured data. However, the assumption of unity temperature mismatch factor in the current study was more a guess than based on scientific data. Therefore, the author reserves the right to update these scale factors in the future based on experimental and/or analytical investigations.

Section 5.0

CONCLUSIONS & LESSONS LEARNED

5.1 CONCLUSIONS

The Space Shuttle OFT flights provided, for the first time, a set of flight measurements which could be used to update the existing math models. The ET was subjected to progressively hotter environments in the DFI flights, and the measured environments were reasonably predicted in most of the DFI locations by updated math models. Although there were obvious limitations in wind tunnel testing insofar as geometry and flight condition simulations are concerned, these STS flights enabled us to bridge the gap in order to build adequate mathematical models for the DFI locations. The problem of temperature mismatch in the shock-interaction regions has been "lumped" in the scale factors that were derived earlier. This was done so that new TPS design evaluations with view towards reducing TPS weight could proceed.

5.2 LESSONS LEARNED

5.2.1 RECOMMENDATIONS

1) The scaling procedure adopted in this report is adequate for regions where the nose shocks from the other Shuttle components impinge the ET surface. The interference factor in these regions is a strong function of local upstream Mach number and can be

scaled to flight as a function of Mach number only, providing that Reynolds number is simulated in the tunnel.

2) No sound basis, however, exists to scale h_i/h_u from wind tunnel to flight in regions where multiple shock interactions exist and flow separations take place. It is very likely that the interference factor may be functions of such quantities as Mach number, Reynolds number, boundary layer thickness etc. In fact, it has been shown from the flight data earlier that h_i/h_u or St_i^*/St_u^* could vary both with Mach number and Reynolds number.

3) Temperature mismatch effects can be successfully factored out of the flight data in undisturbed regions. However, temperature mismatch effects in the interference regions are not dealt with in the existing literature and consequently, were not factored out of the flight measurements. Both numerical experimentation and wind tunnel testing must be conducted to quantify this effect.

5.2.2 PRECAUTIONS

1) Before starting to design a space vehicle, it is imperative that a good wind tunnel data base be generated. This data base must be analyzed for soundness by using the available analytical tools. In fact, it is the judgement of the REMTECH personnel, including this author, that the ET data base was very good. This data base was derived from scaled models tested at Mach numbers and Reynolds numbers which simulated the flight conditions in a design trajectory. While doing this, various model sizes and wind tunnel facilities were used to collect various sets of data.

2) While simulating the flight conditions in the tunnel, care must be taken to simulate the flow in the right regime. One such problem was discovered after the flight of STS-1. The data base which the ET nose provided was actually transitional, but it gave the impression of being interference heating data (Details are given in Ref. 1). As a result, the ET nose cone was under-designed. However, after STS-1 data was analyzed, the data base for the nose was changed and the TPS was changed from SLA to MA-25.

3) The ET protuberance wind tunnel data base was generally not very good to scale to flight. The most important reason was the scaled size of these protuberances that were attached to the wind tunnel model. As a result, the only good data base for the ET protuberances was derived from the Shuttle DFI flights.

4) While conducting the wind tunnel tests on the ET models mounted on tail stings, sting effects were apparent in the heat-transfer and pressure data measured towards the aft section of the vehicle. Thus, care must be exercised in using the measured data from the wind tunnels.

5.2.3 CHOICE OF SENSORS

1) When the ET instrumentation was initiated in the Shuttle program, there was little experience with measuring heating rates on an irregular foam surface such as the SOFI. At that time, no rigorous analysis was made to account for temperature mismatch. As a result, temperature mismatch errors of the magnitudes present in

the OFT measurements confounded many other effects.

2) The choice of sensors for future space vehicles must consider this effect and efforts must be made to reduce the temperature mismatch effects on the measurements.

3) Temperatures along with heat flux should be measured so that one can be derived from the other. This would help eliminate erroneous readings in a much easier fashion.

4) Pressure gages must be installed adjacent to each of the heat-transfer gages to define the flowfield, thus eliminating conjectures in the flight data analysis.

Section 6.0

REFERENCES

1. Praharaj, S.C. and Engel, C.D., "STS-1 ET Aerothermal Flight Evaluation," REMTECH, Inc., Huntsville, Alabama, Technical Report RTR 041-1, April 1982.

2. Praharaj, S.C. and Engel, C.D., "Initial Shuttle External Tank Aerothermal Flight Evaluation," Entry Vehicle Heating and Thermal Protection Systems: Space Shuttle, Solar Starprobe, Jupiter Galileo Probe, AIAA Progress in Astronautics and Aeronautics, Volume 85, edited by Paul E. Bauer and Howard E. Collicott, AIAA, New York, 1983, pp. 325-348.

3. Jones, I.P., "External Tank Aerothermodynamic Flight Instrumentation -- Definition and Operation," NASA Marshall Space Flight Center, Alabama, ED33-79-66, October 1979.

4. ESDB - Available at NASA Marshall Space Flight Center.

5. MIPS - Available at NASA Marshall Space Flight Center.

6. Praharaj, S.C. and Engel, C.D., "STS-1 Raw Measured Data for the Space Shuttle External Tank," REMTECH Report RTN 041-6, REMTECH, Inc., Huntsville, Alabama, April 1981.

7. Hulsey, D.R. and Praharaj, S.C., " ET STS-2 Raw Ascent Flight Data," REMTECH Report RTN 041-9, REMTECH, Inc., Huntsville, Alabama, January 1982.

8. Hulsey, D.R. and Praharaj, S.C., "STS-3 Raw Measured Data for the Space Shuttle External Tank," REMTECH Report RTN 041-11, REMTECH, Inc., Huntsville, Alabama, May 1982.

9. Hulsey, D.R. and Praharaj, "STS-4 Raw Measured Data for the Space Shuttle External Tank," REMTECH Report RTN 041-12, REMTECH, Inc., Huntsville, Alabama, July 1982.

10. Beck, D., Schmitz, C.P., and Praharaj, S.C., "STS-5 Raw Measured Data for the Space Shuttle External Tank," REMTECH Report RTN 041-13, REMTECH, Inc., Huntsville, Alabama, January 1983.

11. Hulsey, D.R. and Praharaj, S.C., "STS-7 Raw Measured Data for the Space Shuttle External Tank," REMTECH Report RTN 041-14, REMTECH, Inc., Huntsville, Alabama, August 1983.

10. Hulsey, D.R. and Praharaj, S.C., "Shuttle External Tank Developmental Flight Heating Rate Comparisons," REMTECH, Inc., Huntsville, Alabama, Technical Note 041-16, August 1983.

11. MINPRE Version of MINIVER - Available at REMTECH, Inc., Huntsville, Alabama.

12. Engel, C.D., "FCAP Program Input Guide," REMTECH, Inc., Huntsville, Alabama, Technical Note RTN 041-3, March 1980.

13. RATE1 Code - Prediction Code Available at REMTECH, Inc., Huntsville, Alabama.

14. Rubesin, M.W., "The Effects of an Arbitrary Surface Temperature Variation Along a Flat Plate on the Convective Heat Transfer in an Incompressible Boundary Layer," NACA TN 2345, April 1951.

15. Westkaemper, J.C., "On the Error in Plug-Type Calorimeters caused by Surface Temperature Mismatch," Journal of Aerospace Sciences, November 1961, pp. 907-908.

16. Eckert, E.R.G., "Survey on Heat Transfer at High Speeds," ARL 189 (AD 274-109), December 1961.

17. Tong, H., "Users Manual - Nonequilibrium Chemistry Boundary Layer Integral Matrix Procedure," Aerotherm Dept. UN-73-37, July 1973.

18. Kutler P., H. Lomax, and R.F. Warming, "Computation of Space Shuttle Flow Fields Using Noncentered Finite-Difference Schemes," AIAA Paper No. 72 - 183, January 1972.

19. Praharaj, S.C., "Interference Data Base Update Based on STS-1 Flight Data," Unpublished Report (Data available at REMTECH, Inc.)

20. Hung, F.T., Greenschlag, S.N., and Scottoline, C.A., "Shock-Ware-Boundary-Layer Interaction Effects on Aerodynamic Heating," Journal of Spacecraft and Rockets, Volume 14, No. 1, January 1977, pp. 25-31.

21. ETFLIT Code - Available at REMTECH, Inc., Huntsville, Alabama.

22. Somers, R.E. and Warmbrod, J.D., "External Tank Acreage Heat Transfer Data Tables for Test IH-97B, "REMTECH, Inc., Huntsville, Alabama, Technical Memo RM 032-8, March 1983.

23. Marroquin, J., DATAMAN Report for Test IH-51A, DMS-DR-2393, NASA-CR-167, 169, Dec. 1983.

24. Carroll, P.R., DATAMAN Report for Test IH-11, DMS-DR-248, NASA-CR-160, 524, Oct. 1980.

25. Carroll, P.R. and Wittliff, C.E., DATAMAN Report for Test IH-43, DMS-DR-2319, NASA-CR-151, 771, April 1979.

26. Quan, M. and Wittliff C.E., DATAMAN Report for Test IH-33, DMS-DR-2249, NASA-CR-151, 775, April 1979.

27. Warmbrod, J.D. and Crain, W.K., Unpublished Report (Data available at REMTECH, Inc.)

28. Warmbrod, J.D., ETCHECK Code - Available at REMTECH, Inc., Huntsville, Alabama.